THE UNIVERSITY OF CHICAGO

TARGETED DESIGN OF DYNAMIC AND MECHANICAL BONDS TOWARDS FUNCTIONAL, RESPONSIVE POLYMERIC NETWORKS

A DISSERTATION SUBMITTED TO

THE FACULTY OF THE PRITZKER SCHOOL OF MOLECULAR ENGINEERING

IN CANDIDACY FOR THE DEGREE OF

DOCTOR OF PHILOSOPHY

BY

KATIE MARIE HERBERT

CHICAGO, ILLINOIS

AUGUST 2019

To all the amazing women in my life, past, present, and future, who gave me the courage and the confidence to pursue my dreams.

Table of Contents

List of Figures

List of Schemes

List of Tables

Acknowledgements

The journey towards higher education follows a twisty and bumpy road, but the people that I've met along the way have helped me keep moving forward and for that, I am forever grateful. There are a few people that I would especially like to thank for the guidance during my graduate experience.

First, I would like to thank my advisor, Prof. Stuart Rowan, whose creative, out-of-the-box ideas captured my scientific imagination and gave this thesis its start. Through the years, his advice and instruction has given me the tools and the insight to pursue my doctoral degree. I would also like to thank the students and faculty in the Macromolecular Science and Engineering Department at Case Western Reserve University for their support in the early years of my degree. A huge thanks goes out to the Rowan group members – past and present – who help to keep the lab and each other's sanity intact. I am supremely grateful to the students, faculty, and staff at the Pritzer School for Molecular Engineering for welcoming me into their world and for their support as I completed my dissertation work.

Finally, I would to thank my friends and family who have stayed by my side through the good times and bad and have always been my cheering section.

Abstract

The implementation of dynamic chemistries into polymeric materials has led the way towards the development of functional materials that express a multitude of targeted responses. The use of dynamic covalent chemistries as well as mechanical bonds have shown great potential in the rapidly growing field of stimuli-responsive polymer materials. This dissertation will focus on moving towards tunable, functional polymer networks based on two different binding motifs: the dynamic thia-Michael addition and the doubly-threaded [3]-rotaxane. Although there is a great deal of dynamic covalent chemistries currently in use for functional materials, the thia-Michael addition reaction has only recently begun to be explored as a reversible bond in polymeric materials. Of particular interest is the benzalcyanoacetate Michael acceptor that undergoes dynamic exchange with thiols under ambient conditions. By mindfully adjusting the chemical composition of the Michael acceptor, it is possible to tune the chemical equilibrium of the thia-Michael reaction and hierarchically program thermomechanical and morphological properties of thia-Michael networks. The dynamic, phase separated films exhibit a range of functionalities including shape memory response and adhesive applications. Similarly, the development of an interlocked binding structure for crosslinked materials will lead to a host of unexplored responsive properties. Utilizing a metal-templated approach to target an interlocked [3]-rotaxane, progress towards the development of slide-ring gel materials will be described.

1 Multi-stimuli, multi-responsive polymer materials

[*] This chapter was adapted from: Herbert, K. M.; Schrettl, S.; Rowan, S. J.; Weder, C. Solid-state multi-stimuli, multi-responsive polymeric materials. *Macromolecules* **2017**, *50*, 8845-8870.

1.1 Introduction

50 years ago, the field of polymer science had emerged from its youth and was growing rapidly. Critical advancements were being made in the synthesis of polymers, the furthering of the understanding of the physics of macromolecules and the structure-property relationships of polymeric materials, as well as in the development of new techniques to probe the properties of these emerging materials. A key objective during this time, when plastics were prominently prophesied to have a great future,[*] was to design and develop polymers that maintain their properties across a broad range of different environmental conditions and, in particular, offer high stability over a large time-temperature space. These efforts led to the commercialization of many long-lived, robust materials that had a tremendous influence in virtually all market segments that impact our daily lives, including food packaging, automotive, and textiles industries. The inaugural issue of *Macromolecules* is a beautiful testament of the research of the field at the time: seven of the nineteen papers focused on either the synthesis of new thermally robust polymers[1] or featured studies aimed at understanding and preventing thermo-[2-4] or photo-degradation[5-7] in such materials. Much has changed in all aspects of polymer science in the intervening 50 years. One

[*]As prophesied, for example, by the actor Walter Brooke in his role as Mr. McGuire in the movie "The Graduate" in 1967: "There is a great future in plastics."

important current area of research that has emerged during this time is the field of stimuli-responsive polymers,[8-11] a subset of which is highlighted in this opening chapter. At first glance, the fundamental idea of materials whose properties are designed to change in response to an external stimulus appears like a 180-degree reversal when considering the goals of early polymer research. However, robust performance in a large parameter space is also important for stimuli-responsive polymers and ideally their property change occurs only in an intended, predictable, and purposeful way upon exposure to a specific stimulus such as heat, light, chemicals, mechanical force, and electric or magnetic fields. Prominent responses that have been demonstrated include changes in mechanical properties, color, fluorescence, shape, or transport (electrical, thermal, chemical) characteristics, and the list of functions that can be achieved only keeps growing. While the term '*stimuli-responsive polymer*' had been used in a few instances in the mid to late 1980's, the expression only gained significant popularity in the scientific literature in the 1990's.[12-14] Examples of what the community nowadays calls stimuli-responsive polymers did exist before, but at the time, these materials were referred to as stimuli-sensitive polymers,[15] environmentally-responsive[16] or environmentally-sensitive polymers,[17] stimuli-reversible polymers,[18] or polymers with phase transitions.[19,20]

The term phase transition harkens to one specific type of mechanism that can be employed to induce a change in the properties of a polymer. There are several types of phase transitions that have been used over the years to impart polymers with stimuli-responsive behavior, including the obvious melting/crystallization and glass transition, as well as transitions involving a lower critical solution temperature (LCST) or upper critical solution temperature (UCST), or liquid crystalline

transition/clearing points. For polymers that display an LCST and/or UCST, the temperature-controlled mixing/demixing of different phases in a solution can be exploited to access responsive materials. Similar phase mixing/demixing behaviors can also be employed in the solid state, for example in block copolymers or ionomers. The controlled breaking or formation of either non-covalent (supramolecular) or covalent bonds is another general approach that can result in pronounced changes of a polymer's structure and consequently its physical properties.[8,10] Controlled conformational or geometric changes (e.g. *cis* ↔ *trans*) within a polymer chain represent another mechanism that can lead to significant property changes. The formation of (nano)composites comprised of a polymeric component and one (or more) filler(s) or the creation of blends of different polymers opens the door to a wide range of additional effects that can be exploited.[21] In addition to any or all of the above mechanisms, the possibility to control interactions between the different interfaces (e.g., polymer-filler, filler-filler, polymer-polymer) can serve to alter the properties of these materials and it is also possible to harness effects that arise from the spatial arrangement of filler particles, for example in photonic structures. Stimuli-responsive composites can also be accessed through the use of one inherently stimuli-responsive component, such as liquid-filled capsules that release their cargo when broken/degraded by a stimulus, while the other component(s) impart other useful properties, for example mechanical stability.[22]

Much of the early work on stimuli-responsive polymers has been focused on materials that (ideally) display one specific property change in response to one pre-defined stimulus.[10,23-28] As such, a wide range of single-stimulus, single-response materials have been developed. One key challenge for this specific class of polymers is to find ways to render their responses highly specific

such that a desired response is only triggered by one stimulus and that a given stimulus causes only one defined response. Indeed, many responsive polymers exhibit some form of (undesired) multi-responsiveness and some of the early examples of multi-stimuli, multi-responsive (MSMR) materials were borne through some lack of specify. Of course, the idea of specifically designing MSMR materials has gained significant traction in recent years. Indeed, if more than one inherently stimuli-responsive component is employed, it is at least conceptually possible to create *multi-responsive polymers*, i.e., materials that respond to different stimuli and/or offer different responses. Somewhat akin to living systems, which have evolved to adapt and respond in complex ways to (combinations of) different environmental cues, multi-responsive polymers can offer a broad range of complex properties and functions. Depending on the design, it is also *a priori* possible to mimic the operation of logic gates on the molecular level[29] and transpose such characteristics into macroscopic materials responses. As will be discussed later, there are many examples of multi-responsive polymer systems in which one stimulus triggers two or more (designed) responses, whereas more complex functions such as triggering two separate responses in an orthogonal manner (i.e., with different stimuli), or materials that require two separate stimuli to trigger an effect (i.e., an "and" function) have proven more difficult to realize. Recent perspectives in the context of (semi)conducting conjugated polymers[30] also apply here, "ideas are cheap, and making things work is the real challenge." Nevertheless, the field has emerged to a point where it is clear that the fundamental idea of creating materials that respond to different stimuli in different ways offers the prospect of accessing completely new, emergent, functions. Looking beyond the horizon (and putting for a moment the practical challenges associated with

the realization of increasingly complex architectures aside), multi-responsive polymers are well poised to serve as the basis for an approach referred to as systems polymer science.

Much work has been devoted to the investigation of multi-responsive polymers in solutions or gels,[31-33] and a number of excellent recent reviews have summarized the related research activities.[9,23,34-46] Multi-stimuli, multi-responsiveness is arguably more difficult to achieve in solids, but this is the state of matter in which the vast majority of polymers are actually used. It therefore stands to reason that this is also the domain in which complex response functions could have the greatest significant impact. Examples of possibly useful materials that have recently been realized include healable polymers in which shape-memory driven actuation leads to improved healing[47] and nanocomposites that combine mechanical adaptation with a drug-release to suppress inflammatory effects[48] when used as biomedical implants.[49,50] Multi-stimuli, multi-responsive materials are also attractive in situations that necessitate limiting the weight of material that can be carried, for example by a solider in the battle field, an astronaut on Mars, or simply a hiker in the wilderness, if different functions, depending on the situational needs, are to be offered. In this Perspective article, we sought to summarize the most important mechanisms used by researchers in the field, highlight important developments, discuss examples that may provide at least a glimpse of the potential (and also the challenges) of the general design approach, and outline some potential new directions and opportunities for the next decade and beyond.

1.2 Stimuli-Responsive Materials – the Basic Mechanisms

To set the scene, a brief summary of some of the most prominent stimuli-induced functions that have been realized in solid polymeric materials over the years and the general concepts that have been employed to access these functions is provided.

Healing and self-healing: One area that has attracted considerable interest in the last decade is the creation of polymers that can be healed or which can heal autonomously.[51-57] In many instances this was demonstrated by removing a scratch or other defect or by mending two broken pieces, usually with the goal of restoring the material's original mechanical properties, but the approach is also applicable to reinstate other properties, e.g. transport (electrical, ions, thermal, etc.), optical characteristics, and so on. Two conceptually different types of healing mechanisms can be distinguished: those that require an external stimulus, such as heat or light (stimuli-responsive healing), and those that offer autonomous healing (self-healing). As it has become common practice to refer to materials based on either mechanism as "self-healing", it is perhaps worthwhile pointing out that in many scenarios where "self-healing" or "autonomous healing" is touted, some form of external action or activation is required, such as bringing the two pieces in contact with each other to allow healing or thermal activation. It is also important to realize that some mechanisms which enable truly autonomously healing can limit the practical usefulness of the resulting materials, for example, room temperature reversible dynamic bonds can result in significant unwanted creep. There are four major mechanisms that have been used to access healable materials, including (1) polymer flow, (2) dynamic/reversible bonds, (3) formation of highly reactive species during damage, and (4) polymer embedded with "healing monomer" filled

microcapsules (Figure 1.1). The various approaches have their pros and cons with different mechanisms being more useful for different applications.

Figure 1.1. Four common mechanisms used to create healable or self-healing polymeric solids: polymer flow (blue), dynamic/reversible bonds (pink), formation of highly reactive species (green), and monomer-filled capsules (amber).

Any linear polymer can in principle be healed by heating above its glass transition temperature (T_g) or, in the case of semicrystalline polymers, melting temperature (T_m), for a sufficient time.[58] The main problem with this approach is that the healing efficiency depends on the diffusion of high-molecular-weight species, which is slow at realistic/useful temperatures and therefore limits the healing process. To circumvent this problem, dynamic (covalent or

supramolecular) bonds can be incorporated into a polymer backbone.[10] This concept exploits the fact that the weaker dynamic bonds will be preferentially broken (either during the damage process or upon exposure to an external stimulus) to yield low-molecular-weight species, which in turn can diffuse more easily/rapidly and lead to faster healing. The advantage of this approach is that the original polymer structure is restored upon healing, which means that the original mechanical properties can be fully reinstated and that the material can be healed repeatedly. However, the addition of weaker/dynamic bonds generally affords materials that are mechanically less robust than their covalently connected counterparts, and unless phase separation effects are exploited to stabilize the dynamic bonds, creep is often an issue, as the dynamic bonds can also re-arrange under normal mechanical load. Alternatively, there are two basic concepts in which the need for diffusion of the polymer strands is omitted, both of which rely on the mechanical damage to generate or release reactive species that are responsible for the healing. For example, if the breaking of the polymer chain results in reactive (radical) species and within the material there are radical "trapping sites", then when one bond breaks and a new bond can be formed.[59] Another approach is to use monomer-filled microcapsules that are embedded within a polymer.[60-63] If the microcapsule is broken during damage, the monomer is released and polymerized (either by a catalyst embedded within the polymer or by exposure to air) to result in healing of the damage. These latter two cases have the distinct advantage that the damage itself can be used as the stimulus to trigger the healing, but the material after healing is not the same as the original matrix and generally will not have exactly the same properties of the original, undamaged material.

Shape memory and shape changing: The design of polymers that have the ability to change their shape in a controlled and predicable way has garnered a lot of attention in the last few decades and there are a number of ways that this can be achieved. One of the most widely explored effects in this area is that of shape memory, which is the ability of a material to be deformed into a temporary fixed state and then recover its original shape upon application of a stimulus.[64-71] Polymers can be equipped with shape-memory characteristics by merging rubber elasticity, which is generally introduced via cross-linking a low-T_g polymer by either physical or covalent means, with a fixing element that can be switched by an external stimulus to enable (i.e., during programming and recovery) or prevent (i.e., to fix/trap a temporary shape) elastic recovery. Conceptually, the easiest way to think about this is that there are two different cross-linking units: one cross-linker is permanent, while the other can be switched off during deformation and then switched back on for fixing. The most widely used fixing elements are the glass transition of an amorphous phase or the melting of crystalline domains. Shape memory materials based on such mechanisms generally need to be heated above T_g or T_m, deformed, then cooled down to below T_g or T_m before the stress is removed. Alternative fixing mechanisms have been devised to expand the property profiles as well as the nature of the stimulus that can be used to trigger the shape memory effect. For example, liquid crystal elastomers exhibit shape memory properties where the liquid crystal clearing temperature ($T_{LC\text{-}I}$) is used as the "fixing" transition.[72,73] Materials based on this framework are elastic in both states and the orientation of the mesogen impacts the overall shape of the film, which allows extension/contraction actuation modes, in addition to bending or twisting modes more commonly seen in the T_g or T_m-based systems. Dynamic/reversible cross-

links (either supramolecular or covalent) represent another way to achieve fixing. One advantage of reversible bonds is that they are often susceptible to stimuli other than heat, such as light or chemicals, allowing access to photo- or chemo- shape memory materials, which is important in the context of multi-stimuli, multi-responsive materials. Another concept is fabrication of (nano)composites that consist of an elastic matrix and a filler that permits fixing the temporary shape.[74] This can be achieved by either the formation/break-up of a mechanically reinforcing filler network on account of changing the interactions among the individual filler particles or a phase transition of the filler itself, which can be induced by a variety of stimuli.

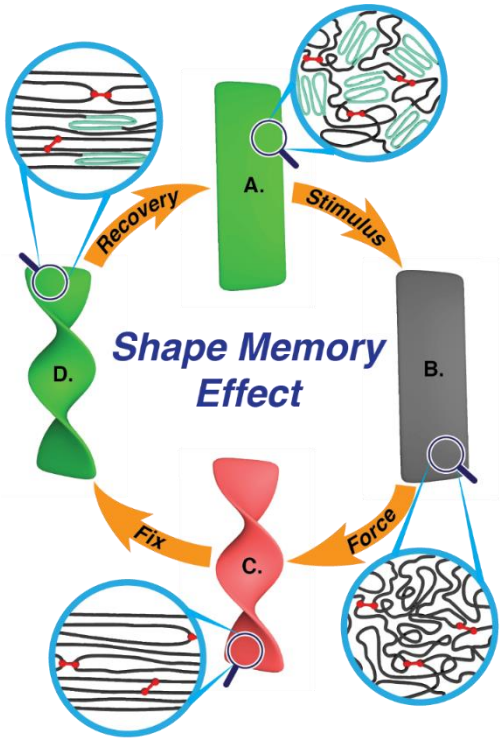

Figure 1.2. Schematic representation of a generic shape memory process A–D with a depiction of the corresponding rearrangements on the molecular level in the insets. Clockwise from the top, A) a specimen in its permanent shape with hard domains (green) and permanent cross-links (red) on the molecular level, B) a stimulus such as heat disrupts the hard domains and the network is held together by the permanent cross-links, which allows for C) deformation of the sample causing strain on the polymer network and D) fixation of the temporary shape by reformation of the hard domains (after removal of the stimulus and force) that locks the network in the strained configuration. Recovery is then triggered by an external stimulus that disrupts the hard domains leading back to the original shape.

Color/Fluorescence Change: Polymers that have the ability to change their absorption and/or fluorescence color upon exposure to a specific stimulus are *a priori* useful in a diverse range of sensor applications; accordingly, examples of such chromogenic materials are abundant and many different mechanisms for the design of stimuli-responsive (fluorescence) color changing

polymers have been developed over the years.[75-80] For example, the use of chemical binding to specific motifs has proved popular in accessing chemo-sensing materials. Here, the binding of the chemical analyte to a chromophore within the polymer results in a color or fluorescence change (e.g. Figure 1.3A). Another general approach is the use of chromophores whose photophysical properties can be switched upon exposing the polymer system to heat, light, or mechanical stress, typically as a result of a (reversible) molecular rearrangement, or a change of the assembly state. For example, the spiropyran moiety,[81,82] which can undergo a reversible ring-opening reaction to a merocyanine form has proved popular, originally as a photochromic, and more recently as a mechanochromic motif (Figure 1.3B). Another widely used family of compounds are "aggregachromic" dyes (Figure 1.3C), whose absorption and/or emission characteristics change upon aggregation or disassembly, on account of electronic interactions between the chromophores and/or conformational changes of the dye molecules upon (dis)assembly.[76,83-85] In the case of fluorescent molecules, aggregation often leads to the formation of static excimers, which emit light of lower energy (longer wavelength) than the solitary molecules. The introduction of non-fluorescent and fluorescent aggregachromic dyes into polymeric matrices has been widely exploited to access stimuli-responsive materials, notably compositions that change their optical properties upon exposure to heat, chemicals, light, and other stimuli. Another prominent approach to create color-changing polymer systems is based on the use of photonic crystals (PCs) (Figure 1.3D), i.e., structured materials with a spatially periodic variation of the dielectric permittivity with a length-scale that is of the order of hundreds of nanometers. This architecture leads to a frequency domain in which no radiation of the respective frequency can propagate (i.e., a photonic band gap)

and is therefore reflected. The optical characteristics of PCs depend primarily on the geometry of the structure and the refractive indices of the components. To exhibit well-defined "structural" colors, the periodic structures must be highly regular, which in the case of polymeric PCs is feasible by using a range of techniques, including the assembly of block copolymers, the assembly of spherical particles into colloidal crystals or "opals" and the preparation of the corresponding inverse-opal structures, as well as the fabrication of multi-layered polymer films by sequential spin-coating or continuous multi-layer co-extrusion. Polymer PCs display stimuli-induced color changes if the stimulus causes either a change of the refractive index contrast between the components or a variation of the dimensions of the periodic structure.[86] This can be easily achieved by exposure to heat (if the components have dissimilar thermal expansion coefficients), chemicals (which preferable swell one of the components), mechanical force (if both components permit deformation) and other stimuli.

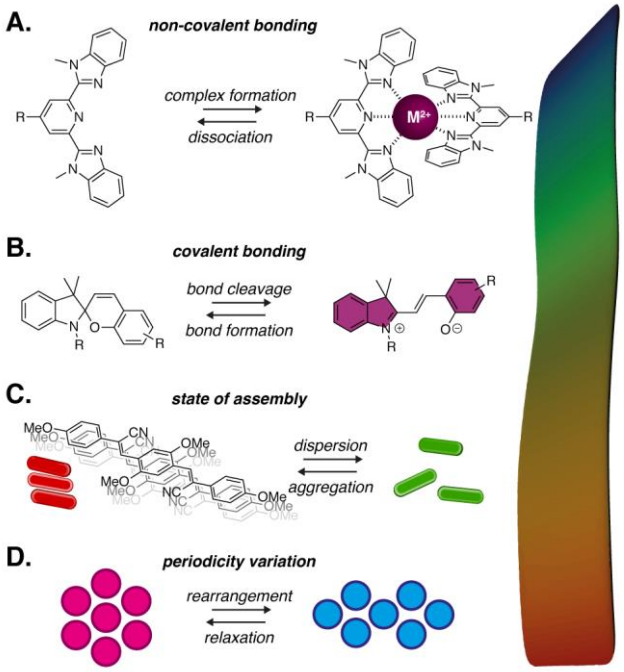

Figure 1.3. Examples of mechanisms that can be used to impart polymers with the ability to change their (fluorescence) color upon exposure to a stimulus. A) Non-covalent chemical binding to a chromophore. B) Change of a chromophore's molecular structure. C) Change of the assembly state of a chromophore. D) Change of the periodic arrangement in a photonic crystal.

Mechanical Property Change: A common objective of many stimuli-responsive polymeric materials is to achieve a change of the mechanical properties as a response. This may include a drop in stiffness as the polymer is heated above T_g or T_m, weakening of a cross-linked network upon disengaging of (supramolecular or dynamic covalent) reversible bonds, or stiffening a material, e.g., through chemical binding of a metal ion to ligands in the polymer backbone. Mechanical property changes along a "normal" thermal transition are trivial and there are a multitude of ways in which a stimulus can be used to impact them without the resulting response

generally qualifying in the sense of a stimuli-responsive behavior. For example, the generally observed increased mobility of polymer chains at elevated temperatures leads to a weakening of the mechanical properties. However, as a rule, materials that exhibit this behavior alone would not be termed thermo-responsive (although they qualify by the strictest definition of the term). Likewise, the simple plasticization of a polymer film though exposure to a solvent would in and of itself not necessitate the term chemo-responsive. However, as is exemplified in shape-memory and healable polymers, such thermally (or chemically) induced transitions can play key mechanistic roles in many stimuli-responsive materials.

On the other hand, supramolecular or dynamic covalent polymers, which can undergo stimuli-induced depolymerization or decross-linking, will also exhibit a massive change of the mechanical properties upon application of a stimulus. This mechanical response is generally referred to as stimuli-responsive and has been used extensively to access stimuli-responsive healing (as described above) and/or stimuli-responsive/rebondable adhesives.[24,87,88] For example, Balkenende et al. have reported the stimuli-responsive adhesive nature of hydrogen-bonded supramolecular polymer networks utilizing the pyridine-isophthalic acid binding motif (Figure 1.4A) that exhibit thermoset-like properties.[89] Inspired by epoxy resins, they prepared two sets of prepolymers based on bisphenol A diglycidyl ether and 5-aminoisophthalic acid with varying concentrations of isophthalic acid groups. These prepolymers were mixed with different difunctional pyridines in equimolar carboxylic acid to amine ratios (Figure 1.4B), furnishing a series of glassy, hydrogen-bonded networks. The resulting supramolecular polymer networks showed high room temperature storage moduli of up to 3.9 GPa, while heating the samples to

temperatures above the T_g (103-132 °C, depending on the composition) sufficiently weakened the supramolecular interactions and allowed for facile melt processing (Figure 1.4C). Lap joints with stainless steel substrates were prepared by applying the supramolecular polymer to the substrate at 150 °C. The cooled lap joints displayed shear strengths of up to 1.5 MPa, and, after failure, heating to 150°C allowed for a rapid rebonding of the lap joints with complete recovery of the mechanical properties. At the same time, the low melt viscosity of the supramolecular polymer network provided for a means to thermally debond by heating the samples.

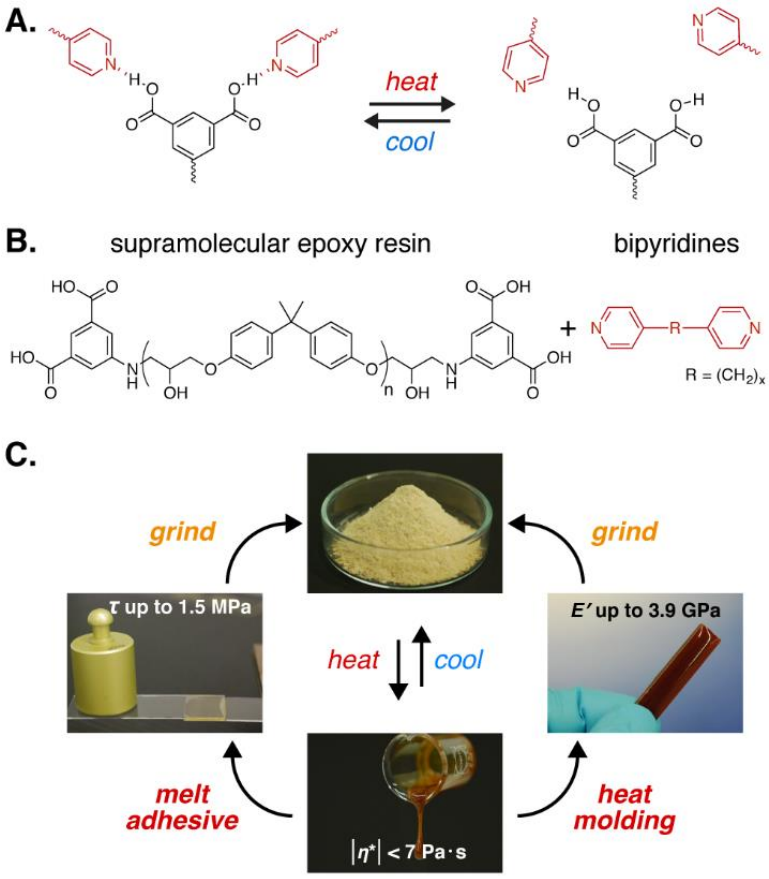

Figure 1.4. A) Schematic of the reversible hydrogen-bonding motif utilized in the supramolecular polymer networks based on B) isophthalic acid-terminated bisphenol A diglycidyl ether prepolymers as supramolecular epoxy resins and different bipyridines. C) Heating of the rigid materials furnishes viscous liquids for facile processing, or use as healable adhesives with facile debond-on-demand properties. Adapted and reproduced with permission from ref 89. Copyright 2016 American Chemical Society.

There is a growing number of polymers that display stimuli-induced mechanical changes and which have been shown to exhibit stimuli-induced healing or switching of adhesive properties, but it is not always clear cut if the qualification as being "stimuli-responsive" is appropriate. For example, most linear polymers can be "healed" if they are heated well above their T_g/T_m and left

for long enough,[58] but this behavior is usually not considered as stimuli-responsive. Similarly, hot melt adhesives, which are simple thermoplastic polymers, are normally not classified as stimuli-responsive materials, although they are rebondable and require heat as a stimulus to exhibit their adhesion capabilities, like the supramolecular polymers discussed above. Does this mean then that in order to consider something stimuli-responsive we require it to exhibit a behavior that goes beyond the expected norm?

Multi-component materials: Conceptually, the easiest way to access multi-responsive materials is to combine two responsive materials together, marrying response A with response B and thereby creating a system where the response of both A and B are available. Thus, it makes sense that the creation of polymer composites is a broadly useful design approach to create stimuli-responsive materials.[21,90-93] Not only is there the possibility for additive responses, composites that use non-polymeric fillers can be used to impart properties that are hard to obtain with just polymers, e.g. enhanced electrical or thermal conductivity, and can lead to new classes of functional materials that are not readily accessible by other means. The interfaces between the different components create further opportunity to tailor the response of a material. For example, in the case of a nanofiller embedded within a polymer matrix, it is known that both the filler-filler and filler-matrix interactions play significant roles in determining the properties of the material. If the nanofiller is conductive, for instance, the material's conductivity could be altered depending on the connectivity of the pathway defined by the filler-filler interactions. Thus, a stimulus that changes the nature of these interactions can also result in a change in the properties of the materials. For example, studies on the mechanical switching ability of the sea cucumber dermis have revealed

that this responsive behavior (Figure 1.5) is related to the multicomponent architecture of the collagenous tissue,[94-96] in which interactions between rigid collagen "filler" fibrils, which are embedded in a viscoelastic matrix, are regulated by neurosecretory proteins. Inspired by this biomodel it has subsequently been shown that cellulose nanocrystal composites also exhibit mechanical switching upon exposure to water. In these materials, it is proposed that in the dry state hydrogen bonding interactions between adjacent CNCs (and the CNC and matrix) play a role in this reinforcing network, transferring mechanical stresses across the sample, and resulting in stiff materials (Figure 1.5). However, once water diffuses into the nanocomposite, it competitively hydrogen bonds to the CNC surfaces disrupting the stress-bearing CNC scaffold and softening the nanocomposite.

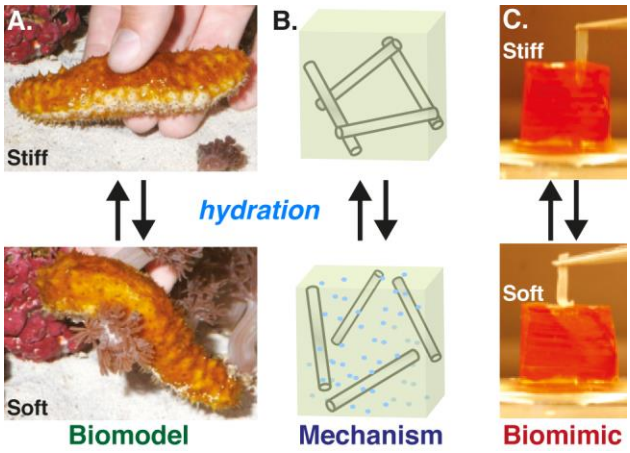

Figure 1.5. A) Images of a sea cucumber in its (top) rigid and (bottom) soft state. B) Schematic of a nanocomposite model highlighting the disengagement of a fiber network with hydration as the mechanism of softening of the material. C) Picture of a PVAc/cellulose nanofiber nanocomposite in its (top) dry rigid state being pierced into jelly and in it (bottom) wet soft state demonstrating its inability to pierce the jelly. Adapted and reproduced with permission from refs 94 and 96. Copyright 2008 American Association for the Advancement of Science and 2008 Wiley-VCH.

Stimulus Transformations. A powerful tool in the development of multi-stimuli, multi-responsive materials is the concept of transforming one stimulus into another. Several mechanisms are known that are capable of converting an external stimulus (i.e. light, sound, electric or magnetic field) into a different signal (i.e. heat) to elicit a response from the material.[97-102] One of the most common examples is the photothermal effect or the ability to transform light into thermal energy.[103-106] While most polymers are not intrinsically responsive to light, adding materials that generate heat in the presence of light, such as metallic nanoparticles or conjugated, light absorbing compounds, creates a medium through which researchers can increase the temperature within the system without directly exposing it to heat. Thus, the thermally responsive properties of the polymer (i.e. T_g, T_m, $T_{LC\text{-}I,}$ reversible bonds) become accessible through exposure to light. Similar

transformations can be achieved using other inputs that include, but are not limited to ultrasound, magnetic fields, and electrical fields.

These illustrations highlight some of the range of mechanisms employed to evoke a variety of responses from a material upon application of a defined external stimulus. When used in combination with one another or when carefully tuned to elicit functionality beyond their standard behavior, these mechanisms can give rise to multifunctional polymer materials that show more than a single type of response to one or more external stimuli. To classify such materials, the number of responses and stimuli seem appropriate denominators. Accordingly, the following discussion focuses on selected representative materials that (1) show multiple responses to a single stimulus, (2) show a single response to multiple stimuli, and (3) yield multiple different responses upon exposure to different stimuli.

1.3 Single Stimulus, Multiple Responses

The first group of *responsive polymers* discussed here includes (increasingly complex) examples of materials in which the same stimulus can elicit different responses, either simultaneously or as a function of the exposure levels.

Perhaps the most prominent family of multi-responsive polymers are materials that involve shape memory effects.[107] In contrast to the "simple" two-way shape memory materials discussed in the introductory section, which can be switched between a permanent and a temporary shape, multi-responsive shape memory materials are designed to either access multiple shapes or to be reprogrammable (Figure 1.6). As the name suggests, multi-shape memory materials display

multiple, distinct shape changes that can, in many embodiments, be triggered by a single stimulus. This allows for complex adaption of the materials' shape into different temporary configurations, and recovery back to the permanent shape. The key to achieving multiple shapes is the design of systems that feature different types of responsive cross-links (physical and/or chemical), which can be accessed individually and provide a means by which more than one temporary shape is programmable.

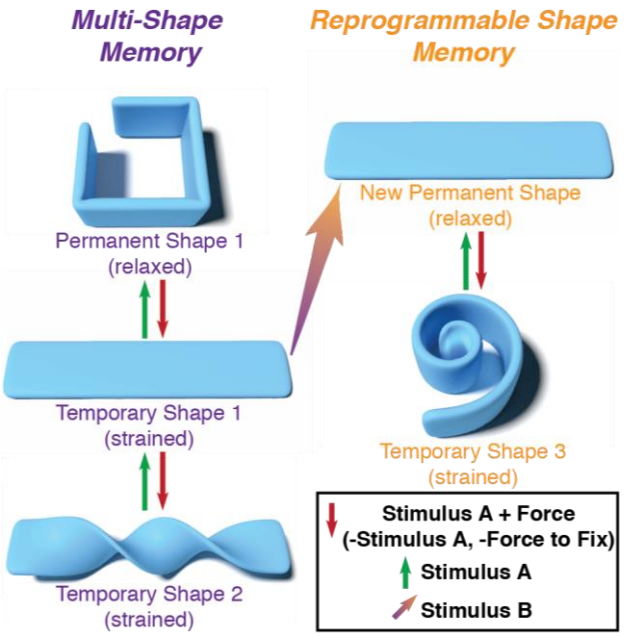

Figure 1.6. Schematic representation of shape changes in multi-responsive shape memory polymers. The first permanent shape can be fixed into a second temporary shape via the application of a stimulus and force followed by the removal of the stimulus, then the removal of the force. In multi-shape memory materials, another strained shape can be programmed into the material and, upon the application of a (different) stimulus, the entire process is reversible so that the original, permanent shape can be restored. For reprogrammable materials, the second shape undergoes a relaxation process that establishes the temporary shape as the new, stress-relaxed, permanent shape into which other temporary shapes can be programmed.

Very broad glass transitions lend themselves as fixing elements that allow for programming multiple temporary shapes at different temperatures across the broad transition. Using this approach, Nafion® (a commercially available copolymer based on tetrafluoroethylene and a perfluorosulphonic acid monomer, Figure 1.7A) has been programmed with up to four distinct temporary configurations.[108] This copolymer, which is normally used for membranes on account of its ion-transport properties, is characterized by two physically complex phase transitions: a very broad glass transition at lower temperatures (60 °C < T_g < 150 °C, Figure 1.7B) and a transition related to its physical ionic cross-links at higher temperatures (> 240 °C).[109-112] While the complex morphology of these perfluorosulfonate ionomers remains a topic of debate, it is generally accepted that the low-temperature transition corresponds to short-range segmental motion between the physical (ionic) cross-links that are stable up to the higher temperature transition.[111] The latter thus fixes the permanent shape, while heating above the lower transition (to 140 °C) allows a temporary shape to be programmed with subsequent recovery at the same temperature. Furthermore, the broad temperature range of this transition allows temporary shapes, with very good fixing and recovery ratios, to also be programmed with these perfluorosulfonate ionomers at the lower end of the transition temperature regime, e.g. just above the onset of the T_g (60 °C). Interestingly, the amount of recovery observed at any given temperature depends on the fixing temperature. The strain-induced deformation at a higher temperature (*e.g.* 140 °C) is found to be only fully recovered at that same temperature; while only an incremental recovery is observed at lower temperatures. It is this behavior that allows one to program different shapes at different temperatures.[113] Thus, researchers were able to program a quadruple-shape memory effect by

successively heating and fixing temporary shapes in Nafion® at discrete temperatures (e.g., 140, 107, and 68 °C in Figure 1.7C; or 140, 90, and 53 °C in Figure 1.7D). While shape recovery was very high, shape fixation of the temporary shapes programmed at higher temperatures was found to be reduced when comparing to the single-shape memory effect of the same material at the same temperature. The loss in shape fixation was found to be closely related to the difference between the temperatures at which the deformations are performed, but the recovery remains sufficiently high for all three temporary shapes.

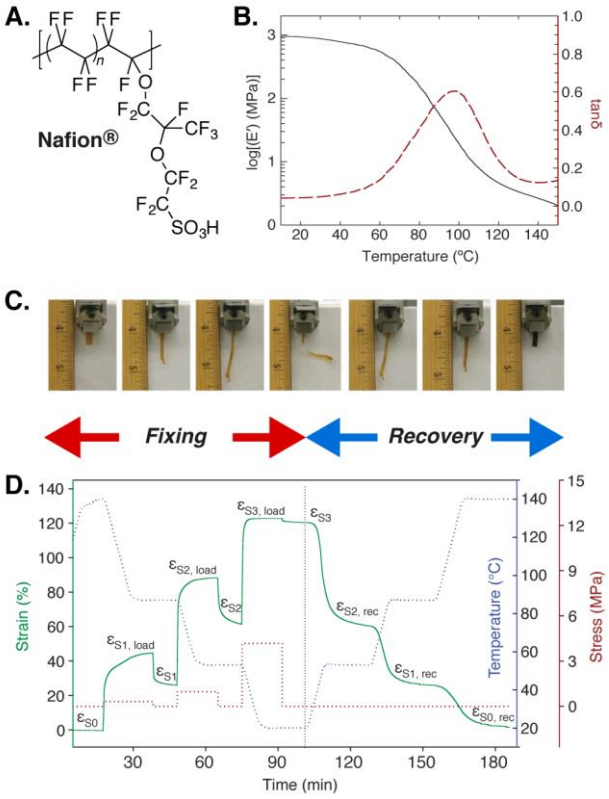

Figure 1.7. Demonstration of multi-shape memory behavior in a polymer exhibiting a broad glass transition temperature. A) Chemical structure of Nafion®. B) Dynamic mechanical analysis (DMA) results showing the breadth of the glass transition in this polymer. C) Shape changes in the film during the quadruple shape memory process with fixing and recovery temperatures of 140, 107, and 68 °C. D) Graphical representation of the shape memory process in terms of time, temperature (blue), stress (red), and strain (green) with fixing and recovery temperatures of 140, 90, and 53 °C. Adapted and reproduced with permission from ref 108. Copyright 2010 Nature Publishing Group.

The conceptual approach of employing a broad glass transition as a means to program shape memory materials has been generalized beyond the special case of perfluorosulfonate ionomers. For example, Shao et al. prepared norbornene copolymers via the ring-opening metathesis copolymerization of norbornene monomers carrying either cholic acid or pendant

triethylene glycol monomethyl ether moeities.[114] In this case, the permanent shape is thought to arise due to the physical entanglement of the high-molecular weight polymers, while the pendant group interactions furnish the broad glass transition used for the programming of the temporary shapes. In another example, Luo et al. prepared compositionally graded styrene-methyl acrylate-styrene copolymers that were styrene-rich at the peripheries and methyl acrylate-rich in the center via reversible addition–fragmentation chain transfer (RAFT) polymerization by controlling the monomer feed.[115] In the solid state, the formation of a morphology with styrene-rich domains in a methyl acrylate-enriched matrix without distinct boundaries was observed that led to an exceedingly broad T_g (20–103 °C), effectively spanning the entire range between the corresponding transitions of the individual homopolymers. The upper limit was defined by styrene-rich glassy domains that served as physical cross-links; up to four temporary shapes could be successfully programmed and recovered at discrete temperatures within the glass transition.

The combination of a covalent or physical network that defines the permanent shape with two or more fixing elements that involve distinct (as opposed to the above-discussed broad/graded) phase transitions is another pathway to multi-shape memory materials. With each additional phase transition, another shape can be programmed. Lendlein and coworkers utilized this approach to create triple-shape memory polymers based on covalently cross-linked phase-segregated networks featuring two types of domains with different melting and glass transition temperatures.[116,117] This was achieved by the polymerization of cyclohexyl methacrylate in the presence of poly(ε-caprolactone) dimethacrylate, affording a polymer network, with two distinct thermal transitions, i.e., the melting of crystalline poly(caprolactone) (PCL) domains at T_m = 50 °C and the glass transition

of amorphous poly(cyclohexyl methacrylate) domains at T_g = 140 °C). In a similar manner, a polymer network of poly(ethylene glycol) acrylate with a poly(ε-caprolactone) dimethacrylate cross-linker was prepared, which exhibited two melting transitions for the PCL (T_m = 50 °C) and the poly(ethylene glycol) domains (T_m = 34 °C). In both cases, the two distinct phase transitions were successfully employed for the programming of a triple-shape memory effect. Besides the glass and melting transitions, Qin and Mather also reported the use of a cross-linked liquid crystalline polyester that combines the glass transition of the polymer with the isotropic-nematic transition of mesogens in the polymer backbone to achieve a triple-shape memory effect,[118] and similar shape memory materials were obtained when the mesogens were implemented as pendant groups.[119]

In addition to multi-shape memory polymers that ultimately return from their temporary shape to the original, permanent configuration, reprogrammable shape memory materials can be designed in such a way that a temporary shape can be "locked", thereby becoming the new permanent geometry. One favored way to achieve this function is to use dynamic bonds that allow stress relaxation in the high-strain temporary shape upon application of a stimulus that initiates the dynamic exchange.[120,121] Targeting such reprogrammable materials, Lawton et al. designed shape memory composites that feature a reconfigurable elastic matrix and an electrospun poly(ε-caprolactone)-based polyurethane fiber network as the percolating phase that fixes the temporary shape through crystallization.[120] Such materials were accessed by imbibing the electrospun fibers with a mixture of 4-pentenoic anhydride and pentaerythritol tetrakis(3-mercaptopropionate). Thiol-ene reactions afforded a polyanhydride network in which the exchange between the dynamic

anhydride groups allowed for the reconfiguration of the matrix into a new permanent shape at elevated temperatures (Figure 1.8). In the absence of the poly(ε-caprolactone)-based polyurethane fibers, the polyanhydride elastomers displayed a time-dependent stress relaxation at temperatures above 50 °C with full reconfiguration to a new, stress-free shape when the temperature was increased to 90 °C. The composite of the poly(ε-caprolactone)-based polyurethane fibers and the polyanhydride matrix displayed simple shape memory behavior when a temporary shape was programmed at 40 °C by melting the crystalline poly(ε-caprolactone) domains (T_m of ca. 30 °C), cooling under deformation, and thermally triggering shape recovery. In addition, heating deformed samples of these composites above 90 °C provided a means to reconfigure the material into a new permanent shape without macroscopic fluidization.

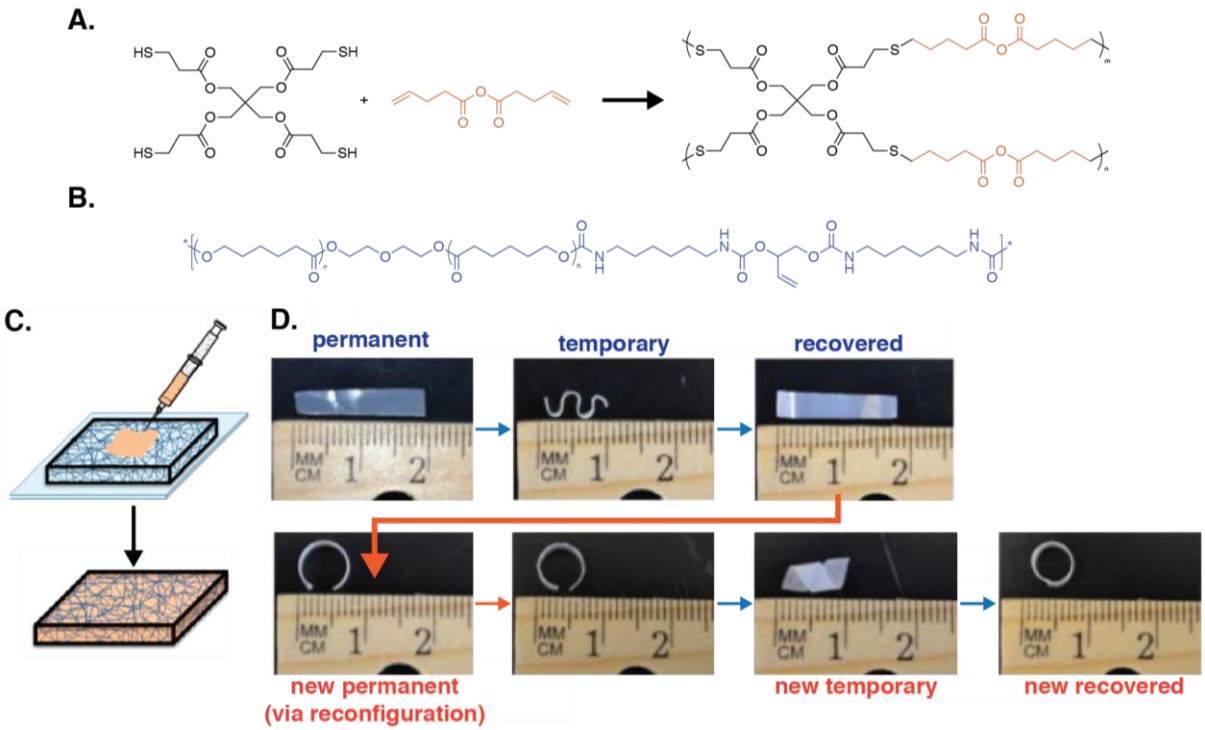

Figure 1.8. Reprogrammable shape memory composites based on a reconfigurable polyanhydride matrix and an electrospun poly(ε -caprolactone)-based polyurethane fiber network. A) Scheme depicting the synthesis of the cross-linked polyanhydride network with exchangeable anhydride bonds. B) Chemical structure of the poly(ε -caprolactone)-based polyurethane. C) Schematic of the preparation process that involved imbibing a fiber mat with the polyanhydride matrix. D) Pictures demonstrating the reprogrammable shape-memory effect. Adapted and reproduced with permission from ref 120. Copyright 2016 American Chemical Society.

The possibility of combining the shape-memory effect with stimulus-induced healing is an attractive method to induce the "automatic" recovery of the pre-damage shape by bringing the surfaces separated during damage into close contact and thereby facilitate the healing of such interfaces. Several groups have reported embodiments of this general idea.[65,70,122-125] Rodriguez et al. achieved such multifunctional responses in a single-phase interpenetrating two-component

blend consisting of a cross-linked poly(ε-caprolactone) network and a linear poly(ε-caprolactone).[126] These materials were prepared from a linear PCL having a weight-average molecular weight (M_w) of ca. 65,000 g/mol, well-above the entanglement molecular weight, a lower-molecular weight telechelic PCL diacrylate (number-average molecular weight, M_n, ca. 3,100 g/mol), and a tetrathiol cross-linker. The latter two components reacted via thiol-ene chemistry to form a poly(ε-caprolactone) network (thermoset), which provided the desired shape-memory response, whereas the linear PCL (thermoplastic) was utilized as the healing agent. The materials displayed a single melting transition of the crystalline PCL domains, which triggered both the shape memory effect as well as the healing. Beyond the conventional shape-memory behavior, the materials also displayed reversible plasticity. In other words, if the deformation from the permanent to a temporary shape was performed below the phase transition of the crystalline domains past the yield point, subsequent heating above the T_m led to full recovery of the permanent shape. Gratifyingly, the shape-memory effect displayed by the materials aided the healing process as intended. Thus, samples without and with inflicted collinear edge cracks at the center of the dogbone-shaped samples were investigated by uniaxial tensile deformation, followed by healing, and repetition of the tensile deformation. Complete healing that left no evidence of the initially inflicted crack was observed directly after the first thermal treatment at 80 °C for all samples with a fraction of at least 25 wt% of linear PCL. Tensile testing of such samples showed an efficient recovery with reversible plasticity as the mechanical strength of the original samples was virtually fully restored ($\geq$ 95%). In cases where samples with edge cracks were healed, repeated tensile deformation furnished a necking effect of the material rather than a reopening of the former cracks.

Thus, a single heating step triggered a shape-memory effect that assisted in the closure of a damaged region of the sample, while the efficient diffusion of the (viscous) liquid linear component successfully healed the sample, restoring its original properties.

In a different example involving a shape-memory effect, Mather, Weder, and coworkers combined a shape-memory polymer featuring a thermally responsive fixing element with a fluorescent chromogenic dye to create a shape-memory polymer with a built-in temperature sensor.[127] The latter was designed to signal reaching of the set/release temperature of the polymer with pronounced changes of the absorption and emission colors (Figure 1.9). This was achieved by incorporating a fluorescent, excimer-forming cyano-substituted oligo(*p*-phenylene vinylene) (cyano-OPV) dye (Figure 1.9A) into a cross-linked poly(cyclooctene) (PCO) matrix. Using a previously reported guest diffusion process, the polymer films were simply swelled with solutions of the dye.[128,129] The concentration of the dye was selected to allow for aggregation of the dye molecules upon drying, resulting in an orange appearance and emission color of the film (Figure 1.9B), on account of the formation of electronic ground-state interactions and emission from excimers. Heating these phase-separated blends to above the PCO's T_m led to dissolution of the aggregates and caused pronounced changes of the materials absorption (yellow) and fluorescence (green) color (Figure 1.9B). The thermally induced optical changes were fully reversible upon cooling and crystallization of the PCO. The absorption and emission characteristics were shown to be dictated by the phase behavior and to be independent of mechanical treatment. The material otherwise displays the characteristic shape-memory behavior of cross-linked PCO,[130,131] i.e., a temporary shape can be programmed into the polymer network by deformation above the melting

transition of the PCO (T_m ca. 50 °C) and subsequent cooling (Figure 1.9C). Recovery of the permanent shape by renewed heating led to a simultaneous dual response, i.e., shape recovery and concomitant optical changes, as the dye molecules were (temporarily) dispersed (Figure 1.9D).

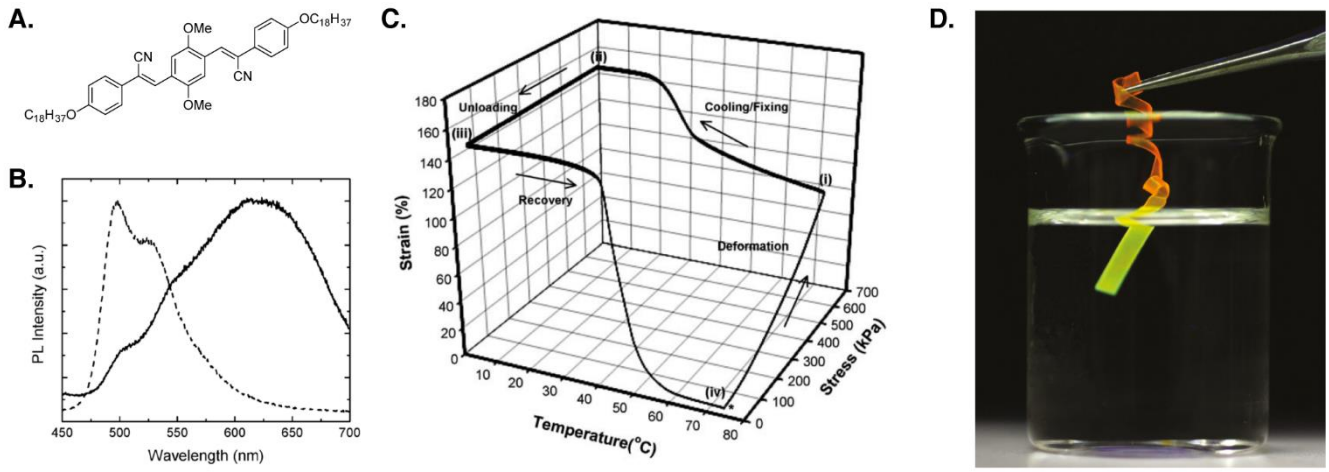

Figure 1.9. Shape-memory effect and color change in cyano-OPV/PCO blends. A) Chemical structure of the cyano-OPV chromophore used. B) Fluorescence spectra of an initially phase-separated PCO/cyano-OPV blend film at 25 °C (solid line) and after annealing for 1 min at 100 °C (dashed line). C) One-way shape memory cycle. The asterix indicates the start of the cycle; the sample was elongated by increasing stress at 75 °C (i) before it was cooled (ii) and the stress was removed (iii) to yields a temporary "fixed" strain that was recovered to the original strain upon heating (iv). D) Picture demonstrating the dual response (fluorescence color change and shape recovery) that is triggered upon immersion of a PCO/cyano-OPV blend film into silicon oil at ca. 80 °C. Adapted and reproduced with permission from ref 127. Copyright 2008 Royal Society of Chemistry.

1.4 Multiple stimuli, single response

Many responsive materials show a single response that can be triggered by the application of different stimuli. Beyond the intrinsic interest in these materials themselves, they also constitute

an important stepping stone for the development of an understanding of the fundamental requirements for the implementation of multi-responsive properties in polymers.

An example of a shape-memory material that was designed to be both thermo and photo-responsive was reported by Pilate et al.,[132] who prepared a poly(ester-urethane) copolymer that contained thermo-responsive, semi-crystalline poly(caprolactone-*co*-*p*-dioxanone) segments and polyurethane segments with photo-responsive cinnamide moieties as side chains (Figure 1.10A). The resulting phase-separated materials are comprised of semi-crystalline polyester regions and amorphous polyurethane regions. When the polyurethane segments were photocross-linked via the dimerization of cinnamide groups (Figure 1.10B) they can act as the permanent cross-linking component and the crystallinity of the polyester regions could be used as the thermally-responsive "fixing" component. As such, simple heating above the T_m, stretching, and then cooling allowed for high degrees of fixing and recovery (>90%) after reheating (Figure 1.10C). Alternatively, light-induced shape memory could be achieved at room temperature by using the crystalline domains as the component providing permanent physical cross-links. Exposure to UV light of specific wavelengths allowed to form ($\lambda > 260$ nm) and remove ($\lambda < 260$ nm) the cross-links by means of the photo-induced dimerization of the cinnamide groups (Figure 1.10D). For highly crystalline polyester derivatives good degrees of shape fixing could be achieved using this approach, while the shape recovery was limited. Decreasing the crystallinity of the polyester segment (by increasing the amount of the *p*-dioxanone in the ester) led to increased shape recovery, but the degree of fixing significantly dropped. Interestingly, however, it was found that the incorporation of ca. 10 wt% of an end-capped linear or four-armed PCL into the material resulted in an increase

of the photo-responsive fixing (up to 75%) and recovery (up to 76%) while the fixity and recovery under thermal stimulation remained excellent (>95%).

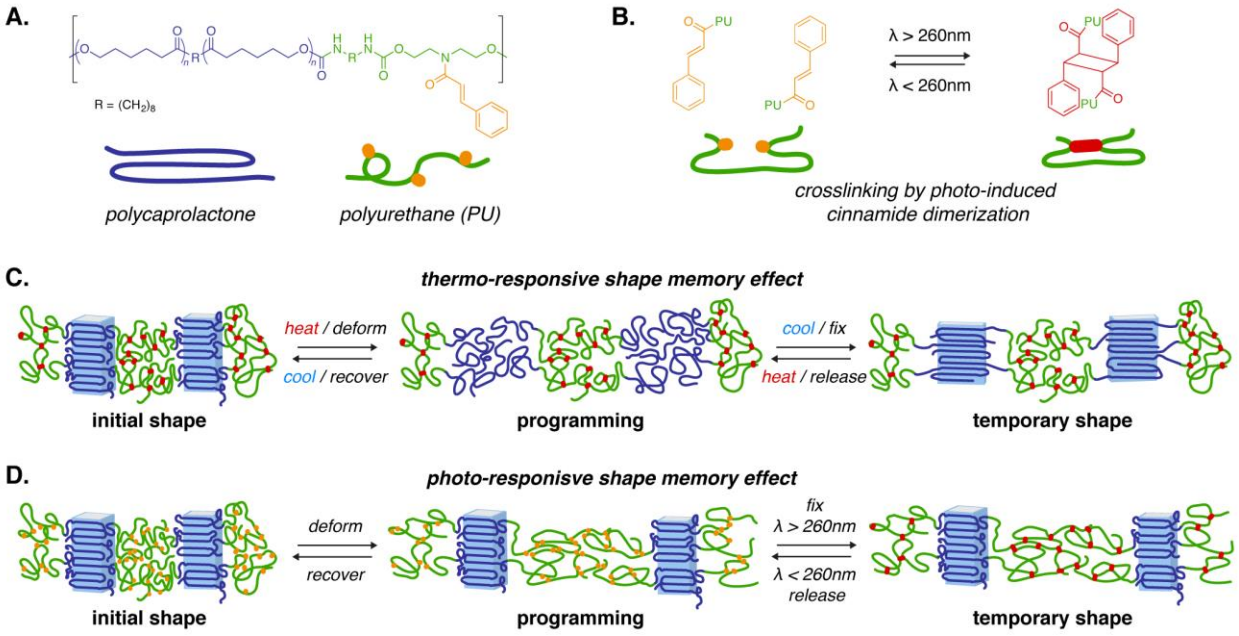

Figure 1.10. A) Chemical structure of a poly(ester-urethane) copolymer with thermo-responsive, semi-crystalline poly(caprolactone-co-p-dioxanone) segments and polyurethane segments with photo-responsive cinnamide moieties. B) Schematic of the reversible, photo-induced dimerization of the cinnamide moieties that was employed to cross-link the polyurethane segments. C) Scheme depicting the thermo-responsive shape-memory effect. D) Scheme depicting the photo-responsive shape-memory effect.

An alternative approach to multi-stimuli single-response materials is to use dynamic/supramolecular bonds that can be disassembled by multiple stimuli. Rowan and coworkers have exploited dynamic, responsive, metal-ligand complexes for the preparation of materials that change their color in response to thermal and chemical stimuli.[133] Ditopic

macromonomers based on low-molecular-weight poly(tetrahydrofuran) (PTHF) cores with terminal terdentate 2,6-bis(1'-methylbenzimidazolyl) pyridine (MeBip) ligands were prepared. These macromonomers formed thermoplastic elastomers when complexed with zinc ions (Zn^{2+}) in a 2:1 ligand:metal ion complex, wherein the phase separation of the metal ligand complexes into a hard domain is the basis for the observed elastomeric behavior. To achieve a dynamic colorimetric response, a fraction of the zinc ions was replaced with europium ions. The 3:1 complexes of the latter are more responsive to external stimuli (on account of weaker binding) in addition to featuring a pronounced optical response in the form of a metal-centered luminescence when coordinated by the ligands. When supramolecular polymer films containing both zinc and europium ions were employed, a colorimetric response was observed upon exposure to either a thermal or chemical stimuli. For example, heating a film with a 70:30 Zn^{2+} to Eu^{3+} ratio to approximately 120 °C shifted the fluorescence color from pink (combined emission from the red Eu^{3+}:MeBip complexes and blue Zn^{2+}:MeBip complexes) to blue on account of a diminishing emission band of the Eu^{3+}:MeBip complexes, an effect that was found to be reversible. Moreover, exposure to reagents that can disrupt the Eu^{3+}:MeBip ion ligand complexes were also found to trigger a similar colorimetric response. Thus, exposure of the films to vapors of triethyl phosphate that can competitively bind to the europium ion and therefore disrupt the Eu^{3+}:MeBip complexes results in a same red to blue change in fluorescence color.

Metal ligand complexes were also found to be useful for the preparation of responsive materials when these complexes were straightforwardly blended with polymers.[134] Square-planar platinum(II) complexes of the MeBip ligands were prepared and dispersed into methacrylate

polymers, to yield mechanically stable polymer films that showed a colorimetric response to chemical or mechanical stimuli. Similar to the previous example of the responsive metallosupramolecular polymers, the metal ligand complexes microphase segregated from the polymer matrix, in this case, in the form of small yellow crystallites. Exposure of these yellow films to solvent vapors that plasticize the crystallites (e.g. acetonitrile) lead to a structural change to the local packing of the square-planar platinum(II) complexes that occurs with a concomitant color change to red. A color change of these blends was also effected by application of mechanical stimuli. Thus, scratching, beating, or stretching the yellow films resulted in a change of the emission color to orange in the damaged area, presumably due to a force-induced rearrangement of the structure of the complex aggregates.

As mentioned before, incorporating "aggregachromic" dyes, whose optical characteristics are altered upon aggregation or disassembly, into a polymeric matrix was found to constitute a very successful strategy for the development of chromogenic materials that respond to multiple stimuli (Figure 1.11A). Weder and coworkers reported the use of blends of either poly(ethylene terephthalate glycol) or linear low-density polyethylene with small amounts (0.5–2 wt%) of the excimer-forming cyano-substituted oligo(*p*-phenylene vinylene) chromophores (see section 1) to elicit colorimetric responses to mechanical and thermal stimuli.[135] In a straightforward process, the dye was melt-mixed with either poly(ethylene terephthalate glycol) or poly(ethylene) under conditions at which the dye dissolves in the matrix. Subsequent quenching of the processed polymer/dye blend kinetically traps the state in which the dyes are molecularly dispersed. When such poly(ethylene terephthalate glycol) films were subsequently heated above the polymers glass

transition temperature (78 °C), the chromophores could diffuse through the matrix, leading to aggregation and an associated, irreversible color change to orange (Figure 1.11B,C). The aggregation rate and corresponding color change were directly controlled by the T_g of the polymer matrix and the concentration of the dye. In blends with low linear low-density poly(ethylene), the chromophores were found to aggregate in the amorphous portion of the low-T_g polymer matrix, even after formation of crystallized polyethylene domains.[136] The resulting, orange- or yellow-colored, nanometer-sized chromophore aggregates equipped these blends with mechanoresponsive properties (Figure 1.11D). Thus, macroscopic mechanical deformation lead to shear-induced disruption of the aggregates furnishing a color change from orange to yellow, or yellow to blue, respectively.

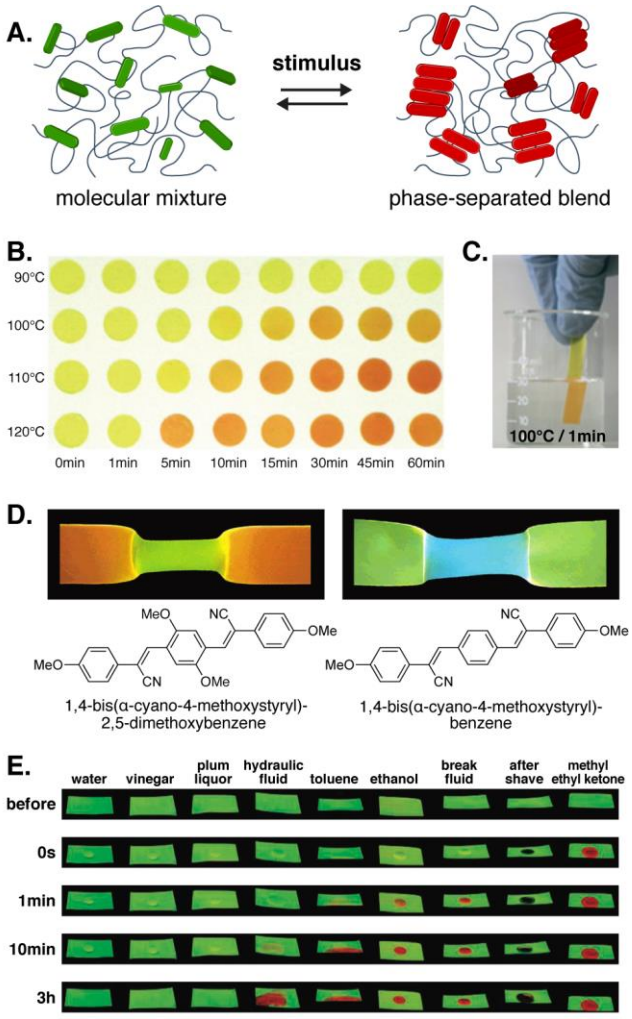

Figure 1.11. A) Schematic representation of the general approach to create (fluorescence) color changing polymers by incorporating "aggregachromic" dyes, whose optical characteristics are altered upon stimuli-induced aggregation or disassembly. B,C) Pictures of quenched blends of poly(ethylene terephthalate glycol) and 1.1% w/w (B) or 3.1% w/w (C) of a cyano-OPV dye, illustrating the time-, temperature-, and concentration-dependent colorimetric response of this platform. D) Pictures demonstrating the mechanochromic behavior of films of poly(ethylene) containing the cyano-OPVs shown. E) Pictures showing the fluorescence color change of cyano-OPV containing epoxy resins upon exposure to various chemicals. Adapted and reproduced with permission from refs 135, 136, and 139. Copyright 2006 Wiley-VCH (B,C), 2003 and 2009 American Chemical Society (D,E).

The same principles of aggregation and re-dispersion of excimer-forming dyes has been successfully employed to prepare a range of materials that display a colorimetric response to multiple stimuli. For examples, binary blends of the oligo(*p*-phenylene vinylene) with polar, semicrystalline poly(ethylene terephthalate) and ductile, amorphous poly(ethylene terephthalate glycol) were explored to prepare materials that feature thermally as well as mechanically-responsive behavior.[137] In addition to these stimuli, it was also observed that the crystallization of domains of the semicrystalline polymer matrix led to changes of the photoluminescence emission. Presumably, the crystallization process increased the concentration of the chromophores in the amorphous fraction of the polymer, promoting aggregation, and increasing the fraction of excimer emission. In addition to these investigations with polyesters, Weder and coworkers also explored polyamide/cyano-OPV blends that additionally respond to the humidity in the atmosphere as a chemical stimulus,[138] and reported epoxy resin-based coatings that respond with a change of the absorption and fluorescence color to a range of chemical stimuli such as organic solvents, water, as well as acid and base (Figure 1.11E).[139]

1.5 Multiple Stimuli, Multiple Responses

The critical development necessary for advancing the next generation of responsive materials comes from going beyond the single stimulus and single response materials to systems that have the ability to react to multiple stimuli with multiple different responses. Using a combination of techniques that have proven successful in the production of either multi-stimuli/single-response or single-stimuli/multi-responsive materials (as discussed in the previous

sections), researchers are now starting to develop systems that have a balance of properties that result in multi-stimuli, multi-responsive (MSMR) materials. One way to target MSMR is to design both the stimuli and response mechanisms to be orthogonal and as such the MSMR behavior is simply the additive of the multiple effects. However, perhaps conceptually a more intriguing and interesting aspect of combining different responsive mechanisms is the potential interplay between the mechanisms and/or components that can lead to more complex (emergent) behavior and greater utility. Drawing an analogy to systems chemistry, in which interactions between different molecules/reaction cycles in a mixture can give rise to emergent properties such as amplification and feedback,[140] if there is synergy between the reversible chemistries, thermal transitions and physical form in a single material then additional properties, and as such greater functionality, to the materials can be obtained.

As discussed in the single-stimuli, multiple-response section, a change of temperature can be used to access multiple responses and therefore one conceptually facile way to impart an additional stimuli sensitivity to such materials is to include components that can convert a different stimulus into heat. As mentioned before, the photothermal effect allows conversion of light into (localized) heat, and this was exploited by Zhang and Zhao to prepare polymer composites that display both shape-memory and healing behaviors in response to an optical stimulus.[141] A permanent (thermoset) polymer network was established by radically induced cross-linking of telechelic, diacrylate-terminated semicrystalline poly(ethylene oxide) (20,000 g/mol) in the presence of gold nanoparticles that had been functionalized with shorter poly(ethylene oxide) chains (2,000 g/mol) (Figure 1.12). A low concentration of gold nanoparticles (0.003 wt%) in the

composites ensured a sufficient transmittance, such that light can serve as an efficient stimulus across the sample. The composite displayed a uniform melting transition (ca. 60 °C) of the crystalline poly(ethylene oxide) (PEO) domains. After such films had been transformed into a temporary shape by deformation above the melting transition and subsequent cooling, light exposure by means of a laser beam (λ = 532 nm) induced local strain energy release and shape recovery as the photothermal effect of the gold nanoparticles (surface plasmon resonance at ca. 530 nm) caused localized heating (> 60 °C) in the light-exposed areas. When the same samples were damaged by imposing a cut, the damage was rapidly repaired after exposure of the damaged region to the laser beam with, e.g., recovery of 62% of the original tensile strength after only 3 s of laser exposure (13 W/cm^2). According to the proposed mechanism, the observed fast healing arises due to the melting of the semicrystalline PEO chains in proximity of the fracture surface and a subsequent recrystallization of entangled polymer chains after cooling. In addition, the constrained local thermal expansion of the region exposed to the laser beams appears to play a role in ensuring that the corresponding crack surfaces are pushed into a close spatial proximity.

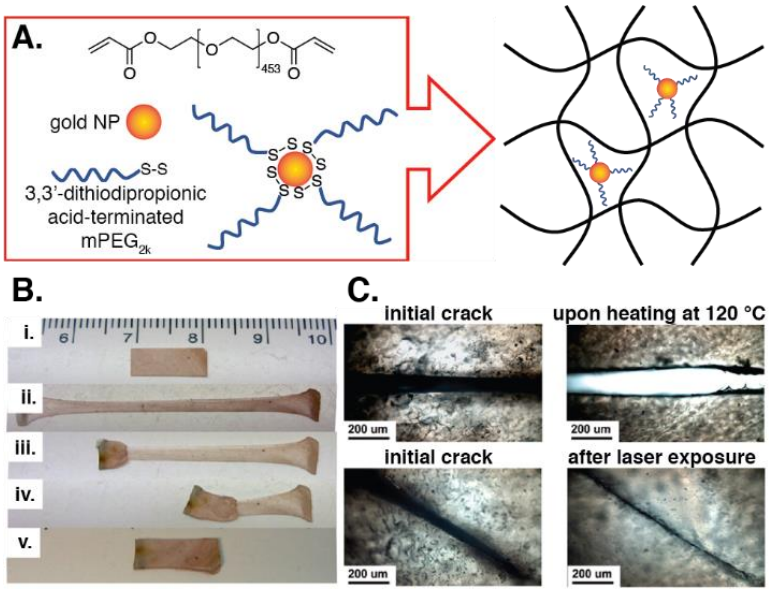

Figure 1.12. Healable shape-memory nanocomposites obtained by the incorporation of functionalized gold nanoparticles in a cross-linked PEO network. A) Schematic of the ingredients used and the structure of the material formed. B) Pictures showing an original composite film (i) that was heated (80 °C), stretched, and cooled into a temporary shape (ii); stepwise recovery (iii to v) was triggered by laser exposure from left to right on the film. C) Pictures revealing the difference in thermal-responsive and photo-responsive behavior in crack healing; thermal heating causes bulk expansion of the film preventing healing of the crack while the laser exposure creates a localized effect that closes the crack. Adapted and reproduced with permission from ref 141. Copyright 2013 American Chemical Society.

Lu et al. developed a cross-linked poly(ε-caprolactone)/poly(urethane) network that features urethane- and caprolactone-rich microdomains and displays shape-memory as well as healing responses upon exposure to high-intensity focused ultrasound.[142] This stimulus provides acoustic energy to a focused area of the sample, resulting in viscous shearing, polymer chain relaxation, and a concomitant localized increase of the sample temperature.[143] The temperature increase in the network polymers could be controlled by the ultrasound power. To render the

material dynamic, furan-maleimide Diels-Alder adducts were incorporated in the polymer network. Ultrasound-induced heating led to retro Diels-Alder reactions in the targeted area, reversibly cleaving the dynamic cross-links and allowing for a reshuffling of the network connectivity (Figure 1.13A). Upon cooling, the dissociated furan and maleimide moieties reformed the cross-links through cycloaddition. The initial investigations of the thermally triggered shape-memory effect of these polymer networks revealed that a temporary shape could be programmed above the melting transition of the PCL domains (T_m at ca. 65 °C) and thermally triggered shape recovery was found to be very efficient (99%). When the ultrasound beam was directed at the fold of a deformed temporary shape, recovery was locally activated for the duration of the sonication, allowing for a spatially and temporally resolved shape recovery.[144] The shape-memory effect also assisted in crack closure and healing of damaged regions of the polymer network (Figure 1.13B). Control experiments corroborated that the healing mechanism was indeed based on the reversibility of the linkage of the Diels-Alder units that allows for a rearrangement of the polymer network, diffusion and entanglement of the chains across the crack surface, and reformation of the linkage after removal of the ultrasound stimulus.

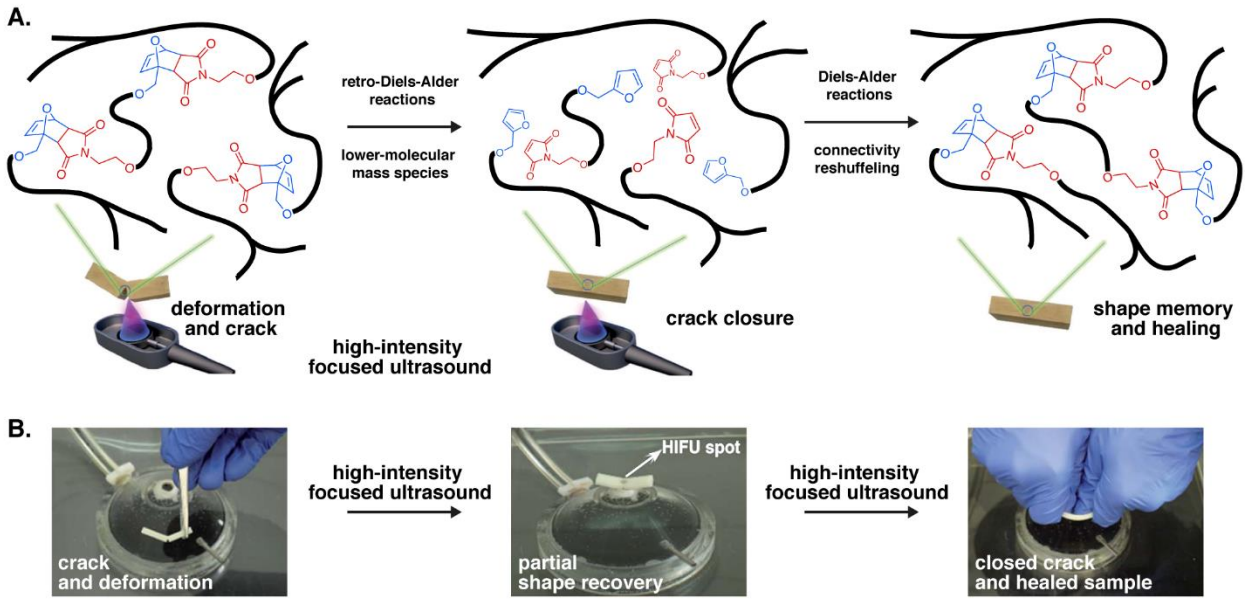

Figure 1.13. Ultrasound-responsive materials combining dual shape-memory and healing characteristics. A) Conceptual depiction of the shape-memory and healing mechanisms based on reversible Diels-Alder chemistry. B) Pictures illustrating the healing and shape-memory behavior of a macroscopic sample treated by high-intensity focused ultrasound. Adapted and reproduced with permission from ref 142. Copyright 2014 Royal Society of Chemistry.

The materials discussed in the two prior examples are effectively multi-stimuli (heat and light or ultrasound), multi-responsive (healing and shape-memory) systems, but in both cases the different stimuli can induce both responses and the ability to separately address either response is limited. A few conceptually different approaches to overcome this problem and access materials that respond in a selective manner to at least one of the stimuli have been proposed. One popular approach is the systematic incorporation of stimuli-responsive units into the polymer architecture. An early example of this design is the addition of metal binding ligands into a polymer network. Ligands impart a system with the ability to respond structurally to the presence of metal ions, and

they have the potential to contribute other responses including color changes and if the ligand is mesogenic also liquid-crystalline transitions. Furthermore, if the ligand is a chromophore (as many are) there is the potential of exploiting the photo-thermal effect. For example, building on the fluorescence-changing metallosupramolecular polymers based on complexes formed by the 2,6-bis(1'-methylbenzimidazolyl)pyridine (MeBip) ligand and Eu^{3+} ions discussed above,[133] Kumpfer et al. accessed thermo-, photo-, and chemo-responsive shape-memory/fluorescence responsive polymers.[145] To achieve this, a telechelic MeBip-terminated polybutadiene macromonomer was assembled into a metallosupramolecular polymer through the formation of metal coordination complexes with europium bistriflimide (3:1 binding of ligand to metal ion) (Figure 1.14A). The materials thus produced consisted of a hard phase formed by the metal ligand complexes and a soft polybutadiene phase. The soft phase was subsequently covalently cross-linked by UV irradiation-induced radical thiol-ene chemistry that involved a tetrathiol cross-linker to fix the permanent shape. Heat, irradiation with UV light, as well as exposure to suitable solvents (e.g. methanol, acetone, amines) resulted in a reversible softening of the metal ion/ligand hard phase, with a concomitant increased decomplexation and reshuffling rate of the metal-ligand complexes. Accordingly, such stimuli could now be used both to program a temporary shape or to trigger the shape-memory effect of these polymer films. Indeed, high strain fixing and recovery ratios were observed when samples were heated to 100 °C (well above the hard phase thermal transition of ca. 50 °C) for fixing of a temporary shape and subsequent shape-recovery. Furthermore, higher intensity UV irradiation (1000 mW/cm^2) generated enough localized heat (through the photo-thermal effect) to decomplex the europium metal ion-ligand complexes and induce a fluorescence

change in the material (Figure 1.14C), shifting the luminescence in the affected region from red (indicative of the ligand:Eu^{3+} complex) to blue (fluorescence of the free ligand). The absorption of light by the metal-ligand complexes and the conversion of this energy to heat, also allows for the activation of the shape-memory effect in a targeted sample area. In this way, selective irradiation of the edges of a folded box allowed a controlled stepwise recovery of the original open shape (Figure 1.14D). The hard phase of the metal-ligand complexes that fixes the temporary shape can also be weakened by exposure to solvents that induce plasticization or even decomplexation. Accordingly, a polymer film that was bent and fixed using UV light irradiation could subsequently exposed to a methanol atmosphere, which led to an almost full recovery of the permanent shape within 2 min of exposure (Figure 1.14E). Variations of metal ions influence the properties of the hard phase and allowed for a tuning of the fixing behavior, and higher covalent cross-link densities in the soft phase were found to further increase the strain fixing ratios.

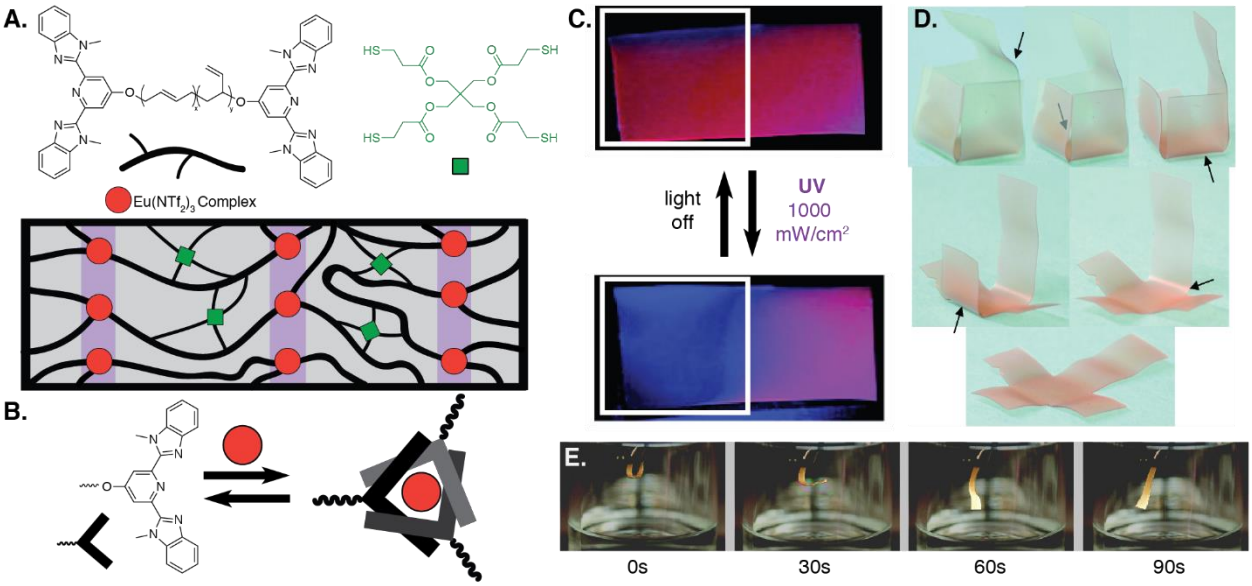

Figure 1.14. Multi-responsive material based on a metallosupramolecular network. A) Chemical structures of the network components, which include a MeBip ligand-terminated telechelic poly(budadiene) (black ropes), a tetrathiol cross-linker (green), and complexed MeBip ligands with Eu(NTf2)3 (red). B) General scheme for the reversible binding of MeBip with Eu3+ ions. C) Pictures demonstrating the UV-induced fluorescence change as the highlighted area is exposed to high-intensity UV light. D) Pictures documenting the step-wise recovery of a permanent box shape by targeted UV exposure (see arrows) of the edges. D) Pictures revealing the solvent-responsive shape recovery after 90s in solvent (methanol) vapor. Adapted and reproduced with permission from ref 145. Copyright 2011 American Chemical Society.

Of course, how exactly the responsive element is incorporated into the polymer architecture can have a significant role on the overall properties of the MSMR materials. For example, in the above metallosupramolecular polymer system, the functional components can be rearranged so that the ligand is incorporated in the backbone of a polymer, as opposed to the chain ends. The resulting polymeric network would retain the multi-stimuli-responsive characteristics of the previous system while accessing new responses; in this case these are a result of the liquid

crystalline behavior inherent to the alkyl functionalized ligand.[146] It had been shown previously that the terdentate EtBip ligand (the *N*-ethyl derivative of the MeBip discussed above) could exhibit liquid crystalline properties if alkyl units are placed on 5′-positions of the benzimidazolyl moiety (Figure 1.15A).[147,148] This combination of characteristics results in a mesogenic ligand with the ability to undergo not only a standard, thermally induced liquid crystal phase transition, but a chemically induced liquid crystal to isotropic transition as well (Figure 1.15B) upon the complexation of the ligand with a metal ion (Figure 1.15 C). By incorporating a bifunctional Bip mesogen into a polymeric network, these stimuli-responsive properties were utilized to create a MSMR material. This liquid crystalline elastomer (LCE) exhibited the standard properties of other LCEs (Figure 1.15 D), such as thermally induced shape-memory and actuation. However, the incorporation of the EtBip ligand imparted additional stimuli-sensitivity to the film. The ligand possesses chromophoric properties and as such UV light can be used to induce a thermal shape change/actuation via the photothermal effect. More exclusively, these films demonstrate the ability to actuate or shape-change upon exposure to metal ions. As such, placing the thermally-fixed film in a solution containing Fe^{2+} ions activates the shape-memory recovery while simultaneously shifting the color of the film to purple on account of the complex formation of the Fe^{2+} and the EtBip (Figure 1.15E). The recovery here is controlled by the metal ion coordination inducing the liquid-crystalline to isotropic transition. The strength of this response was noted in the film's ability to lift a 10 g weight when exposed to a solution containing metal ions, as the presence of metal ion induced the liquid crystalline to isotropic transition which resulted in the contraction of the film (Figure 1.15F).

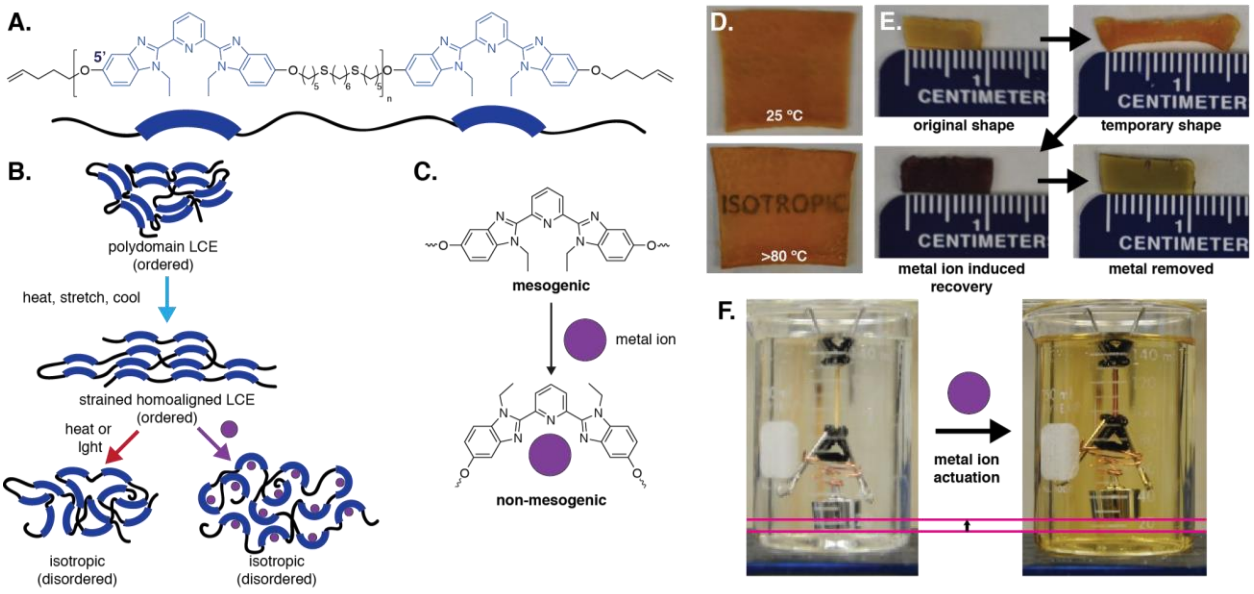

Figure 1.15. A) Chemical structure of a 5′-functionalized EtBip-based elastomer. B) Schematic of ordered and disordered configurations of the mesogenic moieties in response to mechanical, thermal, optical, or chemical stimulus. C) Schematic of the EtBip transition from mesogenic to non-mesogenic upon coordination with a metal ion. D) Photographs documenting the thermally-induced optical clearing of the liquid-crystalline elastomer. E) Pictures showing simple shape-memory behavior with recovery induced by metal ion exposure resulting in color change from orange to deep purple. F) Pictures of the metal-ion induced actuation demonstrated by the lifting of a 10g weight in a 1:1 water/tetrahydrofuran solution containing 1mM Fe(OTf)2. Adapted and reproduced with permission from ref 146. Copyright 2015 American Chemical Society.

Building on the metallopolymers based on similar building blocks as the above-discussed materials, Balkenende et al. demonstrated multiresponsive behavior in the solid state.[149] The Eu^{3+} complexes serve as dynamic binding motifs and built-in fluorophores that allow monitoring the metal-ligand complex (dis)assembly via their characteristic photoluminescence. This was exploited to demonstrate reversible metal-ligand dissociation upon ultrasonication in solution. Such mechanochemical transduction was also possible in the solid state and enabled the mending

of damaged objects through exposure to ultrasound. It was further shown that it is possible to induce a color change by a sequence of stimuli, i.e., the infusion of the solid Eu^{3+}-based metallopolymer with an Fe^{2+} salt, which was selected on account of its much higher binding constant to MeBip (vs. Eu^{3+}) and the deep purple color of the corresponding Fe^{2+}-MeBip complexes, and subsequent exposure to mechanical force. Indeed, while mere swelling with an $Fe(ClO_4)_2$ solution did not trigger any perceptible color change, the color changed to the deep purple color of the metal-to-ligand-charge-transfer transition characteristic of Fe^{2+}-MeBip complexes if the samples were also exposed to a mechanical force, such as gripping with tweezers or puncture by a needle. At the same time the Eu-based fluorescence was switched off. Both optical changes indicate the (irreversible) mechanically induced exchange of Eu^{3+} complexes for those of Fe^{2+}.

The design of supramolecular polymer systems involving multiple types of non-covalent binding motifs is an attractive approach to accessing multi-responsive polymers,[150,151] but many initial experiments to explore this concept were limited to solutions. Coulibaly et al. investigated supramolecular polymer blends composed of a physically cross-linked metallosupramolecular polymer based on a 2,6-bis(1′-methylbenzimidazolyl) pyridine (MeBip) terminated poly(ethylene-*co*-butylene) core (PEB) and metal ions ($[M(MeBip\text{-}PEB\text{-}MeBip)]^{2+}$ (M = Zn, Fe)) and another physically cross-linked supramolecular polymer based on a building block involving the same poly(ethylene-*co*-butylene) core and ureidopyrimidinone (UPy) hydrogen-bonding motifs (UPy-PEB-UPy).[152] The degree of orthogonality of the binding motifs in solution was investigated by UV-vis spectroscopic titrations, and small-angle X-ray scattering and dynamic mechanical

analysis (DMA) were used to characterize the solid-state properties. Blends of UPy-PEB-UPy and [Fe(MeBip-PEB-MeBip)]$(ClO_4)_2$ assembled in an orthogonal manner and adopted microphase separated lamellar morphologies in the solid state, with two hard phases formed by UPy-stacks and the metal-ligand motifs, respectively, that serve as physical cross-links, and a low-T_g phase formed by the PEB cores. DMA experiments revealed that the two hard phases melt and disassemble at different temperatures. The storage modulus of the blend decreased in a step-wise manner upon heating, with discrete steps around ca. 60 and ca. 180 °C, associated with the selective melting/disassembly of the UPy and Fe^{2+}-MeBip hard phases, respectively. The Fe^{2+}-MeBip interactions could also selectively be switched off by immersing the solid blends in solutions of *N*,*N*,*N*′,*N*″,*N*‴-pentanemethyldiethylenetriamine (PMDETA), which binds to Fe^{2+} more strongly than Mebip. This caused the deep purple color of the films to disappear, and the mechanical properties of dried samples suggest the absence of the Fe^{2+}-MeBip hard phase. The results demonstrate that the metal-ligand interactions can be selectively switched off by exposure to PMDETA, while the UPy-UPy interactions appeared largely unperturbed. Thus, the study confirmed the possibility to use supramolecular polymer blends to create multifunctional materials that display orthogonal behavior with respect to stimulus and function.

Supramolecular polymers are inherently responsive and generally show a level of healing ability. Thus, by simply incorporating another stimuli-responsive moiety into the supramolecular polymer will allow access to MSMR materials. This design approach was pursued by Lavrenova et al., who equipped a cyano-substituted oligo(*p*-phenylene vinylene) dye (cyano-OPV, Figure 1.16A), whose mechanically responsive luminescence behavior is associated with different

solid-state assemblies (*vide supra*), with two UPy groups, which support the formation of a dynamic supramolecular polymer.[153] This design exploits two types of orthogonal non-covalent interactions; the hydrogen bonds between the UPy motifs are utilized for supramolecular polymerization, whereas π-π stacking directs the packing of the cyano-OPV moieties (Figure 1.16B) and therewith their emission characteristics. The material exhibits the thermo-mechanical characteristics of a glassy supramolecular polymer, can be readily melt-processed into self-supporting objects, and three different solid-state structures with different emission colors can be accessed. The material exhibits both mechano-responsive and thermo-responsive luminescent behavior; while heating/cooling permits one to reversibly switch between green- and red emitting states, the fluorescence changes from to yellow upon exposure to mechanical force (Figure 1.16C).

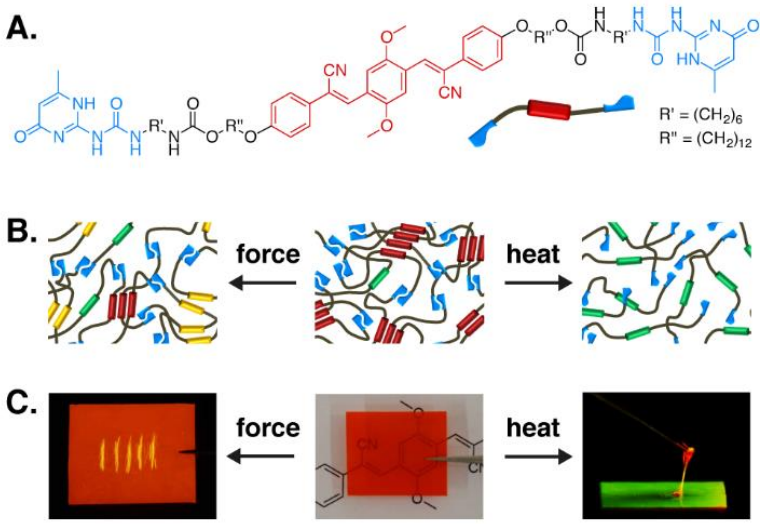

Figure 1.16. A) Chemical structure of the UPy-functionalized cyano-OPV. B) Schematic representation of supramolecular assemblies in which the cyano-OPV motifs display green, yellow, or red photoluminescence. C) Pictures of films made from the UPy-functionalized cyano-OPV, illustrating mechano- (left) and thermo-responsive (right) luminescent behavior. The fluorescence changes from red to yellow upon scratching (left). Upon heating (180 ˚C) a viscous green-light-emitting fluid is formed, which solidifies into a red-light emitting solid when cooled (right). Images displaying fluorescence were recorded under illumination with 365 nm UV light. Adapted and reproduced with permission from ref 153. Copyright 2017 American Chemical Society.

By combining metallosupramolecular motifs and a spiropyrane-based mechanophore, Hong et al. created polymeric materials in which different stimuli permitted healing and a change of color.[154] The materials studied relied on a high-molecular weight polyurethane backbone based on poly(tetrahydrofuran) and hexamethylene diisocyanate, into which the tridentate 2,6-bis(1,2,3-triazol-4-yl)pyridine (BTP) ligand and the spiropyran mechanophore were incorporated (Figure 1.17A). The materials were cross-linked by the addition of either a Zn^{2+} or a Eu^{3+} salt. These metal ions coordinate with the BTP ligands and trigger the formation of a phase-separated

morphology, involving a metal-ligand hard phase and a soft phase comprising (some of) the mechanophores. Deformation of the highly elastic materials causes activation of the mechanophore, which is converted from the closed spiro into the open merocyanine form, concomitant with a pronounced color change (Figure 1.17B). Interestingly, the samples gradually turned blue upon stretching, but assumed a red color upon fracturing and retraction (Figure 1.17C). The explanation provided by the authors involves shattering of the hard phase and (partial) dissociation of the metal-ligand motifs at high extension and binding of the merocyanine to the metal ions liberated from the BTP ligands in that process. Upon exposure to nonpolar solvents such as toluene or chloroform, deliberately applied cuts in the Zn^{2+}-based material disappeared (Figure 1.17D) and the mechanical properties were fully restored, although the process required several hours. The authors argue that the materials' ability to heal is related to the dynamic ligand exchange involving the metal ion:BTP complexes. The healing process is much slower than the light-induced healing of metallosupramolecular polymers in which similar binding motifs are used as chain-extenders.[155,156] This may be related to the much higher molecular weight of the polyurethane used here on the one hand, and the moderate influence of the nonpolar solvent on the ligand-exchange process on the other.

It appears that the design principle of combining a supramolecular motif with a mechanophore can be generalized, as long as the binding motif is strong enough (or trapped in a glass or crystalline phase) to allow enough stress to be focused on the mechanophore. In this respect, combining dynamic covalent chemistry with an appropriate mechanophore may provide an alternative, successful approach. Indeed, it should be possible to combine functions driven by

supramolecular/dynamic covalent (dis)assembly (healing, shape memory, adhesion, etc.) with mechano-responses that include color changes, spontaneous emission, cross-linking, and other intriguing functions.

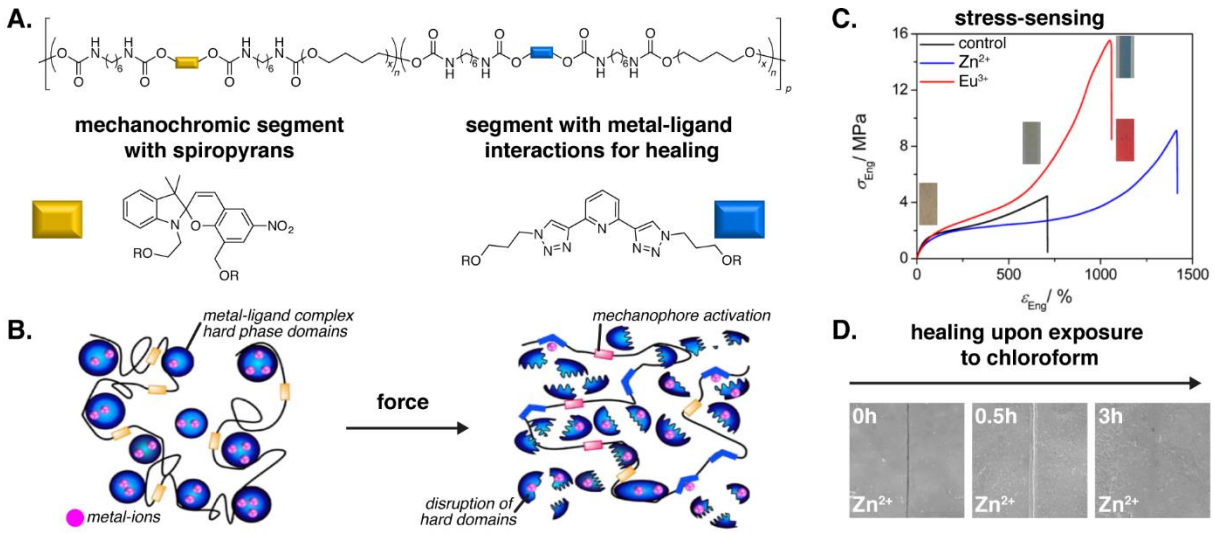

Figure 1.17. A) Chemical structure of a polyurethane with segments featuring a spiropyran mechanophore and segments with tridentate 2,6-bis(1,2,3-triazol-4-yl)pyridine ligands that form metal-ligand complexes. B) Schematic representation of the morphology and force-induced changes the polyurethane. The addition of either a Zn2+ or a Eu3+ salt causes cross-linking via ligand binding and the formation of a metal-ligand hard phase, which shatters upon excessive deformation. At the same time the spiropyran mechanophore is converted to the merocyanine form, which binds to the metal ions released from the complexes upon deformation. C) Stress-strain curves of the neat polymer and the corresponding materials containing Zn2+ or Eu3+ salts. The images shown document the color at various stages of extension. D) Images documenting the healing of a Zn2+ containing film upon exposure to a solvent. Adapted and reproduced with permission from ref 154. Copyright 2013 American Chemical Society.

In addition to chromogenic responses based on chemical changes or aggregation/dispersion of dye molecules, color changes in responsive materials can also be achieved by altering the

periodicity of photonic structures. As discussed before, the bandgap depends primarily on the geometry of the structure and the refractive indices of the components. Stimuli-responsiveness can accordingly be imparted by introducing at least one component that can translate an external stimulus into a change of its refractive index and/or the dimensions of the periodic structure.[76] Achieving a dimensional change with a mechanical stimulus is conceptually straightforward, and crystalline colloidal arrays of polymer spheres in hydrogel- or elastomer matrices have been developed that display a mechanically tunable photonic band gap.[157-163] The incorporation of a light- and temperature-responsive dye that exhibits switchable fluorescence and color into either the core or the shell of such colloidal particles afforded elastomeric opaline films whose optical properties could be altered in a perfectly independent manner via mechanical deformation (addressing the photonic structure) and through exposure to light/heat (addressing the responsive dyes). Thus in an intriguing approach to MSMR materials, the Rehahn group took advantage of a stepwise emulsion polymerization to form responsive beads featuring an incorporated fluorescent dye (Figure 1.18A).[164] The very low dispersity of these beads allowed for their assembly into photonic structures that respond to mechanical strains with color changes and a transition from fluorescent to non-fluorescent in response to light and heat, respectively. By synthesizing a polymerizable version of a light- and temperature-sensitive dye, rhodamine B methacrylamide (RhBMA), the group was able to covalently integrate the dye into either the core or the shell of sub-micrometer sized particles (e.g. 303 ± 19 nm) via emulsion polymerization. The particles were subsequently processed into films using a combination of coagulation, extrusion, and uniaxial compression molding techniques to effectively order the beads into colloidal crystals and

elastomeric opal films were obtained. When placed under strain, the mechanochromic behavior of the opal films was clearly visible as the color changed from red (λ = 660 nm) to green (λ = 560 nm) as the strain on the films increased from 0 to 90%, respectively (Figure 1.18B). The color change was attributed to two sequential processes taking place within the films during deformation: first, from 0 to 30% strain, the shifting of the original 111 crystalline lattice of the beads and second, from 40 to 90% strain, formation of a 200 plane within the film. In addition to the mechanochromic behavior, the materials displayed switchable fluorescence associated with the RhBMA moiety. The fluorophore has two forms, one open (fluorescent) and one closed (non-fluorescent). The fluorescent form is accessed via a ring-opening reaction upon exposure to UV light of a wavelength of 366 nm, whereas conversion back to the closed non-fluorescent form occurs upon heating. By using a mask and irradiating the film with light at 366 nm, a well-defined pattern can be formed on the opal film. This pattern was effectively erased by heating the film to close the dye structure and eliminate and fluorescent that was present (Figure 1.18C).

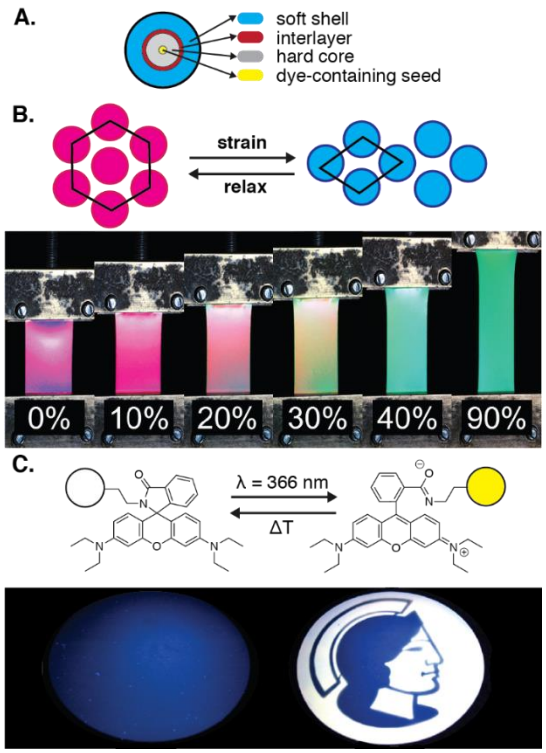

Figure 1.18. A) Schematic representation of the architecture of core-shell particles made via stepwise emulsion polymerization; seed with dye-labeled monomer (yellow), hard core surrounding the seed composed of styrene cross-linked with butanediol diacrylate (gray), interlayer of poly(ethyl acrylate-co-allyl methacrylate), and an outer soft shell comprised of ethyl acrylate, iso-butyl methacrylate, and hydroxyethyl methacrylate monomers for later cross-linking during film formation. B) Schematic and pictures illustrating principle and result of the strain-induced change of the colloidal crystal structure, resulting in color changes within the film with increasing strain. C) Schematic of the light-induced ring-opening and heat-induced ring-closure of the fluorescent and non-fluorescent RhBMA forms, respectively, and pictures demonstrating the erasable printing of a figure on the film. Adapted and reproduced with permission from ref 164. Copyright 2013 American Chemical Society.

In a related approach to multi-stimuli responsive color changing polymer systems, Schäfer et al. relied on the combination of effects that occur at very different length scales in stimuli-responsive photonic crystals (PCs) and light- or thermo-responsive small molecules.[164] The

approach should be readily applicable to other types of responsive photonic crystals, such as multilayer films or responsive PCs based on a (thermally or otherwise triggered) shape-memory polymer.[165] Moreover, other types of responsive molecules can be used in this context, *e.g.*, photoreactive chromogenic compounds,[166,167] or chemical sensor molecules.[168]

Another popular approach to MSMR polymers is the application of structurally dynamic polymers/networks that utilize reversible, dynamic covalent bonds, such as thermally reversible Diels-Alder chemistry discussed above (Figure 1.13). The reversible behavior of these bonds, as previously mentioned, imparts on the material the inherent ability to heal or be reprocessible under appropriate conditions. Thus, for example, Michal et al. have shown that by simply incorporating covalent disulfide bonds, which are dynamic upon exposure to light or heat (ca. 150 °C), into a semi-crystalline polymer network (Figure 1.19A) that exhibits shape-memory properties, a MSMR material can be accessed that can be healed upon exposure light or high temperature (ca. 150 °C) (Figure 1.19B) and which displays a shape-memory effect that can be triggered by heating above the T_m of the crystalline domains (ca. 65°C).[169,170] Thus, healing and shape memory can *a priori* be selectively triggered by separate stimuli. When the films are heated above the melting temperature of the crystalline regions (ca. 60°C, but well below the thermal transition temperature for the disulfide exchange), reshaped (by applying a force), and cooled back to room temperature, a temporary (high strain) shape is fixed. If the force is removed and the sample is simply heated above the T_m, the original (low strain) shape is recovered, i.e. standard shape-memory behavior is observed. In addition, new properties emerge from the combination of the dynamic bond exchange with the melting temperature of the semicrystalline covalent network, which are not simply a

combination of the two responses. One key emergent property here is the ability to reprogram the permanent shape of the material. Thus, if a conventionally accessed temporary shape is exposed to a stimulus that induces the dynamic disulfide exchange (such a light or high temperature if the sample is kept strained), then relaxation processes occur and convert this highly strained "fixed" shape into a new, low energy, reprogrammed "permanent shape" (Figure 1.19C). Thus, it was shown that an original flat tape can be processed such that its new remembered state is a coil. Furthermore, the combination of properties was found to be especially effective in accessing new classes of active adhesives. The dynamic covalent semi-crystalline network is not tacky to the touch and does not act as an adhesive at room temperature. Softening the material by heating above the T_m does result in some adhesion. However, activation of the dynamic disulfide bonds by heating above 150°C (with subsequent cooling) or exposure to light significantly increases the adhesion strength (Figure 1.19D). The hypothesis is that the decrease in viscosity associated with the dissociation of the network upon disulfide exchange, allows better surface wetting and increases the surface contact area. Upon removal of the stimulus, the cohesive strength of the adhesive returned as the semi-crystalline network reformed. The second level of enhanced adhesion also allow the adhesive materials to exhibit shape-memory when bonded, i.e. an active shape-memory adhesive. Thus, simply heating the bond above the T_m allows deformation/repositioning of the joint which can be fixed upon cooling. Reheating the joint to above the T_m allows the joint to recover it original position. (Figure 1.19E)

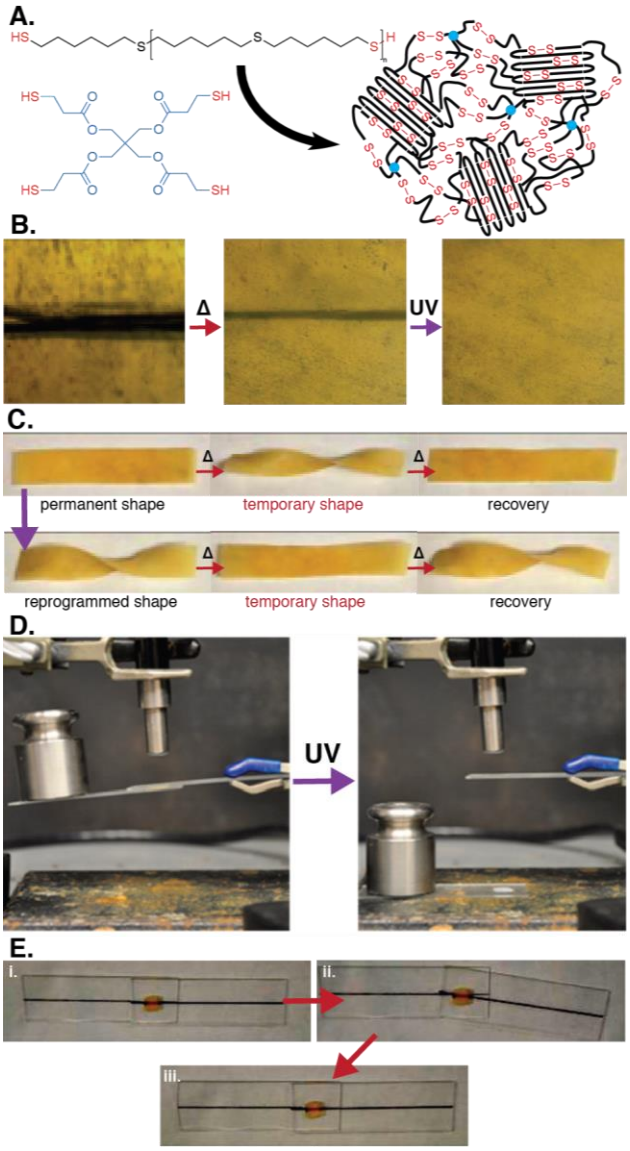

Figure 1.19. A) Chemical structures of disulfide adhesive components that, when combined, form a semi-crystalline network. B) Pictures illustrating the shape-memory-assisted healing of a scratch; the scratched film is heated to push the sides of the scratch together and UV light heals the remaining seam. C) Pictures illustrating the reprogrammable shape memory behavior; the original, permanent shape, capable of simple shape memory, is reprogrammed to a new, relaxed shape (via the introduction of UV light or thermal stimulus >150 °C) that is also capable of simple shape memory, D) release of adhesive (holding 200 g weight) by UV exposure. E) Pictures illustrating the thermal shape memory of the disulfide adhesive; the permanent shape (i) is heated (>80 C), deformed, and cooled to fix the temporary, kinked shape (ii), which can be returned to the original

shape upon reheating (iii). Adapted and reproduced with permission from refs 169 and 170. Copyright 2013 and 2016 American Chemical Society.

The MSMR materials in the above-discussed example relied on the combination of dynamic covalent bonds with a semi-crystalline network that exhibits thermally responsive shape-memory properties. Of course, dynamic networks can be merged with other responsive mechanisms, such as molecular conformational changes. Azobenzene motifs, for example, have been used in many responsive materials as they are inherently responsive to both UV and blue light.[171] When exposed to UV, the azobenzene moiety undergoes a conformational change from a *trans*-isomer to a *cis*-isomer (Figure 1.20A), resulting in a kinked structure that can disrupt any ordered (liquid crystalline) packing of the rod-like *trans*-isomer (Figure 1.20B). Blue light exposure also causes a *trans*-*cis* isomerization, however, the blue light process is a two-way transition as the molecule can return to the original orientation of the *trans*-isomer. Combining azobenzene with a dynamic covalent network, specifically an polyester that can undergo reversible transesterification, an MSMR polymer was prepared that displays a triple shape-memory effect, can be healed/reprocessed, and exhibits photo-activated bending through the interplay of four distinct mechanisms: photo-induced conformational changes of the azobenzene moiety, reversible transesterification reactions, glass transition (T_g), and liquid crystalline phase transitions (T_{lc}) involving the azobenzene mesogens.[172] In this particular example, the azobenzene molecule was functionalized with epoxy end groups to afford a mesogen that could be incorporated into a cross-linked polyester network via the reaction with sebacic acid (Figure 1.20C). Very much like other

systems that use dynamic covalent chemistries, the materials were shown to be healable and reprocessable above the vitrification temperature (T_v ca. 150°C) associated with the dynamic (catalyzed) transesterification reaction between the ester and hydroxyl groups in the network (Figure 1.20D). As a result of the photo-responsive behavior of azobenzene, exposure to blue light caused films of the material to bend selectively, either towards or away from the light source, depending on the orientation of the azobenzene mesogens in relation to the long axis of the film and with respect to the angle of the polarized light (Figure 1.20B). As seen in Figure 1.20Ei, the azobenzene-containing polyester networks exhibited a characteristic opaque to transparent transition upon heating to above T_{lc} (>103 °C). The material demonstrated a triple shape-memory behavior that was illustrated by the folding and unfolding of a box-shaped object. The permanent box shape was heated above T_{lc} (ca. 140 °C) to clear the LC phase, flattened, and cooled to a temperature below T_{lc}, but still above T_g (ca. 85 °C). At this temperature, the LC phase reformed, fixing the flattened, strained configuration and establishing the first temporary shape. The flattened box was then refolded 85 °C and cooled to room temperature (below T_g) to fix the second temporary shape. Upon reheating the box unfolded itself (Figure 1.20Eii) then reformed (Figure 1.20Eiii) as the temperature first passed T_g then T_{lc}, respectively. Given the light absorbing properties of the azobenzene moiety triple shape memory could also be achieved using UV-light via a photo-thermal conversion process.

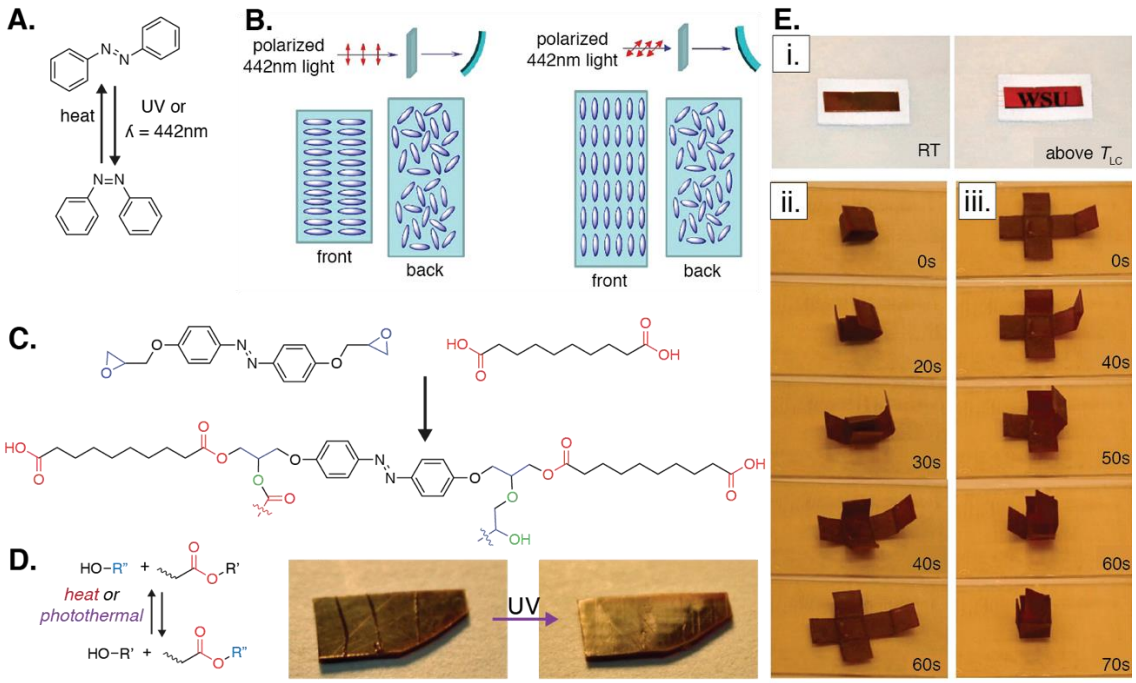

Figure 1.20. A) General schematic of the photo-induced trans-cis isomerization of azobenzene. B) Schematic illustrating the perpendicular alignment of azobenzenes in response to the polarization direction of incident polarized blue light that results in preferential bending of polyester networks containing azobenzene mesogens. C) Scheme showing the synthesis of azobenzene-containing polyester networks based on an epoxide-functionalized azobenzene and sebacic acid. D) Generalized schematic of the dynamic transesterification exchange that imparts the azobenzene networks with thermal- and UV-induced (via a photo-thermal process) healing. E) Pictures showing changes in transparency above TLC (>103 °C) (i) and thermal-responsive triple shape-memory behavior as a temporary shape (box) is recovered to another temporary shape (flattened box) with heating above Tg (ii) and the original, permanent shape (second box) is recovered above the TLC (iii). Adapted and reproduced with permission from ref 172. Copyright 2016 American Chemical Society.

While the systems discussed so far all exhibit responses to physical stimuli (i.e. heat and light), adding a component that is capable of responding to chemical stimuli can extend the utility of a MSMR material. For example, the incorporation of an amino-capped aniline trimer (ACAT) allows access to new responses, such as pH-responsive transmittance changes, color changes

influenced by electric fields, and metal ion absorption, to pre-existing responsive materials. Consider a system containing similar features to the prior example – a polyester-based network that can be reconfigured via transesterification and displays the ability to be healed, welded, and reprocessed – that also incorporates the ACAT (instead of the azobenzene) in the network (Figure 1.21A). The addition of the chemo-responsive component resulted in a material that was shown to have multiple responses to six different stimuli – heat, light, redox, electrical, pH, and metal ion.[173] As in the case of the azobenzene-containing networks discussed above, the material exhibited healing/welding/reprocessing properties made possible by the presence of the dynamic (catalyzed by triazobicyclodecene) transesterification exchange within the polyester network. The ACAT, like azobenzene, also has photothermal properties that convert light (in case, infrared (IR) light was used) to heat and when added to the thermally-responsive network, imparts the network with the ability to access shape memory and healing/welding via a photo-induced process (Figure 1.21B). What makes the ACAT material more unique compared to the previous system is the chemo- and electrochemo-responsiveness of the molecule in the presence of acids/bases, metal ions, redox conditions, and electrical fields. Changes in redox conditions (oxidizing or reducing the aniline trimer) triggered a change in the transmittance of films: in the presence of an oxidant, the film appeared light colored and transparent while the addition of a reductant resulted in a darker film with significantly reduced transparency (Figure 1.21C). A similar effect is observed upon electrochemical stimulation from 0 to 0.8 V. The protonation and deprotonation of the trimer resulted in the expansion and contraction of the bulk film. In the presence of metal ions (Cu^{2+}, in this case), ACAT-containing film binds to the metal ion resulting in bulk contraction of the

network film. It should be noted that in this case, the hydroxyl groups from the epoxy network is proposed to also contribute to the metal ion absorption capability of the film. Interestingly, the group was able to demonstrate numerous methods of combining these properties in unique ways, such as forming ACAT-dynamic network/nonACAT-dynamic network bilayer films (via thermal welding) which exhibit directed bending in response to metal ions (Figure 1.21D) and pH (Figure 1.21E). These techniques highlight the versatility of dynamic systems and demonstrate a different approach to combining responsive mechanisms to create new MSMR materials.

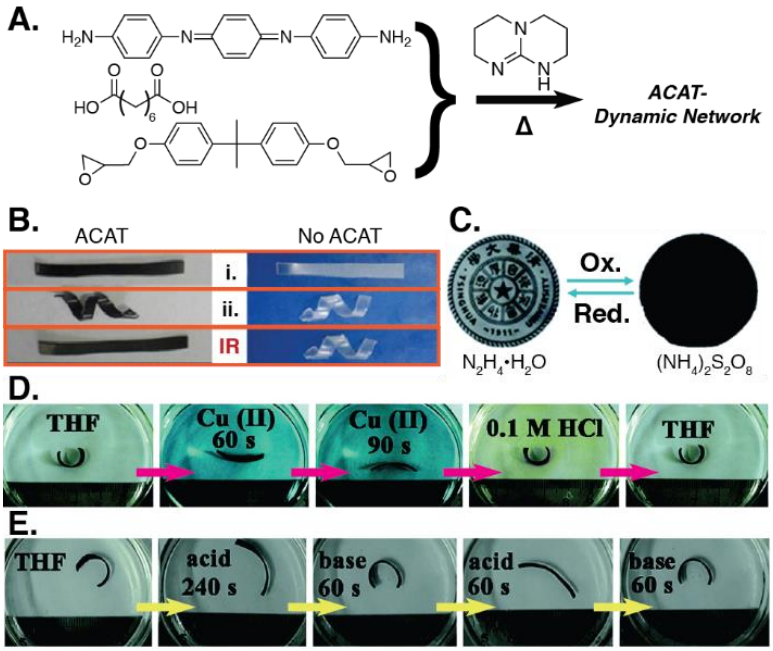

Figure 1.21. A) Chemical structures of the monomers used to create MSMR polyester networks: bisphenol A diglycidyl ether, suberic acid, and the amino-capped aniline trimer (ACAT) combined with triazobicyclodecene (TBD) under heat to form the ACAT-dynamic networks. B) Picture showing a permanent, flat film having been thermally programmed (heating above Tv, deforming, cooling to room temperature, and releasing force) into a coil that is recoverable via infrared (IR) exposure in the case of the ACAT network, but not recoverable by IR in the neat, dynamic network. C) Picture of the MSMR polyester film, demonstrating the optical response of the ACAT molecule upon oxidation/reduction. D) Pictures demonstrating metallo- and acid-response in a bilayer film consisting of one layer made of the ACAT-dynamic network, and one layer made by the neat dynamic network only; the film was placed in THF and exposed to copper ions causing the ACAT-vitrimer side to swell and the shape to change. When the film was subsequently placed into a 0.1M HCl solution the metal coordination and bending were reversed. E) Pictures demonstrating that the bilayer film also exhibits reversible shape changes as the pH of the solution is changed between acidic and basic and the responsive side swells and shrinks. Adapted and reproduced with permission from ref 173. Copyright 2017 Royal Society of Chemistry.

1.6 Conclusions

Nature is awash with fascinating examples of materials that adapt in response to environmental cues, ranging from the complex color changing behavior of chameleons, cuttlefish, and cephalopods to seeds that have the ability to "drill" themselves into the ground, and pine cones that open up and release their seeds upon drying.[174] While all these functions are vital for the survival of the respective species, all of them would certainly be extinct if the materials systems at play would not have evolved to serve their hosts in a multifunctional manner. Indeed, most living materials systems are characterized by a high level of complexity in order to go well beyond a single responsive mechanism. The current generation of MSMR polymers (and short of a major breakthrough in the field, presumably also the next few generations) do not come anywhere close to such a level of complexity, but the first tentative steps towards the lofty target of achieving a comparable multifunctional behavior in artificial materials have been made. Indeed, artificial MSMR polymers have evolved in the last three decades from a few obscure examples to a point where there is no doubt that materials can be programmed to display several functions that can each be triggered in a highly specific manner upon exposure to appropriate stimuli. The vast majority of materials systems have been created by combining at least two "orthogonal" mechanisms/functions in rational ways and first systems that display emergent behavior, i.e. a new property/behavior in addition to the simple addition of the combined responses associated with the individual components, have also been realized. Indeed, it appears that the fact that new properties/behaviors can emerge from the "simple" combination of two or more functionalities or responses is a very powerful tool for polymer scientists and engineers. In the interest of exploring

new methodologies to target this combinatorial approach, this thesis focuses on the design, synthesis, and characterization of functional materials whose properties can be tailored through the molecular engineering of dynamic or mechanical bonds.

1.7 References

(1) Stille, J. K.; Mainen, E. L. Thermally Stable Ladder Polyquinoxalines. *Macromolecules* **1968**, *1*, 36–42.

(2) Brandrup, J.; Peebles, L. H. On the Chromophore of Polyacrylonitrile. IV. Thermal Oxidation of Polyacrylonitrile and Other Nitrile-Containing Compounds. *Macromolecules* **1968**, *1*, 64–72.

(3) Brandrup, J. On the Chromophore of Polyacrylonitrile. V. The Oxidation of Isobutyronitrile. *Macromolecules* **1968**, *1*, 72–79.

(4) Friedlander, H. N.; Peebles, L. H.; Brandrup, J.; Kirby, J. R. On the Chromophore of Polyacrylonitrile. VI. Mechanism of Color Formation in Polyacrylonitrile. *Macromolecules* **1968**, *1*, 79–86.

(5) Maxim, L. D.; Kuist, C. H.; Meyer, M. E. The Ultraviolet Degradation of Terpolymer Scissioning Systems. *Macromolecules* **1968**, *1*, 86–93.

(6) Heskins, M.; Guillet, J. E. Mechanism of Ultraviolet Stabilization of Polymers. *Macromolecules* **1968**, *1*, 97–98.

(7) Trozzolo, A. M.; Winslow, F. H. A Mechanism for the Oxidative Photodegradation of Polyethylene. *Macromolecules* **1968**, *1*, 98–100.

(8) Stuart, M. A. C.; Huck, W. T. S.; Genzer, J.; Müller, M.; Ober, C.; Stamm, M.; Sukhorukov, G. B.; Szleifer, I.; Tsukruk, V. V.; Urban, M.; et al. Emerging Applications of Stimuli-Responsive Polymer Materials. *Nature Mater.* **2010**, *9*, 101–113.

(9) Roy, D.; Cambre, J. N.; Sumerlin, B. S. Future Perspectives and Recent Advances in Stimuli-Responsive Materials. *Prog. Polym. Sci.* **2010**, *35*, 278–301.

(10) Wojtecki, R. J.; Meador, M. A.; Rowan, S. J. Using the Dynamic Bond to Access Macroscopically Responsive Structurally Dynamic Polymers. *Nature Mater.* **2011**, *10*, 14–27.

(11) *Handbook of Stimuli-Responsive Materials*; Urban, M. W., Ed.; Wiley-VCH: Weinheim, 2011.

(12) Irie, M. Stimuli-Responsive Poly(N-Isopropylacrylamide). Photo- and Chemical-Induced Phase Transitions. In *Advances in Polymer Science*; Advances in Polymer Science; Springer-Verlag: Berlin/Heidelberg, 1993; Vol. 110, pp 49–65.

(13) Okano, T. Molecular Design of Temperature-Responsive Polymers as Intelligent Materials. In *Advances in Polymer Science*; Advances in Polymer Science; Springer-Verlag: Berlin/Heidelberg, 1993; Vol. 110, pp 179–197.

(14) Osada, Y.; Gong, J. P. Stimuli-Responsive Polymer Gels and Their Application to Chemomechanical Systems. *Prog. Polym. Sci.* **1993**, *18*, 187–226.

(15) Kwon, I. C.; Bae, Y. H.; Okano, T.; Kim, S. W.; Berner, B. Stimuli Sensitive Polymers for Drug Delivery Systems. *Makromol. Chem., Macromol. Symp.* **2011**, *33*, 265–277.

(16) Gehrke, S. H. Synthesis, Equilibrium Swelling, Kinetics, Permeability and Applications of Environmentally Responsive Gels. In *Advances in Polymer Science*; Dušek, K., Ed.; Responsive Gels: Volume Transitions II; Springer-Verlag: Berlin, Heidelberg, 1993; Vol. 110, pp 81–144.

(17) Hoffman, A. S. Environmentally Sensitive Polymers and Hydrogels. *MRS Bull.* **2013**, *16*, 42–46.

(18) Osada, Y.; Saito, Y. Mechanochemical Energy Conversion in a Polymer Membrane by Thermo-Reversible Polymer-Polymer Interactions. *Makromol. Chem.* **1975**, *176*, 2761–2764.

(19) Tanaka, T. Phase Transitions in Gels and a Single Polymer. *Polymer* **1979**, *20*, 1404–1412.

(20) Tanaka, T. Phase Transitions of Gels. In *Polyelectrolyte Gels*; ACS Symposium Series; American Chemical Society: Washington, DC, 1992; Vol. 480, pp 1–21.

(21) Hsu, L.; Weder, C.; Rowan, S. J. Stimuli-Responsive, Mechanically-Adaptive Polymer Nanocomposites. *J. Mater. Chem.* **2011**, *21*, 2812–2822.

(22) Esser-Kahn, A. P.; Odom, S. A.; Sottos, N. R.; White, S. R.; Moore, J. S. Triggered Release From Polymer Capsules. *Macromolecules* **2011**, *44*, 5539–5553.

(23) Liu, F.; Urban, M. W. Recent Advances and Challenges in Designing Stimuli-Responsive Polymers. *Prog. Polym. Sci.* **2010**, *35*, 3–23.

(24) Heinzmann, C.; Weder, C.; de Espinosa, L. M. Supramolecular Polymer Adhesives: Advanced Materials Inspired by Nature. *Chem. Soc. Rev.* **2016**, *45*, 342–358.

(25) Yan, X.; Wang, F.; Zheng, B.; Huang, F. Stimuli-Responsive Supramolecular Polymeric Materials. *Chem. Soc. Rev.* **2012**, *41*, 6042–6065.

(26) Jochum, F. D.; Theato, P. Temperature- and Light-Responsive Smart Polymer Materials. *Chem. Soc. Rev.* **2013**, *42*, 7468–7483.

(27) Kloxin, C. J.; Bowman, C. N. Covalent Adaptable Networks: Smart, Reconfigurable and Responsive Network Systems. *Chem. Soc. Rev.* **2013**, *42*, 7161–7173.

(28) Wei, M.; Gao, Y.; Li, X.; Serpe, M. J. Stimuli-Responsive Polymers and Their Applications. *Polym. Chem.* **2017**, *8*, 127–143.

(29) de Ruiter, G.; van der Boom, M. E. Surface-Confined Assemblies and Polymers for Molecular Logic. *Acc. Chem. Res.* **2011**, *44*, 563–573.

(30) Swager, T. M. 50th Anniversary Perspective: Conducting/Semiconducting Conjugated Polymers. a Personal Perspective on the Past and the Future. *Macromolecules* **2017**, *50*, 4867–4886.

(31) Chen, L.; Tian, Y.-K.; Ding, Y.; Tian, Y.-J.; Wang, F. Multistimuli Responsive Supramolecular Cross-Linked Networks on the Basis of the Benzo-21-Crown-7/Secondary Ammonium Salt Recognition Motif. *Macromolecules* **2012**, *45*, 8412–8419.

(32) Fullenkamp, D. E.; He, L.; Barrett, D. G.; Burghardt, W. R.; Messersmith, P. B. Mussel-Inspired Histidine-Based Transient Network Metal Coordination Hydrogels. *Macromolecules* **2013**, *46*, 1167–1174.

(33) Gulyuz, U.; Okay, O. Self-Healing Poly(Acrylic Acid) Hydrogels with Shape Memory Behavior of High Mechanical Strength. *Macromolecules* **2014**, *47*, 6889–6899.

(34) Mura, S.; Nicolas, J.; Couvreur, P. Stimuli-Responsive Nanocarriers for Drug Delivery. *Nature Mater.* **2013**, *12*, 991–1003.

(35) Cao, Z.-Q.; Wang, G.-J. Multi-Stimuli-Responsive Polymer Materials: Particles, Films, and Bulk Gels. *Chem. Record* **2016**, *16*, 1398–1435.

(36) Appel, E. A.; del Barrio, J.; Loh, X. J.; Scherman, O. A. Supramolecular Polymeric Hydrogels. *Chem. Soc. Rev.* **2012**, *41*, 6195–6214.

(37) Jeon, S.-J.; Hauser, A. W.; Hayward, R. C. Shape-Morphing Materials From Stimuli-Responsive Hydrogel Hybrids. *Acc. Chem. Res.* **2017**, *50*, 161–169.

(38) Culver, H. R.; Clegg, J. R.; Peppas, N. A. Analyte-Responsive Hydrogels: Intelligent Materials for Biosensing and Drug Delivery. *Acc. Chem. Res.* **2017**, *50*, 170–178.

(39) Salvekar, A. V.; Huang, W. M.; Xiao, R.; Wong, Y. S.; Venkatraman, S. S.; Tay, K. H.; Shen, Z. X. Water-Responsive Shape Recovery Induced Buckling in Biodegradable Photo-Cross-Linked Poly(Ethylene Glycol) (PEG) Hydrogel. *Acc. Chem. Res.* **2017**, *50*, 141–150.

(40) Konieczynska, M. D.; Grinstaff, M. W. On-Demand Dissolution of Chemically Cross-Linked Hydrogels. *Acc. Chem. Res.* **2017**, *50*, 151–160.

(41) Löwenberg, C.; Balk, M.; Wischke, C.; Behl, M.; Lendlein, A. Shape-Memory Hydrogels: Evolution of Structural Principles to Enable Shape Switching of Hydrophilic Polymer Networks. *Acc. Chem. Res.* **2017**, *50*, 723–732.

(42) Ko, H.; Javey, A. Smart Actuators and Adhesives for Reconfigurable Matter. *Acc. Chem. Res.* **2017**, *50*, 691–702.

(43) Shao, Y.; Jia, H.; Cao, T.; Liu, D. Supramolecular Hydrogels Based on DNA Self-Assembly. *Acc. Chem. Res.* **2017**, *50*, 659–668.

(44) Shigemitsu, H.; Hamachi, I. Design Strategies of Stimuli-Responsive Supramolecular Hydrogels Relying on Structural Analyses and Cell-Mimicking Approaches. *Acc. Chem. Res.* **2017**, *50*, 740–750.

(45) Tam, R. Y.; Smith, L. J.; Shoichet, M. S. Engineering Cellular Microenvironments with Photo- and Enzymatically Responsive Hydrogels: Toward Biomimetic 3D Cell Culture Models. *Acc. Chem. Res.* **2017**, *50*, 703–713.

(46) Kahn, J. S.; Hu, Y.; Willner, I. Stimuli-Responsive DNA-Based Hydrogels: From Basic Principles to Applications. *Acc. Chem. Res.* **2017**, *50*, 680–690.

(47) Luo, X.; Mather, P. T. Shape Memory Assisted Self-Healing Coating. *ACS Macro Lett.* **2013**, *2*, 152–156.

(48) Nguyen, J. K.; Jorfi, M.; Buchanan, K. L.; Park, D. J.; Foster, E. J.; Tyler, D. J.; Rowan, S. J.; Weder, C.; Capadona, J. R. Influence of Resveratrol Release on the Tissue Response to Mechanically Adaptive Cortical Implants. *Acta Biomater.* **2016**, *29*, 81–93.

(49) Jorfi, M.; Roberts, M. N.; Foster, E. J.; Weder, C. Physiologically Responsive, Mechanically Adaptive Bio-Nanocomposites for Biomedical Applications. *ACS Appl. Mater. Interfaces* **2013**, *5*, 1517–1526.

(50) Knothe Tate, M. L.; Detamore, M.; Capadona, J. R.; Woolley, A.; Knothe, U. Engineering and Commercialization of Human-Device Interfaces, From Bone to Brain. *Biomaterials* **2016**, *95*, 35–46.

(51) Wu, D. Y.; Meure, S.; Solomon, D. Self-Healing Polymeric Materials: a Review of Recent Developments. *Prog. Polym. Sci.* **2008**, *33*, 479–522.

(52) Wool, R. P. Self-Healing Materials: a Review. *Soft Matter* **2008**, *4*, 400–418.

(53) Burattini, S.; Greenland, B. W.; Chappell, D.; Colquhoun, H. M.; Hayes, W. Healable Polymeric Materials: a Tutorial Review. *Chem. Soc. Rev.* **2010**, *39*, 1973–1985.

(54) Murphy, E. B.; Wudl, F. The World of Smart Healable Materials. *Prog. Polym. Sci.* **2010**, *35*, 223–251.

(55) Syrett, J. A.; Becer, C. R.; Haddleton, D. M. Self-Healing and Self-Mendable Polymers. *Polym. Chem.* **2010**, *1*, 978–987.

(56) Yang, Y.; Urban, M. W. Self-Healing Polymeric Materials. *Chem. Soc. Rev.* **2013**, *42*, 7446–7467.

(57) de Espinosa, L. M.; Fiore, G. L.; Weder, C.; Johan Foster, E.; Simon, Y. C. Healable Supramolecular Polymer Solids. *Prog. Polym. Sci.* **2015**, *49-50*, 60–78.

(58) Kim, Y. H.; Wool, R. P. A Theory of Healing at a Polymer-Polymer Interface. *Macromolecules* **1983**, *16*, 1115–1120.

(59) Ghosh, B.; Urban, M. W. Self-Repairing Oxetane-Substituted Chitosan Polyurethane Networks. *Science* **2009**, *323*, 1458–1460.

(60) Kirkby, E. L.; Michaud, V. J.; Maringnson, J. A. E.; Sottos, N. R.; White, S. R. Performance of Self-Healing Epoxy with Microencapsulated Healing Agent and Shape Memory Alloy Wires. *Polymer* **2009**, *50*, 5533–5538.

(61) Caruso, M. M.; Davis, D. A.; Shen, Q.; Odom, S. A.; Sottos, N. R.; White, S. R.; Moore, J. S. Mechanically-Induced Chemical Changes in Polymeric Materials. *Chem. Rev.* **2009**, *109*, 5755–5798.

(62) Blaiszik, B. J.; Kramer, S. L. B.; Olugebefola, S. C.; Moore, J. S.; Sottos, N. R.; White, S. R. Self-Healing Polymers and Composites. *Annu. Rev. Mater. Res.* **2010**, *40*, 179–211.

(63) Patrick, J. F.; Robb, M. J.; Sottos, N. R.; Moore, J. S.; White, S. R. Polymers with Autonomous Life-Cycle Control. *Nature* **2016**, *540*, 363–370.

(64) Liu, C.; Qin, H.; Mather, P. T. Review of Progress in Shape-Memory Polymers. *J. Mater. Chem.* **2007**, *17*, 1543–1558.

(65) Mather, P. T.; Luo, X.; Rousseau, I. A. Shape Memory Polymer Research. *Annu. Rev. Mater. Res.* **2009**, *39*, 445–471.

(66) Xie, T. Recent Advances in Polymer Shape Memory. *Polymer* **2011**, *52*, 4985–5000.

(67) Hu, J.; Zhu, Y.; Huang, H.; Lu, J. Recent Advances in Shape–Memory Polymers: Structure, Mechanism, Functionality, Modeling and Applications. *Prog. Polym. Sci.* **2012**, *37*, 1720–1763.

(68) Huang, W. M.; Zhao, Y.; Wang, C. C.; Ding, Z.; Purnawali, H.; Tang, C.; Zhang, J. L. Thermo/Chemo-Responsive Shape Memory Effect in Polymers: a Sketch of Working Mechanisms, Fundamentals and Optimization. *J. Polym. Res.* **2012**, *19*, 9952.

(69) Sun, L.; Huang, W. M.; Ding, Z.; Zhao, Y.; Wang, C. C.; Purnawali, H.; Tang, C. Stimulus-Responsive Shape Memory Materials: a Review. *Mater. Des.* **2012**, *33*, 577–640.

(70) Berg, G. J.; McBride, M. K.; Wang, C.; Bowman, C. N. New Directions in the Chemistry of Shape Memory Polymers. *Polymer* **2014**, *55*, 5849–5872.

(71) Hager, M. D.; Bode, S.; Weber, C.; Schubert, U. S. Shape Memory Polymers: Past, Present and Future Developments. *Prog. Polym. Sci.* **2015**, *49-50*, 3–33.

(72) White, T. J.; Broer, D. J. Programmable and Adaptive Mechanics with Liquid Crystal Polymer Networks and Elastomers. *Nature Mater.* **2015**, *14*, 1087–1098.

(73) Iqbal, D.; Samiullah, M. Photo-Responsive Shape-Memory and Shape-Changing Liquid-Crystal Polymer Networks. *Materials* **2013**, *6*, 116–142.

(74) Meng, H.; Li, G. A Review of Stimuli-Responsive Shape Memory Polymer Composites. *Polymer* **2013**, *54*, 2199–2221.

(75) Beaujuge, P. M.; Reynolds, J. R. Color Control in Π-Conjugated Organic Polymers for Use in Electrochromic Devices. *Chem. Rev.* **2010**, *110*, 268–320.

(76) Weder, C. Mechanochromic Polymers. In *Encyclopedia of Polymeric Nanomaterials*; Springer Berlin Heidelberg: Berlin, Heidelberg, 2014; pp 1–11.

(77) Seeboth, A.; Lötzsch, D.; Ruhmann, R.; Muehling, O. Thermochromic Polymers—Function by Design. *Chem. Rev.* **2014**, *114*, 3037–3068.

(78) Ferrara, M.; Bengisu, M. Materials That Change Color: Smart Materials, Intelligent Design. In *Springer Briefs in Applied Sciences and Technology*; Pernici, B., Torre, Della, S., Colosimo, B. M., Faravelli, T., Paolucci, R., Piardi, S., Eds.; Springer: Heidelberg, 2014; pp 9–60.

(79) Bamfield, P.; Hutchings, M. G. *Chromic Phenomena: Technological Applications of Colour Chemistry*, 2nd ed.; Royal Society of Chemistry: Cambridge, 2010.

(80) Lötzsch, D.; Eberhardt, V.; Rabe, C. Chromogenic Materials. In *Ullmann's Encyclopedia of Industrial Chemistry*; Wiley VCH: Weinheim, 2016; pp 1–26.

(81) Berkovic, G.; Krongauz, V.; Weiss, V. Spiropyrans and Spirooxazines for Memories and Switches. *Chem. Rev.* **2000**, *100*, 1741–1754.

(82) Klajn, R. Spiropyran-Based Dynamic Materials. *Chem. Soc. Rev.* **2014**, *43*, 148–184.

(83) Calvino, C.; Neumann, L.; Weder, C.; Schrettl, S. Approaches to Polymeric Mechanochromic Materials. *J. Polym. Sci. Part A: Polym. Chem.* **2017**, *55*, 640–652.

(84) Sagara, Y.; Yamane, S.; Mitani, M.; Weder, C.; Kato, T. Mechanoresponsive Luminescent Molecular Assemblies: an Emerging Class of Materials. *Adv. Mater.* **2016**, *28*, 1073–1095.

(85) Makowski, B.; Kunzelman, J.; Weder, C. Stimuli-Driven Assembly of Chromogenic Dye Molecules: a Versatile Approach for the Design of Responsive Polymers. In *Handbook of Stimuli-Responsive Materials*; Urban, M. W., Ed.; Wiley-VCH: Weinheim, 2011; pp 117–138.

(86) Ge, J.; Yin, Y. Responsive Photonic Crystals. *Angew. Chem. Int. Ed.* **2011**, *50*, 1492–1522.

(87) Heinzmann, C.; Coulibaly, S.; Roulin, A.; Fiore, G. L.; Weder, C. Light-Induced Bonding and Debonding with Supramolecular Adhesives. *ACS Appl. Mater. Interfaces* **2014**, *6*, 4713–4719.

(88) Heinzmann, C.; Lamparth, I.; Rist, K.; Moszner, N.; Fiore, G. L.; Weder, C. Supramolecular Polymer Networks Made by Solvent-Free Copolymerization of a Liquid 2-Ureido-4[1 H]-Pyrimidinone Methacrylamide. *Macromolecules* **2015**, *48*, 8128–8136.

(89) Balkenende, D. W. R.; Olson, R. A.; Balog, S.; Weder, C.; Montero de Espinosa, L. Epoxy Resin-Inspired Reconfigurable Supramolecular Networks. *Macromolecules* **2016**, *49*, 7877–7885.

(90) Gibson, R. F. A Review of Recent Research on Mechanics of Multifunctional Composite Materials and Structures. *Composite Structures* **2010**, *92*, 2793–2810.

(91) McEvoy, M. A.; Correll, N. Materials That Couple Sensing, Actuation, Computation, and Communication. *Science* **2015**, *347*, 1261689.

(92) Qiu, X.; Hu, S. "Smart" Materials Based on Cellulose: a Review of the Preparations, Properties, and Applications. *Materials* **2013**, *6*, 738–781.

(93) Stone, D. A.; Korley, L. T. J. Bioinspired Polymeric Nanocomposites. *Macromolecules* **2010**, *43*, 9217–9226.

(94) Capadona, J. R.; Shanmuganathan, K.; Tyler, D. J.; Rowan, S. J.; Weder, C. Stimuli-Responsive Polymer Nanocomposites Inspired by the Sea Cucumber Dermis. *Science* **2008**, *319*, 1370–1374.

(95) Shanmuganathan, K.; Capadona, J. R.; Rowan, S. J.; Weder, C. Biomimetic Mechanically Adaptive Nanocomposites. *Prog. Polym. Sci.* **2010**, *35*, 212–222.

(96) Craig, S. L. Cool as a Cucumber. *Angew. Chem. Int. Ed.* **2008**, *47*, 8776–8777.

(97) Jain, P. K.; Huang, X.; El-Sayed, I. H.; El-Sayed, M. A. Noble Metals on the Nanoscale: Optical and Photothermal Properties and Some Applications in Imaging, Sensing, Biology, and Medicine. *Acc. Chem. Res.* **2008**, *41*, 1578–1586.

(98) Link, S.; El-Sayed, M. A. Shape and Size Dependence of Radiative, Non-Radiative and Photothermal Properties of Gold Nanocrystals. *Int. Rev. Phys. Chem.* **2000**, *19*, 409–453.

(99) Maier, S. A.; Atwater, H. A. Plasmonics: Localization and Guiding of Electromagnetic Energy in Metal/Dielectric Structures. *J. Appl. Phys.* **2005**, *98*, 011101.

(100) Lu, A.-H.; Salabas, E. L.; Schüth, F. Magnetic Nanoparticles: Synthesis, Protection, Functionalization, and Application. *Angew. Chem. Int. Ed.* **2007**, *46*, 1222–1244.

(101) Laurent, S.; Forge, D.; Port, M.; Roch, A.; Robic, C.; Vander Elst, L.; Muller, R. N. Magnetic Iron Oxide Nanoparticles: Synthesis, Stabilization, Vectorization, Physicochemical Characterizations, and Biological Applications. *Chem. Rev.* **2008**, *108*, 2064–2110.

(102) Gugumus, F. Re-Evaluation of the Stabilization Mechanisms of Various Light Stabilizer Classes. *Polym. Degrad. Stab.* **1993**, *39*, 117–135.

(103) Maity, S.; Downen, L. N.; Bochinski, J. R.; Clarke, L. I. Embedded Metal Nanoparticles as Localized Heat Sources: an Alternative Processing Approach for Complex Polymeric Materials. *Polymer* **2011**, *52*, 1674–1685.

(104) Viswanath, V.; Maity, S.; Bochinski, J. R.; Clarke, L. I.; Gorga, R. E. Thermal Annealing of Polymer Nanocomposites via Photothermal Heating: Effects on Crystallinity and Spherulite Morphology. *Macromolecules* **2013**, *46*, 8596–8607.

(105) Maity, S.; Kozek, K. A.; Wu, W.-C.; Tracy, J. B.; Bochinski, J. R.; Clarke, L. I. Anisotropic Thermal Processing of Polymer Nanocomposites via the Photothermal Effect of Gold Nanorods. *Part. Part. Syst. Charact.* **2013**, *30*, 193–202.

(106) Maity, S.; Bochinski, J. R.; Clarke, L. I. Metal Nanoparticles Acting as Light-Activated Heating Elements Within Composite Materials. *Adv. Funct. Mater.* **2012**, *22*, 5259–5270.

(107) Zhao, Q.; Qi, H. J.; Xie, T. Recent Progress in Shape Memory Polymer: New Behavior, Enabling Materials, and Mechanistic Understanding. *Prog. Polym. Sci.* **2015**, *49-50*, 79–120.

(108) Xie, T. Tunable Polymer Multi-Shape Memory Effect. *Nature* **2010**, *464*, 267–270.

(109) Mauritz, K. A.; Moore, R. B. State of Understanding of Nafion. *Chem. Rev.* **2004**, *104*, 4535–4586.

(110) Rubatat, L.; Rollet, A. L.; Gebel, G.; Diat, O. Evidence of Elongated Polymeric Aggregates in Nafion. *Macromolecules* **2002**, *35*, 4050–4055.

(111) Page, K. A.; Cable, K. M.; Moore, R. B. Molecular Origins of the Thermal Transitions and Dynamic Mechanical Relaxations in Perfluorosulfonate Ionomers. *Macromolecules* **2005**, *38*, 6472–6484.

(112) Schmidt-Rohr, K.; Chen, Q. Parallel Cylindrical Water Nanochannels in Nafion Fuel-Cell Membranes. *Nature Mater.* **2007**, *7*, 75–83.

(113) Miaudet, P.; Derre, A.; Maugey, M.; Zakri, C.; Piccione, P. M.; Inoubli, R.; Poulin, P. Shape and Temperature Memory of Nanocomposites with Broadened Glass Transition. *Science* **2007**, *318*, 1294–1296.

(114) Shao, Y.; Lavigueur, C.; Zhu, X. X. Multishape Memory Effect of Norbornene-Based Copolymers with Cholic Acid Pendant Groups. *Macromolecules* **2012**, *45*, 1924–1930.

(115) Luo, Y.; Guo, Y.; Gao, X.; Li, B.-G.; Xie, T. A General Approach Towards Thermoplastic Multishape-Memory Polymers via Sequence Structure Design. *Adv. Mater.* **2012**, *25*, 743–748.

(116) Bellin, I.; Kelch, S.; Langer, R.; Lendlein, A. Polymeric Triple-Shape Materials. *Proc. Natl. Acad. Sci.* **2006**, *103*, 18043–18047.

(117) Behl, M.; Bellin, I.; Kelch, S.; Wagermaier, W.; Lendlein, A. One-Step Process for Creating Triple-Shape Capability of AB Polymer Networks. *Adv. Funct. Mater.* **2009**, *19*, 102–108.

(118) Qin, H.; Mather, P. T. Combined One-Way and Two-Way Shape Memory in a Glass-Forming Nematic Network. *Macromolecules* **2009**, *42*, 273–280.

(119) Ahn, S.-K.; Deshmukh, P.; Kasi, R. M. Shape Memory Behavior of Side-Chain Liquid Crystalline Polymer Networks Triggered by Dual Transition Temperatures. *Macromolecules* **2010**, *43*, 7330–7340.

(120) Lawton, M. I.; Tillman, K. R.; Mohammed, H. S.; Kuang, W.; Shipp, D. A.; Mather, P. T. Anhydride-Based Reconfigurable Shape Memory Elastomers. *ACS Macro Lett.* **2016**, *5*, 203–207.

(121) Zhao, Q.; Zou, W.; Luo, Y.; Xie, T. Shape Memory Polymer Network with Thermally Distinct Elasticity and Plasticity. *Sci. Adv.* **2016**, *2*, e1501297.

(122) Zhang, J.; Niu, Y.; Huang, C.; Xiao, L.; Chen, Z.; Yang, K.; Wang, Y. Self-Healable and Recyclable Triple-Shape PPDO–PTMEG Co-Network Constructed Through Thermoreversible Diels–Alder Reaction. *Polym. Chem.* **2012**, *3*, 1390–1393.

(123) Wang, Z.; Fan, W.; Tong, R.; Lu, X.; Xia, H. Thermal-Healable and Shape Memory Metallosupramolecular Poly(N-Butyl Acrylate-Co-Methyl Methacrylate) Materials. *RSC Adv.* **2014**, *4*, 25486–25493.

(124) Rivero, G.; Nguyen, L.-T. T.; Hillewaere, X. K. D.; Prez, Du, F. E. One-Pot Thermo-Remendable Shape Memory Polyurethanes. *Macromolecules* **2014**, *47*, 2010–2018.

(125) Nguyen, L.-T. T.; Truong, T. T.; Nguyen, H. T.; Le, L.; Nguyen, V. Q.; Van Le, T.; Luu, A. T. Healable Shape Memory (Thio)Urethane Thermosets. *Polym. Chem.* **2015**, *6*, 3143–3154.

(126) Rodriguez, E. D.; Luo, X.; Mather, P. T. Linear/Network Poly(E-Caprolactone) Blends Exhibiting Shape Memory Assisted Self-Healing (SMASH). *ACS Appl. Mater. Interfaces* **2011**, *3*, 152–161.

(127) Kunzelman, J.; Chung, T.; Mather, P. T.; Weder, C. Shape Memory Polymers with Built-in Threshold Temperature Sensors. *J. Mater. Chem.* **2008**, *18*, 1082–1086.

(128) Crenshaw, B. R.; Burnworth, M.; Khariwala, D.; Hiltner, A.; Mather, P. T.; Simha, R.; Weder, C. Deformation-Induced Color Changes in Mechanochromic Polyethylene Blends. *Macromolecules* **2007**, *40*, 2400–2408.

(129) Lowe, C.; Weder, C. Oligo(P-Phenylene Vinylene) Excimers as Molecular Probes: Deformation-Induced Color Changes in Photoluminescent Polymer Blends. *Adv. Mater.* **2002**, *14*, 1625–1629.

(130) Liu, C.; Chun, S. B.; Mather, P. T.; Zheng, L.; Haley, E. H.; Coughlin, E. B. Chemically Cross-Linked Polycyclooctene: Synthesis, Characterization, and Shape Memory Behavior. *Macromolecules* **2002**, *35*, 9868–9874.

(131) Chung, T.; Romo-Uribe, A.; Mather, P. T. Two-Way Reversible Shape Memory in a Semicrystalline Network. *Macromolecules* **2008**, *41*, 184–192.

(132) Pilate, F.; Mincheva, R.; De Winter, J.; Gerbaux, P.; Wu, L.; Todd, R.; Raquez, J.-M.; Dubois, P. Design of Multistimuli-Responsive Shape-Memory Polymer Materials by Reactive Extrusion. *Chem. Mater.* **2014**, *26*, 5860–5867.

(133) Kumpfer, J. R.; Jin, J.; Rowan, S. J. Stimuli-Responsive Europium-Containing Metallo-Supramolecular Polymers. *J. Mater. Chem.* **2010**, *20*, 145–151.

(134) Kumpfer, J. R.; Taylor, S. D.; Connick, W. B.; Rowan, S. J. Vapochromic and Mechanochromic Films From Square-Planar Platinum Complexes in Polymethacrylates. *J. Mater. Chem.* **2012**, *22*, 14196–14204.

(135) Kunzelman, J.; Crenshaw, B. R.; Kinami, M.; Weder, C. Self-Assembly and Dispersion of Chromogenic Molecules: a Versatile and General Approach for Self-Assessing Polymers. *Macromol. Rapid Commun.* **2006**, *27*, 1981–1987.

(136) Crenshaw, B. R.; Weder, C. Deformation-Induced Color Changes in Melt-Processed Photoluminescent Polymer Blends. *Chem. Mater.* **2003**, *15*, 4717–4724.

(137) Kinami, M.; Crenshaw, B. R.; Weder, C. Polyesters with Built-in Threshold Temperature and Deformation Sensors. *Chem. Mater.* **2006**, *18*, 946–955.

(138) Kunzelman, J.; Crenshaw, B. R.; Weder, C. Self-Assembly of Chromogenic Dyes—a New Mechanism for Humidity Sensors. *J. Mater. Chem.* **2007**, *17*, 2989–2991.

(139) Tang, L.; Whalen, J.; Schutte, G.; Weder, C. Stimuli-Responsive Epoxy Coatings. *ACS Appl. Mater. Interfaces* **2009**, *1*, 688–696.

(140) Ludlow, R. F.; Otto, S. Systems Chemistry. *Chem. Soc. Rev.* **2008**, *37*, 101–108.

(141) Zhang, H.; Zhao, Y. Polymers with Dual Light-Triggered Functions of Shape Memory and Healing Using Gold Nanoparticles. *ACS Appl. Mater. Interfaces* **2013**, *5*, 13069–13075.

(142) Lu, X.; Fei, G.; Xia, H.; Zhao, Y. Ultrasound Healable Shape Memory Dynamic Polymers. *J. Mater. Chem. A* **2014**, *2*, 16051–16060.

(143) Liu, B.; Xia, H.; Fei, G.; Li, G.; Fan, W. High-Intensity Focused Ultrasound-Induced Thermal Effect for Solid Polymer Materials. *Macromol. Chem. Phys.* **2013**, *214*, 2519–2527.

(144) Li, G.; Fei, G.; Xia, H.; Han, J.; Zhao, Y. Spatial and Temporal Control of Shape Memory Polymers and Simultaneous Drug Release Using High Intensity Focused Ultrasound. *J. Mater. Chem.* **2012**, *22*, 7692–7696.

(145) Kumpfer, J. R.; Rowan, S. J. Thermo-, Photo-, and Chemo-Responsive Shape-Memory Properties From Photo-Cross-Linked Metallo-Supramolecular Polymers. *J. Am. Chem. Soc.* **2011**, *133*, 12866–12874.

(146) Michal, B. T.; McKenzie, B. M.; Felder, S. E.; Rowan, S. J. Metallo-, Thermo-, and Photoresponsive Shape Memory and Actuating Liquid Crystalline Elastomers. *Macromolecules* **2015**, *48*, 3239–3246.

(147) McKenzie, B. M.; Miller, A. K.; Wojtecki, R. J.; Johnson, J. C.; Burke, K. A.; Tzeng, K. A.; Mather, P. T.; Rowan, S. J. Improved Synthesis of Functionalized Mesogenic 2,6-Bisbenzimidazolylpyridine Ligands. *Tetrahedron* **2008**, *64*, 8488–8495.

(148) McKenzie, B. M.; Wojtecki, R. J.; Burke, K. A.; Zhang, C.; Jákli, A.; Mather, P. T.; Rowan, S. J. Metallo-Responsive Liquid Crystalline Monomers and Polymers. *Chem. Mater.* **2011**, *23*, 3525–3533.

(149) Balkenende, D. W. R.; Coulibaly, S.; Balog, S.; Simon, Y. C.; Fiore, G. L.; Weder, C. Mechanochemistry with Metallosupramolecular Polymers. *J. Am. Chem. Soc.* **2014**, *136*, 10493–10498.

(150) Yang, S. K.; Ambade, A. V.; Weck, M. Main-Chain Supramolecular Block Copolymers. *Chem. Soc. Rev.* **2011**, *40*, 129–137.

(151) Li, S.-L.; Xiao, T.; Lin, C.; Wang, L. Advanced Supramolecular Polymers Constructed by Orthogonal Self-Assembly. *Chem. Soc. Rev.* **2012**, *41*, 5950–5968.

(152) Coulibaly, S.; Heinzmann, C.; Beyer, F. L.; Balog, S.; Weder, C.; Fiore, G. L. Supramolecular Polymers with Orthogonal Functionality. *Macromolecules* **2014**, *47*, 8487–8496.

(153) Lavrenova, A.; Balkenende, D. W. R.; Sagara, Y.; Schrettl, S.; Simon, Y. C.; Weder, C. Mechano- and Thermoresponsive Photoluminescent Supramolecular Polymer. *J. Am. Chem. Soc.* **2017**, *139*, 4302–4305.

(154) Hong, G.; Zhang, H.; Lin, Y.; Chen, Y.; Xu, Y.; Weng, W.; Xia, H. Mechanoresponsive Healable Metallosupramolecular Polymers. *Macromolecules* **2013**, *46*, 8649–8656.

(155) Burnworth, M.; Tang, L.; Kumpfer, J. R.; Duncan, A. J.; Beyer, F. L.; Fiore, G. L.; Rowan, S. J.; Weder, C. Optically Healable Supramolecular Polymers. *Nature* **2011**, *472*, 334–337.

(156) Coulibaly, S.; Roulin, A.; Balog, S.; Biyani, M. V.; Foster, E. J.; Rowan, S. J.; Fiore, G. L.; Weder, C. Reinforcement of Optically Healable Supramolecular Polymers with Cellulose Nanocrystals. *Macromolecules* **2014**, *47*, 152–160.

(157) Jethmalani, J. M.; Ford, W. T. Diffraction of Visible Light by Ordered Monodisperse Silica-Poly(Methyl Acrylate) Composite Films. *Chem. Mater.* **1996**, *8*, 2138–2146.

(158) Viel, B.; Ruhl, T.; Hellmann, G. P. Reversible Deformation of Opal Elastomers. *Chem. Mater.* **2007**, *19*, 5673–5679.

(159) Aguirre, C. I.; Reguera, E.; Stein, A. Tunable Colors in Opals and Inverse Opal Photonic Crystals. *Adv. Funct. Mater.* **2010**, *20*, 2565–2578.

(160) Schäfer, C. G.; Smolin, D. A.; Hellmann, G. P.; Gallei, M. Fully Reversible Shape Transition of Soft Spheres in Elastomeric Polymer Opal Films. *Langmuir* **2013**, *29*, 11275–11283.

(161) Schäfer, C. G.; Viel, B.; Hellmann, G. P.; Rehahn, M.; Gallei, M. Thermo-Cross-Linked Elastomeric Opal Films. *ACS Appl. Mater. Interfaces* **2013**, *5*, 10623–10632.

(162) Finlayson, C. E.; Baumberg, J. J. Polymer Opals as Novel Photonic Materials. *Polym. Int.* **2013**, *62*, 1403–1407.

(163) Zhao, N.; Wang, Z.; Cai, C.; Shen, H.; Liang, F.; Wang, D.; Wang, C.; Zhu, T.; Guo, J.; Wang, Y.; et al. Bioinspired Materials: From Low to High Dimensional Structure. *Adv. Mater.* **2014**, *26*, 6994–7017.

(164) Schäfer, C. G.; Gallei, M.; Zahn, J. T.; Engelhardt, J.; Hellmann, G. P.; Rehahn, M. Reversible Light-, Thermo-, and Mechano-Responsive Elastomeric Polymer Opal Films. *Chem. Mater.* **2013**, *25*, 2309–2318.

(165) Fang, Y.; Leo, S.-Y.; Ni, Y.; Wang, J.; Wang, B.; Yu, L.; Dong, Z.; Dai, Y.; Basile, V.; Taylor, C.; et al. Reconfigurable Photonic Crystals Enabled by Multistimuli-Responsive Shape Memory Polymers Possessing Room Temperature Shape Processability. *ACS Appl. Mater. Interfaces* **2017**, *9*, 5457–5467.

(166) Kocher, C.; Smith, P.; Weder, C. Aromatic 2-(2′-Hydroxyphenyl)Benzoxazole Esters: a Novel Class of Caged Photoluminescent Dyes. *J. Mater. Chem.* **2002**, *12*, 2620–2626.

(167) Kocher, C.; Weder, C.; Smith, P. Novel Chromogenic Esters of Ortho-Phenylazonaphthols. *Adv. Funct. Mater.* **2003**, *13*, 427–433.

(168) Knapton, D.; Burnworth, M.; Rowan, S. J.; Weder, C. Fluorescent Organometallic Sensors for the Detection of Chemical-Warfare-Agent Mimics. *Angew. Chem. Int. Ed.* **2006**, *45*, 5825–5829.

(169) Michal, B. T.; Jaye, C. A.; Spencer, E. J.; Rowan, S. J. Inherently Photohealable and Thermal Shape-Memory Polydisulfide Networks. *ACS Macro Lett.* **2013**, *2*, 694–699.

(170) Michal, B. T.; Spencer, E. J.; Rowan, S. J. Stimuli-Responsive Reversible Two-Level Adhesion From a Structurally Dynamic Shape-Memory Polymer. *ACS Appl. Mater. Interfaces* **2016**, *8*, 11041–11049.

(171) *Smart Light-Responsive Materials*; Zhao, Y., Ikeda, T., Eds.; John Wiley & Sons, Inc.: Hoboken, NJ, USA, 2009.

(172) Li, Y.; Rios, O.; Keum, J. K.; Chen, J.; Kessler, M. R. Photoresponsive Liquid Crystalline Epoxy Networks with Shape Memory Behavior and Dynamic Ester Bonds. *ACS Appl. Mater. Interfaces* **2016**, *8*, 15750–15757.

(173) Chen, Q.; Yu, X.; Pei, Z.; Yang, Y.; Wei, Y.; Ji, Y. Multi-Stimuli Responsive and Multi-Functional Oligoaniline-Modified Vitrimers. *Chem. Sci.* **2017**, *8*, 724–733.

(174) de Espinosa, L. M.; Meesorn, W.; Moatsou, D.; Weder, C. Bioinspired Polymer Systems with Stimuli-Responsive Mechanical Properties. *Chem. Rev.* **2017**, *ahead of print*, doi: 10.1021/acs.chemrev.7b00168.

2 A tunable, dynamic thia-Michael addition reaction: Studies on the thiol addition to benzalcyanoacetate derivatives

2.1 Introduction

As described in Chapter 1, an attractive method by which to access stimuli-responsive materials is to incorporate dynamic covalent chemistry (DCC) into the polymer structure. DCC refers to covalent chemistries that can undergo dynamic exchange in which the bonds break and reform again, ideally, without the encumbrance of unwanted side reactions.[1,2] Popular examples of these chemistries include Diels-Alder reactions[3–6], disulfide bonds[7–10], and boronic esters[11–13], all of which have been employed to access materials that are recyclable/reprocessable and show healing properties.

In recent years, the reversible thia-Michael (TM) reaction has grown in popularity as a class of dynamic covalent chemical reactions that have utilized to access adaptive polymeric materials. Typically described as the base- or nucleophile-catalyzed addition of a thiol across an electron-deficient double bond (Figure 2.1A), the TM reaction has long been a member of the "click" reactions family[14] and has become a staple synthetic technique in polymer chemistry and materials science.

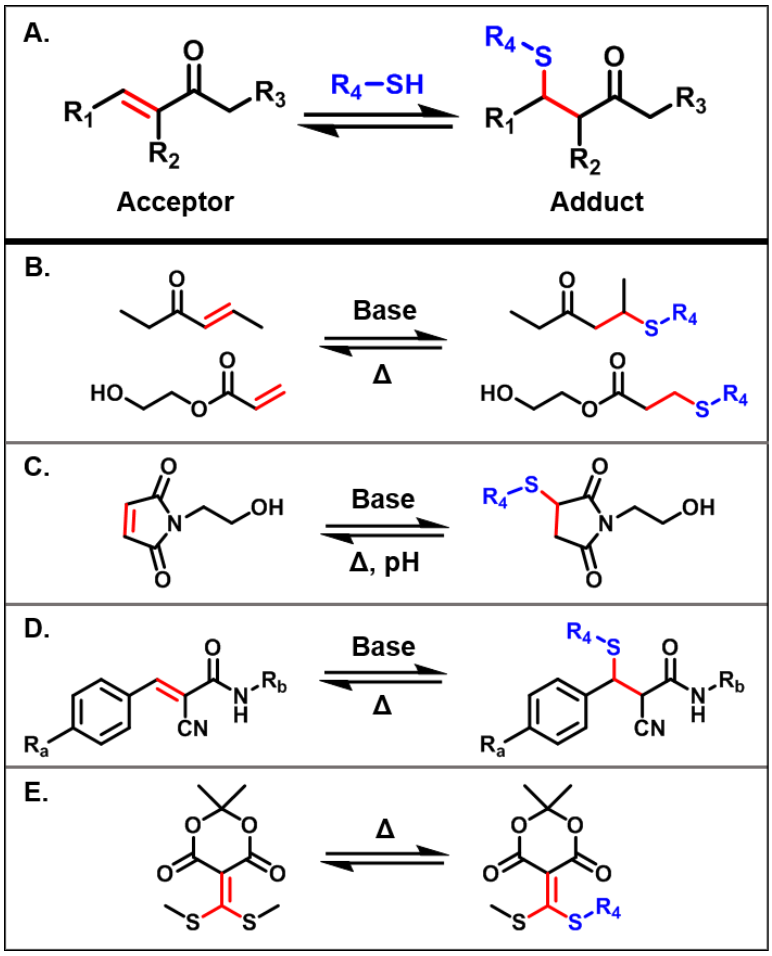

Figure 2.1. A) Generic scheme for reversible thia-Michael conjugate addition. B) Thiol-acrylate Michael addition reaction catalyzed by base and reversible with heat.[15] C) Thiol-maleimide Michael addition reaction catalyzed by base and reversible with heat and changes in pH.[16] D) Thiol-benzalcyanoamide Michael addition reaction catalyzed by base and reversible with heat.[17,18] E) Meldrum's acid derivative capable of reversible thiol conjugate addition with heat.[19]

While its reputation as a versatile addition reaction is well established, its ability to act as a reversible bond has only recently begun to be explored in the realm of dynamic polymeric materials. Although the field is small (but growing rapidly), the current array of thia-Michael chemistries in dynamic polymers is remarkably diverse. For example, Konkolewicz *et al*. showed

that thiol-acrylate-based polymer networks are thermally-reversible at elevated temperatures (90 °C), affording them such properties as healing and malleability (Figure 2.1B).[15] The same group also reported pH-responsive TM systems in which the thiol-maleimide adduct was reversible under basic conditions, again leading to healable films (Figure 2.1C).[16] Schubert and coworkers utilized a polymer with benzalcyanoacetamide side chains in combination with multifunctional thiols to access thermally healable films both in crosslinked small-molecule networks and in crosslinked polymers (Figure 2.1D).[17,18] Small-molecule networks by the same group, composed of a trifunctional thiol crosslinker and bisbenzalcyanoacetamide compound, were formed via base-catalyzed thiol-Michael addition and ultimately resulted in heat-induced, irreversible decomposition of the networks arising from the interactions between the catalyst and the thiol derivative to reportedly form H_2S gas. This limited the applicability and functionality of the materials as the heat necessary for dynamic exchange (> 60 °C) was found to ultimately reduce the mechanical properties of the material over time, due to the loss of viable thiols. Using an alternative approach, Kalow *et al*. developed a Meldrum's acid derivative capable of reversibly crosslinking siloxane polymers containing pendant thiol groups without the use of a catalyst (Figure 2.1E).[19] They showed that the resulting silicone network could be reprocessed at least ten times without significant loss of mechanical properties, demonstrating the viability of a catalyst-free approach to dynamic thia-Michael polymer networks.

In a protein targeting study, Taunton *et al*. explored catalyst-free TM chemistry by investigating the addition of thiols to different electron-deficient Michael acceptors based on α-cyanoacrylates.[20] The results of their studies demonstrated that the presence of the electron

withdrawing nitrile group in the α-position (highlighted in violet in Figure 2.2A) in the acceptor increases the rate of the reverse thia-Michael reaction while maintaining a thermodynamically favorable adduct. Anslyn *et al*. also took interest in the catalyst-free approach to the dynamic reaction, noting that the nature of substituents on the *β*-phenyl ring (highlighted in orange in Figure 2.2A) played a role in determining the kinetics and thermodynamics of the reaction.[21]

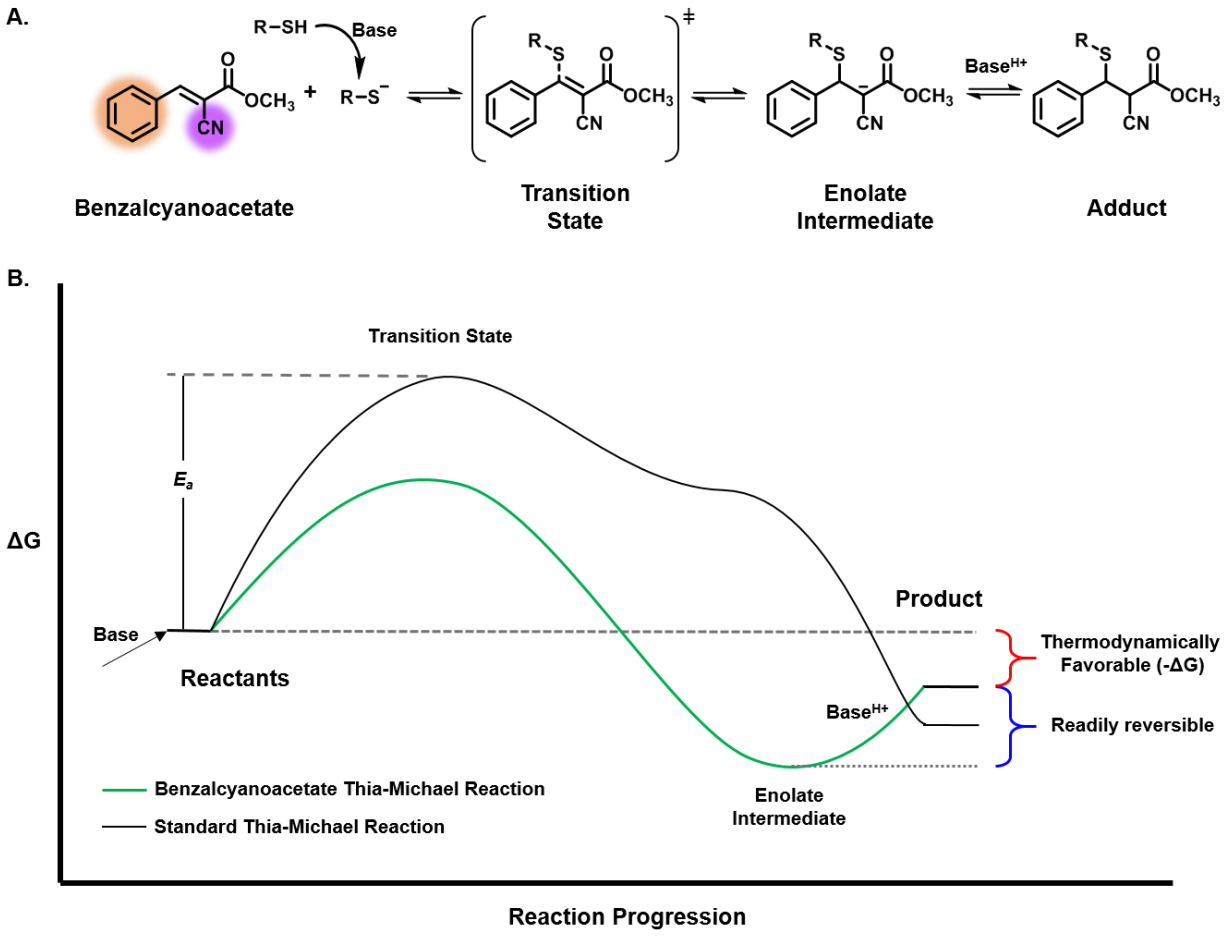

Figure 2.2. Base-catalyzed, reversible reaction of thiol with benzalcyanoacetate (α-nitrile highlighted in violet, β-phenyl highlighted in orange) demonstrating the formation of a transition state followed by an enolate intermediate that eventually progresses towards the final adduct formation.

In 2016, Houk *et al*. executed an extensive computational investigation into the substituent effects on the mechanism of base-catalyzed thiol binding across activated Michael acceptors that provided mechanistic insight of Anslyn's and Taunton's observations.[22] While the *in silico* experiments were conducted to reflect basic conditions, it is expected that similar mechanistic

trends would be in effect in the catalyst-free reaction. According to Houk *et al*., the reversibility of the benzalcyanoacetate species is driven by two primary characteristics. First, the presence of the α-electron withdrawing group (-CN) stabilizes the transition state and enolate intermediate in the thia-Michael reaction. The negative charge on the enolate is delocalized between the methyl acetate group as well as the cyano-substituent, creating an intermediate that is 21 kcal/mol more stable than the same acceptor without the –CN group. The enhanced stability of the transition state increases the rate of reaction for addition while the more stable enolate is responsible for a more facile reversibility in the base catalyzed system.

Second, the presence of the *β*-phenyl group alters the kinetics and thermodynamics of the reaction. The aromatic substituent increases the energy barrier of thiol addition by 3 kcal/mol as compared to an unsubstituted analogue. This effect both reduces the rate of thiol addition to the acceptor and increases the favorability of the reverse reaction back to starting materials. When used in combination with the α-electron withdrawing group (-CN), the thermodynamic equilibrium was found to exhibit a lower overall ΔG than an unsubstituted Michael acceptor. This was determined to be due to the influence of conjugation within the benzalcyanoacetate component. While conjugation works to stabilize the free acceptor, it equally contributes to a destabilization of the non-conjugated adduct that results from its reaction with a thiol. Therefore, the thia-Michael product formed from the benzalcyanoacetate species possesses a higher free energy (and smaller overall -ΔG) than a non-conjugated Michael acceptor. The overall contributions of the substituents on the double bond to the kinetics and thermodynamics of the thiol addition results in a room temperature dynamic covalent bond that weakly favors the formation of the products.

The above work emphasized the fact that an α-electron withdrawing coupled with a β-phenyl substituent on a Michael acceptor aids the reversibility of the thia-Michael reaction.[19,21] In addition to these conclusions, Anslyn, *et al*, showed that the presence of electron-donating or electron-withdrawing species on the β-phenyl ring allows the ability to alter the kinetics and thermodynamics of the reaction without drastically modifying the reactive site.[20] While the chemical behavior of these Michael acceptors is intriguing, the investigation of their reversible and tunable properties has been limited to aqueous, solution-based conditions. The amide-based compound, benzalcyanoamide, was explored by Schubert, *et al*, in organic solvent and in bulk, however, the benzalcyanoamide networks reported required the use of basic conditions which, as discussed earlier, led to the breakdown of the thiol component. The acetate-based acceptors, on the other hand, have been largely set aside due to their reported instability in the presence of water.[20] Preliminary results by Anslyn, *et al*, showed that the benzalcyanoacetate acceptors are indeed capable of participating in thiol-Michael addition although the aqueous conditions applied in those experiments prevented further analysis of their equilibrium properties. Therefore, the utilization of the benzalcyanoacetate motif in catalyst-free and organic conditions remained an important, yet unexplored line of inquiry with the potential to expand the application of the reversible thia-Michael reaction in bulk materials.

With the goal of accessing catalyst-free thia-Michael networks this chapter focuses on model small molecule solution studies on the thiol addition to benzalcyanoacetate derivatives. These solution-state studies were utilized to evaluate two key hypotheses: 1) that the benzalcyanoacetate thia-Michael reaction does indeed proceed in the absence of a catalyst in

organic solvent and 2) that the equilibrium of this reaction can be adjusted by modifying the aryl-substituents on the electrophile. While previous reports (discussed above) have eluded to these hypotheses being correct, the necessary studies had not yet been completed and it was critical to confirm the results before proceeding.

2.2 Results and Discussion

Studies were conducted on a series of four benzalcyanoacetate compounds differentiated by the electron-withdrawing/-donating capabilities of the substituent on the *para*-position of the *β*-phenyl ring (**1**, Scheme 2.1). Nitro- (**1N**), bromo- (**1B**), hydrogen- (**1H**), and methoxy-substituted (**1M**) benzalcyanoacetate were synthesized via a Knovenagel condensation of methyl cyanoacetate with the corresponding benzaldehyde. The benzalcyanoacetate species were titrated with 1-octanethiol in deuterated methyl sulfoxide (d_6-DMSO) (Scheme 2.1) following NMR titration procedures and considerations outlined by Thordarson.[23] The DMSO was treated with activated molecular sieves before use in the titration experiments to reduce the amount of water present. Excess water can promote the hydrolysis of the Knovenagel product resulting in a reformation of methyl cyanoacetate and corresponding benzaldehyde. Stock solutions of **1** (0.025 M in d_6-DMSO, **T1**) were prepared in 5 mL batches. The **T1** solution (0.782 mL) was added to 0.218 mL (50 molar equivalents to **1**) of 1-octanethiol, resulting in a second, concentrated stock solution (**T2**) with total concentrations of **1** and 1-octanethiol at 0.0195 M and 1.25 M, respectively. The **T2** solution was allowed to equilibrate for 18 hours.

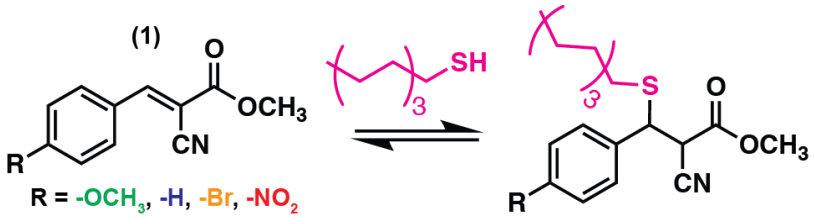

Scheme 2.1. Schematic of benzalcyanoacetate electrophile equilibrium reaction with 1-octanethiol.

Following the equilibration of **T2**, the titration study commenced. In an NMR tube, 0.782 mL **T1** and 0.218 mL of d_6-DMSO were combined, ensuring that the concentration of **1** remained the same throughout the titration experiment. To this sample, 5 µL of **T2** was added followed by an 18 hour equilibration. After the equilibration period, the sample was analyzed via ^{1}H NMR spectroscopy (Figure 2.3), then an additional 5 µL of **T2** was added to the NMR tube and the process was repeated.

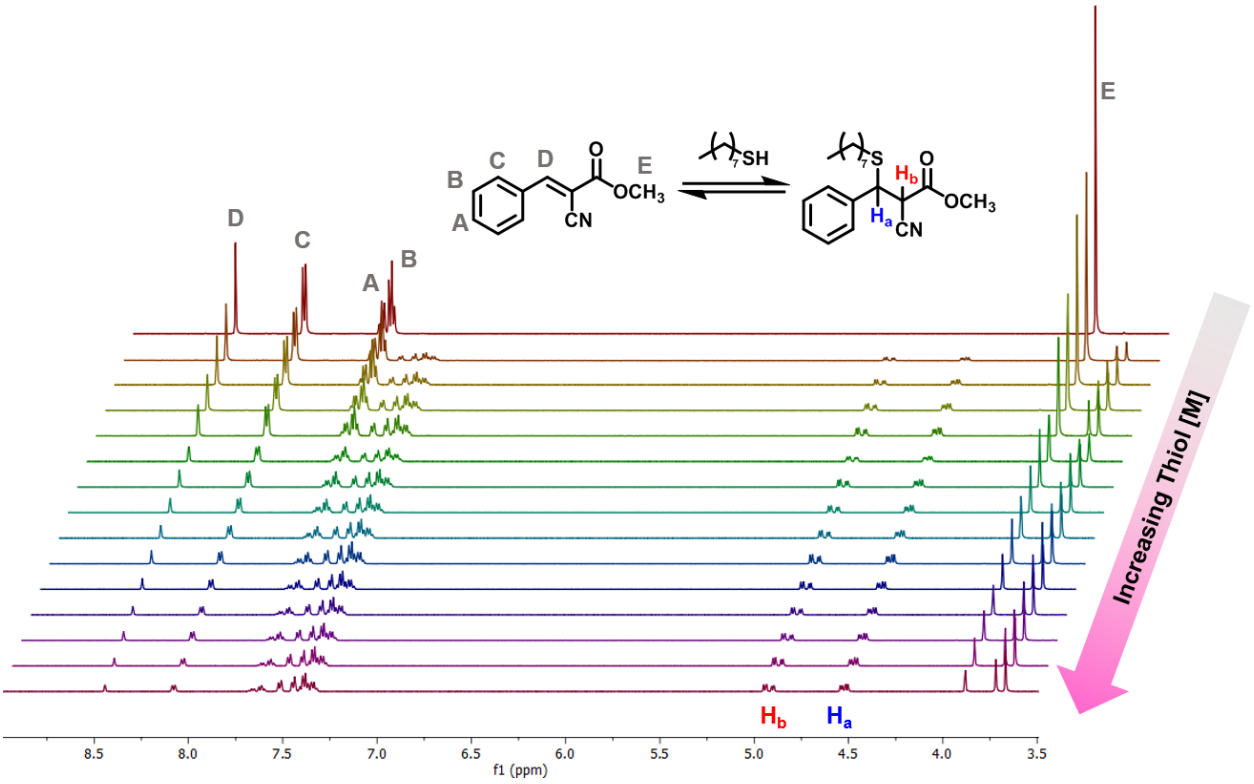

Figure 2.3. Stacked array of ^{1}H-NMR spectra for each thiol addition during the titration of **1H**. Beginning at the top with the free electrophile, each subsequent spectra moving down the stack has an incrementally higher thiol content (6.25 mM added per step). (500 MHz in d_6-DMSO)

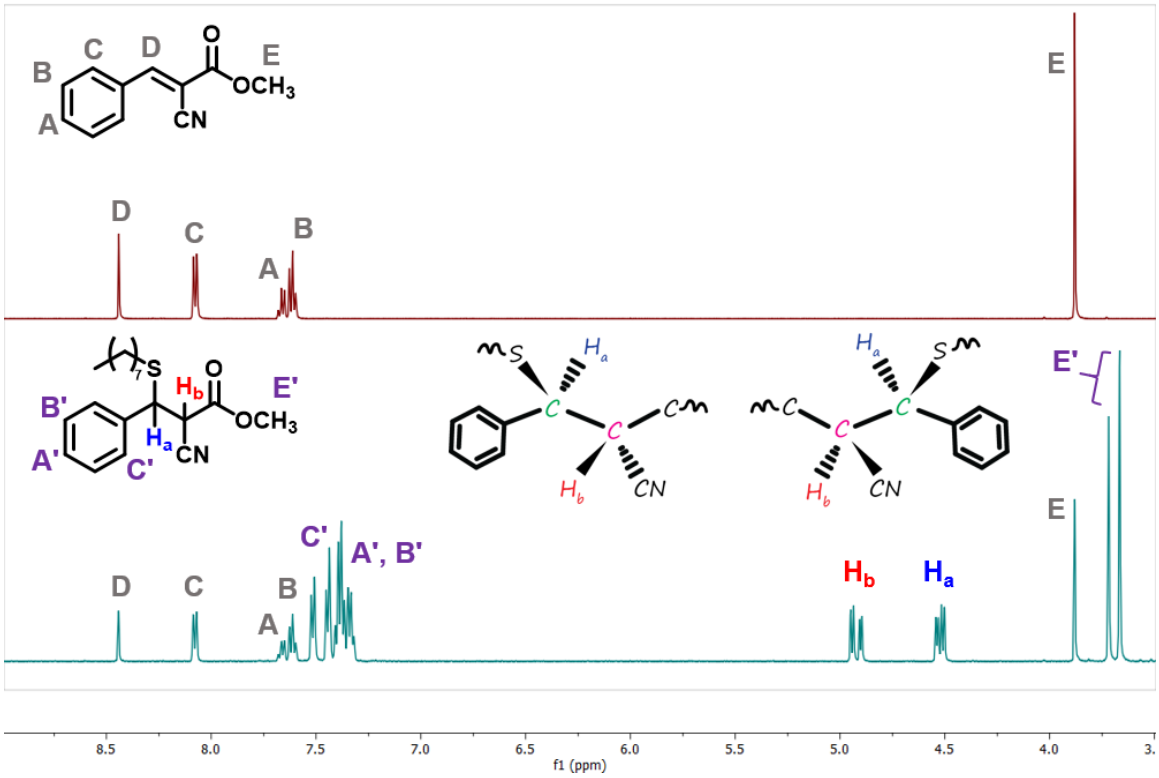

Figure 2.4. Fully annotated ^{1}H NMR of the free **1H** electrophile (top) and the **1H** adduct after titration (bottom) highlighting the appearance of H_a and H_b upon addition of the thiol. Inset illustration shows an example of diastereomers present in the adduct. (500 MHz in d_6-DMSO)

As demonstrated in Figures 2.3 and 2.4, the formation of the thia-Michael adduct was clearly evident by ^{1}H-NMR. Peaks associated with the electrophile shifted upfield (as indicated by the prime labels in Figure 2.4) and several of the new peaks appeared in pairs. This splitting is to be expected given the chiral nature of the α- and β-carbon centers, post-addition. The two chiral centers give rise to four stereoisomers (2^n, n = number of chiral centers) of the adduct and subsequently, two diastereomer pairs are detected via NMR (one pair is illustrated in the inset of Figure 2.4). Quantitatively, the extent of adduct formation was defined by monitoring the growing

doublets between 4.50 – 5.20 ppm (H_a and H_b, respectively in Figure 2.4) in conjunction with the subsequent loss of **1** by the diminishing singlet at ca. 8.50 ppm (D, in Figure 2.4). As the total integration of these peaks accounts for the total amount of benzalcyanoacetate moiety (reacted and unreacted) in the system, the extent of reaction at each titration step could be calculated by comparing the area under each peak. For example, during the titration of **1H** (Figures 2.3 and 2.4), if the integral of the singlet at 8.44 ppm was one and the integral of the doublets at 4.52 ppm was also one, then half of the original electrophile in the solution was reacted with 1-octanethiol and the concentration of both **1** and the adduct at that point would be 9.75 x 10^{-3} M (0.0195 M **1H** in the starting solution divided by two). The equilibrium constant (K_{eq}) could then be extrapolated from the titration experiments by plotting the concentration of the product versus the thiol concentration and fitting the data using a 1:1 binding isotherm.

$$E + SH \underset{k_{-1}}{\overset{k_1}{\rightleftharpoons}} P \tag{2.1}$$

This equilibrium process is represented mathematically as a function of the concentration (represented by brackets around the variables) of E, SH, and P (equation 2.3). When the reaction is in equilibrium, the formation of the adduct does not change with time and therefore can be equated to zero.

$$\frac{d[P]}{dt} = k_1[E][SH] - k_{-1}[P] = 0 \tag{2.2}$$

Rearranging equation 2.3, we arrive at equation 2.4:

$$k_1[E][SH] = k_{-1}[P] \tag{2.3}$$

Given that the initial concentration of the electrophile remains constant throughout the experiment, it is useful to express the free electrophile concentration as a function of the constant, initial electrophile concentration and adduct formation ($[E] = [E]_0 - [P]$) which results in equation 2.5:

$$k_1([E]_0 - [P])[SH] = k_{-1}[P] \tag{2.4}$$

Expanding equation 2.4 and solving for P gives equation 2.5:

$$[P] = \frac{[E]_0[SH]}{\frac{k_{-1}}{k_1} + [SH]} \tag{2.5}$$

The quotient of the rate constants in equation 2.5 is equivalent to the equilibrium dissociation constant, K_d, which is inversely related to the equilibrium association constant, K_a. As K_a is the extent to which the reaction has proceeded towards the products in equilibrium, K_a is used to define the K_{eq} for the thia-Michael reactions. Therefore, the final model for fitting the titration data is equation 2.6[24]:

$$[P] = \frac{[E]_0[SH]}{K_{eq}^{-1} + [SH]} \tag{2.6}$$

By plotting the titration data as $[P]$ versus $[SH]$ (note that this is free thiol, not added thiol and is determined by $[SH] = [SH]_0 - [P]$, for each titration step), it is possible to extrapolate both the K_{eq} and $[E]_0$, which serves to check the fit as the modeled data should match the original

electrophile concentration (Figure 2.5A-D). Table 2.1 summarizes the K_{eq} values determined for each of the benzalcyanoacetate compounds after fitting the titration data with the binding isotherm.

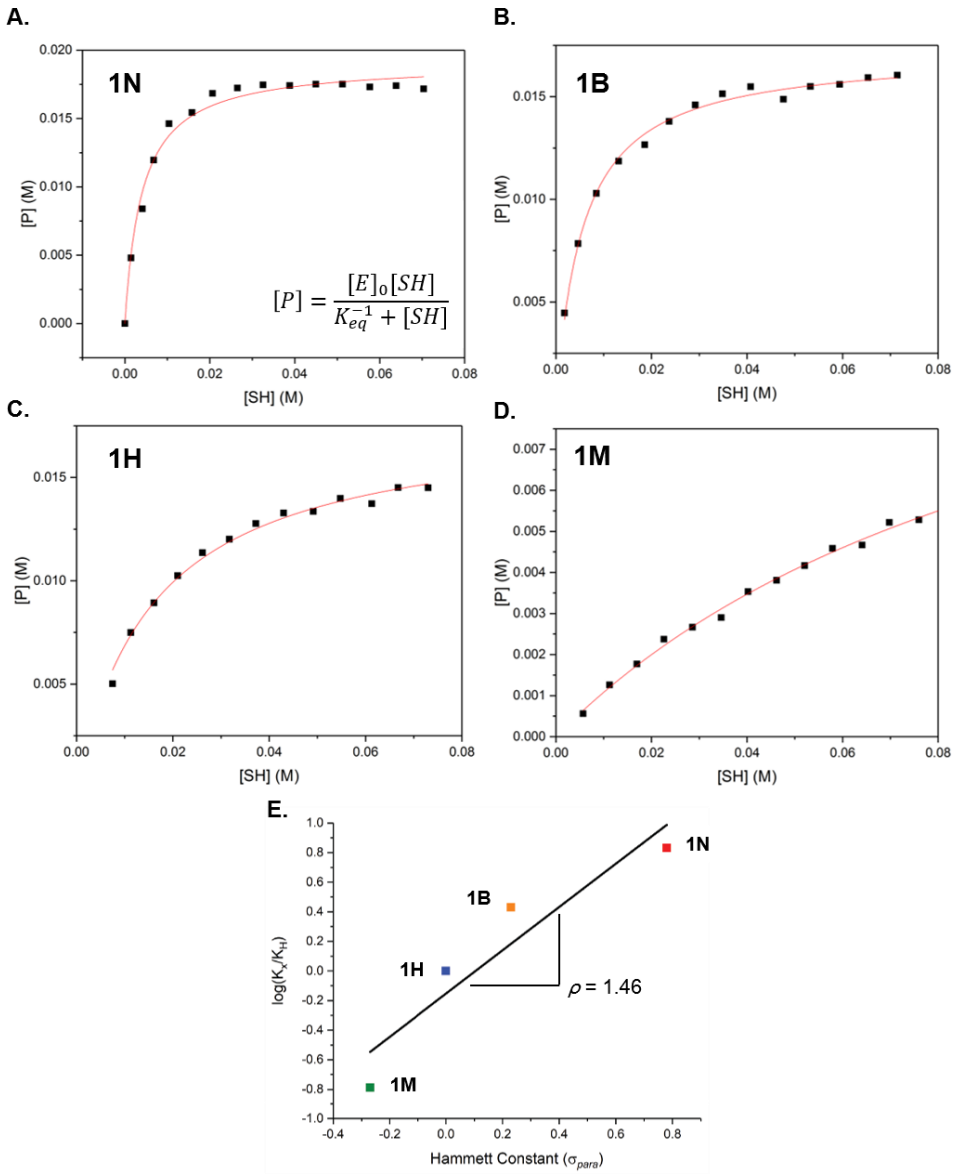

Figure 2.5. Plot of product concentration ([P]) versus free thiol concentration ([SH]) during the titration of A) **1N**, B) **1B**, C) **1H**, and D) **1M** with 1-octanethiol. Result were fit with the 1:1 binding isotherm (red line). E) Hammett plot of average equilibrium constants (K_{eq}) for **1N** (red), **1B** (orange), **1H** (blue), and **1M** (green). The line indicates a linear fit of averaged data with slope, ρ = 1.46.

Table 2.1. Summary of experimental equilibrium constants measure at room temperature in d_6-DMSO.

	1M	**1H**	**1B**	**1N**
σ_{para}	-0.27	0	0.23	0.78
K_{eq} (M^{-1})	9.4 ± 1.0	58.0 ± 3.8	160.0 ± 20.0	470.0 ± 150.0

In order to confirm that the equilibrium constants, as extrapolated from the model, were indeed reflective of the electronic nature of the β-phenyl substituent, the experimental results were evaluated in a Hammett plot (Figure 2.5E). Hammett plots are used to compare the properties (in this case, K_{eq}) of electronically diverse compounds as normalized by the properties of the unsubstituted compounds (R = -H). When these values are plotted versus their respective Hammett sigma values[25] (σ_{para}, Table 2.1), the slope of the linear fit of the data (ρ) reveals whether the given property is dependent ($\rho > 1$) or independent ($\rho < 1$) of the electron-withdrawing or –donating nature of the R-group. A Hammett plot of the benzalcyanoacetate equilibrium constants reveals a positive trend, with $\rho = 1.46$ suggesting a system whose equilibrium properties are dictated by the electron-donating/-withdrawing nature of the β-phenyl substituent. While the overall trend was positive, the data clearly showed a downward curve, typically indicative of changes to the reaction mechanism as a result of changes to the transition state. Interestingly, this data correlates well with findings from the prior work discussed above. Anslyn, *et al*, reported a positively correlated Hammett plot for benzalcyanoacetamides reacted with thiols in aqueous media, but also noted the presence of a slight downwards curve in the data.[19] Moreover, Houk, *et al*., observed significant changes to the energetics of the transition state corresponding to the addition of the β-phenyl group as a result of enhanced delocalization.[21] It is therefore likely that the electron-donating and

electron-withdrawing groups would affect the thiol-benzalcyanoacetate reaction mechanism in response to changes in charge delocalization. Figure 2.6 illustrates how the proposed thiol addition across the benzalcyanoacetate might vary depending on the electronic nature of the benzal moeity (e.g. **1N** vs. **1M)**.

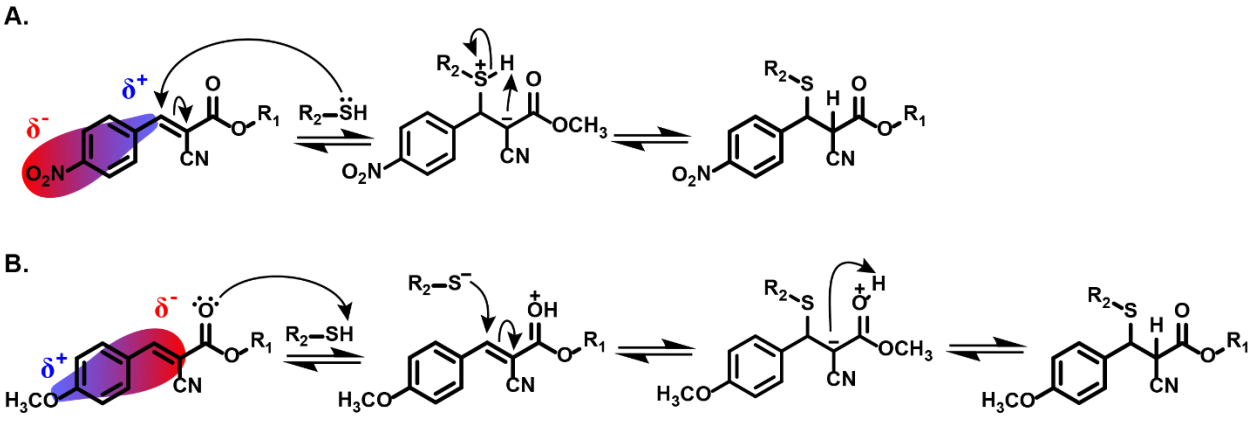

Figure 2.6. Examples of proposed variations in thiol addition mechanism as a consequence of variable electron density between A) **1N** and B) **1M**.

For **1N** (Figure 2.6A), the electron withdrawing capabilities of the nitro group creates an electron density gradient throughout the conjugated molecule, leaving the *β*-carbon electron deficient. This would promote the addition of the thiol to the *β*-position, followed by protonation of the resulting enolate. Conversely, the electron donating power of the methoxy substituent in **1M** pushes electron density into the conjugated system, promoting an acid-base interaction between the more electron-rich carbonyl and the thiol proton (Figure 2.6B). This then leads to addition via the thiolate and tautomerism of the resulting enol derivative. Future studies using combined

computational methods and quantitative chemical analyses will surely elucidate a more definitive description of these mechanisms.

2.3 Conclusions

Using ^{1}H-NMR titrations, it was demonstrated that the electron-withdrawing/-donating capabilities of the *para*-substituent on the β-phenyl ring of the benzalcyanoacetate play a key role in defining the chemical equilibrium of the reversible thia-Michael reaction. The thermodynamic equilibrium of the reaction could be shifted towards the adduct (electron-withdrawing substituents) or towards the reactants (electron-donating substituents), providing a useful platform upon which to tune the reaction in the absence of a catalyst.

2.4 Experimental Methods

2.4.1 Instrumentation

Nuclear Magnetic Resonance (NMR)

Nuclear Magnetic Resonance Spectroscopy was performed using the 500 MHz Bruker AVANCE II^{+} 500; 11.7 Tesla NMR at the NMR facilities at the University of Chicago. Analysis of NMR results was done using MNova NMR processing software.

Gas Chromatography-Mass Spectrometry (GC-MS)

Gas Chromatography-Mass Spectrometry was performed using the Varian Saturn 2200 GCMS/MS at the Mass Spectroscopy facilities at the University of Chicago. Samples were prepared at 10 µM concentration in acetonitrile and were tested at room temperature.

2.4.2 Synthetic Procedures

R-Benzalcyanoacetates (**1**)

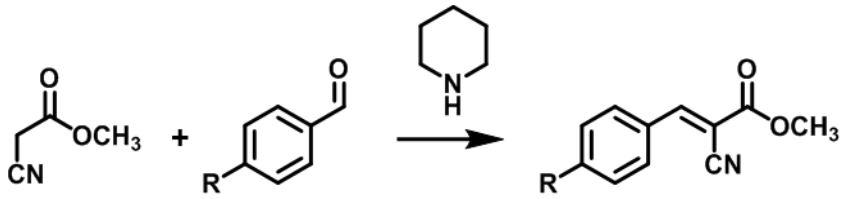

Scheme S2.1. General reaction scheme for formation of benzalcyanoacetate compounds (**1**).

Methyl cyanoacetate (1 mol, 0.11 mL) and R-benzaldehyde (1.05 mol) were combined in a round bottom flask with methanol (15 mL) and catalytic (2-3 drops from glass pipette) piperidine. The reaction was stirred using a magnetic stir bar at room temperature for three hours. After 3 hours, the solution was placed in the freezer for 24 hours and the precipitate was collected via vacuum filtration.

4-Nitrobenzalcyanoacetate (**1N**). ^{1}H-NMR (500 MHz in d_6-DMSO; δ ppm: 3.90 (*s*, 3H), 8.26 (*d*, 2H), 8.42 (*d*, 2H), 8.59 (*s*, 1H)). ^{13}C-NMR (101 MHz in $CDCl_3$; δ 162.11, 152.22, 149.94, 136.98, 131.75, 124.52, 114.68, 107.06, 54.06). GC-MS (MW = 232.20).

4-Bromobenzalcyanoacetate (**1B**). ^{1}H-NMR (500 MHz in d_6-DMSO; δ ppm: 3.88 (*s*, 3H), 7.84 (*d*, 2H), 8.00 (*d*, 2H), 8.43 (*s*, 1H)). ^{13}C-NMR (101 MHz in $CDCl_3$; δ 162.91, 153.98, 132.88, 132.46, 130.35, 128.59, 103.31, 53.73). GC-MS (MW = 266.09).

4-benzalcyanoacetate (**1H**). ^{1}H-NMR (500 MHz in d_6-DMSO; δ ppm: 3.88 (*s*, 3H), 7.61 (*t*, 2H), 7.67 (*t*, 1H), 8.08 (*d*, 2H), 8.44 (*s*, 1H)). ^{13}C-NMR (101 MHz in $CDCl_3$; δ 163.06, 155.41, 133.53, 131.48, 131.21, 129.40, 115.57, 102.62, 53.53). GC-MS (MW = 187.20).

4-Methoxybenzalcyanoacetate (**1M**). ^{1}H-NMR (500 MHz in d_6-DMSO; δ ppm: 3.85 (*s*, 3H), 3.88 (*s*, 3H), 7.18 (*d*, 2H), 8.11 (*d*, 2H), 8.35 (*s*, 1H)). ^{13}C-NMR (101 MHz in $CDCl_3$; δ 164.06, 163.83, 154.86, 133.91, 124.48, 116.41, 114.98, 99.01, 55.84, 53.40). GC-MS (MW = 217.22).

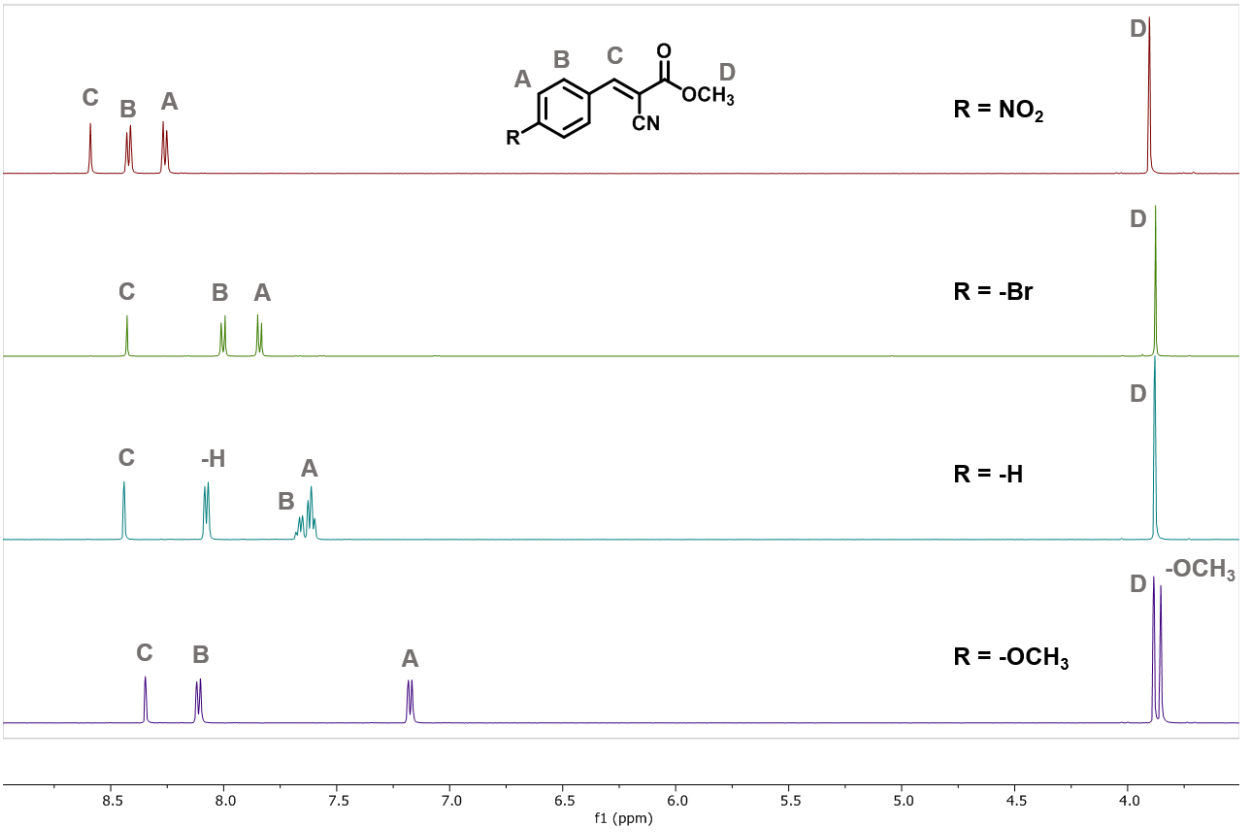

Figure S2.1. ^{1}H-NMR of **1** benzalcyanoacetates. (600 MHz in d_6-DMSO)

2.5 References

(1) Rowan, S. J.; Cantrill, S. J.; Cousins, G. R. L.; Sanders, J. K. M.; Stoddart, J. F. Dynamic Covalent Chemistry. *Angew. Chemie Int. Ed.* **2002**, *41* (6), 898–952.

(2) Chakma, P.; Konkolewicz, D. Dynamic Covalent Bonds in Polymeric Materials. *Angew. Chemie Int. Ed.* **2019**, *58* (29), 9682-9695.

(3) Reutenauer, P.; Buhler, E.; Boul, P. J.; Candau, S. J.; Lehn, J.-M. Room Temperature Dynamic Polymers Based on Diels–Alder Chemistry. *Chem. Eur. J.* **2009**, *15* (8), 1893–1900.

(4) M. Imbesi, P.; Fidge, C.; E. Raymond, J.; I. Cauët, S.; L. Wooley, K. Model Diels–Alder Studies for the Creation of Amphiphilic Cross-Linked Networks as Healable, Antibiofouling Coatings. *ACS Macro Lett.* **2012**, *1* (4), 473–477.

(5) Adzima, B. J.; Aguirre, H. A.; Kloxin, C. J.; Scott, T. F.; Bowman, C. N. Rheological and Chemical Analysis of Reverse Gelation in a Covalently Cross-Linked Diels−Alder Polymer Network. *Macromolecules* **2008**, *41* (23), 9112–9117.

(6) Oehlenschlaeger, K. K.; Mueller, J. O.; Brandt, J.; Hilf, S.; Lederer, A.; Wilhelm, M.; Graf, R.; Coote, M. L.; Schmidt, F. G.; Barner-Kowollik, C. Adaptable Hetero Diels–Alder Networks for Fast Self-Healing under Mild Conditions. *Adv. Mater.* **2014**, *26* (21), 3561–3566.

(7) Canadell, J.; Goossens, H.; Klumperman, B. Self-Healing Materials Based on Disulfide Links. *Macromolecules* **2011**, *44* (8), 2536–2541.

(8) Michal, B. T.; Jaye, C. A.; Spencer, E. J.; Rowan, S. J. Inherently Photohealable and Thermal Shape-Memory Polydisulfide Networks. *ACS Macro Lett.* **2013**, *2* (8), 694–699.

(9) Michal, B. T.; Spencer, E. J.; Rowan, S. J. Stimuli-Responsive Reversible Two-Level Adhesion from a Structurally Dynamic Shape-Memory Polymer. *ACS Appl. Mater. Interfaces* **2016**, *8* (17), 11041–11049.

(10) Cudjoe, E.; Herbert, K. M.; Rowan, S. J. Strong, Rebondable, Dynamic Cross-Linked Cellulose Nanocrystal Polymer Nanocomposite Adhesives. *ACS Appl. Mater. Interfaces* **2018**, *10* (36).

(11) P. Bapat, A.; Roy, D.; G. Ray, J.; A. Savin, D.; S. Sumerlin, B. Dynamic-Covalent Macromolecular Stars with Boronic Ester Linkages. *J. Am. Chem. Soc.* **2011**, *133* (49), 19832–19838.

(12) J. Cash, J.; Kubo, T.; P. Bapat, A.; S. Sumerlin, B. Room-Temperature Self-Healing Polymers Based on Dynamic-Covalent Boronic Esters. *Macromolecules* **2015**, *48* (7),

2098–2106.

(13) R. Cromwell, O.; Chung, J.; Guan, Z. Malleable and Self-Healing Covalent Polymer Networks through Tunable Dynamic Boronic Ester Bonds. *J. Am. Chem. Soc.* **2015**, *137* (20), 6492–6495.

(14) P. Nair, D.; Podgórski, M.; Chatani, S.; Gong, T.; Xi, W.; R. Fenoli, C.; N. Bowman, C. The Thiol-Michael Addition Click Reaction: A Powerful and Widely Used Tool in Materials Chemistry. *Chem. Mater.* **2013**, *26* (1), 724–744.

(15) Zhang, B.; A. Digby, Z.; A. Flum, J.; Chakma, P.; M. Saul, J.; L. Sparks, J.; Konkolewicz, D. Dynamic Thiol–Michael Chemistry for Thermoresponsive Rehealable and Malleable Networks. *Macromolecules* **2016**, *49* (18), 6871–6878.

(16) Chakma, P.; Rodrigues Possarle, L. H.; Digby, Z. A.; Zhang, B.; Sparks, J. L.; Konkolewicz, D. Dual Stimuli Responsive Self-Healing and Malleable Materials Based on Dynamic Thiol-Michael Chemistry. *Polym. Chem.* **2017**, *8* (42), 6534–6543.

(17) Kuhl, N.; Geitner, R.; Bose, R. K.; Bode, S.; Dietzek, B.; Schmitt, M.; Popp, J.; Garcia, S. J.; van der Zwaag, S.; Schubert, U. S.; et al. Self-Healing Polymer Networks Based on Reversible Michael Addition Reactions. *Macromol. Chem. Phys.* **2016**, *217* (22), 2541–2550.

(18) Kuhl, N.; Geitner, R.; Vitz, J.; Bode, S.; Schmitt, M.; Popp, J.; Schubert, U. S.; Hager, M. D. Increased Stability in Self-Healing Polymer Networks Based on Reversible Michael Addition Reactions. *J. Appl. Polym. Sci.* **2017**, *134* (19).

(19) A. Ishibashi, J. S.; A. Kalow, J. Vitrimeric Silicone Elastomers Enabled by Dynamic Meldrum's Acid-Derived Cross-Links. *ACS Macro Lett.* **2018**, *7* (4), 482–486.

(20) Serafimova, I. M.; Pufall, M. A.; Krishnan, S.; Duda, K.; Cohen, M. S.; Maglathlin, R. L.; McFarland, J. M.; Miller, R. M.; Frödin, M.; Taunton, J. Reversible Targeting of Noncatalytic Cysteines with Chemically Tuned Electrophiles. *Nat. Chem. Biol.* **2012**, *8*, 471.

(21) Zhong, Y.; Xu, Y.; Anslyn, E. V. Studies of Reversible Conjugate Additions. *European J. Org. Chem.* **2013**, *2013* (23), 5017–5021.

(22) H. Krenske, E.; C. Petter, R.; N. Houk, K. Kinetics and Thermodynamics of Reversible Thiol Additions to Mono- and Diactivated Michael Acceptors: Implications for the Design of Drugs That Bind Covalently to Cysteines. *J. Org. Chem.* **2016**, *81* (23), 11726–11733.

(23) Thordarson, P. Determining Association Constants from Titration Experiments in Supramolecular Chemistry. *Chem. Soc. Rev.* **2011**, *40* (3), 1305–1323.

(24) Steed, J. W.; Atwood, J. L. *Supramolecular Chemistry*; John Wiley & Sons, Ltd, 2009.

(25) Hansch, C.; Leo, A.; Taft, R. W. A Survey of Hammett Substituent Constants and Resonance and Field Parameters. *Chem. Rev.* **1991**, *91* (2), 165–195.

3 Reaction-induced phase separation in tunable dynamic covalent networks[§]

[§] Contents of this chapter adapted from: Herbert, K. M.; Getty, P.; Hertzog, J.; Lettow, J.; Romulus, J. R.; Rowan, S. J. Reaction-induced phase separation in tunable dynamic covalent networks. *J. Am. Chem. Soc.* **2019** [*in preparation*]

3.1 Introduction

Dynamic covalent networks (or covalent adaptable networks) are polymeric networks that incorporate dynamic covalent chemistries (DCC).[1–3] Dynamic covalent bonds can undergo bond exchange (bonds break and reform again), ideally, without the encumbrance of unwanted side reactions.[4,5] The incorporation of dynamic chemistries such as transesterification[6,7], Diels-Alder reactions[8–11] , disulfide bonds[12–14], and boronic esters[15–17], allows access to adaptive materials that can exhibit (self-)healing, reprocessing, strain relaxation and shape-memory properties. Recently, the reversible thia-Michael (TM) reaction has been added to the list of DCC reactions utilized to access adaptive polymeric materials.[18] Typically described as the base- or nucleophile-catalyzed addition of a thiol across an electron-deficient double bond, the TM reaction has been a staple synthetic technique in polymer chemistry and materials science.[19] While its reputation as a versatile addition reaction is well established, its ability to act as a reversible bond has only recently begun to be explored in the realm of dynamic polymer networks.[20–24] An interesting subset of the TM reaction is the thiol addition to benzalcyanoacetate Michael acceptors. Small molecule studies

by Taunton[25], Anslyn[26], and Houk[27] have shown that thiol addition to such Michael acceptors requires no catalyst, is dynamic at room temperature, and that the thermodynamics and kinetics of these reversible reactions are sensitive to the nature of the substituent on the *β*-phenyl ring. Reported, herein, are studies on a series of dynamic polymeric networks based on this dynamic covalent bond where the tetrathiol (pentaerythritol tetrakis(2-mercaptopropionate), PTMP) is mixed with ditopic benzalcyanoacetate derivatives that differ in the electron-withdrawing/-donating capabilities of the substituent on the *para*-position of the *β*-phenyl ring.

3.2 Results and Discussion

A series of ditopic acceptor compounds were prepared with nitro- (**3N**), bromo- (**3B**), hydrogen- (**3H**), and methoxy-substituted (**3M**) benzalcyanoacetate on the chain ends of a triethylene glycol (TEG). Titration experiments on monotopic analogues of the acceptors with 1-octanethiol determined the equilibrium constant (K_{eq}) of the nitro-, hydrogen-, and methoxy-substituted acceptors in deuterated dimethyl sulfoxide (d_6-DMSO) to be 470 M^{-1}, 58 M^{-1}, and 9 M^{-1}, respectively (See Chapter 2 for details). These ditopic compounds were synthesized in two steps (Scheme 3.1).[30] Triethylene glycol (TEG) was bis-functionalized via esterification with cyanoacetic acid in the presence of catalytic *p*-toluenesulfonic acid (*p*-TSA) (Scheme 2.2A). The resulting TEG-biscyanoacetate compound (**2**) was reacted with two molar equivalents of the desired benzaldehyde compound (containing the appropriate *para* R-group functionalization) using a catalytic amount of trimethylamine (TEA) to aid the Knovenagel condensation (Scheme 2.2B). The subsequent ditopic electrophiles (**3**) were confirmed via ^{1}H-NMR (Figure 3.1), ^{13}C-

NMR, and mass spectrometry (See Experimental Methods for spectra and synthesis details). This synthesis work was done with contributions from undergraduate Patrick Getty at the University of Chicago.

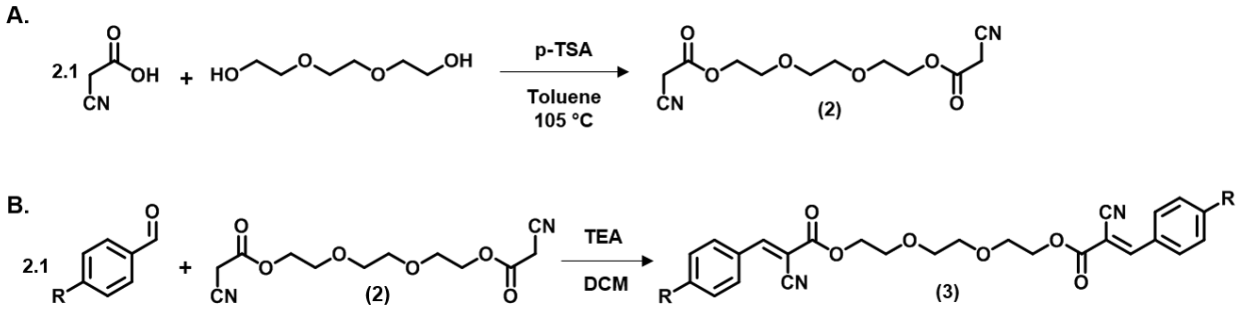

Scheme 3.1. Synthetic schemes for A) triethylene glycol biscyanoacetate (**2**) and B) triethylene glycol bisbenzalcyanoacetate (**3**).

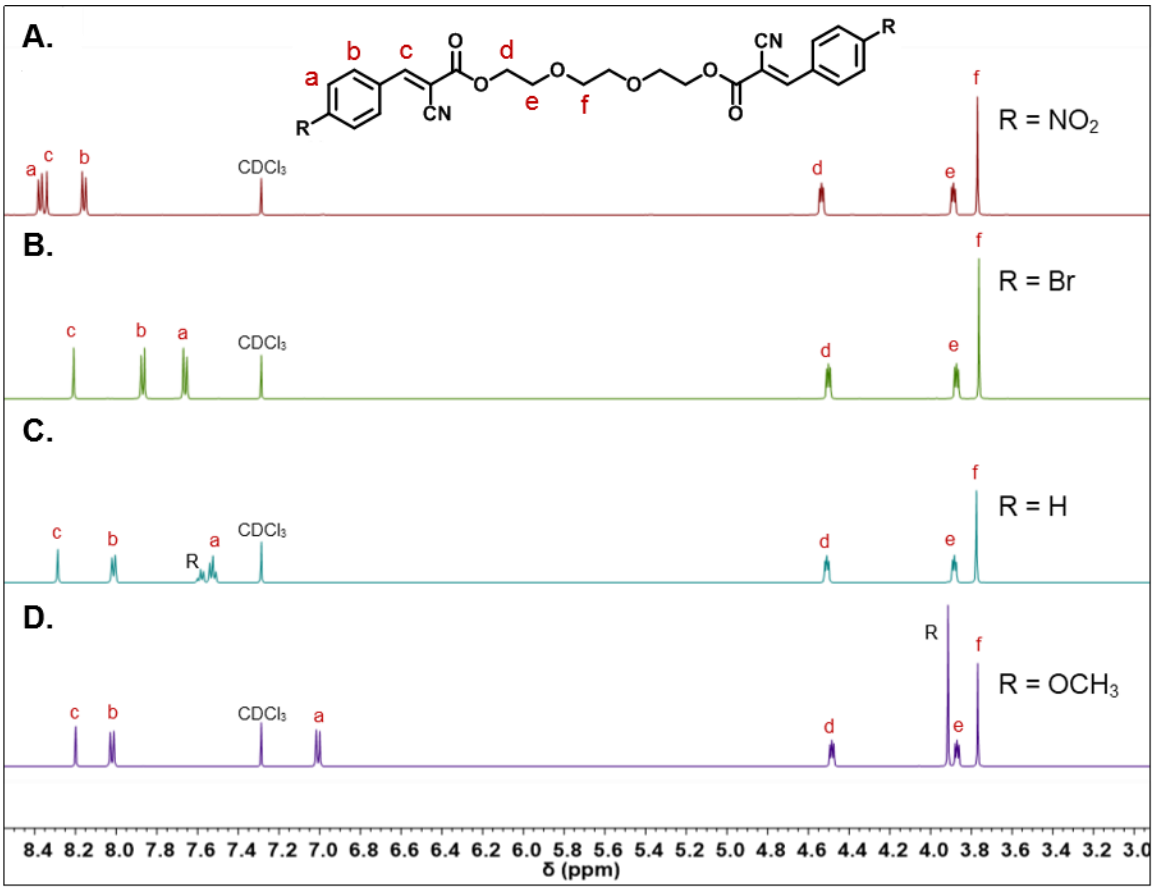

Figure 3.1. ^{1}H NMR (500 MHz, $CDCl_3$) of A) TEG-bis(4-nitrobenzalcyanoacetate) (**3N**), B) TEG-bis(4-bromobenzalcyanoacetate) (**3B**), C) TEG-bis(benzalcyanoacetate) (**3H**), and D) TEG-bis(4-methoxybenzalcyanoacetate) (**3M**).

Thermal characterization was conducted on the derivatives of **3** using thermogravimetric analysis (TGA) and differential scanning calorimetry (DSC) (Figure 3.2, Table 3.1). All Michael acceptor compounds were found to be thermally stable up to approximately 300 °C, as determined by TGA (Figure 3.2A). In DSC (Figure 3.2B), neither **3M** nor **3H** showed any crystalline behavior within the testing range (-80 °C – 200 °C), but rather exhibited a phase transition, likely a glass

transition temperature (T_g), below 0 °C. In contrast, the calorimetric behavior of **3N** was dominated by a broad melting phenomenon (T_m) that peaked at 145 °C. **3B** demonstrated a more complex thermal behavior with a phase transition (T_g) below 0 °C (akin to **3M** and **3H**), a cold crystallization peak (T_c) at 47 °C, before finally, a sharp melting peak at 160 °C.

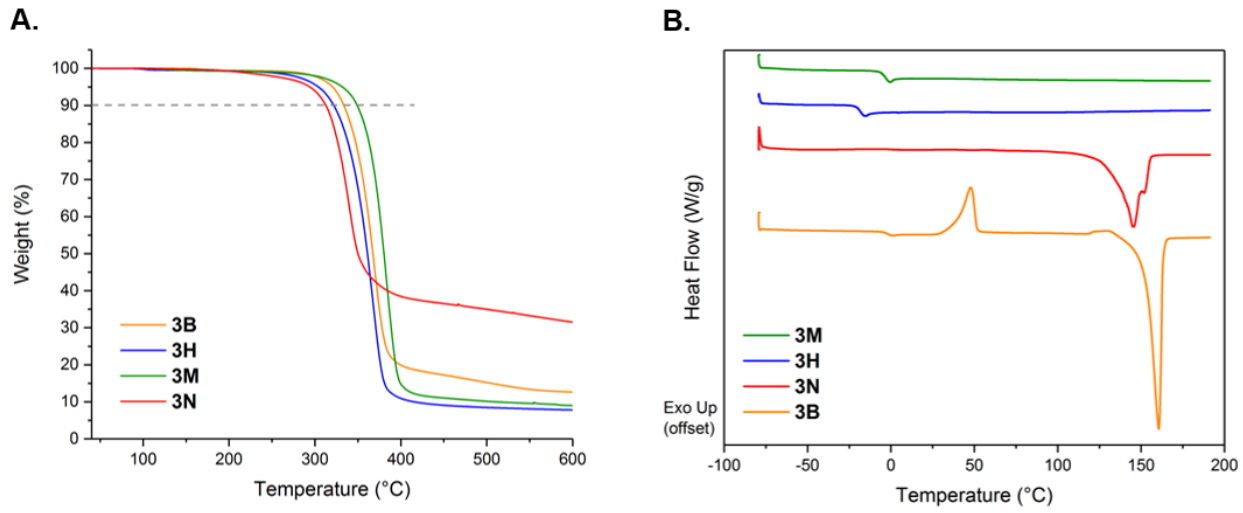

Figure 3.2. A) TGA data for TEG-bisbenzalcyanoacetates. 10% weight loss is marked by the gray dashed line (ramp rate = 10 °C/min). B) DSC curves of TEG- bisbenzalcyanoacetates. Both analyses run at 10 °C/min, DSC showing results of second heating (exotherm up, ramp rate = 10 °C/min, curves offset for ease of viewing).

Table 3.1. Summary of thermal properties of neat electrophiles.

Sample	T_d (°C)[a]	T_m[b]/T_g[c]/T_c[d] (°C)
3N	313	145/8/*
3B	334	160/-4/48
3H	322	*/-21/*
3M	349	***/-7/***

[a]T_d defined as the temperature required to reach 10% weight loss by TGA.
[b]T_m defined as temperature at peak of melt
[c]T_g defined as temperature at onset of glass transition
[d]T_c defined as temperature at peak of crystallization

Networks were formed by simply mixing the **3** with PTMP (Figure 3.3B) in solution and casting onto a Teflon® dish. Although films could be prepared using DMSO to mimic conditions in the titration studies, the nonvolatile nature of the solvent was not conducive to casting films. Therefore, chloroform, a good solvent for both **3** and PTMP, was selected as the casting solvent. The ratio of reactive sites (thiol:alkene) was kept constant to target a 1:1 ratio, unless otherwise noted. These samples are denoted **$4M_x$, $4B_x$, $4H_x$,** and **$4N_x$** to indicate the use of **3M**, **3B**, **3H**, and **3N**, respectively, to form the network. The x relates the mole percent (mol%) of each acceptor site (x = 100 or 50) relative to the total amount of thiol. Hybrid systems were also prepared that utilized networks containing a 50/50 (mol%/mol%) combination of electrophiles (combinations of **3H** with **3M** did not result in robust films suitable for mechanical testing). For example, **$4N_{50}H_{50}$** is comprised of 50 mol% of Michael acceptor groups from **3N** and 50 mol% from **3H**. The cast films were dried (24 hours at 60 °C then 30 minutes at 150 °C) and compression molded (10 minutes,

10 kpsi, 90 °C for **3N**-containing films, 70 °C for others) using a stainless-steel rectangular spacer, resulting in a polymeric film approximately 400 µm thick. It is worthy of note that under these conditions, PTMP alone (without the acceptors) remains a free-flowing, viscous liquid.

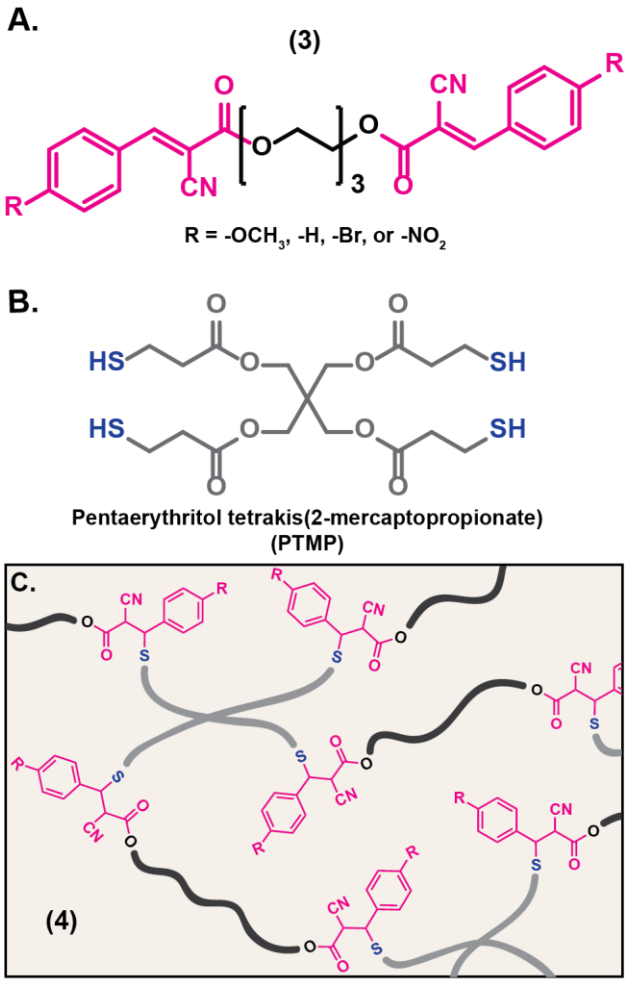

Figure 3.3. Chemical structures of A) ditopic electrophiles and B) tetrathiol crosslinker, PTMP. C) Illustration depicting the network formation of electrophiles crosslinked with PTMP.

Table 3.2. Contents of dynamic thia-Michael films and corresponding material properties.

Sample Name	R1-group	eq.	R2-group	eq.	eq. PTMP	T_g 1 [a] (°C)	T_g 2 [b] (°C)	$G'_{25\,°C}$ [c] (MPa)	$G'_{80\,°C}$ [d] (kPa)
4M$_{100}$	-OCH_3	2	-	-	1	-20.9	113	n/a	n/a
4H$_{100}$	-H	2	-	-	1	-10.8 ± 4.9	114	0.64	46.0
4B$_{100}$	-Br	2	-	-	1	-0.5 ± 1.6	n/a	n/a	n/a
4N$_{100}$	-NO_2	2	-	-	1	19.5 ± 3.7	133	2100	342.3
4N$_{50}$M$_{50}$	-OCH_3	1	-NO_2	1	1	1.0 ± 2.0	110	150	10.4
4N$_{50}$H$_{50}$	-H	1	-NO_2	1	1	1.7 ± 2.9	109	1800	110.6
4N$_{50}$B$_{50}$	-Br	1	-NO_2	1	1	14.0 ± 0.8	135	2200	180.7

[a] Calculated from onset of glass transition (n > 3), [b] Calculated from onset of glass transition, [c] Determined by observed tensile storage modulus (E′) at 25 °C, [d] Determined by observed shear storage modulus (G') at 80 °C.

To probe the ability of the catalyst-free thia-Michael adducts to yield robust films, an initial series of films (**4N$_{100}$, 4B$_{100}$, 4H$_{100}$,** and **4M$_{100}$**) were prepared using the different bis-functional acceptors, in combination with PTMP. Raman spectroscopy was used to analyze the formation of the thia-Michael bond within the network. All spectra were collected using a 633 nm laser source and were post-processed using OriginPro software to smooth, baseline correct, and normalize the data (see Experimental methods for full details). Three key regions within the spectrum were identified as markers for the reaction progress, mainly the alkene regime (C=C stretch, 1550-1640 cm^{-1}), the nitrile regime (C≡N stretch, 2260-2200 cm^{-1}), and the thiol regime (S-H stretch, 2600-2540 cm^{-1}). Figure 3.4 shows the C=C stretch (Figure 3.4A) and the C≡N stretch (Figure 3.4B) regions for the solid, unreacted ditopic electrophiles. While the C≡N shifts are nearly identical (all within 6 cm^{-1}), there is notable variations in peak location within the C=C regime, demonstrating the effect of atomic mass and electron donating/withdrawing behavior on the conjugated double bonds.[28]

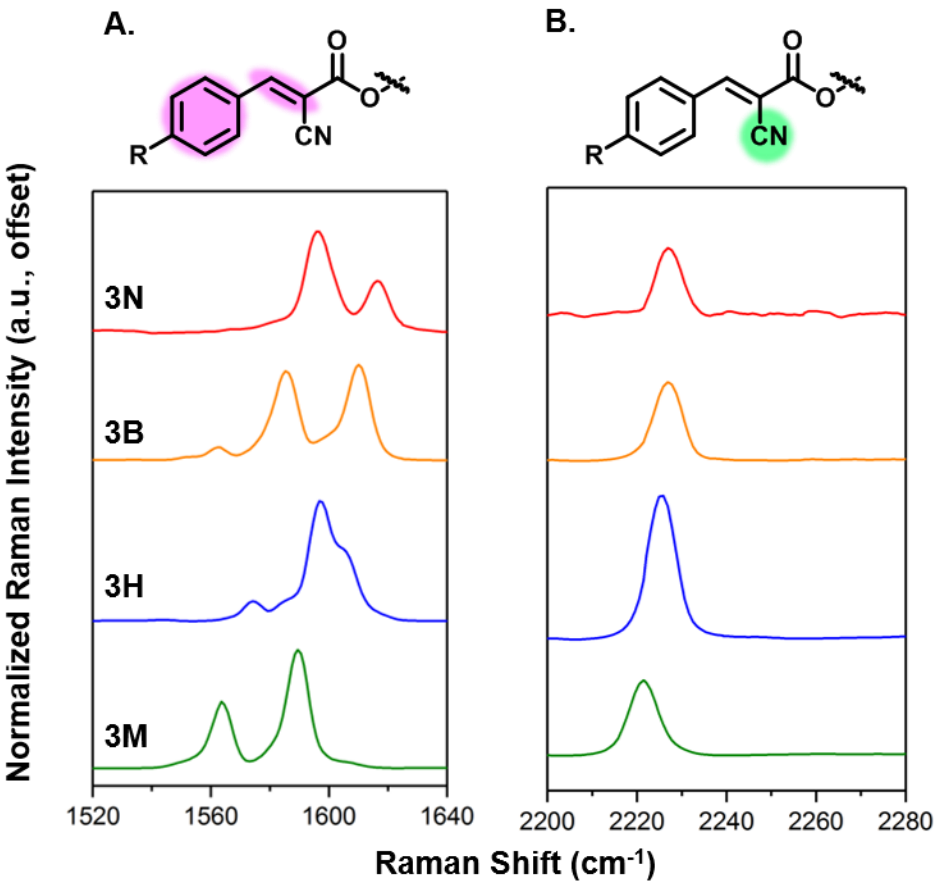

Figure 3.4. Select Raman spectra of ditopic Michael acceptors (**3N** (red), **3B** (orange), **3H** (blue), and **3M** (green)). Isolated regions show A) C=C stretch and B) C≡N stretch.

Once the ditopic compounds are incorporated into thia-Michael networks, shifts in the Raman spectrum indicate the formation of crosslinks via thia-Michael addition. As shown in Figure 3.5, the progress of the reaction can be observed by the disappearance of the C=C peak associated with the reactive alkene (higher frequency C=C signal at 1587 cm^{-1} – 1615 cm^{-1}, Figure 3.5A, C, E, and G) as well as the shift of the C≡N signal to higher frequencies as a result of this

loss of conjugation (Figure 3.5B, D, F, and H). Furthermore, there is a decrease in the thiol peak intensity at 2570 cm^{-1} as a result of the PTMP reactive groups participating the in crosslinking reaction (Figure 3.6A). As the elimination of thiols from the spectra could equally be attributed to disulfide formation within the network, the spectra were compared to a control sample composed of diethylene glycol dithiol and PTMP crosslinked via disulfide bonds using previously reported methods (Sample prepared and donated by Arvin Sookezian). As shown in Figure 3.6, while a broad disulfide peak is clearly visible at ca. 510 cm^{-1} in the control sample, no notable peaks were found in any of the thia-Michael networks that could be definitively characterized as a disulfide bond.

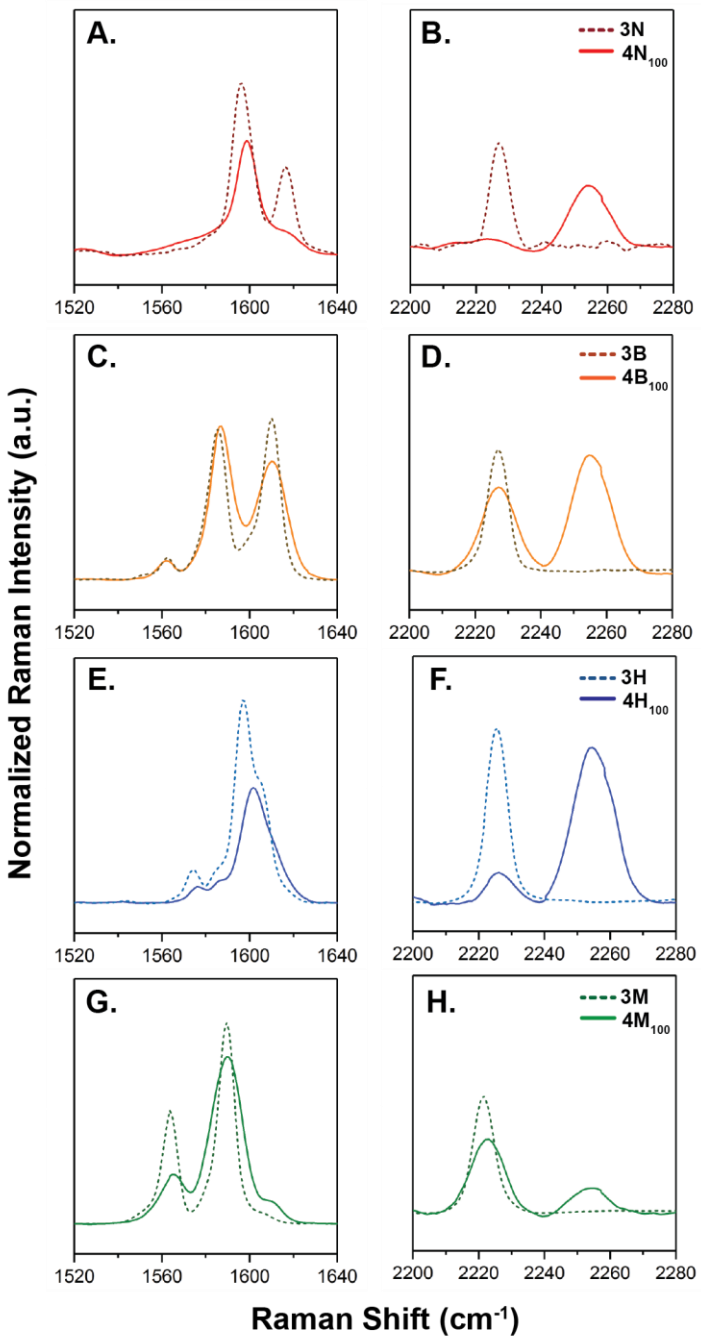

Figure 3.5. (cont. from page 11) Raman spectra of C=C (*left*) and C≡N (*right*) vibrational stretches for the neat electrophiles (dotted lines) overlayed with the respective thia-Michael networks (solid lines). A/B) **3N** and **4N$_{100}$**, C/D) **3B** and **4B$_{100}$**, E/F) **3H** and **4H$_{100}$**, G/H) **3M** and **4M$_{100}$**.

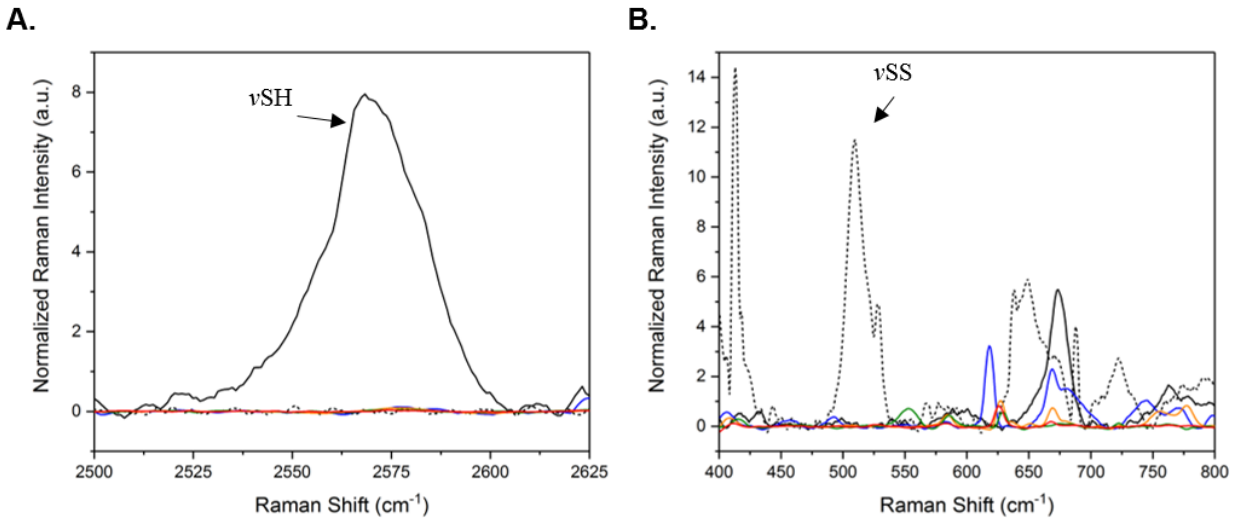

Figure 3.6. Raman spectra of A) thiol regime and B) disulfide regime highlighting the disappearance of the thiol peak as well as the absence of disulfide formation within the thia-Michael networks. PTMP (dotted line), disulfide network (black), **4N$_{100}$** (red), **4H$_{100}$** (blue), **4B$_{100}$** (orange), **4M$_{100}$**.

Aside from confirming the formation of crosslinks based on the thia-Michael reaction, Raman spectroscopy also provided insight concerning the extent of crosslink formation within the different networks. Examination of the network spectra reveals that peaks associated with the neat electrophiles remain (i.e. C≡N stretch at 2226 cm^{-1}), signifying that all of the networks exhibit some percentage of free, unreacted species. The amount of unreacted species was found to vary depending on the electrophile used in the network with **4N$_{100}$** having the least remaining free acceptors and **4M$_{100}$** having the most. **4B$_{100}$** appear anomalous in its high relative concentration of

unreacted species, however, as thermomechanical evaluations will show, this variation likely results from the bulk film phase behavior.

Thermogravimetric analysis (TGA) confirmed the thermal stability of the films reflected the stability of the parent molecules with 10% degradation near 300 °C for all network samples (Figure 3.7A). Differential scanning calorimetry (DSC) of the films revealed that most of the networks exhibited two phase transitions, identified as glass transitions (T_g) (Figure 3.7B). It is worthwhile noting that the T_gs of these films approximately track with equilibrium constant, with higher T_gs being observed for the networks formed with the more thermodynamically stable dynamic bonds. The outlier in the thermal studies was **4B$_{100}$** which demonstrated multiple phase transitions at elevated temperatures, presumably resultant from the cold-crystallization of the electrophile (see Figure 3.2 for **3B** DSC). Consequentially, the **4B$_{100}$** film was unsuitable for mechanical testing as the processing conditions necessary to achieve a dry, pressed film promoted catastrophic phase separation as the electrophile crystallized from the network. This observation further explains the aforementioned Raman spectroscopy results where the **4B$_{100}$** network exhibited more free electrophile than its counterparts. In this case, it is evident that the crystallization event traps the **3B** Michael acceptor compounds, leaving them unable to react further with the PTMP crosslinkers. As for the remaining TM networks, the presence of dual glass transitions is an interesting observation given the fact that only two small molecule monomers are being reacted. The dual transitions suggest that as the networks form, two distinct amorphous phases develop that have significantly different thermal properties.

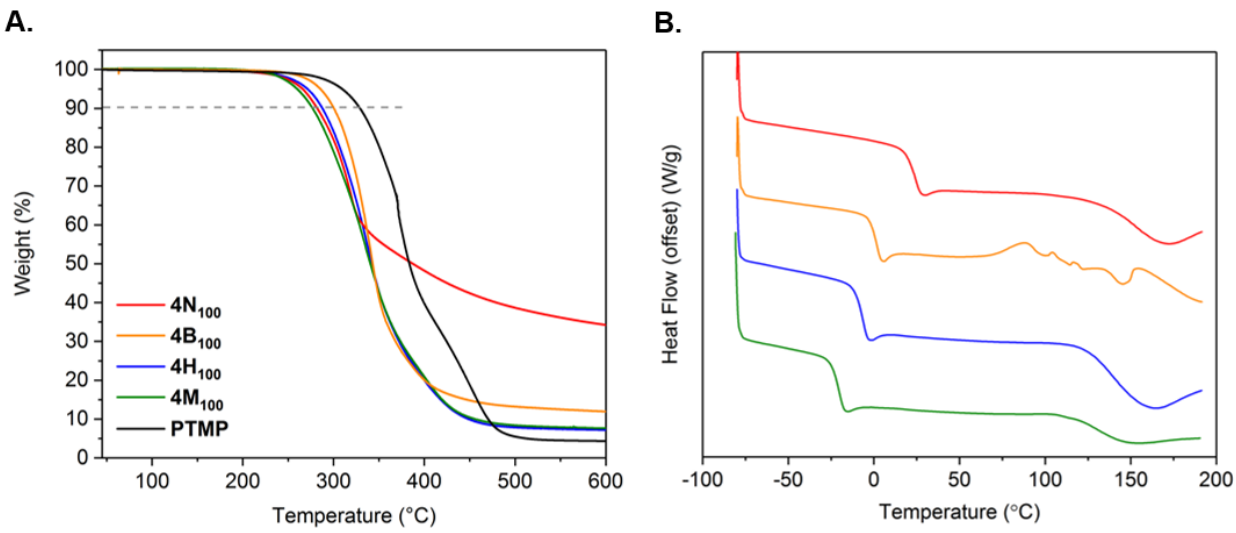

Figure 3.7. A) Thermogravimetric analysis (TGA) of **4N$_{100}$** (red), **4B$_{100}$** (orange), **4H$_{100}$** (blue), **4M$_{100}$** (green), and PTMP (black) with 10% weight loss highlighted by gray dotted line. B) Differential scanning calorimetry (DSC, exotherm up) 2nd heating curve of **4N$_{100}$** (red), **4B$_{100}$** (orange), **4H$_{100}$** (blue), and **4M$_{100}$** (green). DSC plots offset for ease of viewing.

Similar results were found with regards to the thermal properties of the hybrid films, **4N$_{50}$B$_{50}$**, **4N$_{50}$H$_{50}$**, and **4N$_{50}$M$_{50}$** (Figure 3.8). Each hybrid material exhibited degradation temperatures (by TGA) at or near the parent networks (Figure 3.8A) as well as two glass transitions in DSC (Figure 3.8B). Furthermore, the onset of the lower temperature T_g in the hybrid films reflects an approximate Fox-like blend of the glass transitions of the homo-Michael acceptor films. Evaluation of the three hybrid materials with respect to the Fox Equation (inset in Figure 3.9) shows that the lower T_g of the films can generally be described as a blend of the two **R$_{100}$** (where R = N, B, H, or M) components within the hybrid. For example, **4N$_{50}$H$_{50}$** has a low T_g onset at ca.

4 °C, reflecting an approximately equal contribution of **4N$_{100}$** and **4H$_{100}$** lower T_gs at 20 °C and -11 °C, respectively (Table 3.2). The offsets from the predicted Fox behavior provide further evidence towards a phase separated systems where the composition of the phases is slightly asymmetric. A parallel trend is observed for the higher temperature transition, although the breadth of the transition in the hybrid films makes the precise transition temperature difficult to accurately compare.

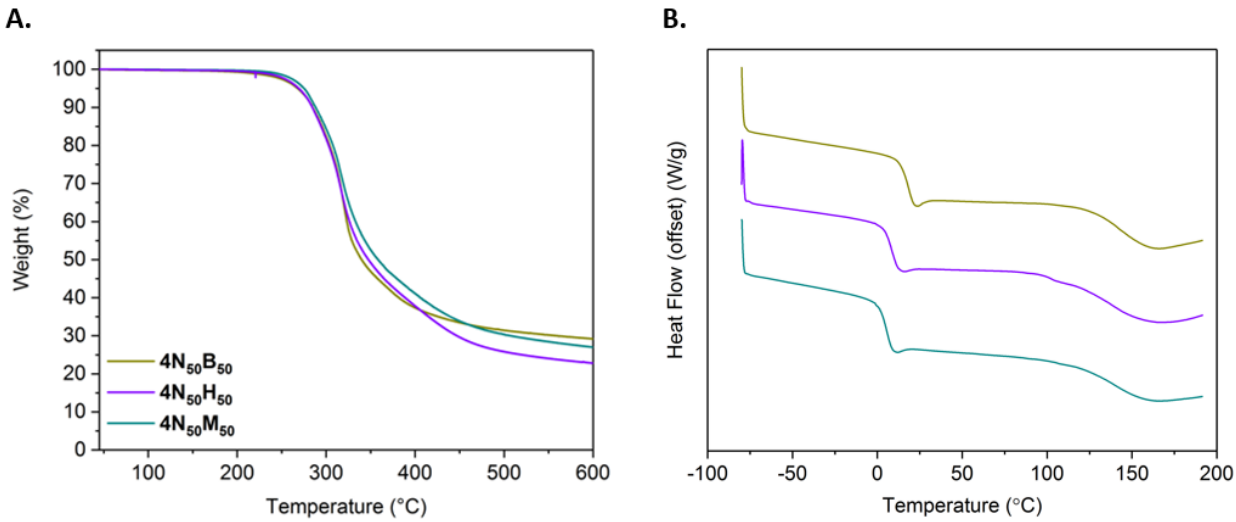

Figure 3.8. A) TGA data for thia-Michael films including hybrids. 10% weight loss is marked by the blue dashed line (ramp rate = 10 °C/min). B) DSC curves for thia-Michael films including hybrids showing results of second heating (exotherm up, ramp rate = 10 °C/min, curves offset for ease of viewing). **4N$_{50}$B$_{50}$** (gold), **4N$_{50}$H$_{50}$** (violet), **4N$_{50}$M$_{50}$** (cyan**)**.

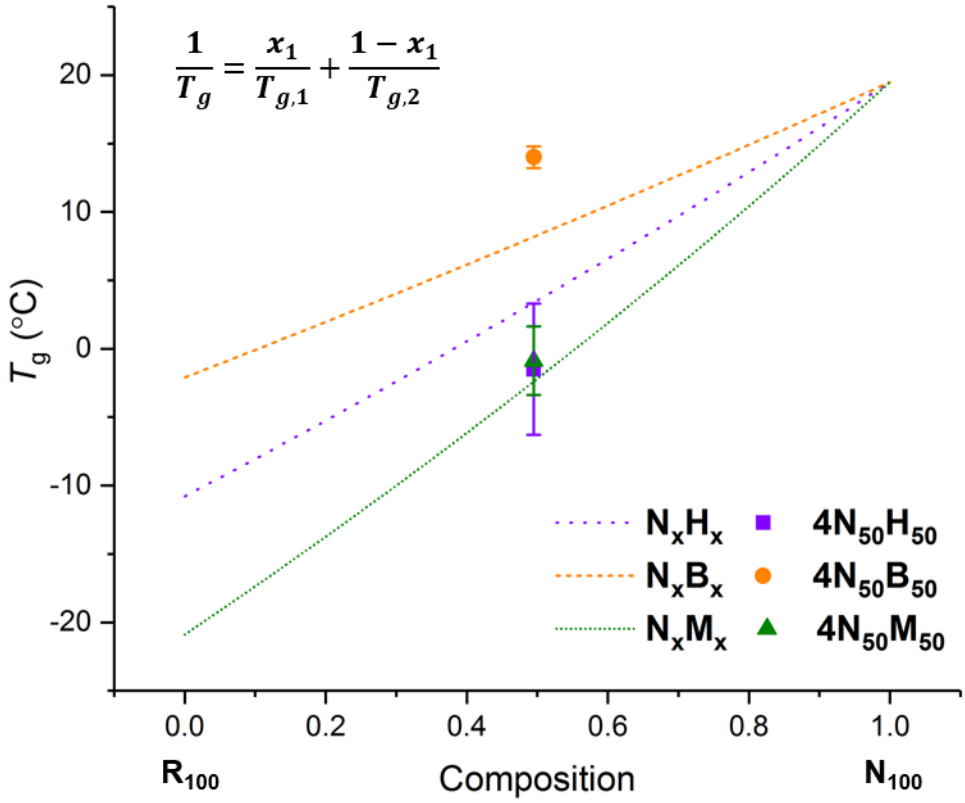

Figure 3.9. Predicted values from Fox equation (inset) for T_gs of hybrid materials containing **3N** and one other biscyanoacetate compound plotted with actual T_g data retrieved from DSC analysis for **4N$_{50}$B$_{50}$** (orange), **4N$_{50}$H$_{50}$** (violet), and **4N$_{50}$M$_{50}$** (green).

As the DSC studies indicated a phase separated internal structure, atomic force microscopy (AFM) of as-cast films was undertaken to confirm and further elucidate the microphase morphology of the networks (Figure 3.10). For the homo-acceptor networks **4H$_{100}$** and **4M$_{100}$** (high T_g of **4N$_{100}$** prevented differentiation of hard/soft regions at the operating temperature of AFM instrument while the crystallinity of **4B$_{100}$** damaged AFM tips and inhibited the use of the technique), the results clearly show a dual-phase system composed of hard, circular regions within

a soft matrix (Figure 3.10A,B). This suggests the possibility of reaction-induced phase separation (RIPS)[29,30] occurring during the casting/processing of these dynamic films. With RIPS, the miscibility of the components within a system changes as a reaction proceeds in forming a polymer (termed polymerization-induced phase separation, PIPS[31,32]) or, as in this case, a network. The evolving properties of the material (i.e. molecular weight, crosslink density, viscosity) eventually promote the differentiation of two phases within what began as a homogeneous system. With the dynamic thia-Michael reactions, the thermal and morphological data suggests that as the films are cast and dried, higher T_g, acceptor-rich regions form that eventually become immiscible with the evolving network matrix.

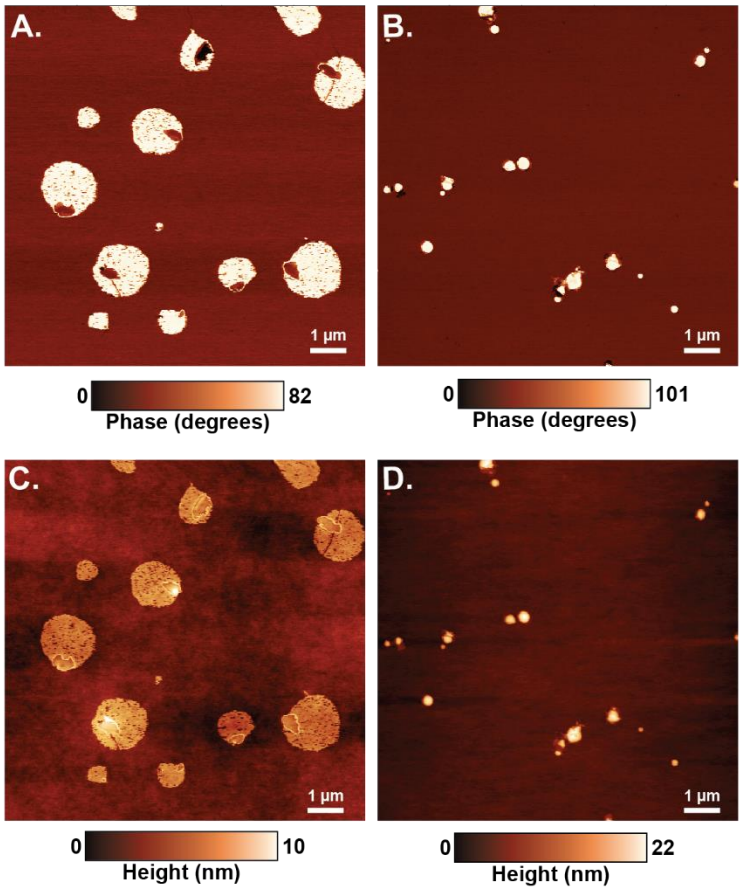

Figure 3.10. Atomic force micrographs showing phase (*top*) and height images (*bottom*). A/C) 4**H**$_{100}$ and B/D) 4**M**$_{100}$. Images taken using tapping mode.

Particle analysis of the images using ImageJ Image Processing Software was used to calculate the two-dimensional area of the bright phases within the films (Figure 3.11). Each film demonstrated a distribution of particle sizes, however, the aggregates of **4M**$_{100}$ reached sizes up to 0.40 µm^2 whereas **4H**$_{100}$ contained larger phases reaching over 5 µm^2. Further analysis revealed that the overall area taken up by the encapsulated phases within a 400 µm^2 image varied considerably between films with **4M**$_{100}$ containing ca. 9%, and **4H**$_{100}$ containing ca. 25%. When

taken into consideration with the relative enthalpic change within the DSC curves for each material (Figure 3.7B), it becomes apparent that the higher percentage of encapsulated phases is reflected in the larger change in heat flow at the second transition of the DSC heating curve. This evidence suggests that the bright phases observed in the AFM images are likely responsible for the high temperature phase transition.

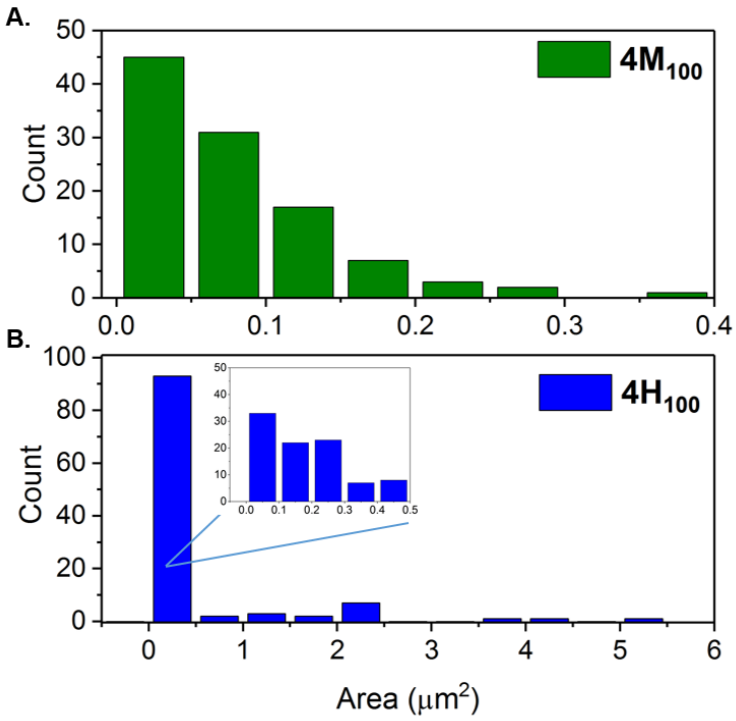

Figure 3.11. Particle size distribution of A) **4M$_{100}$**, and B) **4H$_{100}$** with the inset on B detailing the distribution of particle sizes under 0.5 μm^2.

The hybrid systems, on the other hand, revealed emergent morphologies that are indicative of a physically complex combination of phase separation phenomena (Figure 3.12). For example, **4N$_{50}$H$_{50}$** reveals concentric phase development in which the hard phases have encapsulated softer phases, while the **4N$_{50}$M$_{50}$** shows circular regions of two drastically different phases that are both distinct from the continuous phase. The phases appear inverted in the **4N$_{50}$B$_{50}$** films that were found to have a higher concentration of hard phase within the as-cast sample.

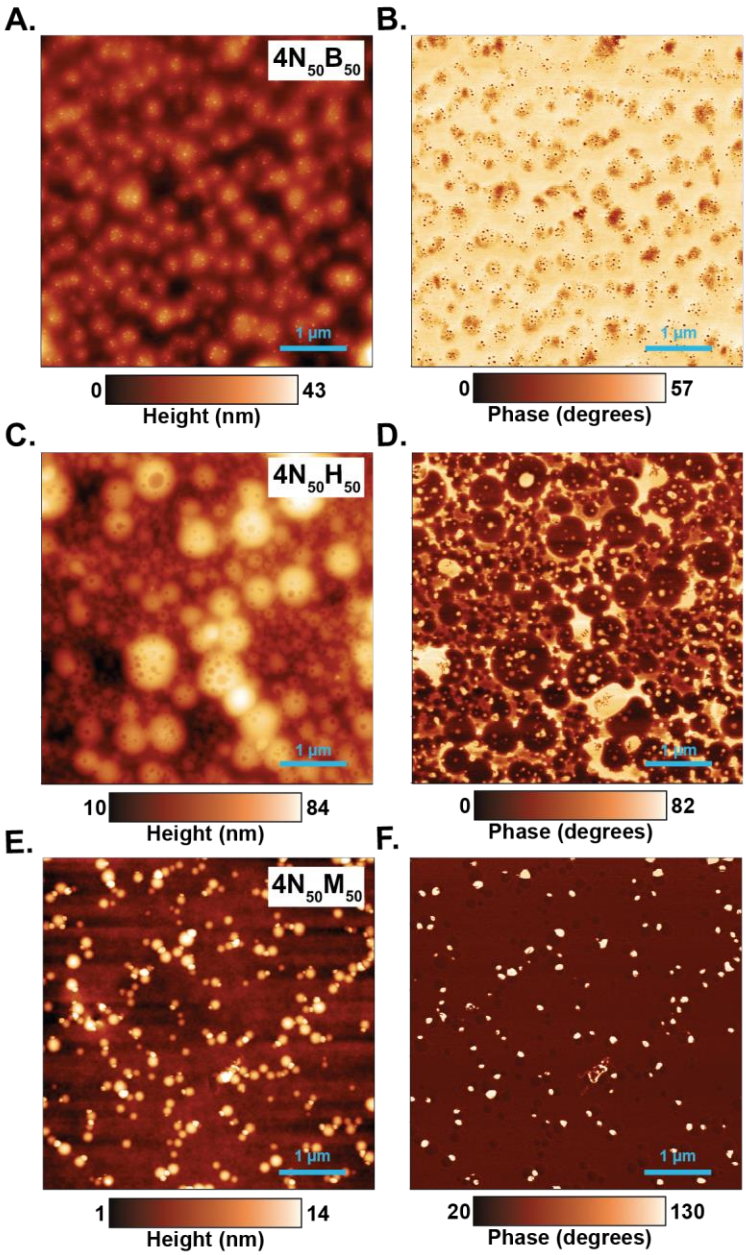

Figure 3.12. Atomic force microscope (AFM) images of **4N$_{50}$B$_{50}$** (A – height, B – phase), **4N$_{50}$H$_{50}$** (C – height, D – phase), and **4N$_{50}$M$_{50}$** (E – height, F – phase). Images taken using tapping mode AFM.

Thermomechanical studies were carried out on **4N$_{100}$**, **4H$_{100}$**, **4N$_{50}$B$_{50}$**, **4N$_{50}$H$_{50}$**, and **4N$_{50}$M$_{50}$**, using dynamic mechanical analysis (DMA). As can be seen in Figure 3.13A, the tensile storage modulus (*E'*) of the crosslinked networks in the glassy state are all on the order of 2 GPa. The lower temperature T_g by DMA was found to be 47.5 °C and 8.9 °C, for **4N$_{100}$** and **4H$_{100}$**, respectively, notably resulting in drastically different mechanical behavior at room temperature. Following the initial glass transition, a significant difference in performance within the rubbery plateau was also observed and evaluated via shear rheology (Figure 3.13B). Where **4N$_{100}$** exhibited a clear plateau on the order of 10^6 Pa up to ca. 120 °C, **4H$_{100}$** was weaker by two orders of magnitude and began its second transition at ca. 90 °C. The relative location of both T_gs as observed via DMA corroborates the trend observed in DSC: higher K_{eq} results in higher T_g.

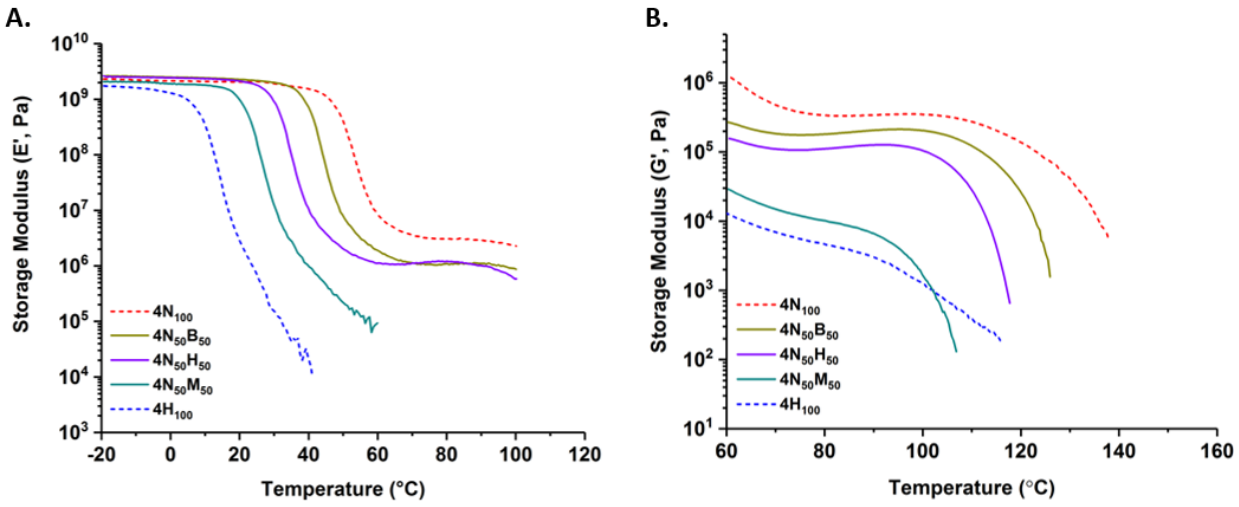

Figure 3.13. A) Dynamic mechanical analysis (DMA) and B) shear rheology results for **2H$_{100}$** (dashed blue), **2N$_{50}$M$_{50}$** (orange), **2N$_{50}$H$_{50}$** (violet), and **2N$_{100}$** (dashed red).

In the hybrid networks, the combination of crosslinks within the system enabled a systematic tuning of T_g. **4N$_{50}$B$_{50}$** exhibited a first T_g at 39 °C, **4N$_{50}$H$_{50}$** at 29 °C, and **4N$_{50}$M$_{50}$** at 21 °C, systematically decreasing the T_g with the use of lower K_{eq} acceptors. Shear rheology (Figure 3.13B) showed that both rubbery moduli and second T_g followed suit, with **4N$_{50}$B$_{50}$** having a higher modulus and higher second T_g than **4N$_{50}$H$_{50}$**, and both **4N$_{50}$B$_{50}$** and **4N$_{50}$H$_{50}$** having higher moduli and second T_g than **4N$_{50}$M$_{50}$**. Thus, these initial evaluations of dynamic reaction-induced phase separation demonstrate the ability to tailor thermal, mechanical, and morphological properties of dynamic networks by shifting the chemical equilibrium of the reaction through mindful compound modification. The implementation of thermally responsive thia-Michael bonds into the network creates a fully reversible, tunable environment that allows the films to be reprocessed and reprogrammed. To demonstrate, **4N$_{50}$H$_{50}$** was annealed at 200 °C for 30 minutes then either cooled slowly (1 °C/min) or quenched in liquid nitrogen. This thermal treatment resulted in a drastically different phase structure as compared to the as-cast films (Figure 3.14). The annealing process allowed the two phases to become more distinct with large, circular hard phases within a continuous soft phase while the cooling process defined the extent of differentiation between the phases.

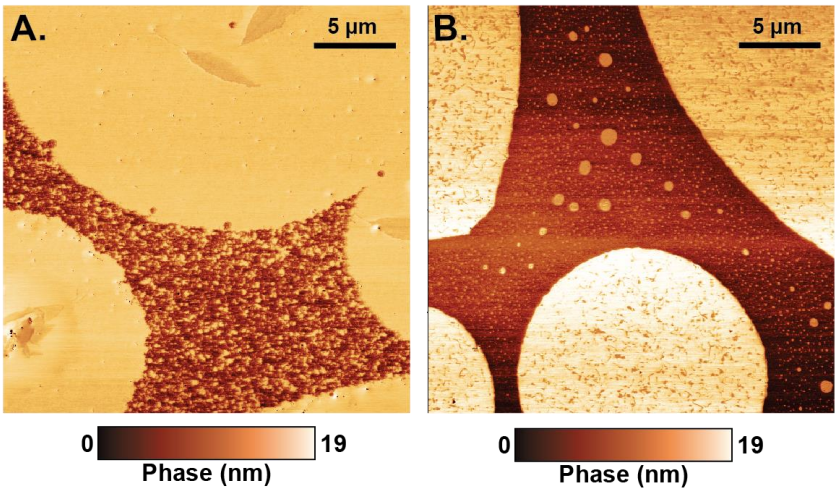

Figure 3.14. AFM images highlighting change morphology of **4N$_{50}$H$_{50}$** after annealing at 200 °C then A) slow cooling (1 °C/min) to room temperature and B) quenching liquid nitrogen.

As a result of the dynamic, phase separated morphology, these systems exhibited reprogrammable shape memory behavior. In a representative example, the one-way and reprogrammable shape memory behavior of the **4N$_{50}$H$_{50}$** film was evaluated using force-controlled DMA shape memory experiments (Figure 3.15). During the course of the one-way shape memory experiment (Figure 3.15A) a temporary shape was imparted at 60 °C and fixed upon cooling below T_g, to room temperature where the applied force was released. The original shape was recovered once the sample was reheated once again to 60 °C. For one-way shape memory, **4N$_{50}$H$_{50}$** demonstrated a perfect fixing ratio of 100%, showing no change in strain after the temporary shape was set (maximum strain, ε_m, and unloading strain, ε_u = 0.365). The sample returned to 90% of its original shape upon reheating (recovery strain, ε_r = 0.0371), with the residual 10% likely lost due

to creep within the sample that occurred throughout the shape memory process (a phenomenon common to dynamic covalent materials).

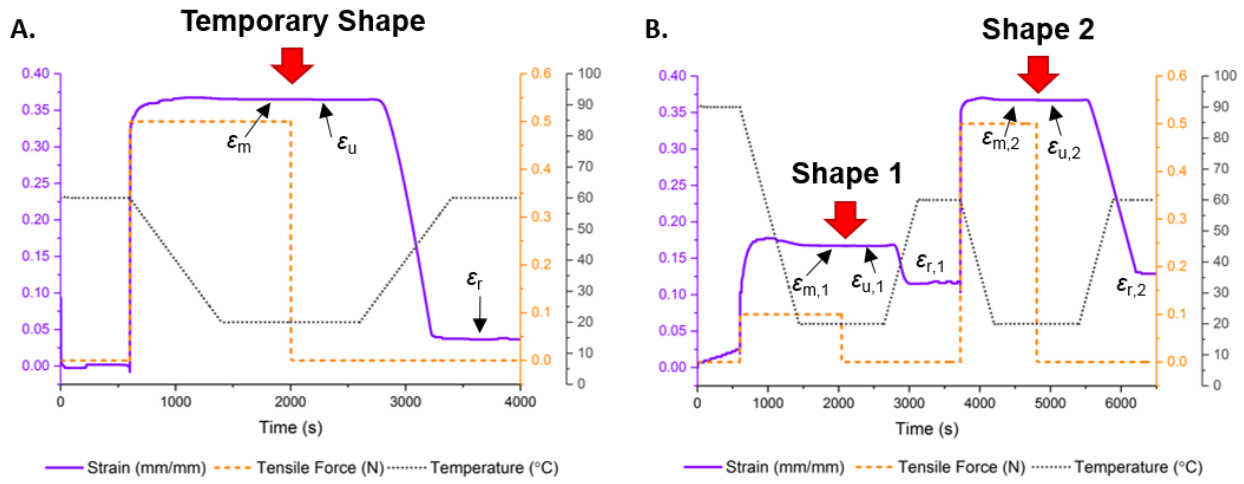

Figure 3.15. Force-controlled dynamic mechanical analysis (DMA) experiments demonstrating A) one-way and B) reprogrammable shape memory behavior of **4N$_{50}$H$_{50}$**. Violet line depicts recorded strain, orange dashed line is applied tensile force, and gray dotted line is applied temperature.

The reprogrammable shape memory experiment was conducted in a similar fashion (Figure 3.15B). Shape 1 was programmed as the new permanent shape by heating a sample to 90 °C (just below the second phase transition temperature) and applying an instantaneous tensile force. Relaxation of the network at this temperature (discussed in detail in Chapter 4) allows the dynamic crosslinks to rearrange in response to the applied force and upon cooling, the bonds are reformed in their new configuration. From this new, permanent Shape 1, a temporary geometry (Shape 2) was set by heating to 60 °C (during reheating, some recovery of the original shape was observed

as the film partially relaxed in response to the heat), applying a force, and cooling once again to room temperature. Once the force was removed, the fixing ratio of the new, temporary shape (Shape 2 in Figure 3.15B) was determined to be 100%. The sample was reheated to 60 °C and the temporary Shape 2 recovered back to the programmed Shape 1. The **4N$_{50}$H$_{50}$** film recovered back to 95% of the relaxed, temporary shape (($\varepsilon_{m,2}$- $\varepsilon_{r,2}$/$\varepsilon_{m,2}$- $\varepsilon_{r,1}$)*100), demonstrating the material's ability to reprogram its permanent shape while still maintaining temporary shape memory properties.

Using this reprogrammable shape memory behavior, it was possible to use the **4N$_{50}$H$_{50}$** material to construct folded architectures (for example, an airplane, Figure 3.16). By folding the films at elevated temperatures (over a hot plate at 105 °C) and cooling them to room temperature, the programmed permanent shape was the folded geometry. Therefore, the films could be unfolded at lower temperatures (45 °C). cooled and fixed into a flat, temporary geometry, and then upon heating again to >45 °C, the sample folded itself into an airplane.

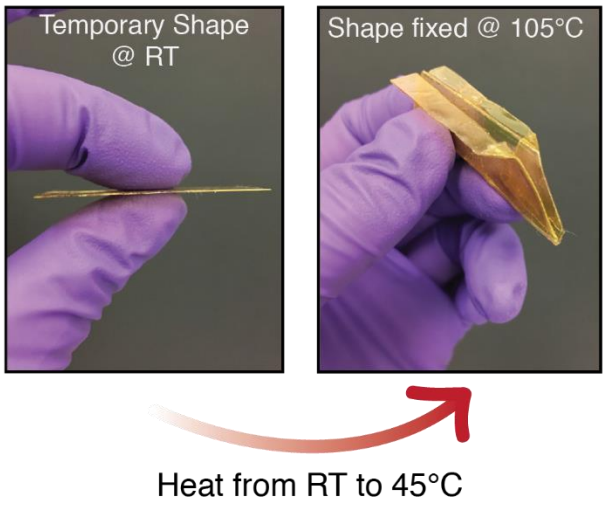

Figure 3.16. Reprogrammable shape memory behavior of **4N$_{50}$H$_{50}$** film. A film is folded into the shape of an airplane at 105°C and fixed by cooling to room temperature. The airplane is then flattened to achieve the room temperature (RT) temporary shape (left), but refolds into an airplane upon heating to 45°C (right).

En route to the shape memory geometry (i.e. the folded airplane), an interesting observation was made upon folding – the films could be creased. Creasing, defined here as plastic, localized, and permanent deformation in the material, is not common among polymeric materials as polymers typically either bend or fail under the conditions necessary for creasing. Above the onset of the lower temperature T_g, the **4N$_{50}$H$_{50}$** film could be folded into the airplane shape and would maintain the crease lines upon unfolding (Figure 3.17). These creases could be used repeatedly and could be reversed (bent in the opposite direction of the original fold), similar to paper. We hypothesize that the dynamic nature of the thia-Michael system allows the locally stressed bonds to exchange during crease formation, creating a deformation that is permanent, but does not immediately fail

due to local relaxation. While this remains simply an observation-based hypothesis until future studies can be conducted on the relevant variables (effect of film thickness, crease radius, micro-morphology along the crease, etc.), it is nonetheless a noteworthy property of these networks.

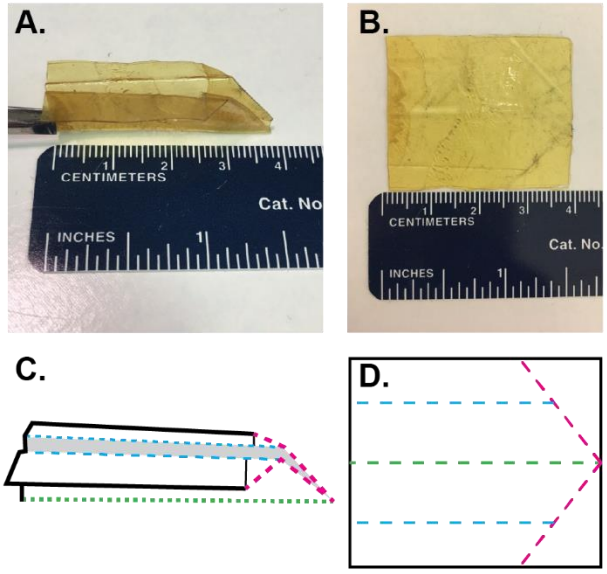

Figure 3.17. A) **4N$_{50}$H$_{50}$** film folded into an airplane geometry, B) film from image A unfolded showing creases where folds were made, C) cartoon showing plane with creases highlighted, D) 2D cartoon of airplane-forming creases as they appear on a flat surface.

In summary, shifting the equilibrium of a reversible TM reaction created the opportunity to tailor the thermal, mechanical, and morphological properties of the resulting materials through dynamic reaction-induced phase separation or DRIPS. In addition to their static physical properties, the networks exhibited reprogrammable shape memory behavior as a result of their dynamic, thermo-responsive transitions.

3.3 Conclusion

These results have demonstrated the ability to form reprocessable, shape memory dynamic covalent networks using the benzalcyanoacetate-based thia-Michael reaction. This tunable equilibrium reaction was used to tailor the thermal, mechanical, and morphological properties of the resulting materials through dynamic reaction-induced phase separation or DRIPS. In addition to their static physical properties, the networks exhibited reprogrammable shape memory behavior as a result of their dynamic, thermo-responsive transitions. Above T_g, the films also demonstrated a creasing behavior similar to paper, presumably a result of the local relaxation of dynamic bonds, but nonetheless, an intriguing avenue of investigation for future studies.

This investigation into the thia-Michael reaction has opened the door to a multitude of fundamental and applied macromolecular research. The ability to form a strong, robust network, without any catalyst or initiator is in itself an attractive feature. Coupled with the added advantage of being able to continuously reprocess these films due to their dynamic nature, this thia-Michael motif has much potential in the applied polymer sciences. The programmable thermomechanical

properties stemming from the fundamental kinetic and thermodynamic effects of substituents adds yet another layer of complexity and intrigue to the system. Continued exploration to understand and improve the functional and mechanical properties of these thia-Michael networks will surely yield exciting results.

3.4 Experimental Methods

3.4.1 Instrumentation

Nuclear Magnetic Resonance (NMR)

Nuclear Magnetic Resonance Spectroscopy was performed using the 500 MHz Bruker AVANCE II^{+} 500; 11.7 Tesla NMR at the NMR facilities at the University of Chicago. Analysis of NMR results was done using MNova NMR processing software.

Thermogravimetric Analysis (TGA)

Thermogravimetric analysis was performed using a TA Instruments Discovery Thermogravimetric Analyzer in the Soft Matter Characterization Facility at the University of Chicago. Samples were tested under nitrogen atmosphere using platinum pans. Tests were conducted using a ramp of 10 °C/min from starting operating temperature (ca. 35 °C) to 600 °C.

Differential Scanning Calorimetry (DSC)

DSC was performed using a TA Instruments Discovery 2500 Differential Scanning Calorimeter in the Soft Matter Characterization Facility at the University of Chicago. Samples were prepared in aluminum hermetic pans from TA Instruments and were hermetically sealed. Typical test conditions involved a heat-cool-heat procedure from (/200 °C/-80 °C/200 °C) run at 10 °C/min.

Raman Spectroscopy

Raman spectroscopy was conducted using a Horiba LabRamHR Evolution confocal Raman microscope in the Materials Preparation and Measurement Laboratory (MPML) that is part of the NSF Materials Research Science and Engineering Center (MRSEC) at the University of Chicago. Data was collected using a Horiba Synapse OE CCD detector and a 633 nm laser source. The spectral range of 400 – 3300 cm^{-1} was probed for all samples using 4 windows with 60 accumulations per window. (Other testing parameters: Objective = 50x LWD [long working distance]; grating = 600 gr/mm; ND Filter (i.e. laser power) = 50%; acquisition time = 1 second; RTD time = 1 second; Hole size = 100)

Raw data collected on the instrument was processed using OriginPro 2017 v9.40 by OriginLab Corporation. For each sample, data was first smoothed using the Savitzky-Golay method (window of 10 points; 2^{nd} order polynomial fit). The baseline of the smoothed data was

calculated using the asymmetric least squares method (parameters: asymmetric factor = 0.001; threshold = 0.01; smoothing factor = 4; iterations = 10) in the software's Peak Analyzer function and then subtracted from the smoothed data. The smoothed, baseline corrected data was then normalized using the standard normal variate (SNV) method in which the Raman intensities of the sample were divided by the standard deviation of the Raman intensities over the entire frequency range of the spectrum.

Atomic Force Microscopy (AFM)

Atomic force microscopy was performed using an Asylum Research Cypher ES AFM with BlueDrive in the University of Chicago's Materials Preparation and Measurement Laboratory as part of the NSF Materials Research Science and Engineering Center (MRSEC). Scans were conducted in tapping mode using a NanoWorld Arrow™ Ultra High Frequency (UHF) AFM probe.

Samples were prepared for AFM by pipetting a small (< 0.5 mL) aliquot of the thia-Michael solution (the same solution to be used to make the bulk film) onto a glass microscope cover slip. The cover slip sample was then exposed to the same drying routine as the bulk films with images taken after the 60 °C drying step and after the 150 °C annealing step.

Dynamic Mechanical Analysis (DMA)

DMA was performed using the TA Instruments RSA-GA DMA with Forced Convection oven (20 °C – 500 °C) attached to an Air Chiller System (-120 °C – 20 °C) and running TA Trios Software in the Soft Matter Characterization Facility at the University of Chicago. Pressed films were cut on a warm plate (temperature slightly above T_g of the network) into strips ca. 4 mm wide and ca. 10 mm long, then cooled back to room temperature on a flat surface. The strips were loaded into the tensile geometry above the T_g of the network (for example, 60 °C for **4N$_{100}$** or 40 °C for **4N$_{50}$H$_{50}$**) and finger tightened to prevent film breakage and ensure good contact with the tensile geometry. A typical procedure included an amplitude sweep (0.01% – 5%) above T_g at a frequency of 1Hz to define the linear viscoelastic region (LVR) as well as maximize the oscillatory force signal being picked up by the instrument. After the amplitude sweep, the samples were cooled to -20 °C using an IsoForce Temperature Ramp (0.01 N tension, 3.0 °C/min). Samples were soaked for 1 minute at -20 °C and a second amplitude sweep (0.01% - 5%) was conducted at a frequency of 1 Hz to optimize conditions below T_g. The samples were quite brittle at low temperatures and as such, it was important to closely monitor both the cooling process and the amplitude sweep for critically high force values (> 15 N) that could break the films.

Once parameters had been identified for optimal amplitude and frequency, temperature ramps could be conducted. Samples were loaded as previously described. A typical procedure included cooling to -20 °C using the IsoForce temperature ramp (0.01 N tension, 3.0 °C/min) and holding at -20 °C for 1 minute. Following the cooling step, conditioning options were enabled to account for automatic axial force adjustment (0.01 N ± 0.5 N tension, Set Initial Value box

unchecked) and automatic strain adjustment set to the minimum oscillatory force for LVR above T_g and maximum oscillatory force for LVR below T_g as determined by the amplitude sweeps.

Samples were then heated using the oscillatory temperature ramp procedure from -20 °C to 150 °C (or until failure) at a rate of 3.0 °C/min with an amplitude set in the LVR of the -20 °C amplitude sweep and a frequency of 1 Hz.

Shape Memory

A sample was cut into a strip (ca. 10 mm x 3 mm x 0.4 mm) and mounted onto the tensile geometry in the DMA instrument. During the course of the one-way shape memory experiment, the samples were equilibrated at 60 °C for 10 minutes under no tensile force. After equilibration, an instantaneous tensile force of 0.5 N was applied to the sample and held while the internal oven temperature was cooled to 20 °C at a rate of 5 °C/minute. The sample was held under 0.5 N force for 10 additional minutes after cooling and the strain was recorded as the maximum strain, ε_m. The force was removed, revealing the sample's new, temporary shape and the unloading strain, ε_u, was measured. The fixing ratio (sample's capacity to hold its shape in the absence of applied force, R_f) was determined by calculating the percent strain change after unloading, $(\varepsilon_u/\varepsilon_m)*100$. After 10 minutes at 20 °C under no tensile force, the sample was reheated to 60 °C at 5 °C/minute and the strain after recover, ε_r, was evaluated. Finally, the recovery ratio (extent to which the sample returns to its original shape, R_r) was determined as the percent strain recovered from the maximum strain, $(\varepsilon_m- \varepsilon_r/\varepsilon_m)*100$.

The reprogrammable shape memory experiment was conducted in a similar fashion. A sample strip was equilibrated in the tensile fixture of a DMA at 90 °C (just below the second phase transition temperature) for 10 minutes. At this temperature, the film creep can be seen as the instrument moves to keep the force on the material at zero. After ten minutes, an instantaneous 0.1 N tensile force was applied to the strip and the film was cooled to 20 °C at a rate of 5 °C/minute. Once cooled, the force was removed from the film and the first fixing ratio of the new, permanent shape was determined ($R_{f,1}$ = 100%). Then the sample was reheated to 60 °C to set a temporary shape. Upon reheating, some recovery of the original shape was observed ($R_{r,1}$ = 31%). Once equilibrated at 60 °C, 0.5 N tensile force was applied (same force as used in the one-way shape memory experiments) and the sample was once again cooled to 20 °C. Once the force was removed, the fixing ratio of new, temporary shape was determined ($R_{f,2}$ = 100%). The sample was reheated to 60 °C and the temporary Shape 2 recovered back to the programmed Shape 1.

Shear Rheology

Rheology was performed using the TA Instruments RSA-G2 ARES with Forced Convection oven (20 °C – 500 °C) attached to an Air Chiller System (-120 °C – 20 °C) and running TA Trios Software in the Soft Matter Characterization Facility at the University of Chicago. An 8 mm parallel plate was used for all tests.

Pressed films were cut into 8 mm circles using a die on a warm surface (just above T_g of the sample). Circular samples were loaded onto the parallel plate geometries above T_g, centered, and heated further to pressing temperatures (70 °C or 90 °C) with an axial compression force of 0.1 N. Samples were held at pressing temperatures for 1-5 minutes until geometry gap was no longer increasing indicating an equilibrated sample. Compression force was adjusted to 0.01 and sample was cooled to 80 °C for amplitude and frequency sweeps to establish a linear viscoelastic region (LVR). The LVR amplitude and frequency were used to parameterize the temperature sweeps.

Samples were cooled to 60 °C, held for 5 minutes, and temperature ramp studies were conducted. Conditioning options were set to 0.01 N axial compression force and strain adjustments were disabled. Temperature sweeps were conducted at 3 °C/min from 60 °C to 150 °C, held at 150 °C for 10 minutes, then ramped down to 60 °C again at the same rate. After holding isothermally at 60 °C for 10 minutes, the sample was ramped once again to 150 °C. The second heating was used for reported measurements. This method ensured equivalent thermal history between samples and allowed each network ample time to reorganize and reform the network upon cooling.

3.4.2. Synthetic Procedures

Triethylene glycol bis(cyanoacetate) (**2**)

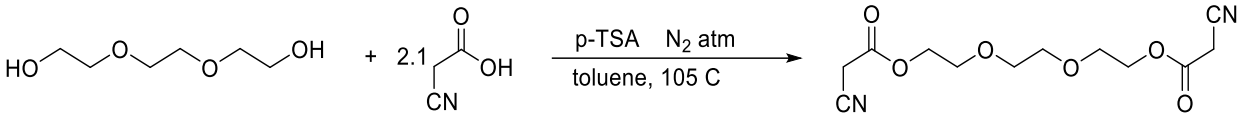

Scheme S3.1. Reaction scheme for the synthesis of the triethylene glycol bis(cyanoacetate) core.

The ditopic compounds were synthesized in two steps as previously reported by Sassi and Gupta.[33] In the first step, building the bis-cyanoacrylate core, triethylene glycol (TEG, 20.0 g, 0.13 mol, 0.78 M) and cyanoacetic acid (23.2 g, 0.27 mol) were combined in a 500 mL round bottom flask with 0.12 molar equivalents of catalytic *p*-toluenesulfonic acid monohydrate (3.0 g, 0.016 mol) in toluene (166.7 mL). The setup was equipped with a waterless condenser and Dean-Starks trap, heated to 105 °C under nitrogen atmosphere, and stirred using a magnetic stir bar for ca. 18 hours (overnight). Once complete, the solvent was removed via rotary evaporation. The resulting yellow oil was diluted with ca. 300 mL methylene chloride (DCM) and remaining salts were filtered out. The filtrate was washed thoroughly (3 or more times) with brine (sodium chloride -saturated water) and dried with magnesium sulfate. DCM was removed from the solution via rotary evaporation and the resulting yellow oil was dried overnight under high vacuum (MW = 284.15 g/mol, yield = 70% by mass). ^{1}H NMR (500 MHz in $CDCl_3$; δ ppm: 3.54 (*s*, 2H), 3.68 (*s*, 2H), 3.76 (*t*, 2H), and 4.39 (*t*, 2H)). ^{13}C NMR (101 MHz in $CDCl_3$; δ 163.11, 112.99, 70.68, 68.62, 65.77, 24.73). This TEG bis(cyanoacetate) product routinely contained some contaminate of

starting material, however the contaminate did not affect the second step and was sufficiently removed in the workup of the final product.

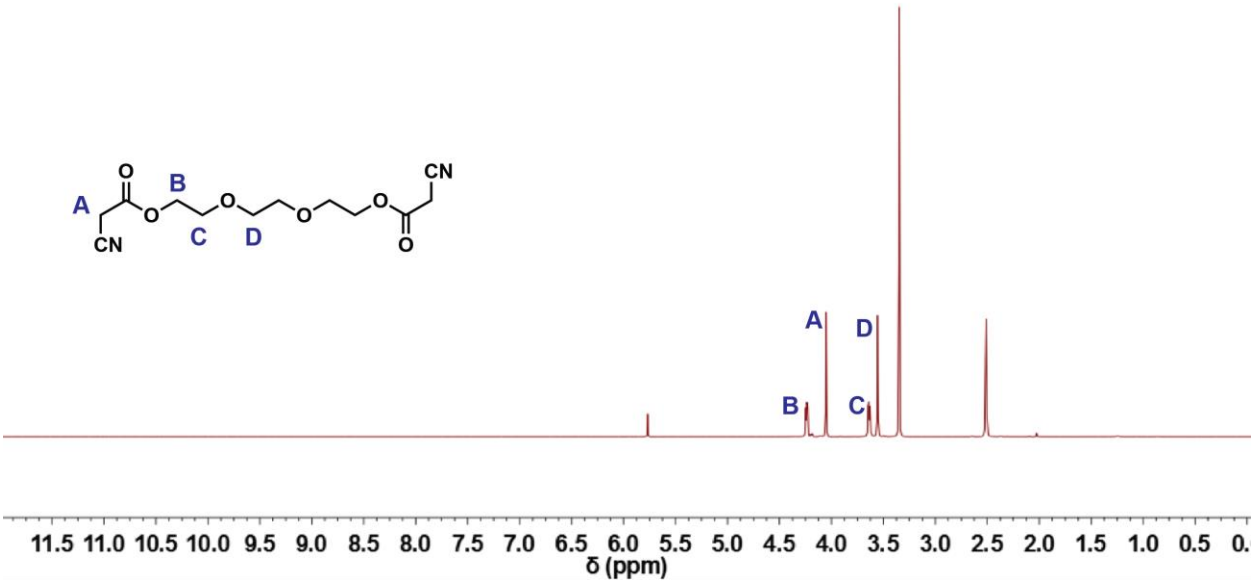

Figure S3.1. ^{1}H NMR of TEG bis(cyanoacetate) with peaks at 3.55 (*d*, 2H), 3.62 (*d*, 2H), 4.03 (*d*, 2H), and 4.18 (*d*, 2H) in deuterated methyl sulfoxide (d_6-DMSO) with water (3.33) and DMSO (2.50) solvent peaks visible. Remaining impurities removed in subsequent reactions.

Triethylene glycol bis(4-nitrobenzalcyanoacetate) (**3N**)

TEG bis(cyanoacetate) (5 g, 0.018 mol. 0.14 M) and 4-nitrobenzaldehyde (5.74 g, 0.038 mol) were added a 250 mL flask round bottom flask with dichloromethane (DCM, 130 mL) and 0.15 molar equivalents of catalytic triethylamine (TEA, 0.3 mL, 0.003 mol). The flask was then placed under a nitrogen atmosphere and allowed to stir using a magnetic stir bar overnight. DCM was removed using rotary evaporation and the resultant oil was triturated in MeOH two hours. The solution was filtered and a solid powder was collected. This trituration process was repeated until the filtrate was clear and colorless, leaving behind a reddish, clumpy powder. ^{1}H NMR (500 MHz in $CDCl_3$; δ ppm: 3.77 (*s*, 2H), 3.89 (*t*, 2H), 4.54 (*t*, 2H), 8.16 (*d*, 2H), 8.34 (*s*, 1H), and 8.37 (*d*, 2H)), ^{13}C NMR, and mass spectrometry. Yield by mass = 45%.

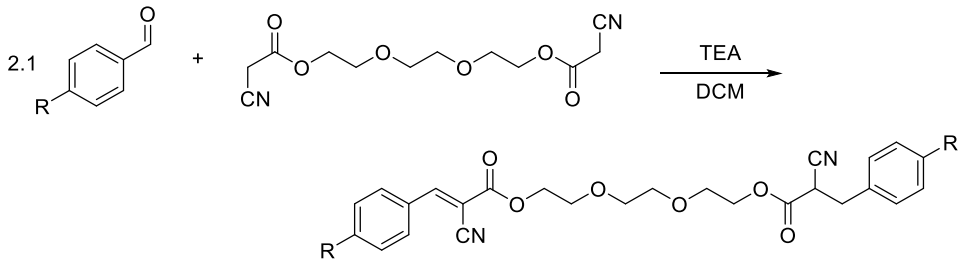

Scheme S3.2. General reaction scheme for the synthesis of TEG-core crosslinker.

Triethylene glycol bis(4-bromobenzalcyanoacetate) (**3B**)

TEG bis(cyanoacetate) (5.00 g, 0.018 mol. 0.14 M) and 4-bromobenzaldehyde (7.03 g, 0.038 mol) were added to a 250 mL flask round bottom flask with dichloromethane (DCM, 130 mL) and 0.15 molar equivalents of catalytic triethylamine (TEA, 0.3 mL, 0.003 mol). The flask was then placed under a nitrogen atmosphere and allowed to stir using a magnetic stir bar overnight. DCM was removed using rotary evaporation and the resultant oil was triturated in MeOH two hours. The solution was filtered and a solid powder was collected. This trituration process was repeated until the filtrate was clear and colorless. ^{1}H NMR (500 MHz in $CDCl_3$; δ ppm: 3.76 (*s*, 2H), 3.87 (*t*, 2H), 4.50 (*t*, 2H), 7.66 (*d*, 2H), 7.87 (*d*, 2H), and 8.21 (*s*, 1H)), ^{13}C NMR (101 MHz in $CDCl_3$; δ 162.25, 153.81, 132.71, 132.30, 130.23, 128.42, 115.14, 103.39, 70.90, 68.76, 65.92). Yield by mass = 64%.

Triethylene glycol bis(benzalcyanoacetate) (**3H**)

TEG bis(cyanoacetate) (5.00 g, 0.018 mol. 0.14 M) and benzaldehyde (4.03 g, 0.038 mol) were added to a 250 mL flask round bottom flask with dichloromethane (DCM, 130 mL) and 0.15 molar equivalents of catalytic triethylamine (TEA, 0.3 mL, 0.003 mol). The flask was then placed under a nitrogen atmosphere and allowed to stir using a magnetic stir bar overnight. DCM was removed using rotary evaporation and the resultant oil was triturated in MeOH two hours. The solution was filtered and a solid powder was collected. This trituration process was repeated until the filtrate was clear and colorless. ^{1}H NMR (500 MHz in $CDCl_3$; δ ppm: 3.77 (*s*, 2H), 3.88 (*t*, 2H), 4.51 (*t*, 2H), 7.53 (*t*, 2H), 7.58 (*t*, 1H), 8.01 (*d*, 2H) and 8.28 (*s*, 1H)). ^{13}C NMR (101 MHz in

$CDCl_3$; δ 162.51, 155.35, 133.40, 131.45, 131.15, 129.30, 115.36, 102.80, 70.91, 68.80, 65.81). Yield by mass = 51%.

Triethylene glycol bis(4-methoxybenzalcyanoacetate) (**3M**)

TEG bis(cyanoacetate) (5.00 g, 0.018 mol. 0.14 M) and 4-methoxybenzaldehyde (5.17 g, 0.038 mol) were added to a 250 mL flask round bottom flask with dichloromethane (DCM, 130 mL) and 0.15 molar equivalents of catalytic triethylamine (TEA, 0.3 mL, 0.003 mol). The flask was then placed under a nitrogen atmosphere and allowed to stir using a magnetic stir bar overnight. DCM was removed using rotary evaporation and the resultant oil was triturated in MeOH two hours. The solution was filtered and a solid powder was collected. This trituration process was repeated until the filtrate was clear and colorless. ^{1}H NMR (500 MHz in $CDCl_3$; δ ppm: 3.77 (*s*, 2H), 3.87 (*t*, 2H), 3.91 (*s*, 3H), 4.48 (*t*, 2H), 7.01 (*d*, 2H), 8.02 (*d*, 2H), and 8.20 (*s*, 1H)). ^{13}C NMR (101 MHz in $CDCl_3$; δ 163.86, 163.14, 154.66, 133.74, 124.36, 116.08, 114.79, 99.14, 70.90, 68.87, 65.54, 55.64). Yield by mass = 51%.

3.4.3 Film Preparation Procedure

The electrophile(s) (100 mg/mL) and PTMP (300 mg/mL) were dissolved separately in chloroform, then combined and stirred for two hours at 50°C, allowing the system to homogenize. It is important to note here that heat is not required for this reaction to take place (as demonstrated

by the initial NMR studies at room temperature), however, the samples were heated in order to ensure that all components were sufficiently soluble. After two hours, the solution was poured onto a Teflon dish and dried, overnight, at room temperature. An additional 24 hours of drying in a vacuum oven at 60 °C under vacuum was carried out to remove as much residual solvent as possible, followed by a final drying step under vacuum at 150 °C for 30 minutes to complete the drying process, as confirmed by TGA. The dried films were compression molded at 90 °C (70 °C for films containing only **3H** or **3M**) for ten minutes under 10,000 psi. A 400 μm spacer and Kapton®/Teflon® blend substrates were used to limit adhesion and deformation of the films at higher temperatures. It is important to note that under these conditions, PTMP alone (without the acceptors) remains a free-flowing, viscous liquid.

3.4.4 Processing Conditions Case Study: $\mathbf{4N_{50}B_{50}}$

As described in the main text, the processing conditions for these thia-Michael films were critically important to the final properties of the films. In particular, the process of drying the films proved to be more difficult than initially expected and had a notable effect on the mechanical performance of the films. In this section, the $\mathbf{4N_{50}B_{50}}$ film serves as a case study to describe the evolution of the final drying procedure and its effect on the thia-Michael networks.

When the TEG-based thia-Michael networks were first conceived, they were stirred at 50 °C for 2 hours in chloroform ($CHCl_3$), cast onto a Teflon dish, and dried overnight at room

temperature. It was important to allow the films to dry overnight in air, without vacuum as the immediate addition of heat and vacuum after casting resulted in bubbling of the volatile solvent within the network. As $CHCl_3$ is a volatile solvent (boiling point = 61.2 °C at room temperature and atmospheric pressure), it was expected to be mostly removed at room temperature with any residual solvent removed via drying oven. However, given that these thia-Michael networks were constructed using a triethylene glycol core that is prone to the absorption of water, there was the possibility that water contamination within the films would also present a problem. Therefore, the initial drying procedure after the room temperature evaporation was to move the film into a desiccator under house vacuum.

Thermogravimetric analysis (TGA) of this sample clearly showed the deficiency of this procedure as there was approximately 17% weight loss due to solvent within the film (Figure S3.2). Upon realizing this, the procedure was modified by eliminating the desiccator step and instead moving the films to a vacuum oven at 60 °C and under vacuum after room temperature drying and letting them dry overnight (18-24 hours). TGA showed a marked improvement in the weight loss between 40 °C – 200 °C, decreasing it to 3.3 % total weight loss. Curiously, the same sample was tested three days later after spending three days in ambient conditions, and the weight loss profile had changed. Not only had the total mass loss increased to 5.5 %, but the onset of the additional 2% weight loss was at ca. 130 °C, higher than would be expected for either water or chloroform. This sample was then melt processed for 10 minutes at 60 °C and 10k psi and the resulting TGA was slightly improved, yet followed the same path as the previous iteration.

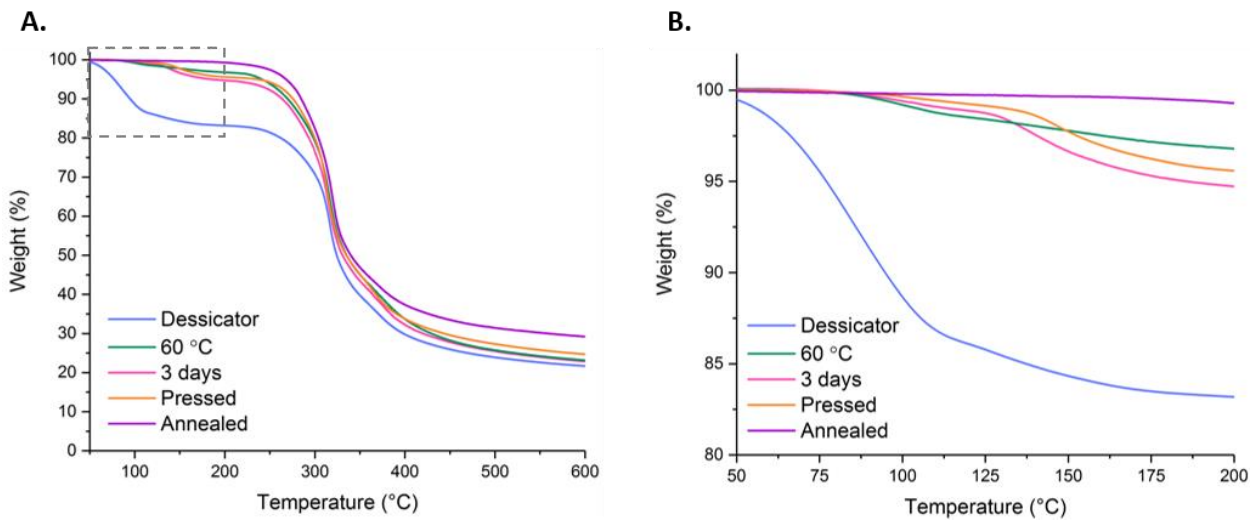

Figure S3.2. A) Full TGA curve of **$4N_{50}B_{50}$** showing different drying procedures. B) Enlarged region highlighted in A showing initial weight loss before 200 °C.

The differences in these results led to significant inconsistences in the thermal and mechanical properties (i.e. T_g and crosslink density). Therefore, to ensure that all residual material was removed, an extra step was added to anneal the samples at 150 °C under vacuum for 30 minutes. At this temperature, all materials were in the melt and, according to TGA results, all residual material was eliminated from the sample.

3.5 Supplemental Results

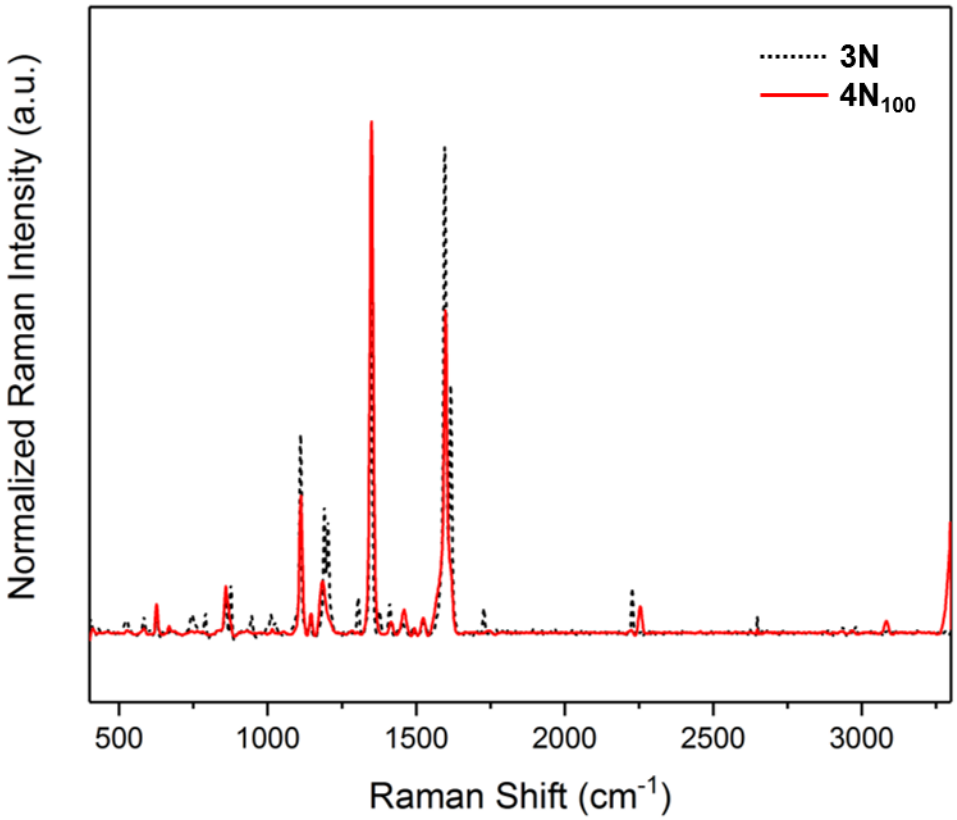

Figure S3.3. Raman spectra of **3N** and **4N$_{100}$**.

Table S3.1. Raman spectroscopic assignments for **3N**.

Wavenumber (cm^{-1})	Assignment[a]
2226	υC≡N
1724	υC=O
1615	υC=C
1594	υCC (ring)
1347	υNO_2 (sym.)
1109	υC-NO_2

[a] υCX: stretching

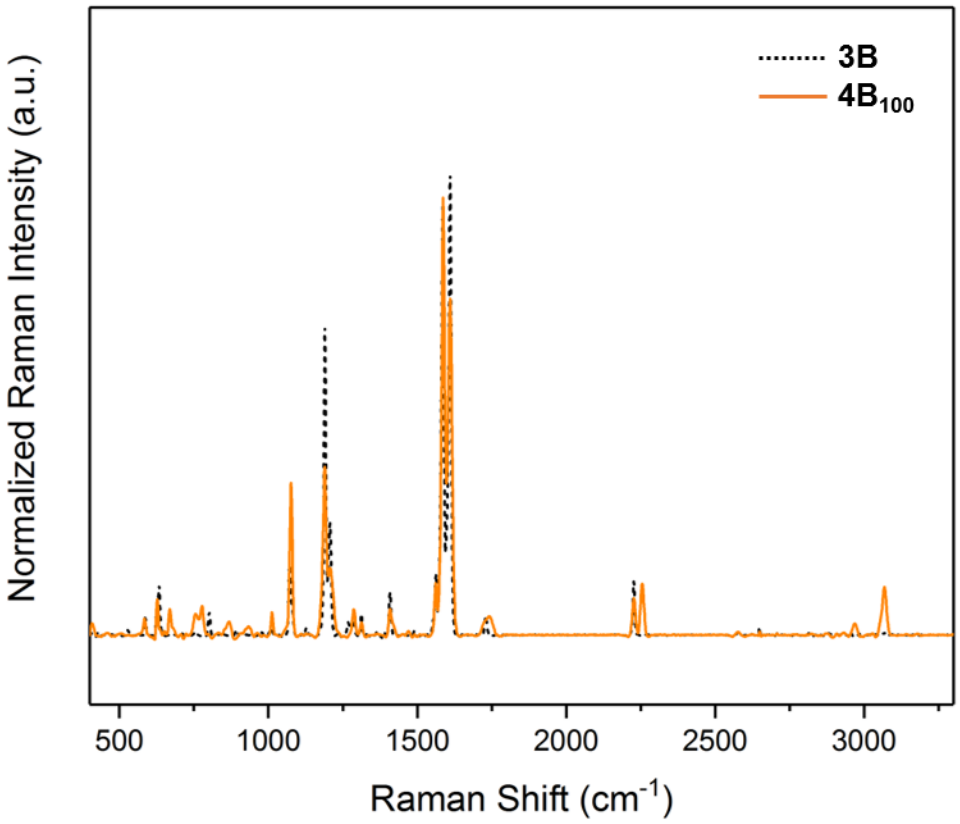

Figure S3.4. Raman spectra of **3B** and **4B$_{100}$**.

Table S3.2. Raman spectroscopic assignments for **3B**.

Wavenumber (cm^{-1})	Assignment[a]
2260/2226	υC≡N
1729	υC=O
1608	υC=C
1584	υCC (ring)
1070	υCC (ring) + υC-Br

[a] υCX: stretching

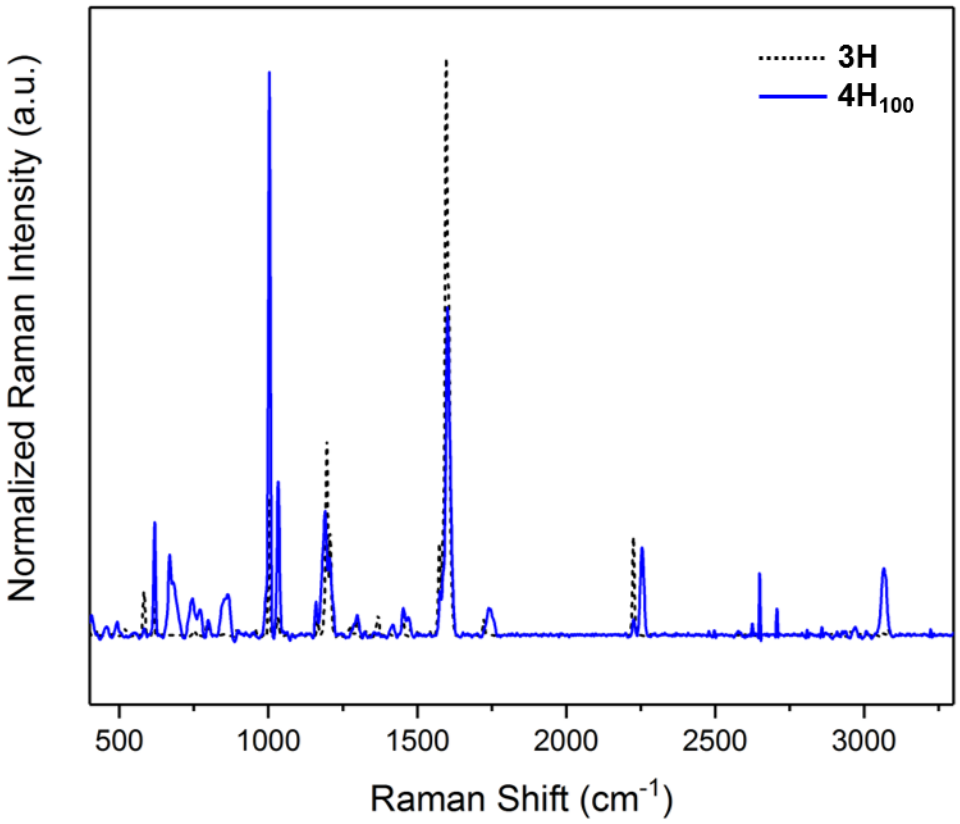

Figure S3.5. Raman spectra of **3H** and **4H$_{100}$**.

Table S3.3. Raman spectroscopic assignments for **3H**.

Wavenumber (cm^{-1})	Assignment[a]
2260/2226	υC≡N
1721	υC=O
1603	υC=C (shoulder)
1595	υCC (ring)
1000	αCC

[a] υCX: stretching, αCC: in-plane ring bending

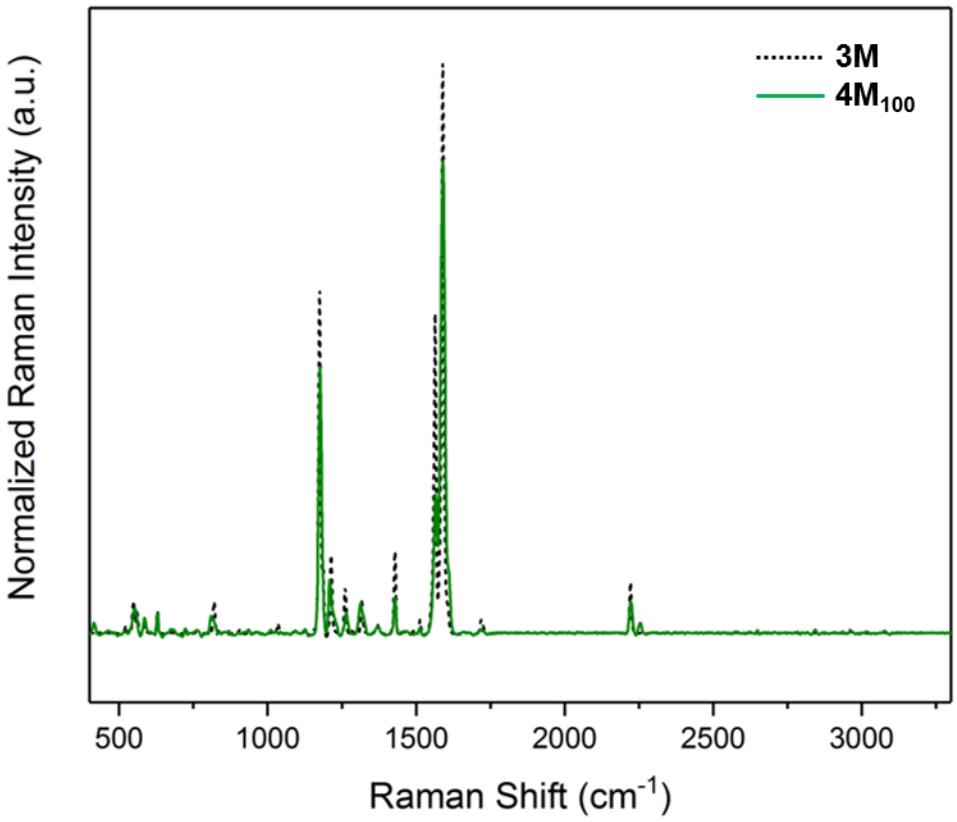

Figure S3.6. Raman spectra of **3M** and **4M$_{100}$**.

Table S3.4. Raman spectroscopic assignments for **3M**.

Wavenumber (cm^{-1})	Assignment[a]
2260/2226	υC≡N
1718	υC=O
1587	υC=C
1562	υCC (ring)

[a] υCX: stretching

3.6 References

(1) Kloxin, C. J.; Bowman, C. N. Covalent Adaptable Networks: Smart, Reconfigurable and Responsive Network Systems. *Chem. Soc. Rev.* **2013**, *42* (17), 7161–7173.

(2) Bowman, C. N.; Kloxin, C. J. Covalent Adaptable Networks: Reversible Bond Structures Incorporated in Polymer Networks. *Angew. Chemie Int. Ed.* **2012**, *51* (18), 4272–4274.

(3) J. Kloxin, C.; F. Scott, T.; J. Adzima, B.; N. Bowman, C. Covalent Adaptable Networks (CANs): A Unique Paradigm in Cross-Linked Polymers. *Macromolecules* **2010**, *43* (6), 2643–2653.

(4) Rowan, S. J.; Cantrill, S. J.; Cousins, G. R. L.; Sanders, J. K. M.; Stoddart, J. F. Dynamic Covalent Chemistry. *Angew. Chemie Int. Ed.* **2002**, *41* (6), 898–952..

(5) Jin, Y.; Yu, C.; Denman, R. J.; Zhang, W. Recent Advances in Dynamic Covalent Chemistry. *Chem. Soc. Rev.* **2013**, *42* (16), 6634–6654.

(6) Montarnal, D.; Capelot, M.; Tournilhac, F.; Leibler, L. Silica-Like Malleable Materials from Permanent Organic Networks. *Science* **2011**, *334* (6058), 965 – 968.

(7) Zhang, H.; Cai, C.; Liu, W.; Li, D.; Zhang, J.; Zhao, N.; Xu, J. Recyclable Polydimethylsiloxane Network Crosslinked by Dynamic Transesterification Reaction. *Sci. Rep.* **2017**, *7* (1), 11833.

(8) Reutenauer, P.; Buhler, E.; Boul, P. J.; Candau, S. J.; Lehn, J.-M. Room Temperature Dynamic Polymers Based on Diels–Alder Chemistry. *Chem. Eur. J.* **2009**, *15* (8), 1893–1900.

(9) M. Imbesi, P.; Fidge, C.; E. Raymond, J.; I. Cauët, S.; L. Wooley, K. Model Diels–Alder Studies for the Creation of Amphiphilic Cross-Linked Networks as Healable, Antibiofouling Coatings. *ACS Macro Lett.* **2012**, *1* (4), 473–477.

(10) J. Adzima, B.; Alan Aguirre, H.; J. Kloxin, C.; F. Scott, T.; N. Bowman, C. Rheological and Chemical Analysis of Reverse Gelation in a Covalently Cross-Linked Diels−Alder Polymer Network. *Macromolecules* **2008**, *41* (23), 9112–9117.

(11) Oehlenschlaeger, K. K.; Mueller, J. O.; Brandt, J.; Hilf, S.; Lederer, A.; Wilhelm, M.; Graf, R.; Coote, M. L.; Schmidt, F. G.; Barner-Kowollik, C. Adaptable Hetero Diels–Alder Networks for Fast Self-Healing under Mild Conditions. *Adv. Mater.* **2014**, *26* (21), 3561–3566.

(12) T. Michal, B.; J. Spencer, E.; J. Rowan, S. Stimuli-Responsive Reversible Two-Level Adhesion from a Structurally Dynamic Shape-Memory Polymer. *ACS Appl. Mater. & Interfaces* **2016**, *8* (17), 11041–11049.

(13) T. Michal, B.; A. Jaye, C.; J. Spencer, E.; J. Rowan, S. Inherently Photohealable and Thermal Shape-Memory Polydisulfide Networks. *ACS Macro Lett.* **2013**, *2* (8), 694–699.

(14) Canadell, J.; Goossens, H.; Klumperman, B. Self-Healing Materials Based on Disulfide Links. *Macromolecules* **2011**, *44* (8), 2536–2541.

(15) J. Cash, J.; Kubo, T.; P. Bapat, A.; S. Sumerlin, B. Room-Temperature Self-Healing Polymers Based on Dynamic-Covalent Boronic Esters. *Macromolecules* **2015**, *48* (7), 2098–2106.

(16) P. Bapat, A.; Roy, D.; G. Ray, J.; A. Savin, D.; S. Sumerlin, B. Dynamic-Covalent Macromolecular Stars with Boronic Ester Linkages. *J. Am. Chem. Soc.* **2011**, *133* (49), 19832–19838.

(17) R. Cromwell, O.; Chung, J.; Guan, Z. Malleable and Self-Healing Covalent Polymer Networks through Tunable Dynamic Boronic Ester Bonds. *J. Am. Chem. Soc.* **2015**, *137* (20), 6492–6495.

(18) Chakma, P.; Konkolewicz, D. Dynamic Covalent Bonds in Polymeric Materials. *Angew. Chemie Int. Ed.* **2019**, *0* (0).

(19) P. Nair, D.; Podgórski, M.; Chatani, S.; Gong, T.; Xi, W.; R. Fenoli, C.; N. Bowman, C. The Thiol-Michael Addition Click Reaction: A Powerful and Widely Used Tool in Materials Chemistry. *Chem. Mater.* **2013**, *26* (1), 724–744.

(20) Zhang, B.; A. Digby, Z.; A. Flum, J.; Chakma, P.; M. Saul, J.; L. Sparks, J.; Konkolewicz, D. Dynamic Thiol–Michael Chemistry for Thermoresponsive Rehealable and Malleable Networks. *Macromolecules* **2016**, *49* (18), 6871–6878.

(21) Chakma, P.; Rodrigues Possarle, L. H.; Digby, Z. A.; Zhang, B.; Sparks, J. L.; Konkolewicz, D. Dual Stimuli Responsive Self-Healing and Malleable Materials Based on Dynamic Thiol-Michael Chemistry. *Polym. Chem.* **2017**, *8* (42), 6534–6543.

(22) A. Ishibashi, J. S.; A. Kalow, J. Vitrimeric Silicone Elastomers Enabled by Dynamic Meldrum's Acid-Derived Cross-Links. *ACS Macro Lett.* **2018**, *7* (4), 482–486.

(23) Kuhl, N.; Geitner, R.; Bose, R. K.; Bode, S.; Dietzek, B.; Schmitt, M.; Popp, J.; Garcia, S. J.; van der Zwaag, S.; Schubert, U. S.; et al. Self-Healing Polymer Networks Based on

Reversible Michael Addition Reactions. *Macromol. Chem. Phys.* **2016**, *217* (22), 2541–2550.

(24) Kuhl, N.; Geitner, R.; Vitz, J.; Bode, S.; Schmitt, M.; Popp, J.; Schubert, U. S.; Hager, M. D. Increased Stability in Self-Healing Polymer Networks Based on Reversible Michael Addition Reactions. *J. Appl. Polym. Sci.* **2017**, *134* (19).

(25) Serafimova, I. M.; Pufall, M. A.; Krishnan, S.; Duda, K.; Cohen, M. S.; Maglathlin, R. L.; McFarland, J. M.; Miller, R. M.; Frödin, M.; Taunton, J. Reversible Targeting of Noncatalytic Cysteines with Chemically Tuned Electrophiles. *Nat. Chem. Biol.* **2012**, *8*, 471.

(26) Zhong, Y.; Xu, Y.; Anslyn, E. V. Studies of Reversible Conjugate Additions. *European J. Org. Chem.* **2013**, *2013* (23), 5017–5021.

(27) H. Krenske, E.; C. Petter, R.; N. Houk, K. Kinetics and Thermodynamics of Reversible Thiol Additions to Mono- and Diactivated Michael Acceptors: Implications for the Design of Drugs That Bind Covalently to Cysteines. *J. Org. Chem.* **2016**, *81* (23), 11726–11733.

(28) Long, D. A. Infrared and Raman Characteristic Group Frequencies. Tables and Charts George Socrates John Wiley and Sons, Ltd, Chichester, Third Edition, 2001. Price £135. *J. Raman Spectrosc.* **2004**, *35* (10), 905.

(29) Williams, R. J. J.; Rozenberg, B. A.; Pascault, J.-P. Reaction-Induced Phase Separation in Modified Thermosetting Polymers BT - Polymer Analysis Polymer Physics; Springer Berlin Heidelberg: Berlin, Heidelberg, 1997; pp 95–156.

(30) Yamanaka, K.; Takagi, Y.; Inoue, T. Reaction-Induced Phase Separation in Rubber-Modified Epoxy Resins. *Polymer* **1989**, *30* (10), 1839–1844.

(31) Liu, Y. Polymerization-Induced Phase Separation and Resulting Thermomechanical Properties of Thermosetting/Reactive Nonlinear Polymer Blends: A Review. *J. Appl. Polym. Sci.* **2013**, *127* (5), 3279–3292.

(32) Torbati, A. H.; Nejad, H. B.; Ponce, M.; Sutton, J. P.; Mather, P. T. Properties of Triple Shape Memory Composites Prepared via Polymerization-Induced Phase Separation. *Soft Matter* **2014**, *10* (17), 3112–3121.

(33) Sassi, T. P.; Gupta, R. B. Dimeric Cyanoacrylate Compounds as Red-Shifted UV Absorbers. WO 2010/056452 A2, 2009.

4 Rheological investigation of dynamic, phase-separated thia-Michael networks

4.1 Introduction

In dynamic covalent or supramolecular networks, the thermodynamic stability and kinetic lability of the reversible/dynamic bond is often tied to the material's responsive and adaptive properties, which can include shape memory characteristics, healing properties, and reprocessability.[1,2] In a conceptual network where the connectivity and mechanical robustness of the material is controlled primarily by a dynamic bond (as opposed to crystallinity, phase separation or entanglement, for example), the overall relaxation of the system can be directly linked to the dissociation rate (k_d) of the reversible reaction. This relationship between bond kinetics and bulk material properties provides a useful means by which to tune the functionality and mechanical robustness of a polymeric system through hierarchical design. For instance, Craig, *et al*, used a metal-ligand coordination motif to demonstrate that "strong means slow" or, in other words, that a slow kinetic exchange between transient crosslinks in polymer gel results in more mechanically robust materials.[3] In a later publication, the same group showed that the rheological properties of the same gel system could be scaled based on the dissociation rate of the dynamic metal-ligand bond, revealing the direct effect on the kinetics of bond dissociation on the rheological profiles of the dynamic polymer networks.[4] By simply modifying the kinetic properties of the coordination complex, the overall mechanical performance of the gels could be drastically altered.

Since this pioneering work by Craig, *et al*, other studies have also been conducted to further investigate the relationship between dynamic bond kinetics and material properties in systems

based on supramolecular motifs or dynamic covalent bonds.[5–8] For example, Guan, *et al*, explored the differences in mechanical behavior within dynamic boronic ester-based polymeric networks.[9] By modifying the *ortho*-substituent on diphenylboronic acid, they were able to tune the exchange rate of the boronic ester exchange reaction. By implementing this motif into a polymeric network, the study demonstrated that the "fast" exchanging reaction contributed to more efficient malleability and healing behavior in the final material. The boronic ester transesterification was later used by Anderson, *et al*, to tune the mechanical response of hydrogels.[10] By combining a "fast" and "slow" boronic acid in a transesterification network at variable molar ratios, the relaxation rates of the hydrogels could be systematically adjusted. Zhang, *et al*, also noted variable relaxation behavior in dynamic polyurethane networks. By increasing the steric hindrance of the substituent associated with the dynamic bond and thereby weakening the dynamic bond, the networks (at a similar crosslinked density) exhibited increased stress relaxation rates.[11]

The aforementioned studies draw connections between the kinetics of bond formation/breaking and the rheological relaxation behavior of a dynamic network, however, oftentimes it is difficult to decouple the kinetic lability of the bond influence from other considerations. For example, it is common for more labile bonds to also have a smaller thermodynamic driving force for formation and as such a common conundrum in dynamic networks is that more labile bonds will also result in networks with decreasing crosslink density: does the loss of crosslink density afford greater chain mobility and therefore faster relaxation times or is the larger bond dissociation rate mainly responsible for the network relaxation? Other, equally complex phenomena to account for include the effect of bond reassociation after breaking ("sticky" Rouse behavior)[12–15], increased relaxation rate of segmental clusters (Semenov/Rubinstein

model)[16,17], and the effect of phase separation in dynamic networks, which to the best of our knowledge, has yet to be studied in detail.

Thus far, the studies detailed in Chapters 2 and 3 have revealed an ability to tailor the thermodynamic equilibrium of the thia-Michael reaction by altering the *para*-substituent on a benzalcyanoacetate-based Michael acceptor. This resulted in control of thermomechanical (plateau modulus, glass transition, etc.) and morphological aspects of the resulting networks. Previous studies by other groups suggest that the kinetics of the reversible thia-Michael reactions are also reliant on the nature of the acceptor's substituents. According to work by Houk, *et al.*, that details the computational kinetics and thermodynamics of the reversible thia-Michael reaction, changes to the electronic nature of the Michael acceptor (i.e. presence of electron-donating and/or electron-withdrawing groups) not only shifts the thermodynamic equilibrium, but also significantly affects the kinetics of the reaction.[18] As an example, the addition of an electron-withdrawing nitrile group to the α-position (as shown in Scheme 4.1) stabilized the reaction intermediate by 21 kcal/mol as opposed to an unsubstituted acceptor. This stable intermediate facilitates both the forward and reverse reactions by significantly lowering the activation energies for both processes. The substituent effect was also observed by Taunton, *et al*, and Anslyn, *et al.*, during their experimental evaluations of the reversible thia-Michael reaction in small molecules.[19,20] While these *in silico* and solution-state studies initially exposed the intriguing behavior of the benzalcyanoacetate-based thia-Michael addition, the question remained as to how this tunable equilibrium would manifest in a bulk polymeric material. Furthermore, the observation of phase separation within the thia-Michael networks creates an intriguing opportunity to evaluate the rheological properties of dynamic networks whose reversible bonds exist in multiple phase environments. With this in mind, we employed rheological methods to probe how the electronic nature of the Michael acceptor and

the resulting phase separated morphology affects the relaxation behavior of the dynamic thia-Michael networks.

4.2 Results and Discussion

The benzalcyanoacetate-based thia-Michael reaction is the catalyst-free reversible formation of a thia-Michael adduct from the addition of a thiol to a benzalcyanoacetate acceptor as shown in Scheme 4.1.

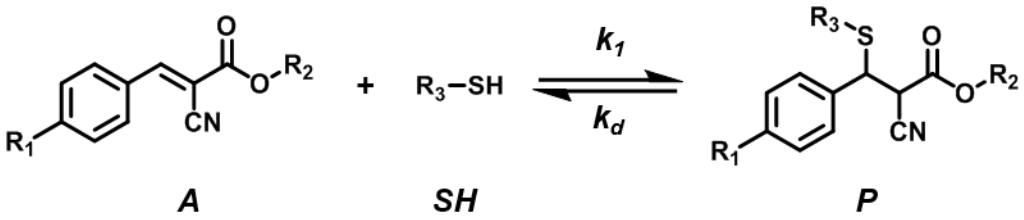

Scheme 4.1. Chemical structure of reversible thia-Michael reaction based on benzalcyanoacetate acceptor.

The overall reaction is governed by the rate laws

$$\frac{d[A]}{dt} = -k_1[A][SH] + k_d[P] \tag{4.1}$$

$$\frac{d[P]}{dt} = k_1[A][SH] - k_d[P] \tag{4.2}$$

where [*A*], [*SH*], and [*P*] are the concentrations of the Michael acceptor, thiol, and adduct (or product), respectively. The formation of the adduct proceeds at a rate denoted by k_1 while the

reverse reaction rate, the dissociation rate, is denoted by k_d. At equilibrium, equations 4.1 and 4.2 are equivalent and equal to zero, therefore the equilibrium constant (K_{eq}) for the reaction can be written as

$$K_{eq} = \frac{[P]}{[A][SH]} = \frac{k_1}{k_d} \tag{4.3}$$

In a dynamic thia-Michael network, the dynamic bonds formed within a film is proportional to the equilibrium constant. The rate at which these bonds are formed is dictated by k_1 whereas the rate at which the bonds disengage is controlled by k_d.

Chapter 2 demonstrated the dependence of K_{eq} on the electron-withdrawing or electron-donating abilities of the R_1 group on the Michael acceptor with K_{eq} of R = -OCH_3 < -H < -Br < -NO_2, varying from 9 M^{-1} to 470 M^{-1} in deuterated dimethyl sulfoxide (d_6-DMSO). Chapter 3 applied this concept in reversible thia-Michael networks, revealing an ability to tune the mechanical, functional, and morphological properties by varying the acceptor substituent. In order to probe the substituent effect on the relaxation behavior of the network, the same series of triethylene glycol (TEG) bisbenzalcyanoacetate compounds containing (from most electron-withdrawing to electron-donating) a nitro-substituted (**3N**), bromo-substituted, (**3B**), unsubstituted (**3H**), and methoxy-substituted (**3M**) bisbenzalcyanoacetate (Figure 4.1) was prepared using previously described synthetic methods (See Chapter 3 for full details). Networks based on the thia-Michael reaction were assembled targeting a 1:1 ratio of thiol:double bond, by combining one molar equivalent of PTMP (300 mg/mL in chloroforom) with two molar equivalents of **3** (150 mg/mL in chloroform) and stirring for two hours at 50 °C. After two hours, the solutions were cast onto a Teflon® dish and dried at room temperature for ca. 18 hours. The films were further dried

under vacuum at 60 °C for 24 hours then heated to 150 °C for 30 minutes to remove any remaining solvent residue. Dried films were compression molded at 90 °C for 10 minutes using a stainless-steel spacer to control thickness (400 µm – 600 µm).

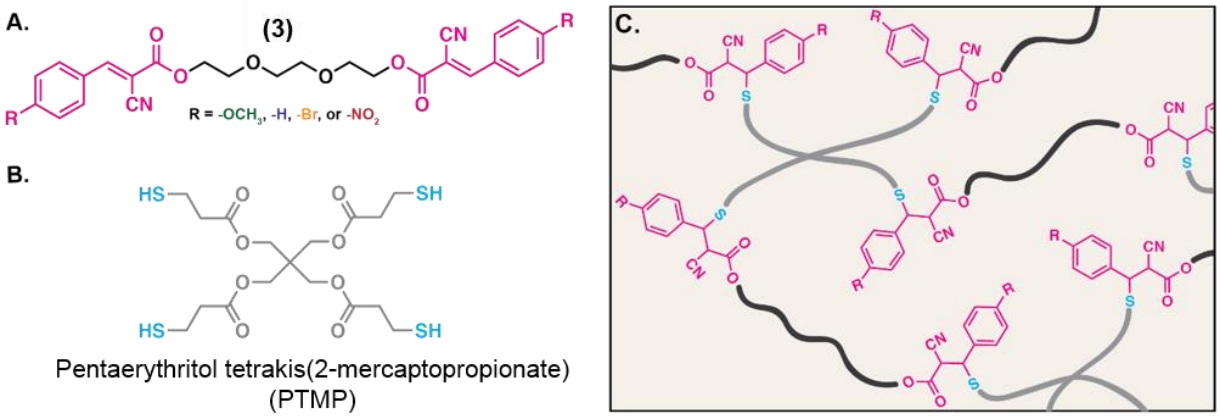

Figure 4.1. Chemical structures of A) ditopic electrophiles and B) tetrathiol crosslinker, PTMP. C) Illustration depicting the network formation of electrophiles crosslinked with PTMP.

The networks are denoted **4M$_x$, 4B$_x$, 4H$_x$,** or **4N$_x$** to indicate the incorporation of **3M**, **3B**, **3H**, and **3N**, respectively, as well as the mole percent (x mol%) of each acceptor relative to the amount of thiol groups added to the network. Films that utilize more than one TEG-bisbenzalcyanoacetate are named in a similar fashion. For example, **4N$_{100}$** only incorporates **3N** which accounts for 100 mol% of the reactive alkenes, whereas **4N$_{50}$H$_{50}$** contains **3N** and **3H**, each accounting for 50 mol% of the total acceptor sites.

Before addressing the relaxation behavior of the dynamic networks, it is important to revisit the thermomechanical properties of the films discussed in the previous chapter (see Chapter 3 for

full details). Key observations (as they pertain to this current study) include: 1) the presence of two glass transition temperatures (T_gs) in each film, 2) the tunable nature of the T_gs and rubbery plateau based on selection of ditopic acceptor, and 3) the manifestation of a phase separated morphology for all films. Figure 4.2 summarizes these findings.

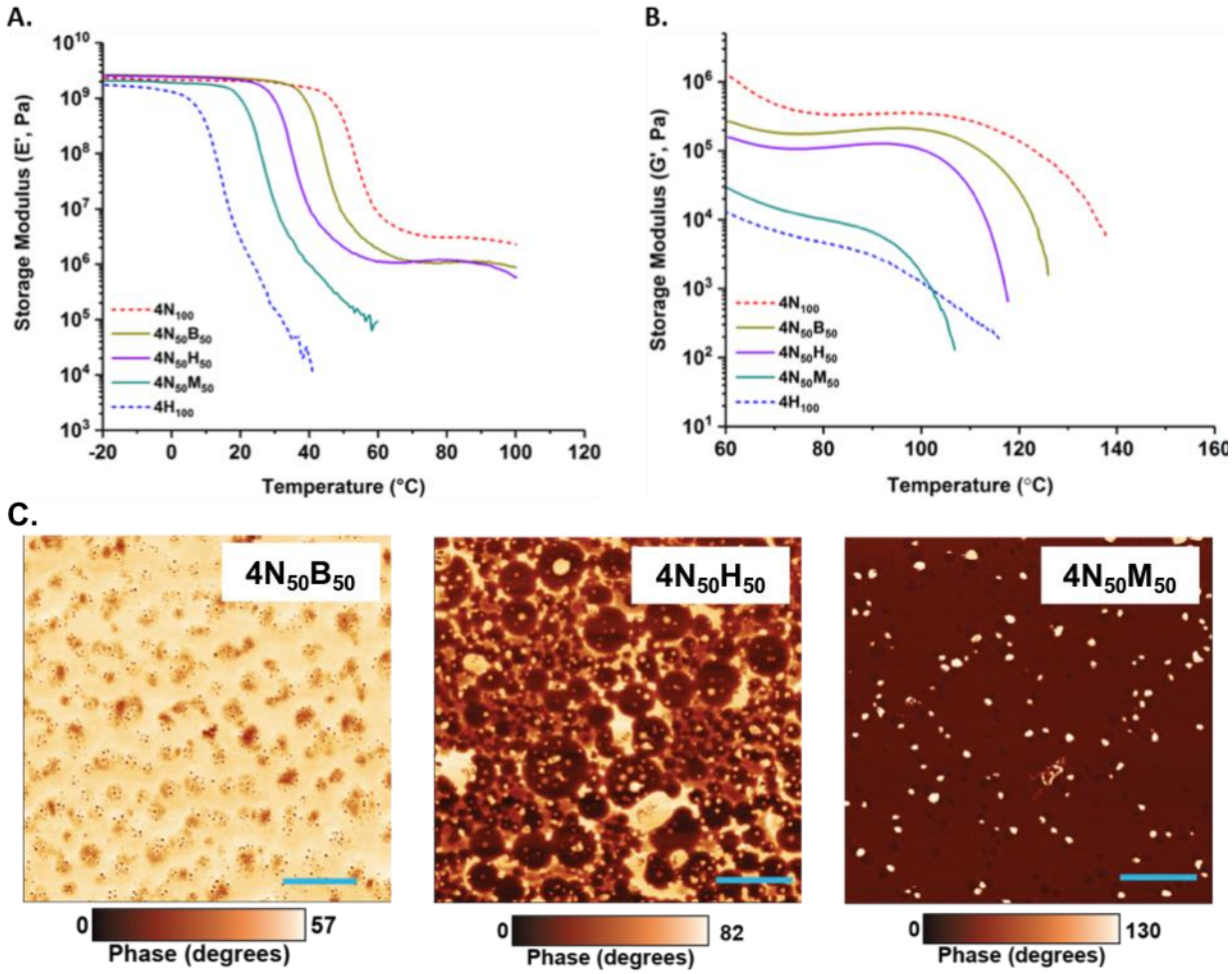

Figure 4.2. A) Dynamic mechanical analysis (DMA) and B) shear rheology results for **4H$_{100}$** (dashed blue), **4N$_{50}$M$_{50}$** (orange), **4N$_{50}$H$_{50}$** (violet), **4N$_{50}$B$_{50}$** (yellow), and **4N$_{100}$** (dashed red). C) AFM phase images for (left to right) **4N$_{50}$B$_{50}$**, **4N$_{50}$H$_{50}$**, and **4N$_{50}$M$_{50}$** (scale bar = 1 μm).

To evaluate the relaxation behavior of the thia-Michael networks, experiments were focused on two rheological regimes: the rubbery plateau and terminal relaxation. The relaxation processes on the rubbery plateau were probed using stress relaxation experiments conducted using shear rheology (Figure 4.3). By applying a small strain to the material and monitoring its stress response over time, it is possible to observe the relaxation of internal stresses within the material. While typical thermosets lack the ability to relax on these short time scales, dynamic bonds enable the release of stresses caused by application of strain through the exchange of reversible bonds. This technique facilitates the evaluation of the relaxation behavior of the films at temperatures on the rubbery plateau where the storage modulus of the film remains constant, but bond exchange in the soft segment is accessible as the system is above its lower T_g. For these experiments, a 0.1% strain was applied to a sample and the relaxation of internal stress was monitored over the course of 10 minutes (Figure 4.3). This procedure was repeated at multiple temperatures to establish a trend in the relaxation time with respect to temperature. In accordance with Maxwellian behavior, the characteristic relaxation time (τ) was reported as the time at which the storage modulus relaxed to 37% (G'/G_0 = 1/e) of its maximum modulus immediately following the instantaneous strain (marked by the dashed grey line in Figure 4.6).

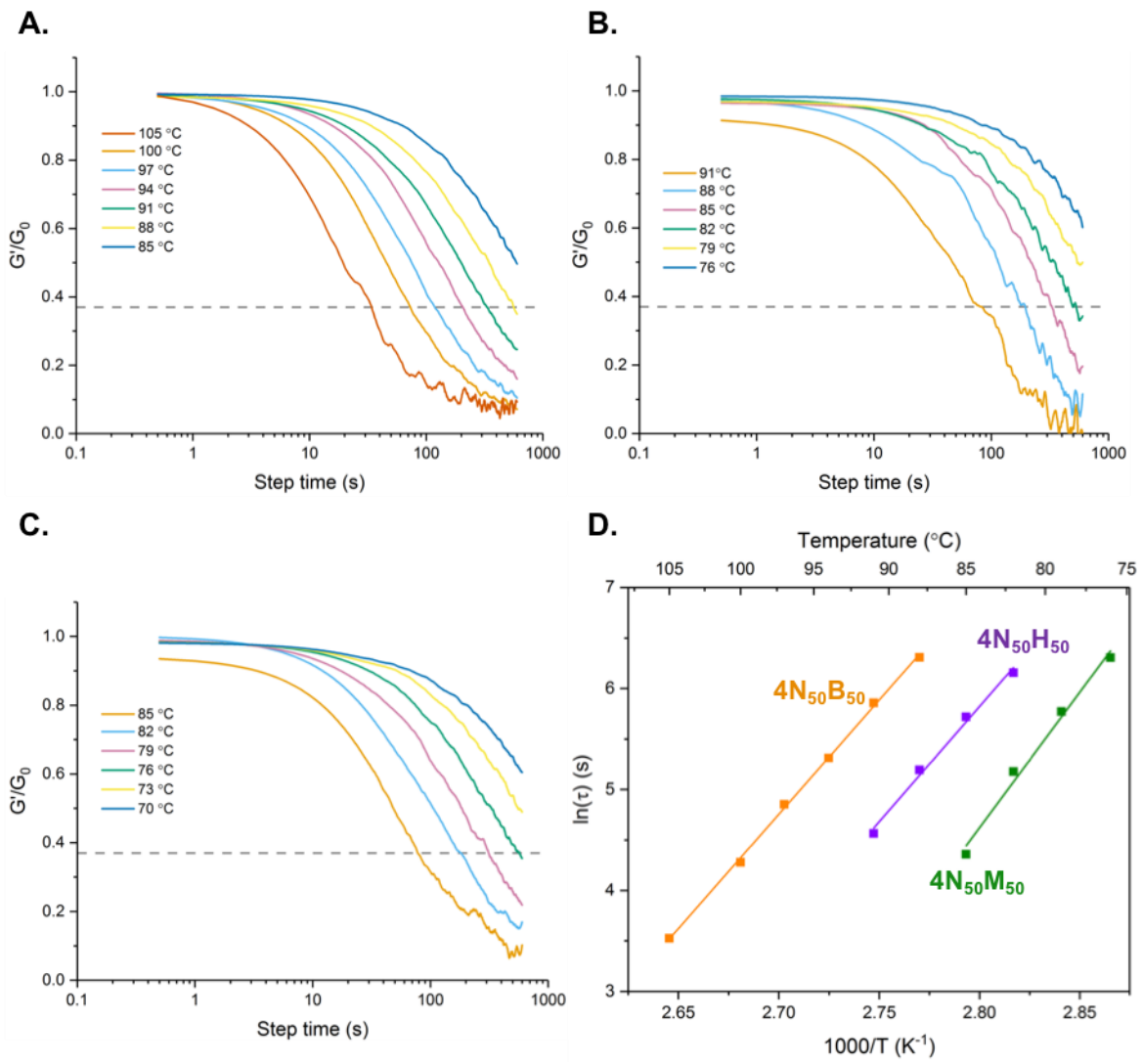

Figure 4.3. Stress relaxation curves of A) **4N$_{50}$B$_{50}$**, B) **4N$_{50}$H$_{50}$**, and C) **4N$_{50}$M$_{50}$** at increasing temperatures with 37% (1/e) total relaxation highlighted (grey line). D) Plots showing natural logarithm of characteristic relaxation time versus inverse temperature and demonstrating Arrhenius behavior as shown by linear fit of data. (0.1% strain applied, test duration = 10 minutes)

The characteristic relaxation times determined by the stress relaxation studies were plotted versus inverse temperature to evaluate their fit to Arrhenius law (Figure 4.3D). In dynamic

polymeric systems, the relaxation behavior of the network can be related to activation energy required for the relaxation mechanism to occur by

$$\tau_c = \tau_0 \exp(E_a/RT) \tag{4.4}$$

where τ_c is the characteristic relaxation time, τ_0 is the relaxation time at infinite temperature, E_a is the activation energy, R is the gas constant (8.413 $J \cdot mol^{-1} \cdot K^{-1}$), and T is temperature in kelvins. A plot of the natural logarithm of τ_c versus 1/T results in a linear regression fit with slope of E_a/R and y-intercept of τ_0. As shown in Figure 4.3D, the thia-Michael networks follow Arrhenius law at temperatures that correspond to their plateau modulus and indeed exhibit a clear linear trend. The overall activation energy of the materials (E_a) calculated from the slope of the Arrhenius plot and was found to be 190.5, 192.1, and 225.6 kJ/mol for the **4N$_{50}$B$_{50}$**, **4N$_{50}$H$_{50}$**, and **4N$_{50}$M$_{50}$** films, respectively. The relaxation times of the networks were shown to decrease with increasing temperature, with τ_c at a given temperature inversely associated with the K_{eq} of the hybrid films.

The fact that the films' relaxation exhibits Arrhenius behavior suggests that there is one dominant, temperature-dependent relaxation process occurring in these materials within this temperature range. Using linear van't Hoff relationships as a first approximation, K_{eq} values are predicted to reduce by roughly half at 100 °C (K_{eq} at 100 °C: **3N** = 136 M^{-1}, **3B** = 58 M^{-1}, **3H** = 26 M^{-1}, and **3M** = 6 M^{-1}), indicating that as the temperature increases, the dynamic bonds become increasingly labile within the soft phase limiting the contribution of the soft phase to the plateau modulus at elevated temperatures. Considering the low equilibrium constants for the dynamic thia-Michael bonds, the activation energy of relaxation is disproportionately high making it unlikely that the stress relaxation studies directly observe the thia-Michael bond exchange. One potential

source of the elevated observed activation energy is the presence of a phase separated internal structure. As observed in the AFM images of cast samples (Figure 4.2C), there is a variable amount of hard phase (light regions) within the hybrid films. Those with a higher percentage of hard phase (e.g. **4N$_{50}$B$_{50}$**) exhibit a higher plateau modulus and higher 2nd T_g than thia-Michael films with less hard phase (e.g. **4N$_{50}$M$_{50}$**). The presence of a hard phase creates an energy barrier for the relaxation process and therefore would require a higher energy of activation than a non-phase separated system relaxing solely on the basis of dynamic bonds.

To explore the impact of phase separation further, studies were conducted to investigate the relaxation behavior of the films approaching the terminal flow regime. Using small amplitude oscillatory shear rheology, each thia-Michael network was subject to frequency sweeps (0.01 rad/s – 100 rad/s) at discrete temperatures approaching the terminal flow regime of the dynamic networks. The temperatures at which flow is observed coincide closely with the second glass transition observed for the thia-Michael networks (2nd T_g onset temperatures by DSC as reported in Chapter 3: **4N$_{100}$** = 133 °C, **4N$_{50}$B$_{50}$** = 135 °C, **4N$_{50}$H$_{50}$** = 109 °C, and **4N$_{50}$M$_{50}$** = 110 °C). Figure 4.4 shows the results of these sweeps for all samples at four different temperatures. Each sample exhibits a plateau in the storage modulus at higher frequencies and a crossover of the storage and loss modulus (G' and G'', respectively) at lower frequencies consistent with the presence of a dynamic network.[24] With increasing temperature, the plateau modulus drops and the terminal peak of the loss modulus shifts to higher frequencies, resulting in the crossover frequency (ω_c) being observed at higher frequencies. The same trend is observed in all thia-Michael systems within this series, however, the temperature at which the frequency sweeps were conducted was kept sample dependent in order to maintain a linear viscoelastic testing regime on the rubbery plateau while simultaneously observing the crossover point.

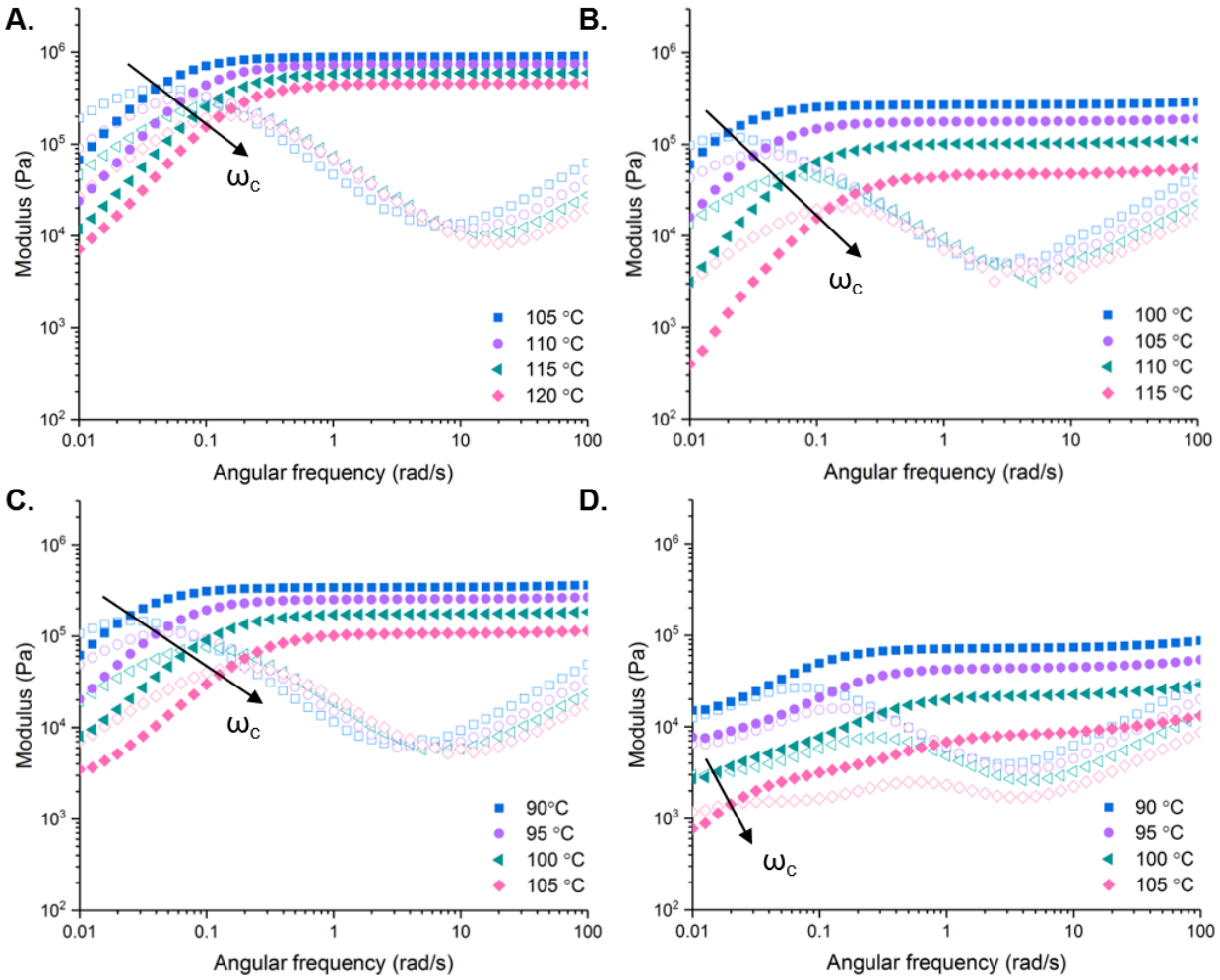

Figure 4.4. Oscillatory shear rheology frequency sweeps of A) **4N$_{100}$**, B) **4N$_{50}$B$_{50}$**, C) **4N$_{50}$H$_{50}$**, and D) **4N$_{50}$M$_{50}$** at increasing temperatures demonstrating crossover of *G'* (closed symbols) and *G"* (open symbols) at higher frequencies as temperature is increased.

Figure 4.5 shows the frequency curves for each sample at 105 °C fit to two different rheological models used to describe the relaxation behavior of the films. The standard Maxwell model (dashed lines in Figure 4.5) provides a reasonable first-estimation fit for some thia-Michael systems, however, the data deviates from the model in the terminal regime at low frequencies (a phenomenon that is exaggerated at higher temperatures). This suggests the presence of multiple processes being associated with the global terminal relaxation of the network as opposed to the

single relaxation process assumed by the Maxwell equation. This is especially apparent in the **4N$_{50}$M$_{50}$** sweeps where an intermediate peak in *G″* indicates another relaxation process not attributed to the Rouse relaxation or terminal behavior. In order to more accurately describe the complex relaxation behavior of the dynamic networks, the frequency data was fit using an infinite relaxation spectrum (solid lines in Figure 4.5).[24] The relaxation spectrum accounts for a continuous distribution of relaxation times brought on by infinite parallel Maxwell elements, rather than a discrete relaxation time associated with a single dashpot. This allows multiple relaxation modes to be considered.

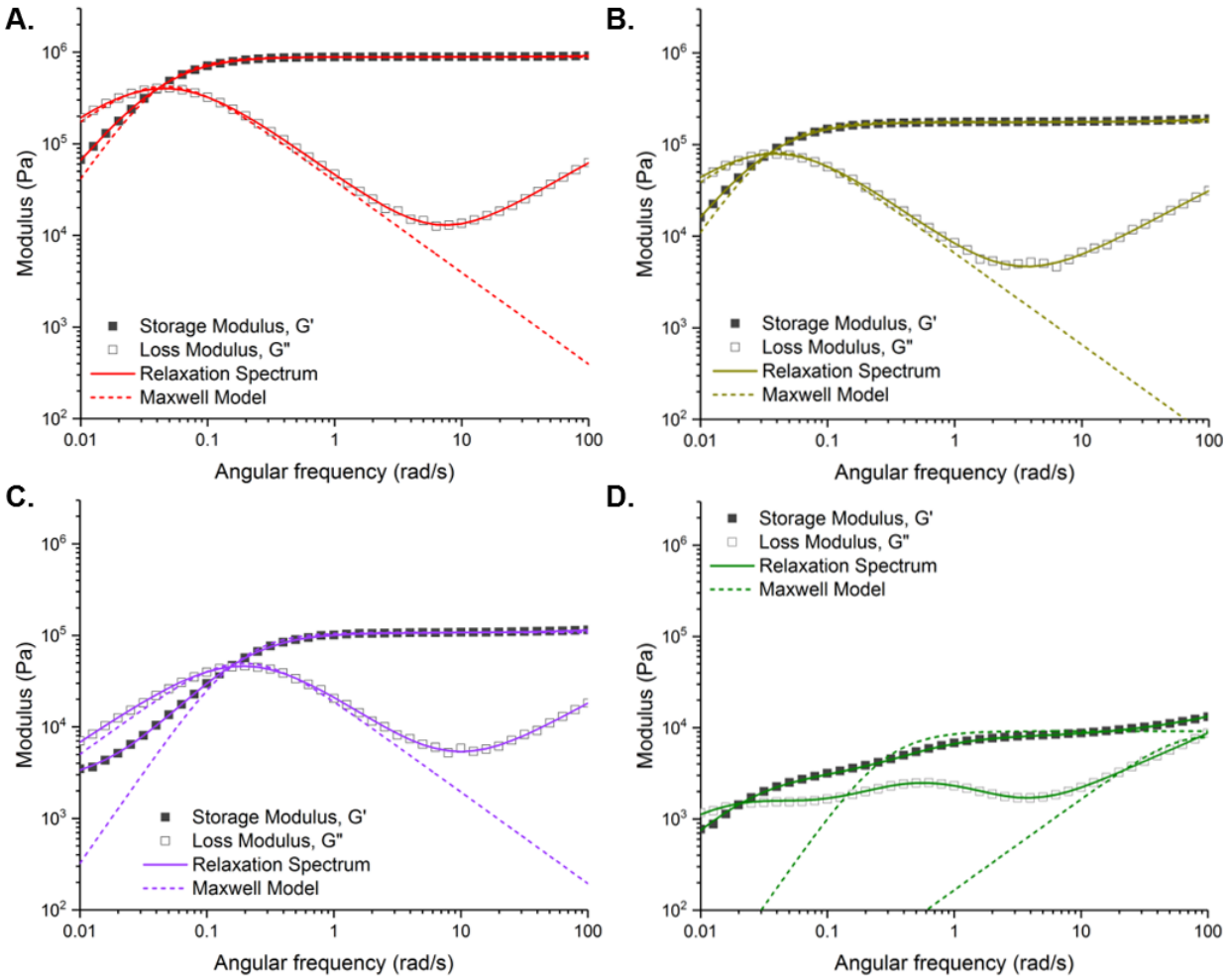

Figure 4.5. Frequency sweeps at a single temperature (105 °C) demonstrating the Maxwell model fit for A) **4N$_{100}$**, B) **4N$_{50}$B$_{50}$**, C) **4N$_{50}$H$_{50}$**, and D) **3N$_{50}$M$_{50}$**.

The same frequency data as described in Figure 4.4 was fit with the following equations using TA Instruments TRIOS software:

$$G'(\omega)=\int_{-\infty}^{\infty} H(\tau)\frac{\omega^2\tau^2}{1+\omega^2\tau^2}\,d\ln(\tau) \tag{4.6}$$

$$G''(\omega)=\int_{-\infty}^{\infty} H(\tau)\frac{\omega\tau}{1+\omega^2\tau^2}\,d\ln(\tau) \tag{4.7}$$

where ω is the measurement frequency (rad/s), τ is the relaxation time equivalent to $1/\omega$, and $H(\tau)$ is the continuous relaxation function (fitting curves for G' and G'' plotted as solid lines in Figure 4.5). Plotting the function of $H(\tau)$ versus τ, reveals the distribution of relaxation modes over the timescales covered in the experiment (Figure 4.6). Within a single distribution, the area under the $H(\tau)$ curve corresponds to the energy stored in the network (i.e. the storage modulus, G') while the height of the curve at a given time corresponds to the energy dissipated. The presence of peaks along the distribution curve indicate local maxima of the loss modulus, G''.

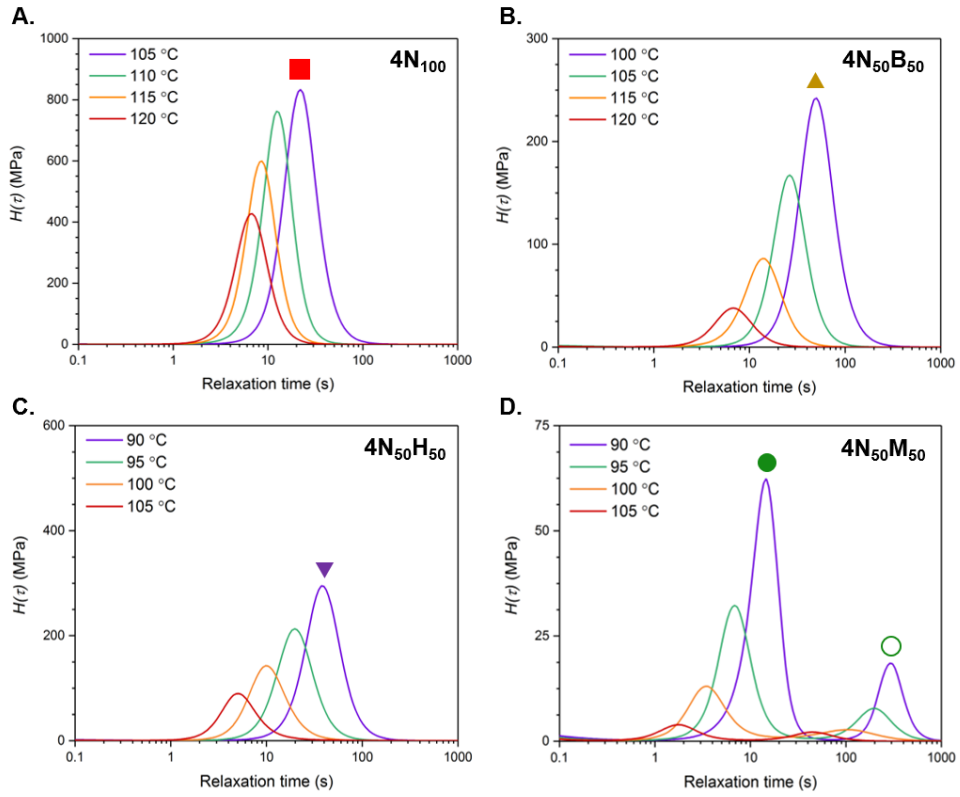

Figure 4.6. Relaxation spectrum for A) **4N$_{100}$**, B) **4N$_{50}$B$_{50}$**, C) **4N$_{50}$H$_{50}$**, and D) **4N$_{50}$M$_{50}$**. Symbols correspond to markers used in Arrhenius plot to indicate different timescales.

The relaxation spectra for the thia-Michael networks revealed a distribution of relaxation modes for all the samples in the terminal flow regime, with clear changes in the magnitude and location of the peaks as temperatures were increased. The differences in magnitude with elevated temperatures correspond to the decrease in the plateau modulus (as observed in the raw data shown in Figure 4.4) whereas the peaks shifting along the x-axis is associated with faster relaxation times. In other words, the higher the temperature, the faster the rate of the relaxation in the thia-Michael network, and the softer the overall material. Of particular note was the relaxation behavior of **4N$_{50}$M$_{50}$**. This hybrid system clearly demonstrated multiple relaxation modes – both fast and slow – indicating a complex combination of processes contributing to the overall relaxation of the network.

Once again, the relaxation results were plotted versus inverse temperature to evaluate their fit to Arrhenius law (Figure 4.7), substituting τ_c with the peak relaxation time (τ_{max}).

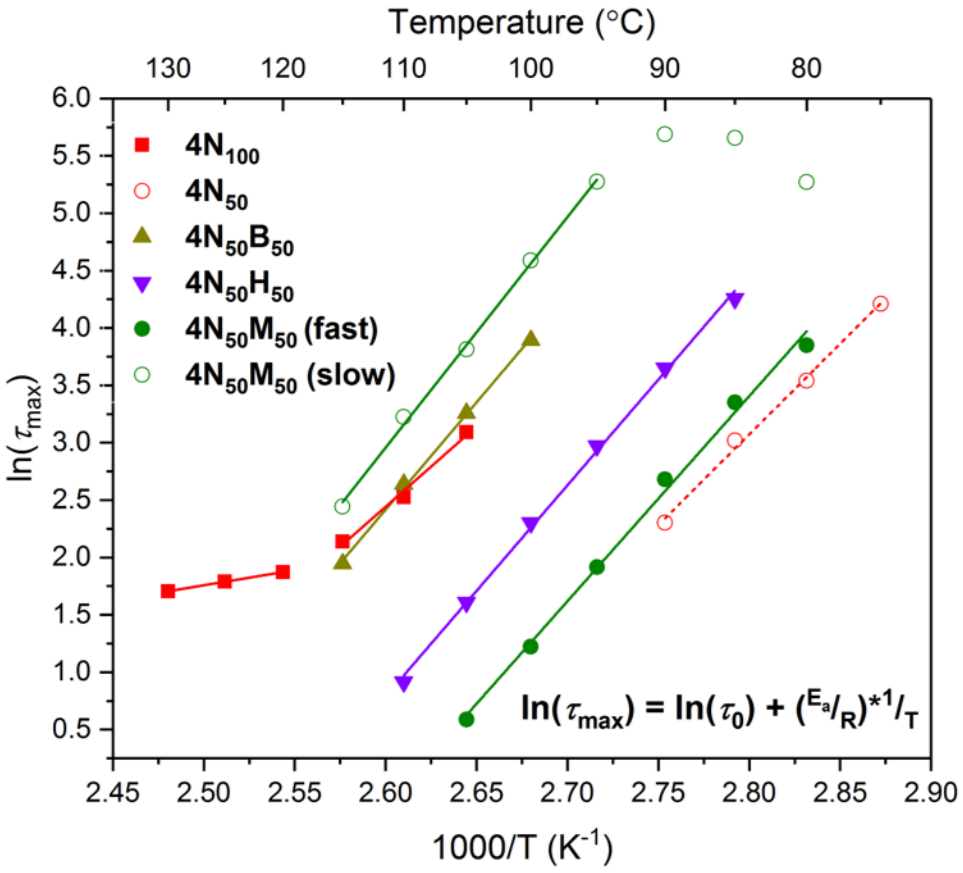

Figure 4.7. Arrhenius plots of τ_{max} for thia-Michael films. Symbols indicate experimental peak relaxation times (τ_{max}) derived from relaxation spectra at given temperatures; lines highlight linear fit to Arrhenius law (inset equation).

From this information, it is apparent that the terminal relaxation process for the thia-Michael networks is also Arrhenius in nature. Activation energies for these terminal relaxation processes derived from the slope of the linear fit (equation 3.9), were found to be 117.5, 157.3, and 154.9 kJ/mol for **4N$_{100}$**, **4N$_{50}$B$_{50}$**, and **4N$_{50}$H$_{50}$**, respectively. Since **4N$_{50}$M$_{50}$** exhibits both a "fast" and "slow" relaxation mechanism, the two were plotted separately in the Arrhenius plot. The "fast" relaxation which corresponds to the intermediate *G″* peak follows the trend of an increasingly fast relaxation time with lower K_{eq} compounds. Conversely, the "slow" relaxation

mechanism that corresponds with the *G'*/*G"* crossovers takes place at longer times than any of the other networks' terminal processes. The activation energies for these processes were 148.6 kJ/mol and 167.1 kJ/mol for fast and slow, respectively. It is interesting to observe the deviation from the initial Arrhenius law in the **4N$_{100}$** film beginning at 120 °C. Above 120 °C, the material maintains a linear relationship, but with a dramatically lower slope than the lower temperature regime. Calculating the activation energy from this high temperature data reveals E_a = 22.3 kJ/mol, much more realistic in describing the lifetime of the thia-Michael bond.

The persistently elevated activation energy throughout all the thia-Michael networks poses a compelling line of inquiry in the fundamental understanding of bulk reversible networks. It suggests that while the dynamic nature of the thia-Michael bonds may influence the relaxation behavior, it is not the primary source of stress relaxation in the films. Rather, it is more likely that the rheological properties of the films are dominated by the presence of the phase separated morphology. Although the precise mechanism of relaxation is not yet understood, several parallels can be drawn between these phase-separated dynamic networks and rheologically similar materials. Consider the mathematical models proposed by Rubinstein and Semenov[17,25,26] that detail the viscoelastic behavior of dynamic or associating polymers. According to Semenov-Rubinstein (SR) theory, dynamic networks assemble and disassemble on timescales that are reflective of a complex combination of intrinsic polymeric properties, rather than being solely dependent on the kinetics of the reversible reaction. The theory proposes that the relaxation behavior of "sticky" (i.e. reversible, dynamic) molecules can be attributed to the relaxation of "clusters" of these molecules in addition to the relaxation of the crosslinking bond (Figure 4.4A). The motion of the clusters through a network enables a secondary, diffusion-related relaxation

process to occur that often manifests with a higher activation energy than the typical bond dissociation.

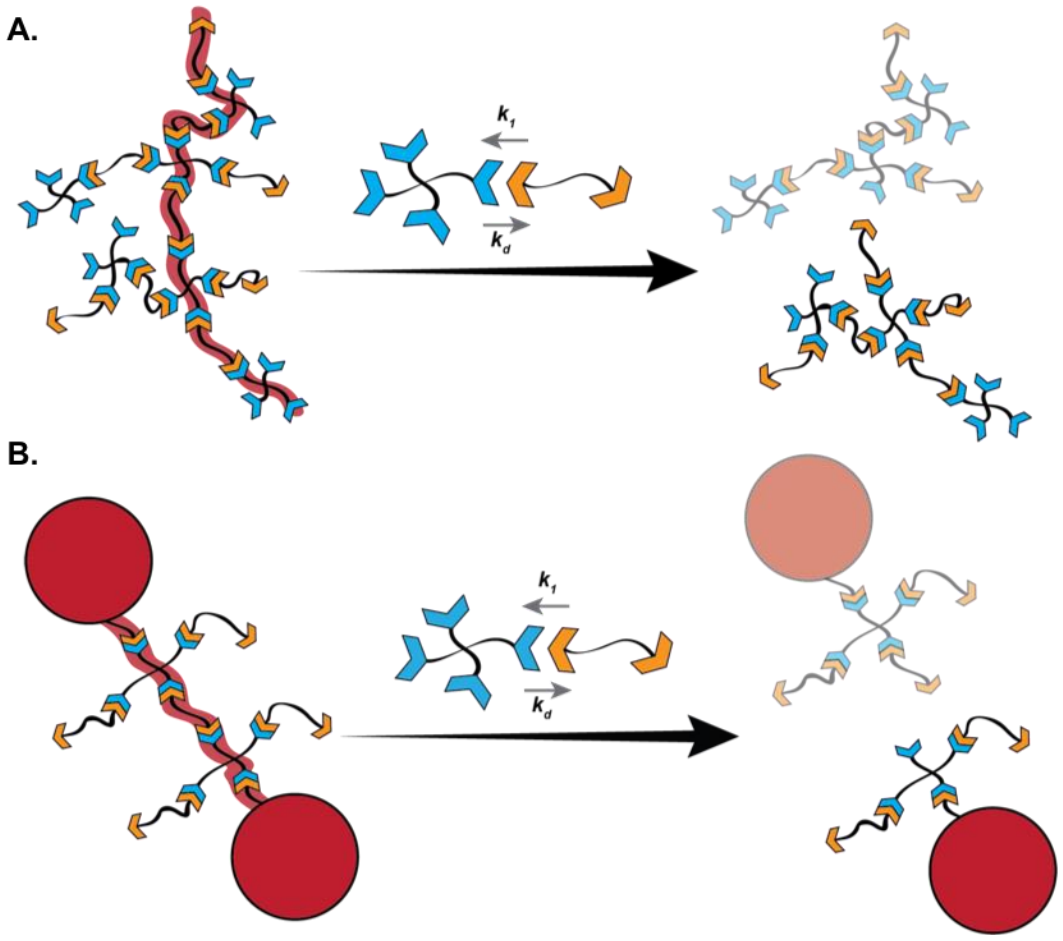

Figure 4.8. A) Illustration of Semenov-Rubinstein cluster formation. B) Illustration of the proposed relaxation mechanism in phase separated dynamic networks.

It is hypothesized that a similar effect is observed with dynamic phase separated systems, but on a larger scale. On the rubbery plateau, the high T_g hard phase acts as the proposed hyperbranched clusters that are released by the exchange and relaxation of dynamic bonds (Figure

4.4B). As with the molecular clusters, the relaxation of these phases is more responsive to temperature change and thereby exhibits a higher observed activation energy than would be expected from a dynamic bond.

As the temperatures approach the terminal flow regime, the observed activation energies are lower, although they are still higher than can be attributed to the dynamic bond. At these elevated temperatures, the hard phase begins to pass through its glass transition, contributing yet another potential relaxation mechanism. As the phase softens, the activation energy of relaxation deviates from the lower temperature Arrhenius behavior, decreasing the slope of the Arrhenius behavior and reflecting a lower activation energy for relaxation at the higher temperatures. Future studies will further elucidate the relaxation mechanisms behind these complex systems and grant a deeper understanding as to the bulk structure-property relationships of phase-separated, dynamic covalent networks.

4.3 Conclusions

From these studies, it is apparent that the morphology of dynamic, phase separated thia-Michael networks plays a key role in defining the rheological profile of the systems. By combining different acceptor compounds within the same thia-Michael network, it was possible to tailor the phase composition of the films, thereby tuning the relaxation behavior of the networks. The temperature dependent relaxation behavior of the networks followed Arrhenius law, however, the activation energies derived from Arrhenius were higher than expected for dynamic covalent networks based on the thia-Michael bond. The elevated activation energies pointed towards a complex rheological profile reflective of relaxation mechanisms beyond just the kinetics of the

dynamic bond. It was hypothesized that the observed activation energy results from a Semenov-Rubinstein type cluster relaxation of the hard phases.

4.4 Experimental Methods

Shear rheology sample loading

Rheology was performed using the TA Instruments RSA-G2 ARES with Forced Convection oven (20 °C – 500 °C) attached to an Air Chiller System (-120 °C – 20 °C) and running TA Trios Software in the Soft Matter Characterization Facility at the University of Chicago. An 8 mm stainless steel parallel plate was used for all tests.

Samples were cut from a larger film into 8 mm disks approximately 400-600 um thick. A sample was loaded onto an 8 mm stainless steel parallel plate geometry equipped with thermocouples that had been preheated to 90 °C and trimmed of any excess overlap. The loaded sample was heated to 150 °C using a forced convection oven and the gap was manually controlled to minimize normal force, yet retain contact with both plates. At 150 °C, the sample was a viscous liquid. After approximately 30 seconds at 150 °C, the sample was subject to 1.0 rad/s steady shear for 10 seconds to remove any inhomogeneity or bubbles. After 10 seconds, the shearing was halted and the axial position was adjusted to ensure the sample was flush with the edges of the 8 mm plate. Satisfied with the sample configuration, the temperature in the oven was cooled in 10 °C increments until 0.01 N axial force could be applied (if the temperature was too high, 0.01N axial force caused the sample to seep out of the geometry, creating erroneous conditions for testing). Once the sample was stable enough to be tested, an isoforce (0.01 N) temperature ramp of 3 °C/min was used to bring the sample to the lowest testing temperature. At the lowest temperature, the axial

force was set to automatically maintain 0.1 N (± 0.05 N) compressive force on the sample, ensuring good contact throughout the tests.

Small amplitude oscillatory shear frequency sweeps

The sample was equilibrated at testing temperature for 5 minutes before the experiment was started. After equilibration, a frequency sweep from 0.01 rad/s to 100.0 rad/s was done at 1.0% strain. Subsequent sweeps were conducted by increasing the temperature by 5 °C and re-equilibrating for 5 minutes before beginning the frequency experiment.

Shear stress relaxation

The sample was equilibrated at testing temperature for 5 minutes before the experiment was started. Following equilibration, an instantaneous 0.1% strain was applied to the sample and the relaxation of the modulus was monitored over the course of 10 minutes. This process was repeated for subsequent tests 2 °C intervals. Raw data was smoothed in OriginLab OriginPro software using the Savitzky-Golay smoothing method.

4.5 References

(1) Kloxin, C. J.; Bowman, C. N. Covalent Adaptable Networks: Smart, Reconfigurable and Responsive Network Systems. *Chem. Soc. Rev.* **2013**, *42* (17), 7161–7173.

(2) Wojtecki, R. J.; Meador, M. A.; Rowan, S. J. Using the Dynamic Bond to Access Macroscopically Responsive Structurally Dynamic Polymers. *Nat. Mater.* **2010**, *10* (1), 14–27.

(3) Yount, W. C.; Loveless, D. M.; Craig, S. L. Strong Means Slow: Dynamic Contributions to the Bulk Mechanical Properties of Supramolecular Networks. *Angew. Chemie Int. Ed.* **2005**, *44* (18), 2746–2748.

(4) Yount, W. C.; Loveless, D. M.; Craig, S. L. Small-Molecule Dynamics and Mechanisms Underlying the Macroscopic Mechanical Properties of Coordinatively Cross-Linked Polymer Networks. *J. Am. Chem. Soc.* **2005**, *127* (41), 14488–14496.

(5) J. Adzima, B.; Alan Aguirre, H.; J. Kloxin, C.; F. Scott, T.; N. Bowman, C. Rheological and Chemical Analysis of Reverse Gelation in a Covalently Cross-Linked Diels−Alder Polymer Network. *Macromolecules* **2008**, *41* (23), 9112–9117.

(6) Liu, F.; Li, F.; Deng, G.; Chen, Y.; Zhang, B.; Zhang, J.; Liu, C.-Y. Rheological Images of Dynamic Covalent Polymer Networks and Mechanisms behind Mechanical and Self-Healing Properties. *Macromolecules* **2012**, *45* (3), 1636–1645.

(7) Kuang, X.; Liu, G.; Dong, X.; Wang, D. Correlation between Stress Relaxation Dynamics and Thermochemistry for Covalent Adaptive Networks Polymers. *Mater. Chem. Front.* **2017**, *1* (1), 111–118.

(8) Chao, A.; Negulescu, I.; Zhang, D. Dynamic Covalent Polymer Networks Based on Degenerative Imine Bond Exchange: Tuning the Malleability and Self-Healing Properties by Solvent. *Macromolecules* **2016**, *49* (17), 6277–6284.

(9) Cromwell, O. R.; Chung, J.; Guan, Z. Malleable and Self-Healing Covalent Polymer Networks through Tunable Dynamic Boronic Ester Bonds. *J. Am. Chem. Soc.* **2015**, *137* (20), 6492–6495.

(10) Yesilyurt, V.; Ayoob, A. M.; Appel, E. A.; Borenstein, J. T.; Langer, R.; Anderson, D. G. Mixed Reversible Covalent Crosslink Kinetics Enable Precise, Hierarchical Mechanical Tuning of Hydrogel Networks. *Adv. Mater.* **2017**, *29* (19), 1605947.

(11) Zhang, L.; Rowan, S. J. Effect of Sterics and Degree of Cross-Linking on the Mechanical Properties of Dynamic Poly(Alkylurea–Urethane) Networks. *Macromolecules* **2017**, *50* (13), 5051–5060.

(12) Green, M. S.; Tobolsky, A. V. A New Approach to the Theory of Relaxing Polymeric Media. *J. Chem. Phys.* **1946**, *14* (2), 80–92.

(13) Baxandall, L. G. Dynamics of Reversibly Crosslinked Chains. *Macromolecules* **1989**, *22* (4), 1982–1988.

(14) Leibler, L.; Rubinstein, M.; Colby, R. H. Dynamics of Reversible Networks. *Macromolecules* **1991**, *24* (16), 4701–4707.

(15) Chen, Q.; Tudryn, G. J.; Colby, R. H. Ionomer Dynamics and the Sticky Rouse Model. *J. Rheol.* **2013**, *57* (5), 1441–1462.

(16) Semenov, A. N.; Rubinstein, M. Thermoreversible Gelation in Solutions of Associative Polymers. 1. Statics. *Macromolecules* **1998**, *31* (4), 1373–1385.

(17) Rubinstein, M.; N. Semenov, A. Thermoreversible Gelation in Solutions of Associating Polymers. 2. Linear Dynamics. *Macromolecules* **1998**, *31* (4), 1386–1397.

(18) H. Krenske, E.; C. Petter, R.; N. Houk, K. Kinetics and Thermodynamics of Reversible Thiol Additions to Mono- and Diactivated Michael Acceptors: Implications for the Design of Drugs That Bind Covalently to Cysteines. *J. Org. Chem.* **2016**, *81* (23), 11726–11733.

(19) Serafimova, I. M.; Pufall, M. A.; Krishnan, S.; Duda, K.; Cohen, M. S.; Maglathlin, R. L.; McFarland, J. M.; Miller, R. M.; Frödin, M.; Taunton, J. Reversible Targeting of Noncatalytic Cysteines with Chemically Tuned Electrophiles. *Nat. Chem. Biol.* **2012**, *8*, 471.

(20) Zhong, Y.; Xu, Y.; Anslyn, E. V. Studies of Reversible Conjugate Additions. *European J. Org. Chem.* **2013**, *2013* (23), 5017–5021.

(21) Montarnal, D.; Capelot, M.; Tournilhac, F.; Leibler, L. Silica-Like Malleable Materials from Permanent Organic Networks. *Science* **2011**, *334* (6058), 965 – 968.

(22) Denissen, W.; Winne, J. M.; Du Prez, F. E. Vitrimers: Permanent Organic Networks with Glass-like Fluidity. *Chem. Sci.* **2016**, *7* (1), 30–38.

(23) Zhang, Z. P.; Rong, M. Z.; Zhang, M. Q. Polymer Engineering Based on Reversible Covalent Chemistry: A Promising Innovative Pathway towards New Materials and New Functionalities. *Prog. Polym. Sci.* **2018**, *80*, 39–93.

(24) Cogswell, F. N. Viscoleastic Properties of Polymer. J. D. Ferry John Wiley & Sons, Chichester, 1980 (3rd Edition).

(25) N. Semenov, A.; Rubinstein, M. Thermoreversible Gelation in Solutions of Associative Polymers. 1. Statics. *Macromolecules* **1998**, *31* (4), 1373–1385.

(26) Semenov, A. N.; Rubinstein, M. Dynamics of Entangled Associating Polymers with Large Aggregates. *Macromolecules* **2002**, *35* (12), 4821–4837.

(27) Chen, Q.; Huang, C.; A. Weiss, R.; H. Colby, R. Viscoelasticity of Reversible Gelation for Ionomers. *Macromolecules* **2015**, *48* (4), 1221–1230.

(28) Huang, C.; Wang, C.; Chen, Q.; Colby, R. H.; Weiss, R. A. Reversible Gelation Model

Predictions of the Linear Viscoelasticity of Oligomeric Sulfonated Polystyrene Ionomer Blends. *Macromolecules* **2016**, *49* (10), 3936–3947.

(29) Zhang, Z.; Chen, Q.; Colby, R. H. Dynamics of Associative Polymers. *Soft Matter* **2018**, *14* (16), 2961–2977.

(30) Sheridan, R. J.; Adzima, B. J.; Bowman, C. N. Temperature Dependent Stress Relaxation in a Model Diels–Alder Network. *Aust. J. Chem.* **2011**, *64* (8), 1094.

(31) Sheridan, R. J.; Bowman, C. N. A Simple Relationship Relating Linear Viscoelastic Properties and Chemical Structure in a Model Diels–Alder Polymer Network. *Macromolecules* **2012**, *45* (18), 7634–7641.

5 Dynamic thia-Michael networks as multi-stage adhesives

5.1 Introduction

Chapters 2, 3, and 4 highlighted the tunable mechanical and functional properties of polymeric networks based on the reversible thia-Michael reaction. Using a combination of chemical, thermomechanical, and rheological analysis, the bulk material properties of the crosslinked networks were shown to be linked to the electronic nature of the benzalcyanoacetate Michael acceptor. Control of the thermodynamic equilibrium was achieved by altering the electron-donating or electron-withdrawing character of the β-phenyl substituent on the benzalcyanoacetetate component (Figure 5.1A). Electron-withdrawing groups promoted a higher equilibrium constant (K_{eq}) in reactions with thiols which resulted in a more mechanically robust network than those with electron-donating groups whose K_{eq} was lower. Kinetic trends were also found to relate to the β-phenyl substituent with electron-donating groups having faster relaxation rates than groups with electron-withdrawing properties.

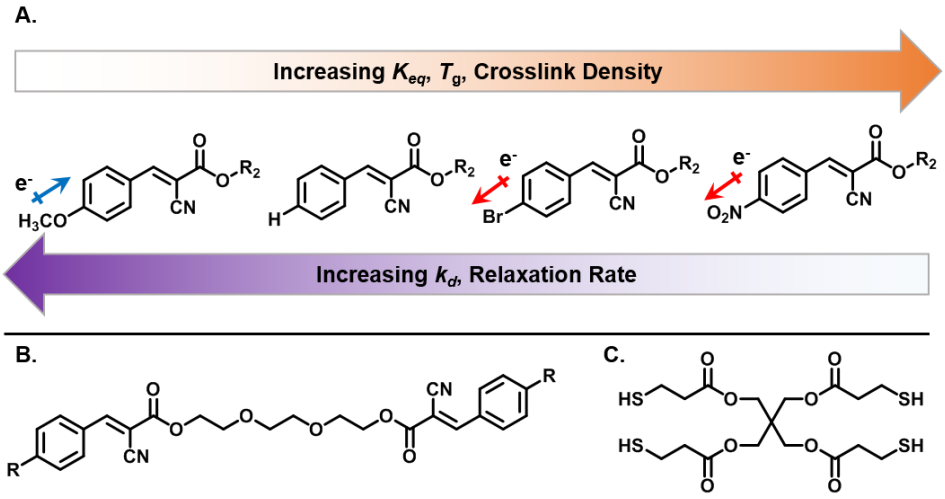

Figure 5.1. A) Schematic summary of the property trends associated with electron-withdrawing and electron-donating groups on the benzalcyanoacetate compounds. B) Chemical structure of bis-benzalcyanoacetate triethylene glycol Michael acceptor used in Chapter 2 and 3. C) Tetrathiol crosslinker (PTMP) used in thia-Michael networks in Chapters 2 and 3.

The studies described in the previous chapters focused on benzalcyanoacetate-based thia-Michael materials constructed using a ditopic, triethylene glycol-core acceptor (Figure 5.1B) in conjunction with the tetrathiol crosslinker, pentaerythritol tetrakis(3-mercaptopropionate) (PTMP). Moving forward, the focus shifted towards expanding the utility of the benzalcyanoacetate-based system beyond this initial small-molecule network and branching into such domains as multi-stimuli responsive materials and application-driven material design. This sparked an exploratory investigation to evaluate the efficacy of the thia-Michael reaction in various network environments *en route* to the next generation of dynamic TM materials. Thus, new systems were designed with two goals in mind: 1) to assess the functional and mechanical properties of dynamic networks that utilizes the previously developed Michael acceptors in

combination with an oligomeric thiol component, and 2) to evaluate the ability of a thia-Michael network to perform in adhesive applications.

The integration of dynamic bonds into covalent networks has previously been shown to impart adhesive behavior into thermosets that are otherwise be incapable of adhesion.[1–8] The dynamic bonds' ability to continuously break/reform in response to a stimulus without unwanted, irreversible side reactions[9–12] provides a means through which critical adhesion properties (i.e. surface wetting) can be achieved. For example, Michal, *et al*,[13] and Cudjoe, *et al*,[7] both demonstrated the adhesive application of dynamic covalent networks containing disulfide bonds. By disengaging the disulfide bond using heat (>150 °C) or UV light, an adhesive bond could be formed between two glass or metallic substrates. Moreover, this adhesion was reversible given the dynamic nature of the disulfide bond and was shown to be rebondable even after failure. Unfortunately, this system's utility was limited to either optically clear, UV inert substrates or substrates that were capable of withstanding high temperatures. The room-temperature dynamic behavior of the thia-Michael bond makes it a promising candidate for dynamic covalent adhesives targeting applications in ambient conditions.

While the dynamic chemistry of the thia-Michael reaction provide the opportunity for adhesive properties, it is the viscoelastic behavior of the dynamic polymeric system that dictates the application of the resulting adhesive. Soft, viscoelastic solids are well suited for pressure sensitive adhesives (PSAs), such as those on the back of Post-It® notes or adhesive tapes.[14] These are commonly characterized as having high dissipation properties which allow the material to readily deform and adhere to a substrate with minimal pressure and without a curing agent.[15] While this high dissipation helps the material to quickly adhere to a substrate, it is not typically attributed

to a material that is suited to withstanding large structural loads. On the other hand, a hot melt adhesive, such as hot glue, is designed to permanently withstand large loads and as such, is often referred to as a type of structural adhesive.[16] The hot melt adhesive bond is generally formed in the melt, but evaluated for performance in the solid state once the adhesive has cooled. Although this type of adhesive is classically a thermoplastic polymer, previous chapters have demonstrated the thia-Michael networks' ability to reversibly "melt" and reform as a high modulus material, giving them the potential to act as hot-melt adhesives.

One potential issue surrounding the thia-Michael materials discussed in the prior chapters is the temperature of their 1st glass transition (T_g). The robust PTMP networks had low temperature T_gs (as determined by loss modulus peak in dynamic mechanical analysis, DMA) ranging from ca. 21 °C to 48 °C, depending on the β-substituent on the acceptor prohibiting their use as a pressure sensitive adhesive. Ideally, a pressure sensitive adhesive has a broad T_g roughly 25-45 °C below operating temperatures in order to achieve the dissipation necessary for adhesion.[15] Thus, with an eye toward accessing thia-Michael networks with lower T_gs, the commercially available poly(mercaptopropyl methyl) siloxane (PMMS, Figure 5.2) was used in place of PTMP. This reactive thiol-containing polymer not only functions as the polymer matrix, but has the added advantage of possessing numerous pendant thiol groups (one per silicon atom) that are accessible to the Michael-accepting crosslinker. By incorporating a siloxane polymer, it was hypothesized that low glass transition (T_g) networks would be accessed thus granting access to dynamic exchange at or below room temperature.

The studies reported herein focus on the preparation and evaluation of the thia-Michael, PMMS system towards multi-stage adhesive applications. Utilizing benzalcyanoacetate-based

Michael acceptors in conjunction with PMMS (Figure 5.2), several polymeric networks were assembled and analyzed (See Appendix for preliminary work involving hexyl-core compounds). The resulting materials exhibit a broad range of working conditions as well as an aptitude for both structural and pressure sensitive adhesion.

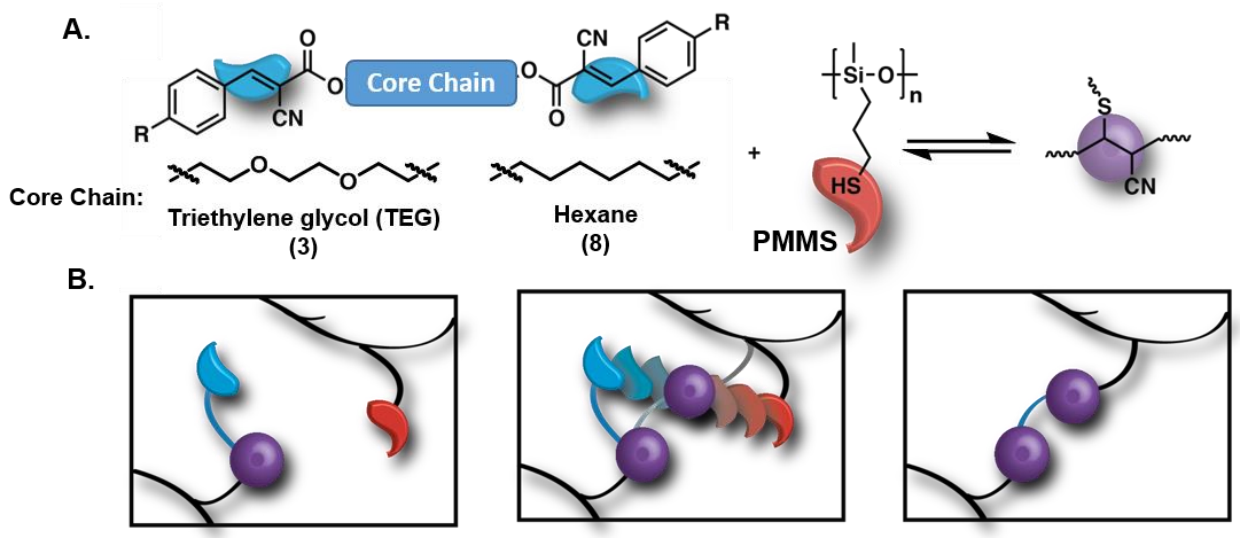

Figure 5.2. A) Chemical structures involved in generally assembly scheme for thia-Michael crosslinking reaction between alkyl bisbenzalcyanoacetate and poly(mercaptopropyl methyl) siloxane (PMMS). B) Cartoon depicting the dynamic formation of a crosslink between PMMS chains.

5.2 Results and Discussion

Thia-Michael films composed of the ditopic Michael acceptors (Figure 5.3A, see Chapter 3 for synthesis details) with poly(mercaptopropyl methyl)siloxane (Figure 5.3B, PMMS, Gelest SMS-992, 4k-7k Da) were prepared following procedures similar to those reported in previous chapters. Briefly, the acceptors and PMMS were dissolved in chloroform, stirred for 2 hours at 50

°C, and cast onto Teflon® drying dishes. The films were allowed to dry overnight at room temperature then transferred to a vacuum oven at 60 °C and dried under reduced pressure for 24 hours. The networks were then heated to 200 °C and held isothermally under reduced pressure for 30 minutes to remove any trapped solvent before the final compression molding step. PMMS films were pressed at 70 °C for 10 minutes under 10 kpsi (films containing only **3N** were pressed at 90 °C).

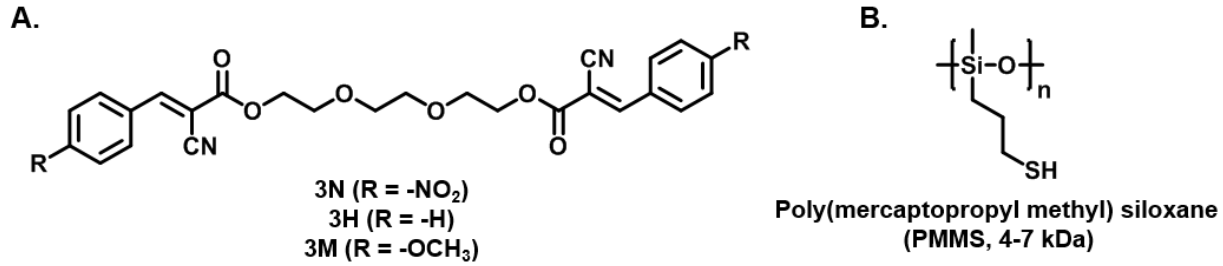

Figure 5.3. Chemical structures for A) TEG-core bisbenzalcyanoacetate compounds and B) poly(mercaptopropyl methyl) siloxane (PMMS).

Five samples were prepared: **5M$_{100}$, 5H$_{100}$,** and **5N$_{100}$** to indicate the use of **3M**, **3H**, and **3N**, respectively, as well as two hybrid materials composed of **3N** with **3H** (**5N$_{50}$H$_{50}$**) and **3N** with **3M** (**5N$_{50}$M$_{50}$**). The x relates the mole percent (mol%) of each acceptor site (x = 100 or 50) relative to the total amount of thiol.

Raman spectroscopy was employed to verify the formation of thia-Michael linkages within the network. Previous solution-state studies have shown that the chemical equilibrium of the benzalcyanoacetate-based thia-Michael reaction is reflective of the substituents on the β-phenyl ring. Electron-withdrawing groups (i.e. NO_2) result in higher K_{eq} that pushes the reaction towards completion whereas electron-donating groups (i.e. OCH_3) exhibit lower K_{eq} and form fewer

linkages. This trend can be observed in the Raman spectra of the films by noting shifts and changes to the intensity of peaks affected by the thia-Michael reaction, mainly, the peaks corresponding to the stretching modes of the C=C (1520 cm^{-1} – 1640 cm^{-1}, Figure 5.4A/C/E) and C≡N (2200 cm^{-1} – 2280 cm^{-1}, Figure 5.4B/D/F) bonds in **3**. Figure 5.4 A and B show the spectral changes within these regions when **3N** (dashed red line) is incorporated into a TM network with PMMS to form **5N$_{100}$** (solid red line). A minor shift to higher frequencies is observed in the C=C stretch, however, the presence of reacted acceptor group is clearer in the C≡N frequency range. For **3N**, an unreacted, conjugated C≡N peak is clearly visible at 2227 cm^{-1}. The addition of the thiol across the double bond of **3N** eliminates the conjugation surrounding the C≡N group, thereby causing the stretching mode to shift to higher frequencies and appear at 2255 cm^{-1}. The presence of the non-conjugated peak serves as evidence towards the formation of thia-Michael crosslinks within the PMMS network. In comparison, films formed using **3M** demonstrated minimal formation of the non-conjugated adduct (Figure 5.3E/F) at room temperature which likely contributes to their inability to form robust films.

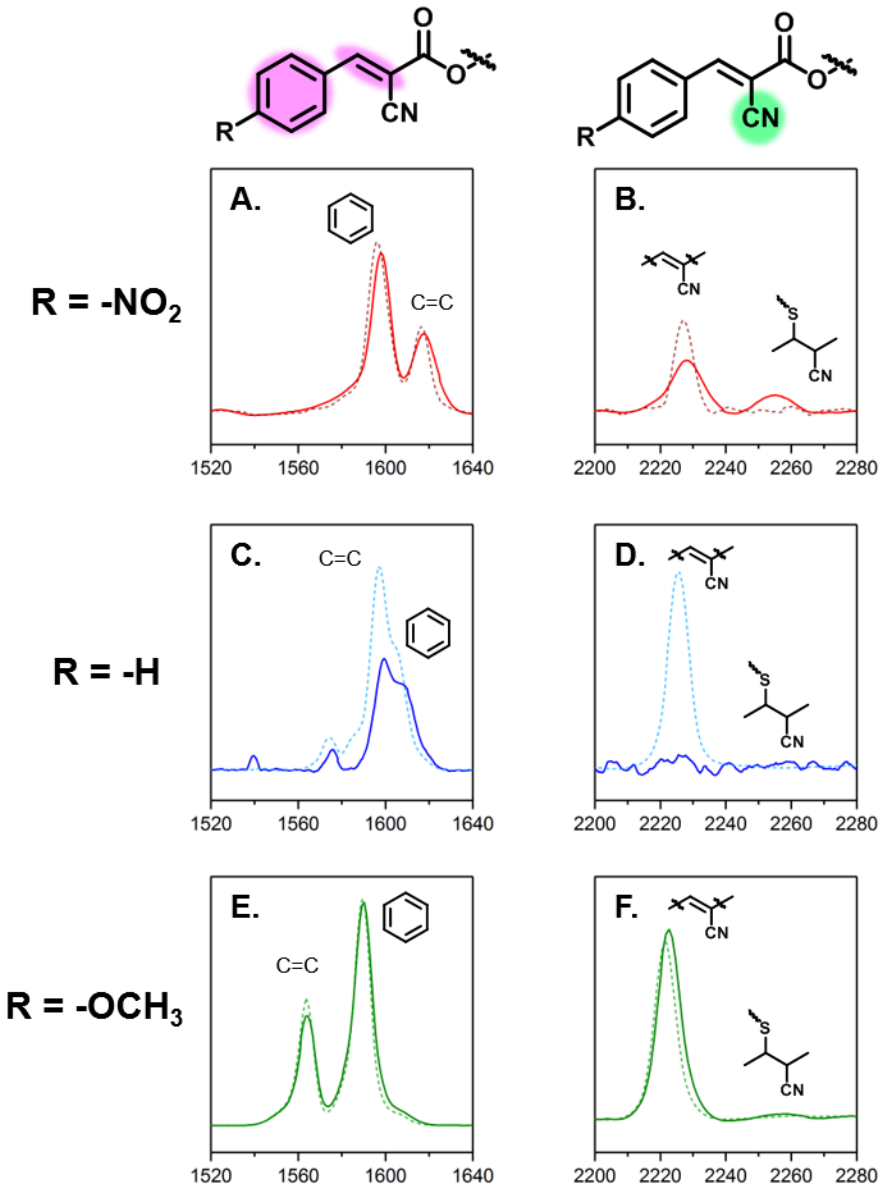

Figure 5.4. Raman spectra of C=C (*left*) and C≡N (*right*) vibrational stretches for the neat electrophiles (dashed lines) overlaid with the respective thia-Michael networks (solid lines). A/B) **3N** and **5N$_{100}$**, C/D) **3H** and **5H$_{100}$**, E/F) **3M** and **5M$_{100}$**.

In addition to identifying changes in the structure of **3**, Raman was also useful for tracking changes to the thiols present in PMMS. Regions associated with free thiol (2500 cm^{-1} – 2625 cm^{-1}, Figure 5.5A) and lower frequency ranges associated with disulfide formation (400 cm^{-1} – 600

cm^{-1}, Figure 5.5B). While PMMS has a prominent S-H stretch at 2572 cm^{-1}, the thia-Michael networks showed no peaks differentiable from baseline that could be associated with free thiol, even though analysis of the acceptors suggested that there was free, unreacted species within the films. The presence of a medium intensity peak at 502 cm^{-1} provides a potential explanation for the missing thiols: formation of disulfide bonds. From the spectrum of the as-received PMMS, it appears that the oligomer contains a percentage of disulfide bonds which could account for the absence of free thiol as well as the presence of unreacted acceptor compounds.

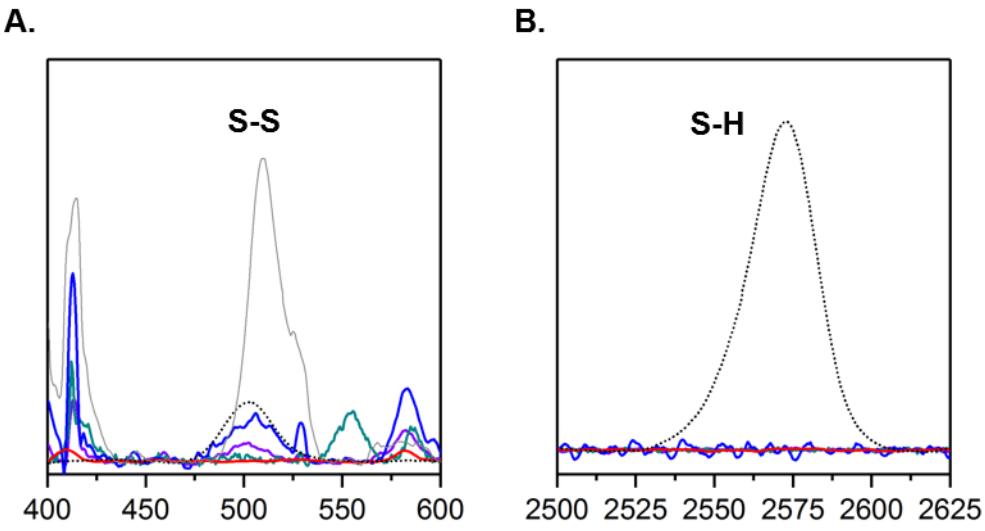

Figure 5.5. Raman spectra of A) disulfide region and B) thiol region. Disulfide network (solid gray), as-received PMMS (dotted black), **5N$_{100}$** (red), **5H$_{100}$** (blue), **5N$_{50}$H$_{50}$** (violet), **5N$_{50}$M$_{50}$** (cyan).

Following the chemical characterization of the crosslinking reaction, each film was evaluated via thermogravimetric analysis (TGA, Figure 5.6A) and differential scanning calorimetry (DSC, Figure 5.6B). The TM films demonstrated improved thermal stability over the

neat PMMS oligomer (10% weight loss at 265 °C), with degradation temperatures (calculated at 10% weight loss in TGA) of 286 °C for all films except **5M$_{100}$** which was slightly more stable with 10% degradation occurring at 296 °C. DSC results exhibited dual glass transitions (T_g) in these films that were characteristic of dynamic reaction-induced phase separation (DRIPS) in previous thia-Michael films (see Chapter 3 for details). The first T_g (as calculated by onset of the transition) in all of the films occurs well below room temperature with the highest at 11 °C for **5N$_{100}$** and the lowest at -36 °C for **5H$_{100}$**. The hybrid films, **5N$_{50}$H$_{50}$** and **5N$_{50}$M$_{50}$**, had low T_gs intermediate to the low T_gs of the parent networks at -13 °C and -12 °C, respectively. The second glass transition is prominent in **5N$_{100}$** as well as the hybrid systems, however, the same transition for **5H$_{100}$** and **5M$_{100}$** was not apparent within the DSC testing conditions. It is worth noting that PMMS does not show any phase transitions between -80 °C and 200 °C.

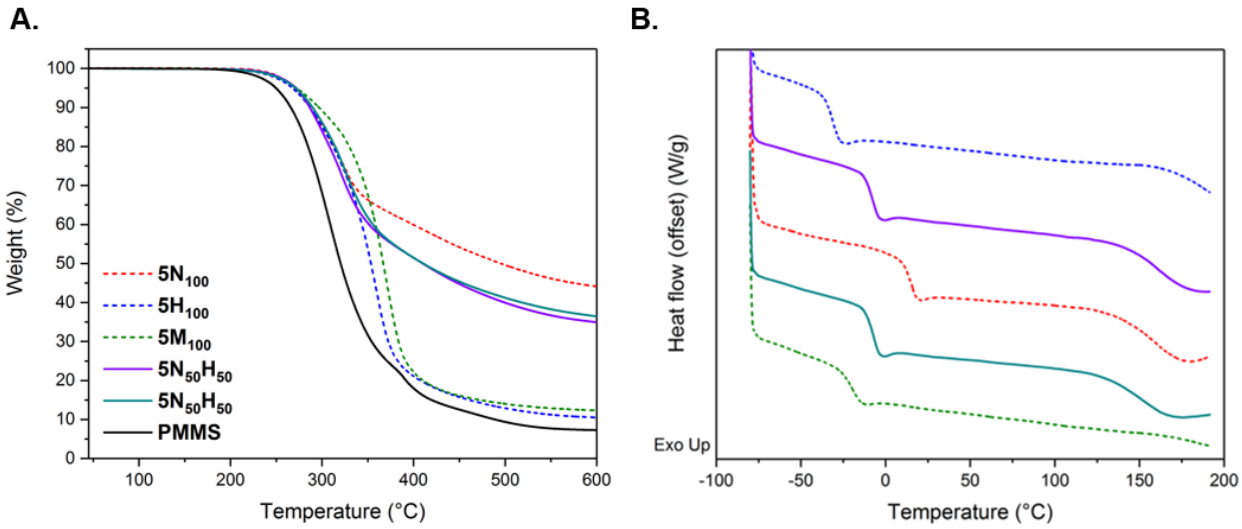

Figure 5.6. A) TGA data for thia-Michael/disulfide films including hybrids (ramp rate = 10 °C/min). B) DSC curves for thia-Michael/disulfide films including hybrids showing results of third heating (exotherm up, ramp rate = 10 °C/min, curves offset for ease of viewing). **5N$_{100}$** (red dashed), **5H$_{100}$** (blue dashed), **5M$_{100}$** (green dashed), **5N$_{50}$H$_{50}$** (violet), **5N$_{50}$M$_{50}$** (cyan).

As briefly mentioned above, the dual glass transitions in DSC for the films suggests a phase separated morphology akin to that which was observed in previous studies with the bisbenzalcyanoacetate Michael acceptors. With **5M$_{100}$** and **5H$_{100}$**, this phase separation was catastrophic preventing the formation of a robust film. These samples could be heated again to 200 °C (as they were in the final drying step of film preparation) and would appear as tacky, transparent viscous liquid, but over time (1-6 hours) an opaque, waxy solid would form, presumably as a result of the weakly bound acceptors separating from the matrix. While still phase separated, **5N$_{100}$**, **5N$_{50}$H$_{50}$**, and **5N$_{50}$M$_{50}$** were all capable of forming testable films. Optical microscopy (OM) was employed to observe the physical phases within drop-cast samples of the networks (Figure 5.7). Small aliquots of the starting thia-Michael solution (ca. 200 μL) were cast onto glass coverslips. The samples were dried following the standard protocol for the bulk films as outlined earlier. For the hybrid films (Figure 5.7), a bicontinuous phase separated structure was observed with small inclusions present in either phase.

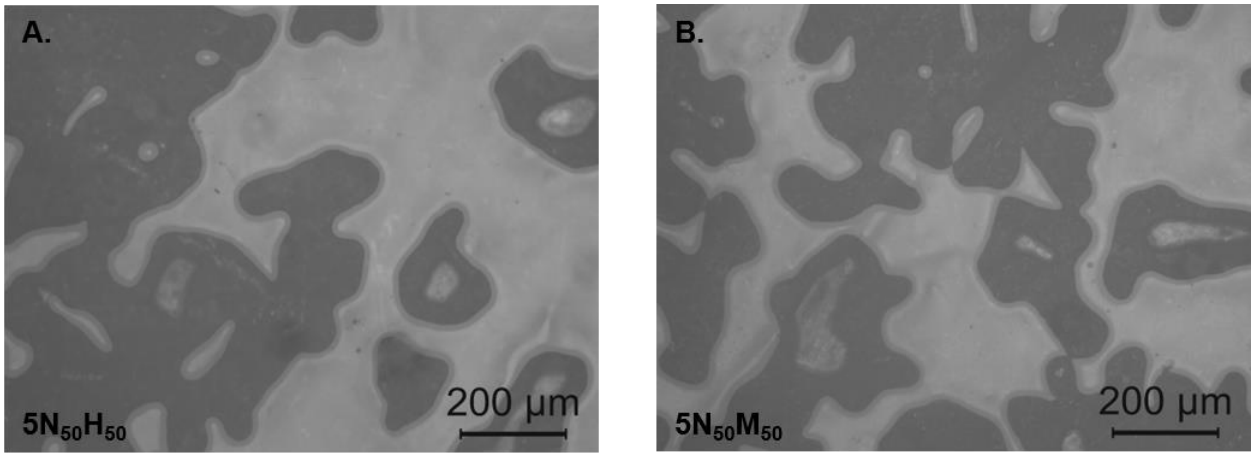

Figure 5.7. Optical microscope (OM) images of A) **5N$_{50}$H$_{50}$** and B) **5N$_{50}$M$_{50}$** taken at 10x magnification.

Small amplitude oscillatory shear (SAOS) rheological analysis was used to investigate the mechanical behavior of these materials. For the thia-Michael films, SAOS rheology was conducted using 8 mm parallel plates on a TA Instruments ARES-G2 rheometer equipped with a force convection oven (FCO) and low temperature range chiller (See Experiment Methods for detailed procedures). Temperature-dependent mechanical behavior was first evaluated using a temperature ramp from -30 °C to 200 °C with an oscillatory frequency of 1 Hz (Figure 5.8). To accommodate changes in material stiffness, the oscillatory strain was automatically adjusted using the instrument's software (Trios).

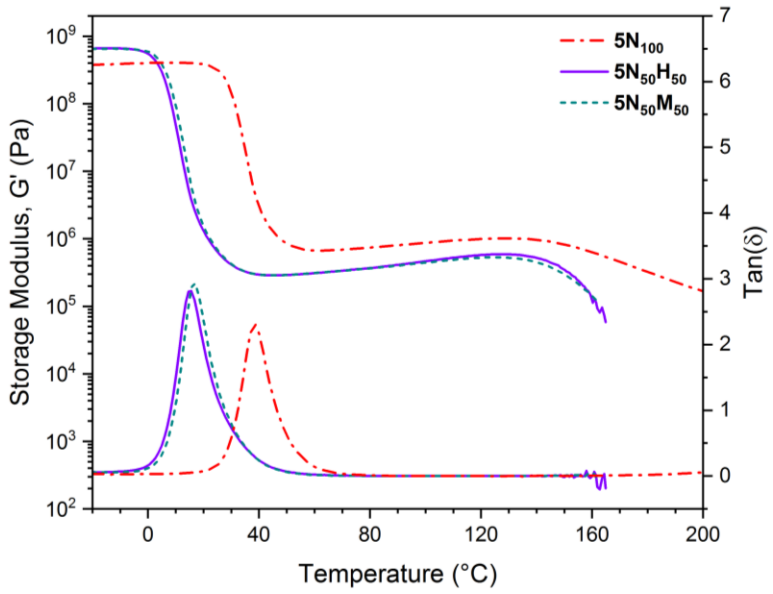

Figure 5.8. Small amplitude oscillatory shear (SAOS) rheology temperature sweep of **5N$_{100}$** (red dot-dash line), **5N$_{50}$H$_{50}$** (violet solid line), and **5N$_{50}$M$_{50}$** (cyan dash line) showing storage modulus (*top*) and tan δ (*bottom*).

The temperature ramp revealed two transitions for the systems tested (**5H$_{100}$** and **5M$_{100}$** were both phase separated liquids at room temperature and as such, were not tested). The first glass

transition (as defined by tan δ) occurred at 38 °C for **5N$_{100}$**, while both **5N$_{50}$H$_{50}$** and **5N$_{50}$M$_{50}$** had initial glass transitions below room temperature, at 15 °C and 16 °C, respectively. As shown in Figure 5.8, the temperature dependence of the hybrid materials is remarkably similar, suggesting that the composition of the continuous phase in the two films is similar. Furthermore, the two hybrid samples exhibited a rubbery plateau modulus of ranging from ca. 2.8 x 10^5 Pa to ca. 5.8 x 10^5 (a slight increase in modulus was noted from all samples that is likely a result of entropic gain within the network with increased temperature) over a temperature range of more than 100 °C, creating a large window of operation before the films fail mechanically. At higher temperatures, the thia-Michael films reach their second T_g which is accompanied by the onset of macroscopic flow for the systems. Above this temperature (ca. 140 °C for hybrids), the dynamic networks demonstrate a significant drop in modulus, thereby creating an opportunity for hot-melt adhesion. On the other hand, **5N$_{100}$** gradually softens following this second transition (ca. 145 °C) and does not enter a Newtonian-like flow regime.

The SAOS rheology temperature studies suggest that the hybrid thia-Michael films have the potential to act as both PSAs and hot-melt adhesives, depending on the careful selection of composition and working conditions. In the interest of exploring adhesive applications for these TM systems, evaluations were focused on the hybrid materials, given their lower T_g and notable modulus drop at higher temperatures. SAOS frequency studies were used to further probe the PSA characteristics of the hybrid systems (Figure 5.9A/B). Frequency sweeps from 0.01 rad/s to 100 rad/s were conducted at different temperatures centered around the target operating temperature of 25 °C. Using time-temperature superposition (TTS), a master curve was generated at a reference temperature of 25 °C. Figure 5.9C/D shows the master curves for **5N$_{50}$H$_{50}$** and **5N$_{50}$M$_{50}$** as

determined by multiple frequency sweeps shifted according to WLF fit. Using these master curves, two principles were applied to define their ability to act as pressure sensitive adhesives: the Dahlquist criterion and the viscoelastic window. According to the Dahlquist criterion, for materials to be useful as pressure sensitive adhesives, they should possess a storage modulus (G') less than 3 x 10^5 Pa (at 1.0 rad/s) at the operating temperature.[17] This criterion is highlighted with dashed lines in Figure 5.9C/D and it is clear that **5N$_{50}$M$_{50}$** meets this criterion at room temperature. On the other hand, **5N$_{50}$H$_{50}$** has a modulus slightly higher than would be ideal according to Dahlquist, however, the material was close enough to still be considered for this investigation.

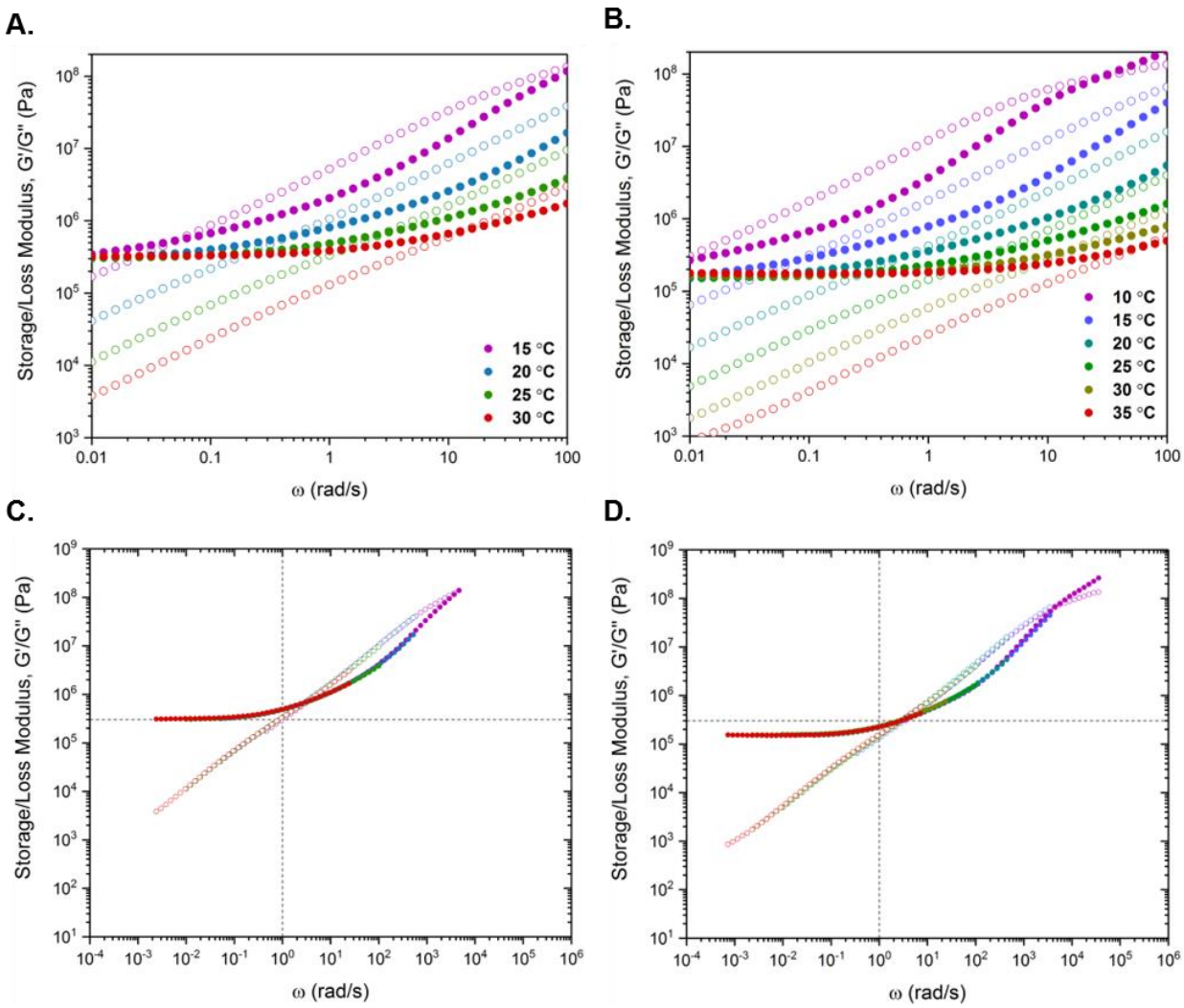

Figure 5.9. Small amplitude oscillatory shear (SAOS) rheology frequency studies on A) **5N$_{50}$H$_{50}$** and B) **5N$_{50}$M$_{50}$** at temperatures surrounding 25 °C. Master curves based on the WLF shift of the frequency data for C) **5N$_{50}$H$_{50}$** and D) **5N$_{50}$M$_{50}$**. Dashed lines in C/D highlight Dahlquist criterion (3 x 10^5 Pa at 1 rad/s).

While useful as a first approximation, the Dahlquist criterion serves only as a benchmark for PSAs and does little to categorize the potential function of an adhesive. To this end, Chang defined PSAs by identifying a viscoelastic window (VW) within which PSA applications could be identified.[18] Using isothermal frequency studies, a VW is defined by the operating temperature

storage and loss modulus (G'') at 0.01 rad/s and 100 rad/s. In a plot of storage versus loss modulus (Figure 5.10), the values can be plotted as coordinates to form four corners of a rectangle which constitutes the VW: 1) G' at 0.01 rad/s and G'' at 0.01 rad/s, 2) G' at 0.01 rad/s and G'' at 100 rad/s, 3) G' at 100 rad/s and G'' at 0.01 rad/s, and 4) G' at 100 rad/s and G'' at 100 rad/s. Their investigation determined that this window varies depending on the PSA application and as a result they were able to identify five viscoelastic regimes for PSAs based on the location of their VW in the G'/ G'' plot: non-PSA (quadrant 1), high shear PSA (quadrant 2), removable PSA (quadrant 3), cold temperature PSA (quadrant 4), and general PSA (central region).

Using the frequency data acquired for the master curves, it was possible to establish viscoelastic windows for **5N$_{50}$H$_{50}$** and **5N$_{50}$M$_{50}$**. As shown in Figure 5.10, much of the VW for **5N$_{50}$H$_{50}$** and **5N$_{50}$M$_{50}$** falls in quadrant 2, suggesting that the two materials would perform as high shear PSAs. These types of PSAs are typically characterized by a high storage modulus which contributes to the higher shear strength relative to other PSAs. When this high storage modulus is accompanied by a low loss modulus, the material falls into quadrant 1 (non-PSAs) and is unable to function as a pressure sensitive adhesive. However, when the loss modulus is also high, there exists a mechanism within the material that allows dissipation to take place, promoting adhesion. The location of the VWs for both hybrid materials spans into quadrant 1 and beyond the standard plots as defined by Chang (upper limits in Chang's plots were 1 x 10^6 Pa, moduli higher than the original limits are highlighted in gray in Figure 5.10). The addition of **3M** to the hybrid network shifted the VW moduli further into a typical PSA regime, suggesting that future optimization of the network composition could target specific PSA applications for the thia-Michael systems.

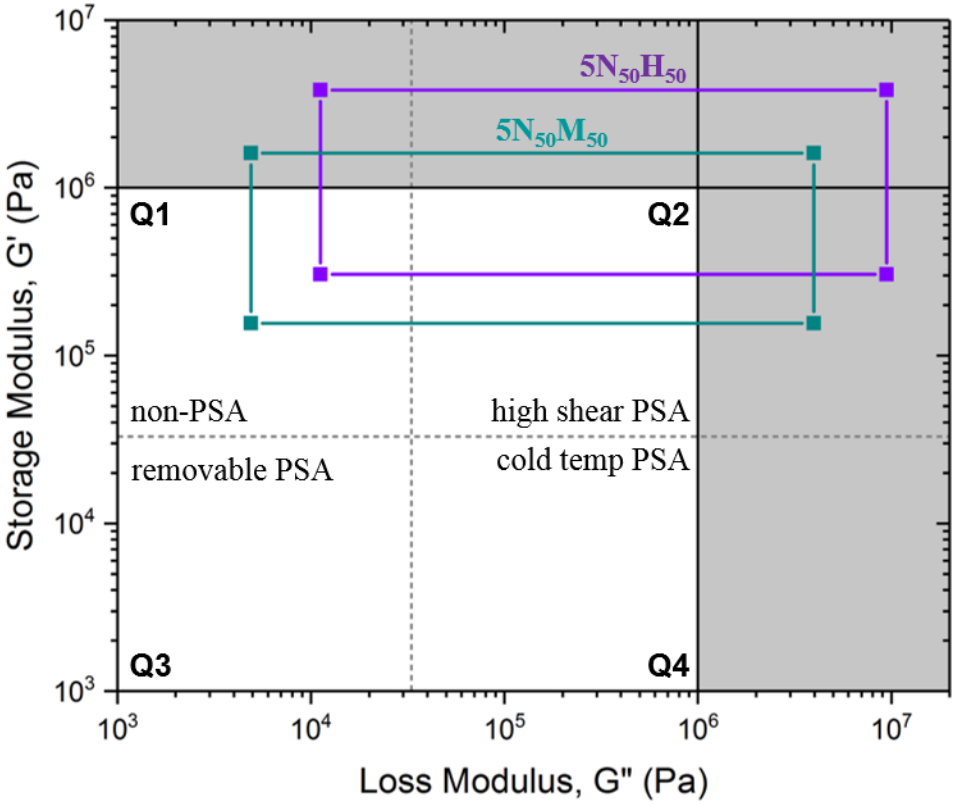

Figure 5.10. Viscoelastic windows for **$5N_{50}H_{50}$** (violet) and **$5N_{50}M_{50}$** (cyan). Gray region highlights moduli outside of typical viscoelastic window plot

Inspired by the rheological characteristics of the TM hybrid films indicating potential adhesive behavior, the mechanical performance of these materials was assessed for both pressure-sensitive and hot-melt adhesion. Three different testing methods were employed to evaluate the adhesive properties of the films: tack and 180-degree peel tests for probing their PSA abilities, and normal force pull-off tests to determine their adhesive strength as hot-melt adhesives (Figure 5.11). To test the films as PSAs, the networks were prepared as rough "tapes" with a Kapton backing. Briefly, **$5N_{50}H_{50}$** (or **$5N_{50}M_{50}$**) was prepared following the procedure outlined earlier. The resultant film was re-pressed between two Kapton sheets at 200 °C and 1 kpsi (lower limit of current press) for 10 minutes, creating an adhesive layer that was approximately 100 µm thick. To

use, the desired shape was cut from the Kapton-**5N$_{50}$H$_{50}$**-Kapton sample and the two Kapton sheets were pulled apart to expose the adhesive material. This process served to protect the adhesive surface from contaminants and oxidation while also ensuring that the material was firmly attached to the Kapton substrate, facilitating an accurate measurement of PSA properties.

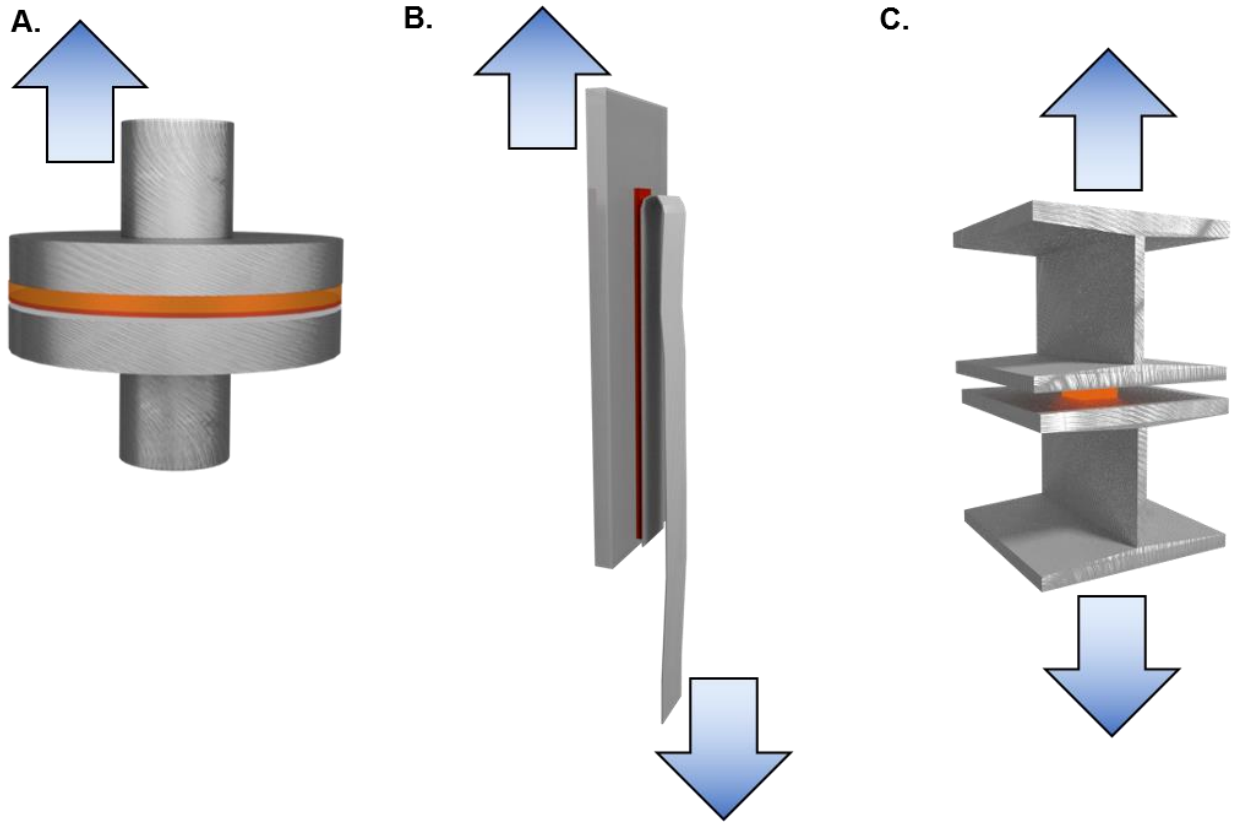

Figure 5.11. Schematic illustration of adhesive test setup for A) tack, B) 180-degree peel strength, and C) hot-melt adhesive strength.

The tack of the TM tapes was evaluated using the ARES-G2 rheometer equipped with an 8 mm stainless steel parallel plate. Samples were cut in 8 mm x 8 mm squares and mounted onto the lower plate using double-sided tape. An axial force (0.1 N, 1.0 N, or 10 N) was applied to the

sample for a pre-determined period of time (20s, 60s, or 120s) after which the upper plate was removed from the adhesive at a constant rate of 0.1 mm/s. The resultant force curve was then evaluated for both pull-off strength (peak force reached during tack test) and area under the force curve (adhesive/cohesive strength of tack). Figure 5.12 summarizes the effect of both time and applied force on these adhesive properties of **$5N_{50}H_{50}$**.

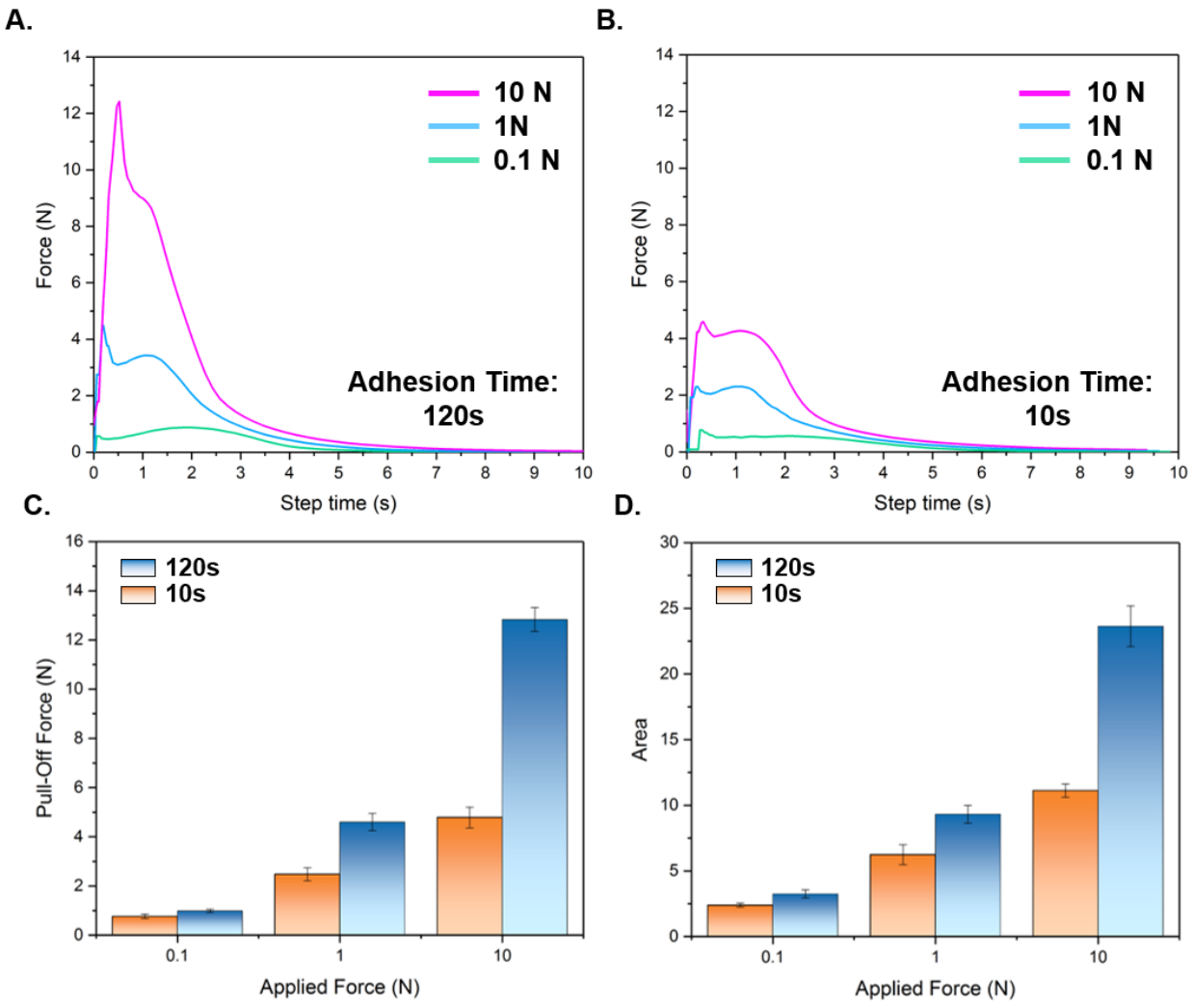

Figure 5.12. Force curves showing tack test results for **5N$_{50}$H$_{50}$** with different applied forces and adhesion times of A) 120s and B) 10s. Graphical summary of A) pull-off force and B) area under the curve for tack test of **5N$_{50}$H$_{50}$** at different adhesion times and applied forces. 8 mm parallel plate and 0.1 mm/s strain rate.

Longer application times and higher applied forces resulted in an increase in both peak force and adhesive/cohesive tack strength. However, a typical PSA functions under working conditions that are relatively short in adhesion time and small in applied force. Therefore, a middling set of parameters (60 second adhesion time and 1 N applied force) was selected for comparing the two hybrid materials. Using the same tack test setup as previously described, five

different samples of each material were tested for 10 consecutive rounds at room temperature (Figure 5.13). From this analysis, it became clear that the PSA properties for both TM hybrids was relatively consistent over the course of the 10 repeated adhesions, indicating the PSAs ability to re-adhere to a surface after failure. When comparing the tack of the two hybrid materials, **5N$_{50}$H$_{50}$** consistently outperforms **5N$_{50}$M$_{50}$**. On average, **5N$_{50}$H$_{50}$** had a peak tack of 5.2 ± 0.2 N (peak force of first test was excluded as an outlier) and an adhesive/cohesive strength of 21 ± 2 N whereas **5N$_{50}$M$_{50}$** had a peak tack force of 4.1 ± 0.3 N and an adhesive/cohesive strength of 12.0 ±0.7 N.

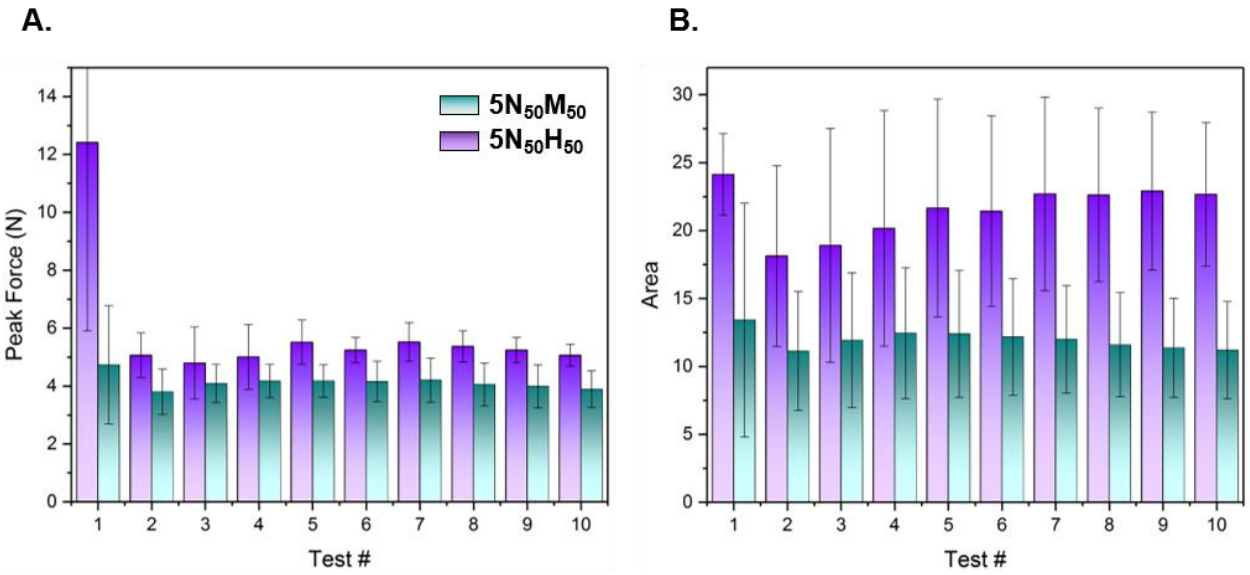

Figure 5.13. Graphical summary of A) peak force and B) area under the curve for 10 consecutive repeat tack experiments on **5N$_{50}$H$_{50}$** (violet) and **5N$_{50}$M$_{50}$** (cyan). 8 mm parallel plates, 0.1 mm/s strain rate, 60 second adhesion time, 1.0 N applied force.

It was also intriguing to compare the effect of time and applied force on the two different hybrid samples. As stated earlier, increasing adhesion time and applied force results in an increase in the peak pull-off force and adhesive/cohesive strength of the PSA bond. However, these changes

impacted the two hybrid materials to a different extent. Figure 5.14 shows that with a 10 second adhesion time, **5N$_{50}$H$_{50}$** still hold a slight edge on **5N$_{50}$M$_{50}$** in peak force, but the adhesive/cohesive strength of **5N$_{50}$M$_{50}$** is equal to or higher than **5N$_{50}$H$_{50}$** on this time scale. This demonstrates a time-dependent factor that impacts the PSA performance of the two materials: the lower moduli of **5N$_{50}$M$_{50}$** (as demonstrated by its VW) allows this slightly weaker adhesive to deform quickly, allowing the material to more fully contact the substrate, thereby creating a stronger adhesive bond than the higher moduli of **5N$_{50}$H$_{50}$** can form. Therefore, depending on the intended application, an adhesive could be tailored to adhere faster or more strongly by modifying the composition of the dynamic adhesive.

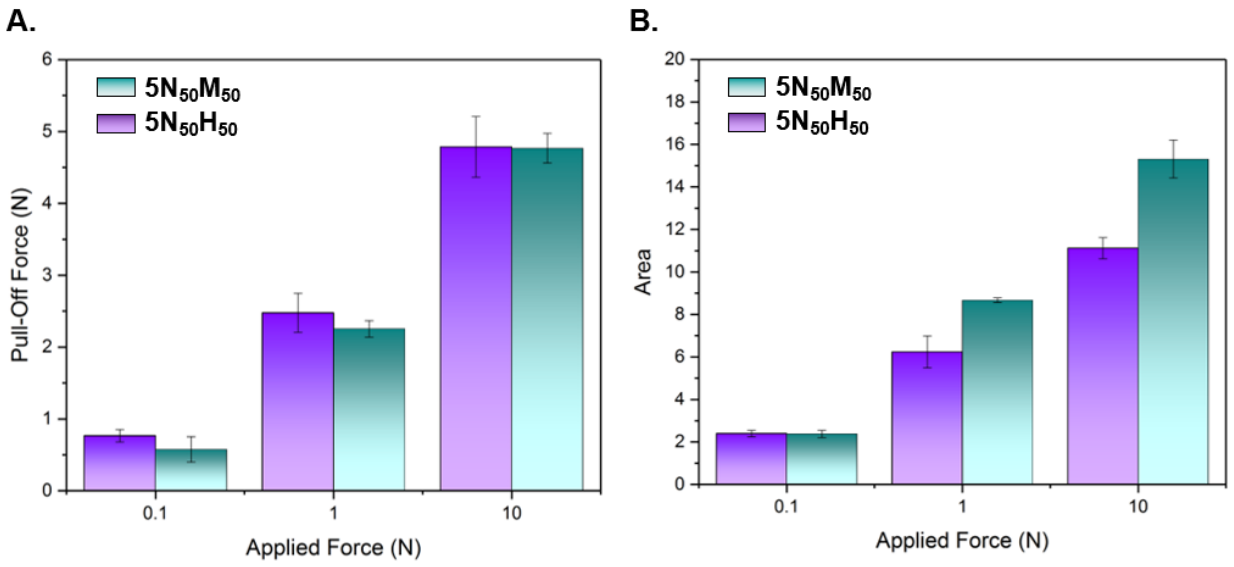

Figure 5.14. Graphical summary of A) pull-off force and B) area under the curve for tack test of **5N$_{50}$H$_{50}$** (violet) and **5N$_{50}$M$_{50}$** (cyan) with variable applied force. 8 mm parallel plate, 10 second application time and 0.1 mm/s strain rate.

The PSA properties of the hybrid systems were further evaluated using a 180-degree peel test on a Zwick-Roell zwickiLine Z0.5 materials testing instrument. The adhesive "tape" was cut into a strip ca. 5 mm wide and 75 mm long. The strip was adhered to a glass microscope slide using double-sided tape. The Kapton not adhered to the slide was then removed and a strip of aluminum foil (approximately 10 mm wide and 200 mm long) was pressed by hand to the exposed thia-Michael adhesive. The aluminum foil was folded in half and the setup was mounted into the Zwick grips. Peel tests were run for a travel distance of 50 mm after the first peak and at a strain rate of 10 mm/min. Figure 5.15A shows a representative peel test result for each film. As highlighted in the figure, the average peel strength and the maximum peel strength were calculated for each series. As shown in Figure 5.15B, the average peel strength of the hybrid materials falls within error of each other while the maximum peel strength was stronger with the **5N$_{50}$M$_{50}$** film. In the future, the optimization of tape preparation and testing conditions could improve the error in the test and allow for better differentiation between the two similar samples.

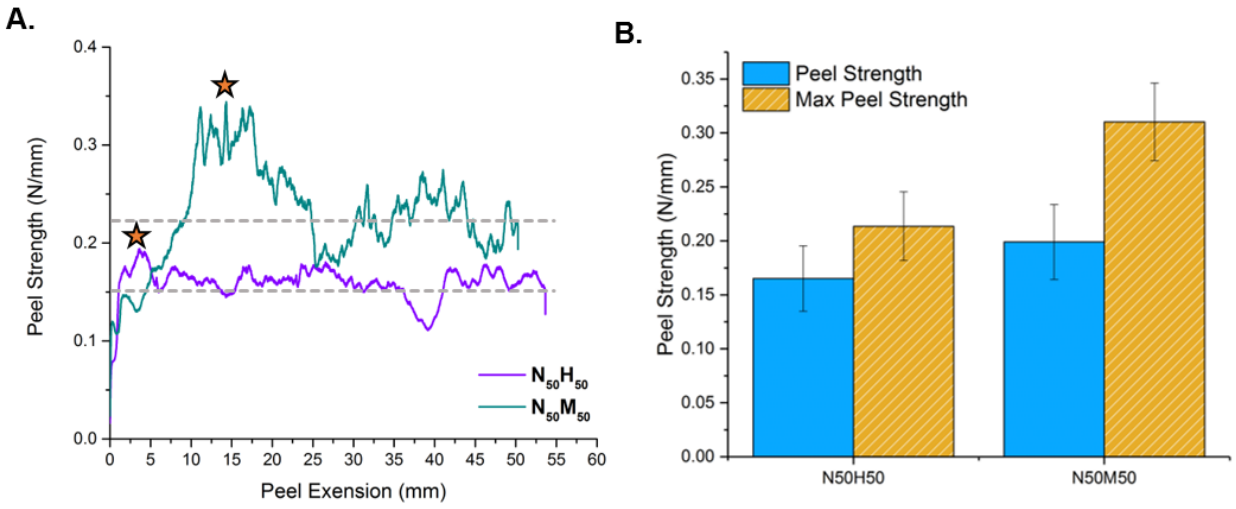

Figure 5.15. A) representative peel test curves for **5N$_{50}$H$_{50}$** (violet) and **5N$_{50}$M$_{50}$** (cyan) highlighting the average peel strength (dashed line) and maximum peel strength (star).

Finally, the hybrid films were evaluated as hot-melt adhesives. A 5 mm x 5 mm square of the original pressed films (not tape) was situated between two aluminum I-bars which were then clamped together using 1-inch binder clips. The entire setup was placed in an oven at 180 °C for 10 minutes after which it was removed and allowed to cool on the benchtop with the clips attached for another 10 minutes. Once cooled, the clips were removed and the adhered I-bars were loaded onto the Zwick clamps. Adhesive strength of the hot-melt bond was measured at 1 mm/min and the area used for calculating the adhesive strength was estimated from the average area of the circular adhesive footprint left after the bond failed (ca. 0.3 cm^2). The average hot-melt adhesive strength of **$5N_{50}H_{50}$** was determined to be 0.8 MPa (± 0.1 MPa), enough to hold over 50 pounds of tensile force.

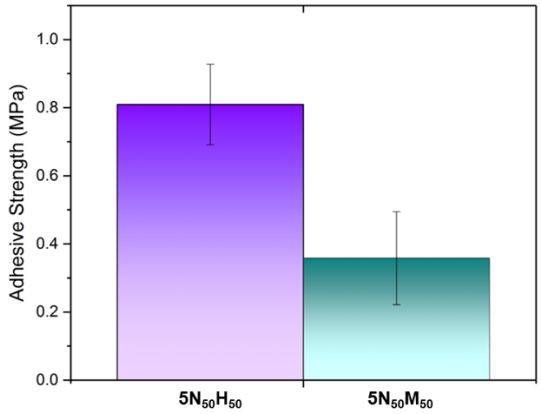

Figure 5.16. Graphical comparison of adhesive strength of **$5N_{50}H_{50}$** (violet) and **$5N_{50}M_{50}$** (cyan) binding two aluminum substrates adhered at 200 °C. Test parameters: adhesive area = 0.3 cm^2; strain rate = 1 mm/min.

Currently, the investigation of the thia-Michael/PMMS materials as adhesives has been localized to high surface energy substrates (i.e. aluminum and stainless steel). However,

throughout the course of these studies, qualitative explorations have revealed that the films have the ability to adhere to a range of surface energies and topologies. The photograph below (Figure 5.17) demonstrates a single strip of **5N$_{50}$H$_{50}$** holding (from left to right) a Styrofoam cube, a strip of aluminum foil, a glass microscope slide, and a strip of PTFE, all of which were simple pressed to the adhesive surface at room temperature. Although these results are merely preliminary demonstrations, they reveal a great deal of potential for future applications of the dynamic thia-Michael materials as multi-functional adhesives.

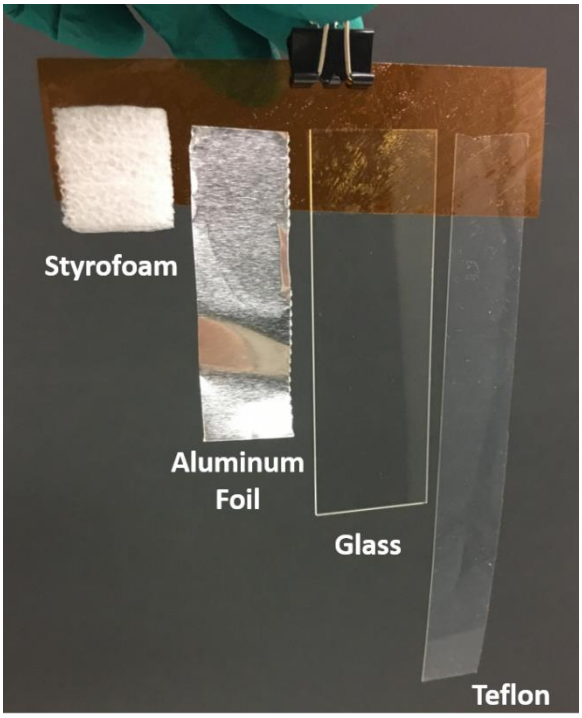

Figure 5.17. Photograph of various substrates pressed and adhered to **5N$_{50}$H$_{50}$.**

5.3 Conclusions

Hybrid thia-Michael networks composed of an oligomeric thiol component (PMMS) demonstrated the ability to function as multi-stage adhesives. Their viscoelastic behavior at room

temperature met the Dahlquist criterion (modulus < 3 x 10^5 Pa at a testing frequency of 1.0 rad/s) indicating their potential for use as pressure sensitive adhesives (PSAs). Small angle oscillatory shear rheology near the operating temperature established a viscoelastic window for the two materials that highlighted their ability to act as high shear PSAs. In addition to their PSA properties, the adhesives demonstrated viscoelastic flow at elevated temperatures (>150 °C) making them also candidates for hot-melt adhesives. Both pressure sensitive and hot-melt adhesive behavior was evaluated using tensile techniques (tack test and 180° peel test for PSA and normal force test for hot-melt adhesion) that demonstrated the multi-stage adhesive characteristics of hybrid thia-Michael networks.

5.4 Experimental Methods

Raman Spectroscopy

Raman spectroscopy was conducted using a Horiba LabRamHR Evolution confocal Raman microscope in the Materials Preparation and Measurement Laboratory (MPML) that is part of the NSF Materials Research Science and Engineering Center (MRSEC) at the University of Chicago. Data was collected using a Horiba Synapse OE CCD detector and a 633 nm laser source. The spectral range of 400 – 3300 cm^{-1} was probed for all samples using 4 windows with 60 accumulations per window. (Other testing parameters: Objective = 50x LWD [long working distance]; grating = 600 gr/mm; ND Filter (i.e. laser power) = 50%; acquisition time = 1 second; RTD time = 1 second; Hole size = 100)

Raw data collected on the instrument was processed using OriginPro 2017 v9.40 by OriginLab Corporation. For each sample, data was first smoothed using the Savitzky-Golay

method (window of 10 points; 2nd order polynomial fit). The baseline of the smoothed data was calculated using the asymmetric least squares method (parameters: asymmetric factor = 0.001; threshold = 0.01; smoothing factor = 4; iterations = 10) in the software's Peak Analyzer function and then subtracted from the smoothed data. The smoothed, baseline corrected data was then normalized using the standard normal variate (SNV) method in which the Raman intensities of the sample were divided by the standard deviation of the Raman intensities over the entire frequency range of the spectrum.

Optical Microscopy (AFM)

Thermogravimetric Analysis (TGA)

Thermogravimetric analysis was performed using a TA Instruments Discovery Thermogravimetric Analyzer in the Soft Matter Characterization Facility at the University of Chicago. Samples were tested under nitrogen atmosphere using platinum pans. Tests were conducted using a ramp of 10 °C/min from starting operating temperature (ca. 35 °C) to 600 °C.

Differential Scanning Calorimetry (DSC)

DSC was performed using a TA Instruments Discovery 2500 Differential Scanning Calorimeter in the Soft Matter Characterization Facility at the University of Chicago. Samples were prepared in aluminum hermetic pans from TA Instruments and were hermetically sealed. Typical test conditions involved a cool-heat-cool-heat procedure from (-20 °C/200 °C/-80 °C/200 °C) run at 10 °C/min.

Small amplitude oscillatory shear (SAOS) rheology

Shear rheology sample loading

Rheology was performed using the TA Instruments RSA-G2 ARES with Forced Convection oven (20 °C – 500 °C) attached to an Air Chiller System (-120 °C – 20 °C) and running TA Trios Software in the Soft Matter Characterization Facility at the University of Chicago. An 8 mm parallel plate was used for all tests.

Samples were cut from a larger film into 8 mm disks approximately 400-600 um thick. The samples were loaded onto an 8 mm stainless steel parallel plate geometry equipped with thermocouples and trimmed of any excess overlap. The loaded sample was heated to 200 °C using a forced convection oven and the gap was manually controlled to minimize normal force, yet retain contact with both plates. At 200 °C, the sample was a viscous liquid. After approximately 30 seconds at 200 °C, the sample was subject to 1.0 rad/s steady shear for 10 seconds to remove any inhomogeneity or bubbles. After 10 seconds, the shearing was halted, and the axial position was adjusted to ensure the sample was flush with the edges of the 8 mm plate. Satisfied with the sample configuration, the temperature in the oven was cooled in 10 °C increments until 0.01N axial force could be applied (if the temperature was too high, 0.01N axial force caused the sample to seep out of the geometry, creating erroneous conditions for testing). Once the sample was stable enough to be tested, an Isoforce (0.01 N) temperature ramp of 3 °C/min was used to bring the sample to the lowest testing temperature. At the lowest temperature, the axial force was set to automatically maintain 0.1 N (± 0.05 N) compressive force on the sample, ensuring good contact throughout the tests.

Small amplitude oscillatory shear frequency sweeps

The sample was equilibrated at testing temperature for 5 minutes before the experiment was started. After equilibration, a frequency sweep from 0.01 rad/s to 100.0 rad/s was done at 1.0% strain. Subsequent sweeps were conducted by increasing the temperature by 5 °C and re-equilibrating for 5 minutes before beginning the frequency experiment.

Tensile analysis

Tensile analysis was performed using a Zwick-Roell zwickiLine Z0.5 Materials Testing Instrument with a 100N load cell in the Soft Matter Characterization Facility at the University of Chicago.

5.5 References

(1) Lafont, U.; van Zeijl, H.; van der Zwaag, S. Influence of Cross-Linkers on the Cohesive and Adhesive Self-Healing Ability of Polysulfide-Based Thermosets. *ACS Appl. Mater. Interfaces* **2012**, *4* (11), 6280–6288.

(2) Meng, Y. Z.; Tjong, S. C.; Hay, A. S. Synthesis of Cocyclic(Arylene Disulfide) Oligomers and Their Adhesion Properties as Heating-Melt Adhesive. *Polymer* **2001**, *42* (12), 5215–5224.

(3) Abdolah Zadeh, M.; van der Zwaag, S.; Garcia, S. J. Adhesion and Long-Term Barrier Restoration of Intrinsic Self-Healing Hybrid Sol–Gel Coatings. *ACS Appl. Mater. Interfaces* **2016**, *8* (6), 4126–4136.

(4) Aubert, J. H. Note: Thermally Removable Epoxy Adhesives Incorporating Thermally Reversible Diels-Alder Adducts. *J. Adhes.* **2003**, *79* (6), 609–616.

(5) Heinzmann, C.; Weder, C.; de Espinosa, L. M. Supramolecular Polymer Adhesives: Advanced Materials Inspired by Nature. *Chem. Soc. Rev.* **2016**, *45* (2), 342–358.

(6) T. Michal, B.; J. Spencer, E.; J. Rowan, S. Stimuli-Responsive Reversible Two-Level Adhesion from a Structurally Dynamic Shape-Memory Polymer. *ACS Appl. Mater. Interfaces* **2016**, *8* (17), 11041–11049.

(7) Cudjoe, E.; Herbert, K. M.; Rowan, S. J. Strong, Rebondable, Dynamic Cross-Linked Cellulose Nanocrystal Polymer Nanocomposite Adhesives. *ACS Appl. Mater. Interfaces* **2018**, *10* (36).

(8) Courtois, J.; Baroudi, I.; Nouvel, N.; Degrandi, E.; Pensec, S.; Ducouret, G.; Chanéac, C.; Bouteiller, L.; Creton, C. Supramolecular Soft Adhesive Materials. *Adv. Funct. Mater.* **2010**, *20* (11), 1803–1811.

(9) Chakma, P.; Konkolewicz, D. Dynamic Covalent Bonds in Polymeric Materials. *Angew. Chemie Int. Ed.* **2019**, *0* (0).

(10) Jin, Y.; Yu, C.; Denman, R. J.; Zhang, W. Recent Advances in Dynamic Covalent Chemistry. *Chem. Soc. Rev.* **2013**, *42* (16), 6634–6654.

(11) Rowan, S. J.; Cantrill, S. J.; Cousins, G. R. L.; Sanders, J. K. M.; Stoddart, J. F. Dynamic Covalent Chemistry. *Angew. Chemie Int. Ed.* **2002**, *41* (6), 898–952.

(12) J. Kloxin, C.; F. Scott, T.; J. Adzima, B.; N. Bowman, C. Covalent Adaptable Networks (CANs): A Unique Paradigm in Cross-Linked Polymers. *Macromolecules* **2010**, *43* (6), 2643–2653.

(13) Michal, B. T.; Spencer, E. J.; Rowan, S. J. Stimuli-Responsive Reversible Two-Level Adhesion from a Structurally Dynamic Shape-Memory Polymer. *ACS Appl. Mater.*

Interfaces **2016**, *8* (17), 11041–11049.

(14) Benedek, I. *Pressure-Sensitive Adhesives and Applications*, 2nd Editio.; CRC Press: New York, NY, 2004.

(15) Creton, C. Pressure-Sensitive Adhesives: An Introductory Course. *MRS Bull.* **2003**, *28* (6), 434–439.

(16) Skeist, I. *Handbook of Adhesives*, 3rd Editio.; Chapman & Hall: New York, 1989.

(17) Dahlquist, C. A. Pressure-Sensitive Adhesives. In *Treatise Adhes. Adhes.*; Marcel Dekker, Inc., 1969; Vol. 2, pp 219–260.

(18) Chang, E. P. Viscoelastic Windows of Pressure-Sensitive Adhesives. *J. Adhes.* **1991**, *34* (1–4), 189–200.

6 Towards the preparation of slide-ring gels utilizing doubly threaded [3]-rotaxane architectures

*The synthesis and characterization in this chapter was done in collaboration with Eric Bruckner whose Master's thesis compliments this work: Bruckner, E. P. Integrated synthetic and computational techniques for the design of poly[3]rotaxanes. Masters Thesis, Case Western Reserve University, Cleveland, OH 44106.

6.1 Introduction

In the continued pursuit of soft materials engineered with dynamic crosslinks, a new line of inquiry was started with an eye towards polymeric networks based on topologically bound compounds. Topologically interlocked compounds are held together by a mechanical bond defined by Stoddart, *et al*, as, "an entanglement in space between two or more molecular entities (component parts) such that they cannot be separated without breaking or distorting chemical bonds between atoms."[1] Architectures including catenanes, rotaxanes, and molecular knots, are all part of the mechanically interlocked family.[2] Rotaxanes and their relatives, in particular, have shown great potential for applications[3] that include dynamic signaling,[4] catalysis,[5] and molecular muscles.[6,7] While the historical focus on interlocked compounds has been on synthesis and theory, the path forward requires a fundamental understanding of their behavior in bulk materials. As such, the studies described herein look to move towards these fundamental studies by providing a foundation upon which future investigations of interlocked materials can be built.

These compounds are comprised of two key components: a dumbbell, which consists of large stopper groups (Figure 6.1A) attached to either end a linear molecule referred to as a thread (Figure 6.1B), and a macrocycle (Figure 6.1C). Together, one dumbbell and one macrocycle can form a [2]rotaxane (generic [2]rotaxane pictured in Figure 6.1D) whose structure is composed of two discrete molecules assembled to constitute a single, interlocked unit. Given the fact that covalent bonds must be broken to disassemble a [2]rotaxane, it acts as a single molecule rather than an assembly of individual components.

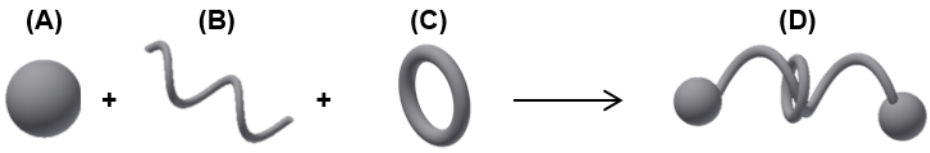

Figure 6.1. Schematic of a stopper group (A), thread (B), and macrocycle (C) to form a generalized [2]rotaxane (D).

While the utility of the rotaxane molecule has led to numerous applications of the individual species, the architecture also provides an intriguing route to mechanically interlocked polymer networks commonly known as slide-ring gels.[8] These slide-ring gels, so named for their uniquely mobile interlocked crosslinks, have been shown to exhibit fascinating mechanical properties due to their energy dissipating abilities.[9] Inspired by theoretical work by de Gennes,[10] successful reports of slide-ring gels prepared on laboratory as well as industrial scale have been documented throughout the last few decades. Important advancements in this area have been accomplished by implementing the popular self-assembly combination of α-cyclodextrin (α-CD) and polyethylene glycol (PEG) (Figure 6.2). The PEG chain is incorporated into the cavity of the

α-CD units via hydrophobic interactions between the polymer chain and the inner circumference of the macrocycle. In this way, multiple α-CD molecules can be introduced to the PEG chain, creating a polyrotaxane.[11] The α-CD can then be crosslinked to form a figure-eight crosslink that holds the chains together, but allows reptation through the rings.[12] Using this approach, Ito, *et al*, has described a "pulley effect" between the chains that contributes to the high extensibility and mechanical strength of the gels.[13,14] Rather than the stress of deformation being localized to the crosslinking bonds between chains, the PEG chains are able to slide through the α-CD rings,[15] allowing the stress to be dissipated throughout the entire material.

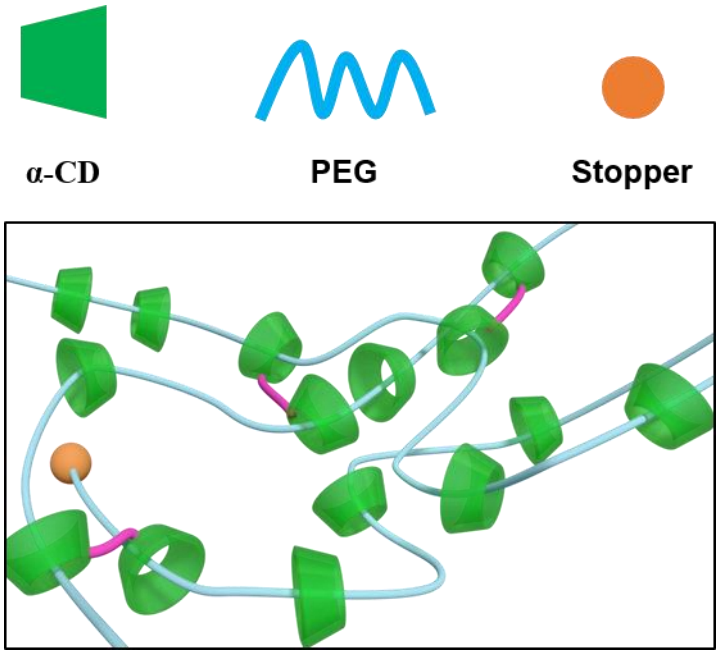

Figure 6.2. Cartoon depicting a slide-ring network formed via crosslinking (highlighted in pink) of α-CD on PEG chains to form polyrotaxane networks connected with mobile, topological bonds.

The success of the α-CD/PEG slide-ring materials has rapidly generated a host of investigations probing both the fundamental and applied aspects of the materials. Inspired by these results, we sought to probe a variant of the slide-ring gel that connects the unique mechanical behaviors of the topological networks with the stimuli-responsive behavior of a metal:ligand coordination bond. In the past, the 2,6-bis(N-alkyl-benzimidazolyl)pyridine (Bip) ligand, in coordination with several different metals (zinc, iron, europium, etc.), has demonstrated significant versatility as a stimuli-responsive motif.[16–18] In systems where it has been incorporated into a polymeric chain (i.e. metallo-supramolecular polymers, MSPs), the Bip:metal complex has been shown to respond to multiple stimuli including light, heat, and chemical treatments. In response to these stimuli, the polymeric materials have demonstrated healing, shape-memory, and changes in stiffness that are a result of the reversible association/dissociation of the metal:ligand interaction.

In addition to responsive behavior, the Bip ligand can be utilized in the metal-templated assembly of interlocked molecules. The assembly of components to construct an interlocked macromolecule can take on a wide variety of forms and employ equally diverse methodologies.[19] Where the α-CD/PEG systems takes advantage of host-guest supramolecular interactions to ensure that the PEG chain is threaded through the cyclodextrin molecule, metal-templating utilizes metal-ligand complexes to direct the assembly of an interlocked molecule. Pioneered through the works of Sauvage, metal-templating has been successfully implemented to form a variety interlocked structures.[20,21] As an example, Wu, *et al*, recently reported the formation of a metal-templated poly[n]catenane using bis-functionalized, Bip-based rings.[22] Self-assembly of the tridentate Bip-ligand into a 2:1 metal:ligand complex (Figure 6.3A) served as a driving force to promote the linkage of rings upon addition of a transition metal ion (Figure 6.3B). Using the metal-templated

technique for the construction of [3]-rotaxanes and slide ring gels provides a controlled, predictable method of assembly. This promotes a systematic approach to investigating the effect that variables such as crosslink density, polymeric backbone composition, and entropic effect of extra rings along a slide ring gel chain might have on the material properties of a resultant network.

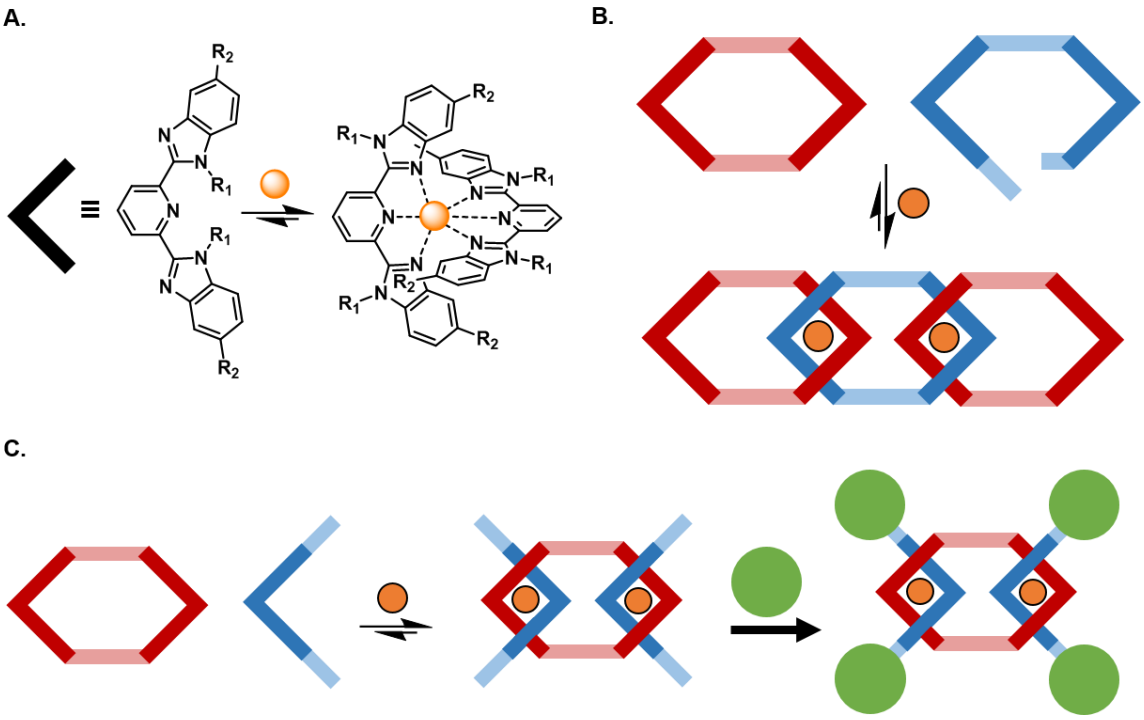

Figure 6.3. A) Chemical structure of Bip ligand and its 2:1 binding assembly with transition metal ions. B) Simplified schematic showing catenane self-assembly with Bip-metal coordination. C) Schematic depicting targeted [3]rotaxane assembly with Bip-metal coordination and stopper group addition.

Building on these developments, we identified an opportunity to expand the Bip-based topological motif into stimuli-responsive materials that included rotaxanes, polyrotaxanes, and

slide-ring gels. Whereas the poly[n]catenane focused on linking macrocycles together, the assembly of the rotaxane would consist of the ditopic macrocycle with two Bip-based dumbbells, forming a [3]rotaxane (Figure 6.3C). Alternatively, the pseudo[3]rotaxane (a metallated, interlocked molecule without stopper groups attached) could be used as a tetra-functional, topological crosslinker in polymer networks. We hypothesize that this Bip-based slide-ring material could mark the beginning of a host of explorations into multi-stimuli, multi-responsive topological gels whose unique mechanical properties could be coupled with tunable, reversible functionality.

In order to pursue these lines of inquiry, the first objective was to establish synthetic routes for the principal components of the interlocked structure, mainly the macrocycle, thread, and stopper groups. Second, the methodology for the metal-templated assembly of the [3]rotaxane needed to be determined as well as the characterization of the interlocked species. Finally, the integration of the topological bond into a polymeric system would complete the development of the slide-ring material and would open the door to further studies as to the functional and mechanical properties of the system. The study described herein focuses on these three primary objectives and lays the groundwork for future exploration of Bip-based slide-ring gels.

6.2 Results and Discussion

6.2.1 [3]Rotaxane component design

The targeted design of the doubly-threaded [3]rotaxane involved a ditopic macrocycle capable of binding two threading components that could then be stoppered with bulky end groups.

An integral component in this construction is the 2,6-bis(N-alkyl-benzimidazolyl)pyridine (Bip) ligand whose metal binding ability facilitates the templating process necessary to form the interlocked structure (Figure 6.3A). Following previously reported methods, a modified Bip ligand was synthesized in order to optimize its incorporation into the [3]rotaxane assembly.[22,23] The structure of the ligand was adapted to include an *N*-butyl chain at the $\mathbf{R_1}$ position to improve solubility and a phenol extension at the $\mathbf{R_2}$ position to promote further functionalization of the compound.

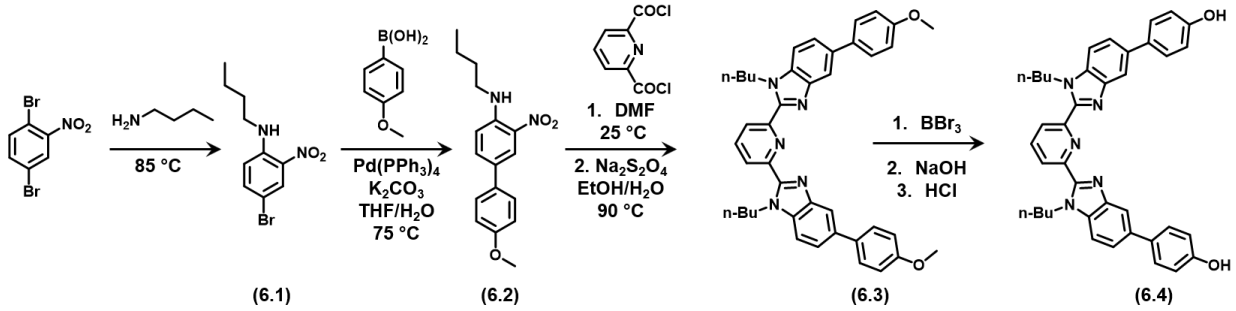

Scheme 6.1. Chemical structures and scheme for synthesis of modified Bip ligand, **6.4**.

The modified Bip was synthesized in four steps (Scheme 6.1, see Experimental section for detailed synthetic procedures and characterization). First, 2,5-dibromonitrobenzene was combined with 1-butylamine to form **6.1** in 90% yield. Next, a Suzuki reaction was carried out using equimolar quantities of **6.1** and 4-methoxyphenylboronic acid with a palladium catalyst (tetrakis(triphenylphosphine)palladium(0) ($Pd(PPh_3)_4$)) to yield the desired biphenyl derivative, **6.2** (85% yield). The ligand, **6.3**, was formed by combining two molar equivalents of **6.2** with 2,6-pyridinedicarbonyl dichloride in anhydrous dimethylformamide (DMF) to yield **6.3** in 70% yield

after purification. The targeted, hydroxylated compound was formed by exposing **6.3** to boron tribromide (BBr_3) in dichloromethane (DCM) under cold (0 °C water bath), inert conditions. The solution of **3** and BBr_3 was stirred for 24 hours and slowly warmed to room temperature over that time. The reaction was quenched in 1 M NaOH and neutralized. The resulting precipitate was collected and recrystallized in a solution of chloroform and methanol to obtain the final product, **6.4**, in 93% yield from **6.3**.

With the templating ligand in hand, the focus shifted to the selection and synthesis of the individual [3]rotaxane components. Previous work by Wu and Wojtecki extensively investigated the viability of a variety of ditopic macrocycles for catenane architectures.[24,25] Based on their observations, the 68-membered macrocycle (count reflective of atoms constituting the inner circumference) (Figure 6.3, **6.5**) composed of tetraethylene glycol linkers (4PEG) connecting two molecules of **6.4**, was chosen as the initial interlocking component in the [3]rotaxane. Its solubility in organic solvents, ability to allow threading of two Bip-based moieties, and its inability to self-bind in the presence of a single metal made it a suitable candidate for the [3]rotaxane assembly.[11] The synthesis of the macrocycle was conducted by Dr. Qiong Wu following procedures reported for the poly[n]catenane (see Supplemental Methods for full details).

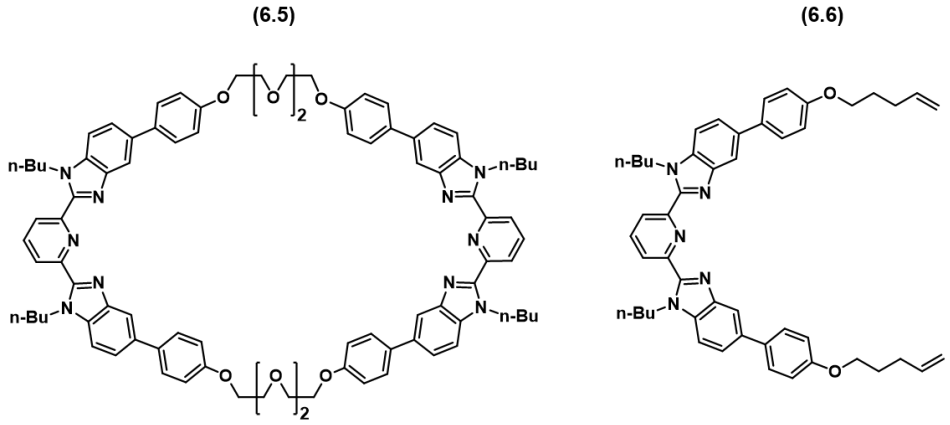

Figure 6.4. Chemical structures of the 4PEG macrocycle **(6.5)** and alkene-terminated thread **(6.6)**.

The thread molecule (**6.6**) was derived from the same ligand (**6.4**) utilized for the formation of **6.5**. The *N*-butyl functionality on the ligand had previously been shown to fit into a 68-membered ring in addition to the advantages imparted on the molecule given the improved solubility in organic solvents.[22,24,25] In order to make the component accessible to a variety of facile reaction conditions (including thiol-ene click reactions) both ends of the ligand were modified with an alkene-terminated 5-carbon extension that would promote future utility. The thread was synthesized in one step as shown in Scheme 6.2. Following procedures for a typical Williamson-ether reaction, **6.4** was reacted with 3 equivalents of 5-bromo-1-pentene in a 3:1 solution of dimethylformamide/acetonitrile (DMF/MeCN) in the presence of excess potassium carbonate. Following 18 hours of stirring at 65 °C, the product, **6.6**, was isolated in 68% yield using silica gel column chromatography.

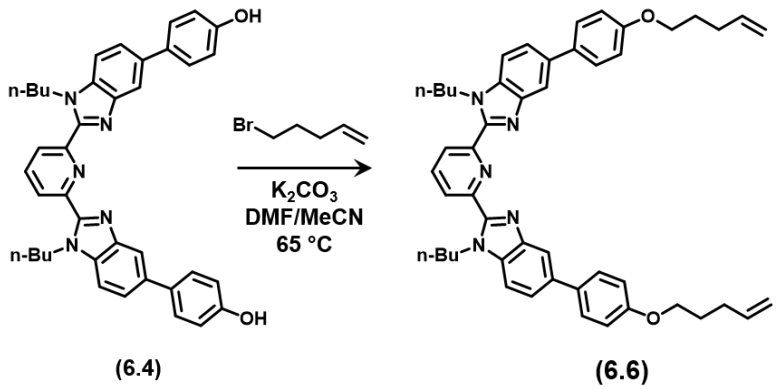

Scheme 6.2. Chemical structures and scheme for synthesis of thread compound (**6.6**).

The final component necessary for the [3]rotaxane assembly was the stopper group. As mentioned earlier, the key to the successful formation of a rotaxane is the ability of the end group to ensure that the macrocycle is confined to the length of the thread. Two different bulky molecules were synthesized and evaluated as stopper groups for the 4PEG macrocycle. The smaller, first generation stopper (Scheme 6.3, **6.7**) was composed of three, 4-*tert*-butyl-phenyl groups surrounding a carbon center.

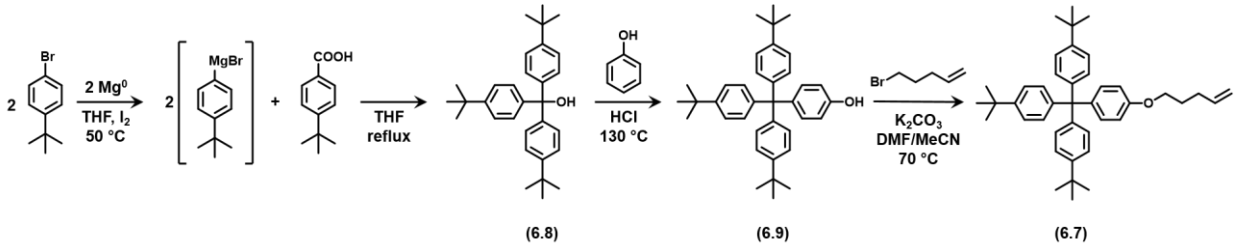

Scheme 6.3. Chemical structures and scheme for synthesis of 4-*tert*-butyl-phenyl stopper compound (**6.7**).

This stopper group was synthesized using three sequential reactions (Scheme 6.3). First, a Grignard reaction was preformed, initiated by the formation of the Grignard reagent of 1-bromo-4-*tert*-butylbenzene. Once the reagent was formed, methyl-4-*tert*-butyl benzoate was slowly added to the Grignard solution followed by 18 hours under reflux. Upon completion, the reaction mixture was quenched in an acidic ice bath and the tri-aryl compound, **6.8**, was isolated from the remaining material.

The second step of the stopper group formation involved a Friedel-Crafts reaction that introduced a phenol group to the tri-functional carbon center. **6.8** was dissolved in excess (ca. 10 eq.) phenol at 60 °C (above the melting point of phenol) along with a catalytic amount of 36% HCl. The system was flushed with argon and reacted at 110 °C for 24 hours while stirring. Once the reaction was finished, **6.9** was purified from the reaction.

Finally, the stopper group underwent a Williamson-ether reaction to functionalize the final compound with a terminal alkene. In the same manner as the alkene termination reaction for the thread compound, **6.9** was combined with 4 equivalents of 5-bromo-1-pentene and 4 equivalents of potassium carbonate in a 3:1 solution of DMF/MeCN at 65°C. After reacting for 18-24 hours, the first generation stopper, **6.7**, was extracted with dichloromethane and purified using silica gel column chromatography.

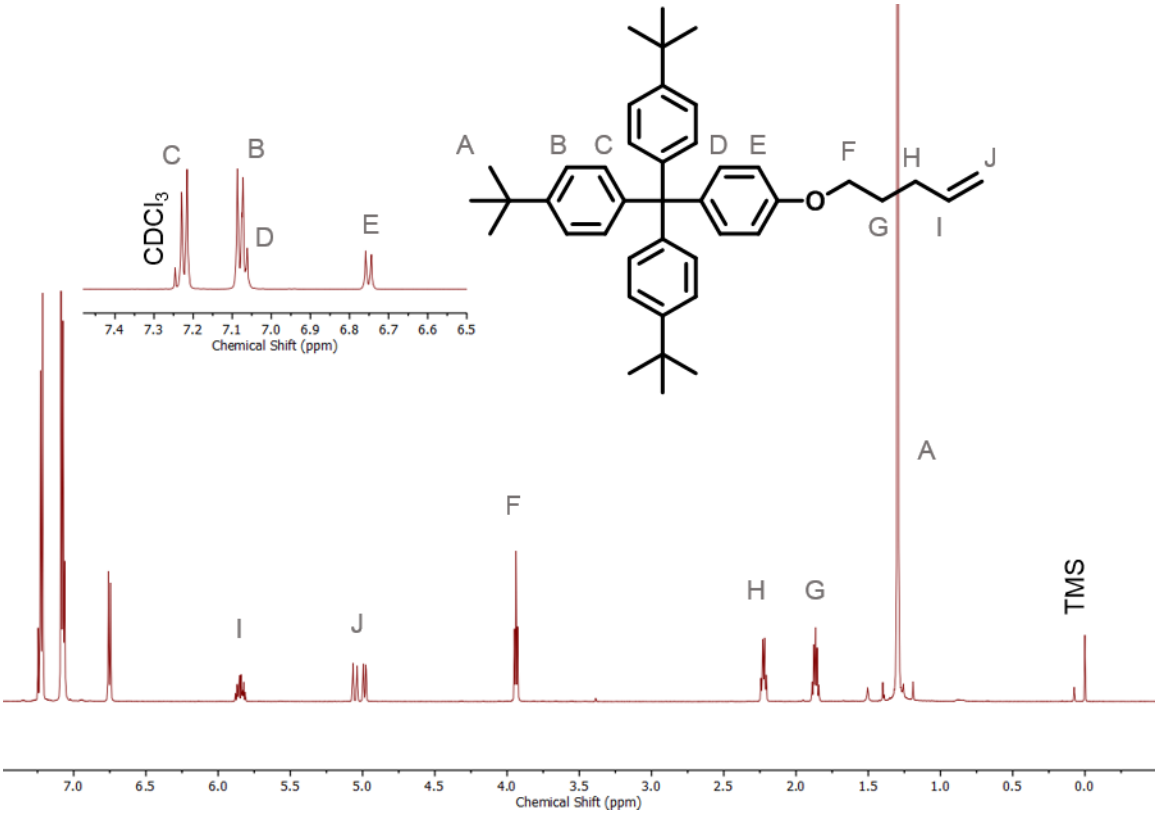

Figure 6.5. ^{1}H-NMR of 4-*tert*-butylphenyl stopper group (**6.7**). (600 MHz in $CDCl_3$)

The second generation stopper (Scheme 6.4, **6.10**) had a similar chemical structure as **6.7**, but with biphenyl substituents rather than single benzene rings. As with **6.7**, the formation of the larger stopper was done in three steps (Scheme 6.4). For the Grignard reaction, the Grignard reagent of 4-bromo-4'-*tert*-butylbiphenyl was reacted with diethyl carbonate following the same method as for **6.7** to form **6.11**. The Grignard reaction was followed by the Friedel-Crafts synthesis to yield **6.12** and then by the Williamson-ether reaction to finally arrive at **6.10**, again using the same conditions as for the smaller compound.

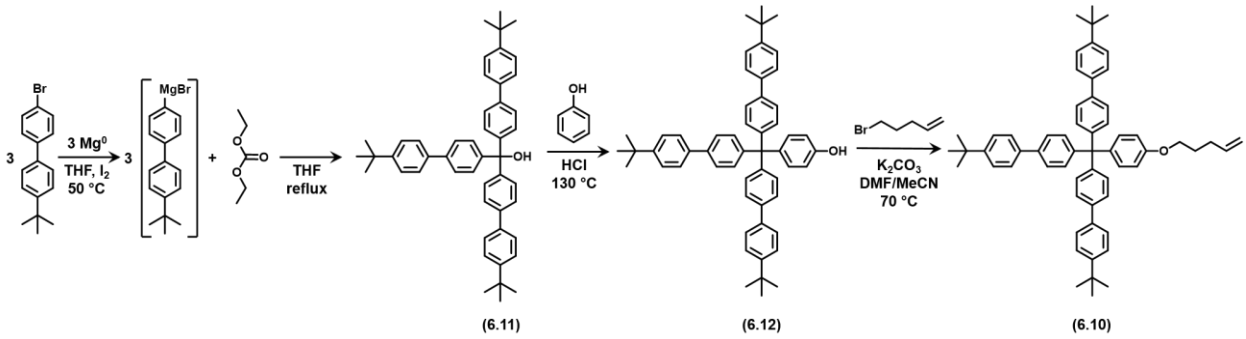

Scheme 6.4. Chemical structures and scheme for synthesis of 4-*tert*-butyl-biphenyl stopper compound (**6.10**).

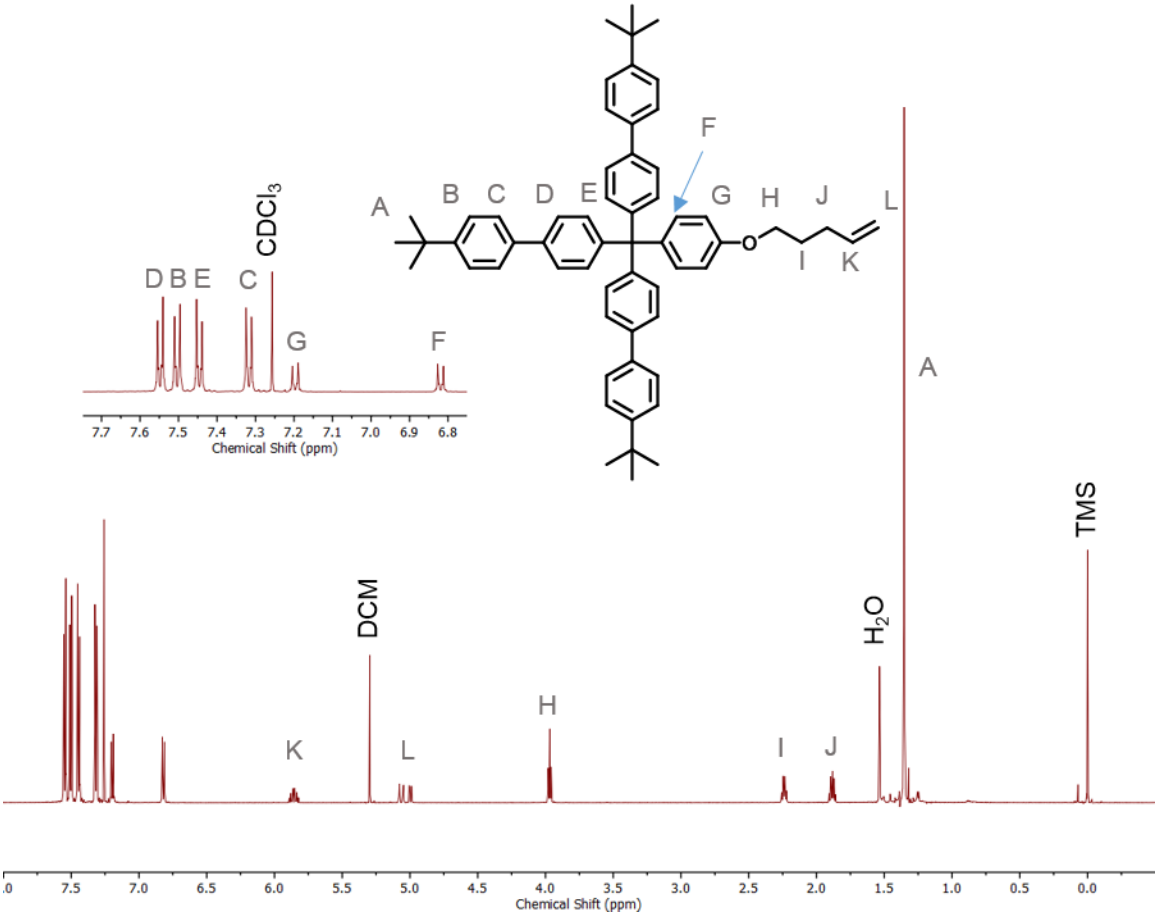

Figure 6.6. ^{1}H NMR of biphenyl stopper group, **6.10**. (600 MHz in $CDCl_3$)

6.2.2 Metal-templated assembly of pseudo[3]rotaxane

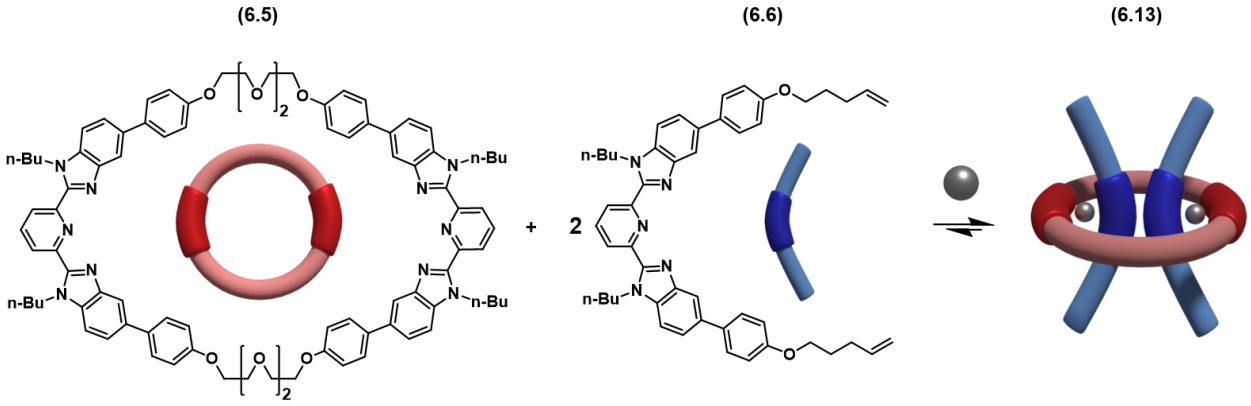

Figure 6.7. Schematic assembly of pseudo[3]rotaxane (**6.13**).

The assembly of the precursor, pseudo[3]rotaxane, **6.13** (Figure 6.7), (pseudo indicating that there is no stoppering group present) was carefully monitored using proton nuclear magnetic spectroscopy (^{1}H NMR) (Figure 6.8). A solution of **6.6** in deuterated chloroform ($CDCl_3$, 20 mg/mL) was titrated in 20 µL aliquots into an NMR tube containing a solution of **6.5** in $CDCl_3$ (10 mg/mL). Peaks corresponding to protons at the 3- and 4-position of the Bip pyridine were located 8.30 ppm ($2H_b$; *d*, 2H per thread) and 8.02 ppm ($2H_a$; *t*, 1H per thread) for **6.6** and 8.35 ppm ($1H_b$; *d*, 4H per macrocycle) and 8.07 ppm ($1H_b$; *t*, 2H per macrocycle) for **6.5**. The titration proceeded until the integration of the pyridine protons from the thread and macrocycle were equivalent, indicating a 2:1 ratio of thread:macrocycle (i.e. one thread-Bip per every macrocycle-Bip).

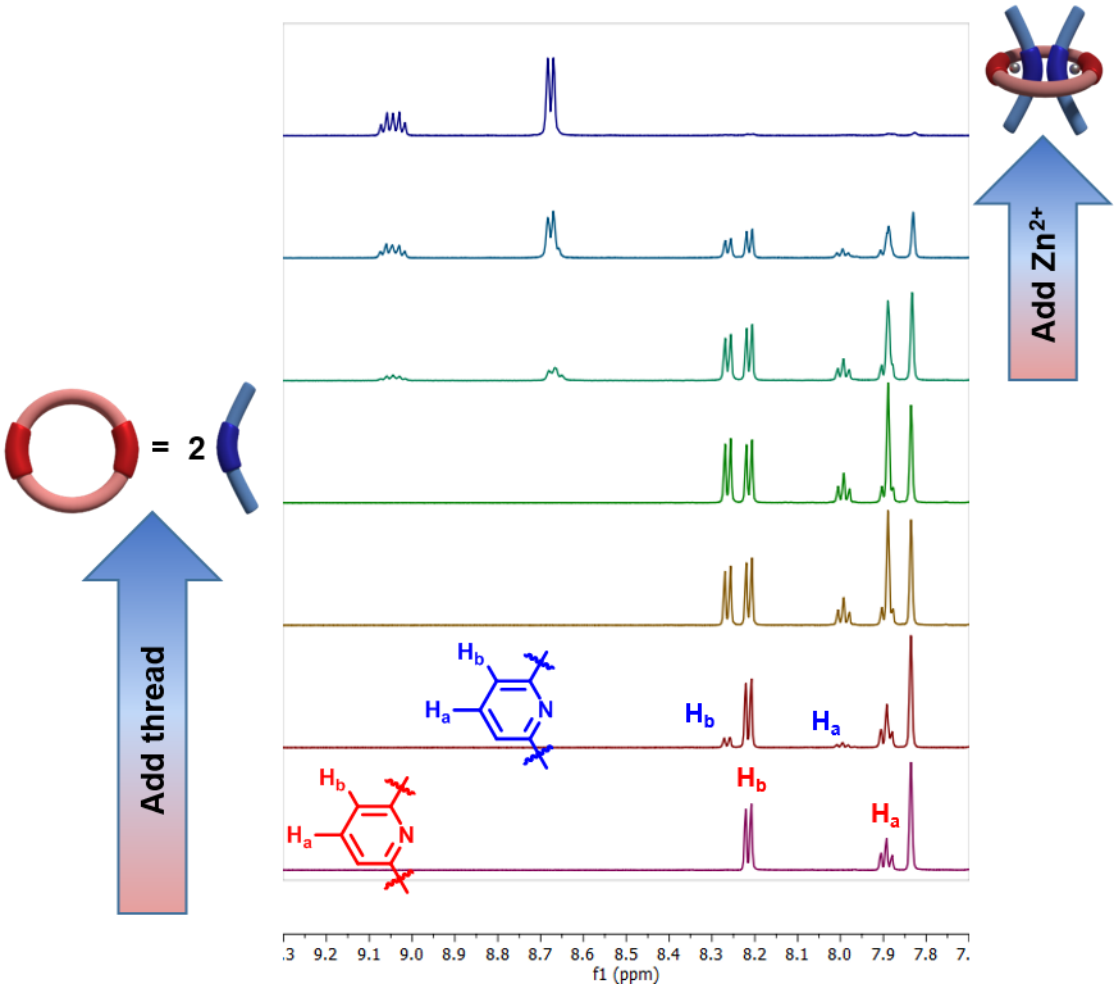

Figure 6.8. ^{1}H-NMR spectra showing assembly process of **6.13**. *From bottom to top* Pyridine peaks for free macrocycle (**6.5**, red) are integrated versus free thread peaks (**6.6**, blue) as the thread is titrated into the solution of macrocycle. Once the integrations are equivalent, Zn^{2+}, is added to the solution and the pyridinal peaks shift upfield until the free species are no longer present. (Solvent = $CDCl_3$ (+CD_3CN with Zn^{2+} addition), 600 MHz NMR, 25 °C)

Once a 2:1 ratio of the organic components was achieved, a solution of zinc bistriflimide ($Zn(NTf_2)_2$) in deuterated acetonitrile (d_3-MeCN) was titrated into the thread/macrocycle solution in 40 µL aliquots. Bip is known to bind to Zn^{2+} metal ions in a 2:1 stoichiometry and as such, the

ligands contained within the thread and macrocycle were assembled in an interconnected, 2:1 fashion. With increasing amounts of $Zn(NTf_2)_2$, the ^{1}H-NMR pyridine peaks shifted upfield as the metal-ligand complexes were formed until no free ligand remained (Figure 6.7). The fully metallated pseudo[3]rotaxane was then isolated from solution using rotary evaporation yielding a quantitative formation of **6.13**.

6.2.3 Towards the assembly of the [3]rotaxane

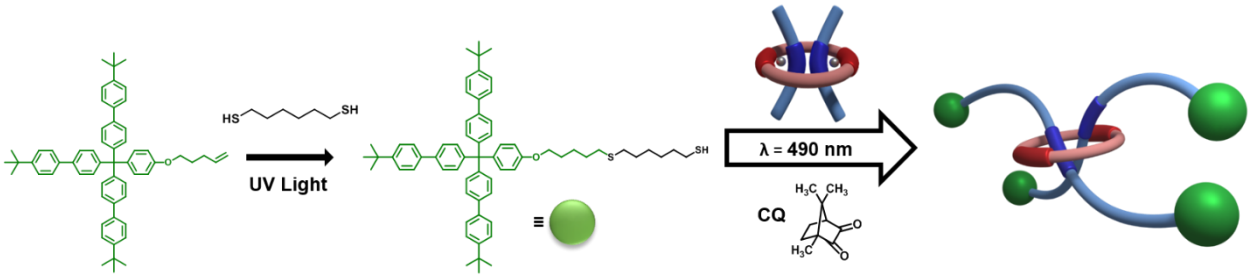

Figure 6.9. Schematic of the proposed assembly of a doubly threaded [3]rotaxane.

In order to construct a [3]rotaxane, the stopper group molecules were extended using 1,6-hexanedithiol to impart a thiol functional group to the terminus of **6.7** and **6.10** to yield **6.14** and **6.15**, respectively (Figure 6.10). To synthesize the thiol terminated compounds, **6.7** (or **6.10**) was combined with an excess of 1,6-hexanedithiol in DCM. A catalytic quantity of the photoinititor Irgacure-19® (IR-19, phenylbis(2,4,6-trimethylbenzoyl)phosphine oxide) was added and the solution was exposed to high intensity UV light (320-390 nm, 50 mW/cm^2) for 1 hour. The thiol-ene product was precipitated in cold hexanes and **6.14** (or **6.15**) was isolated via vacuum filtration.

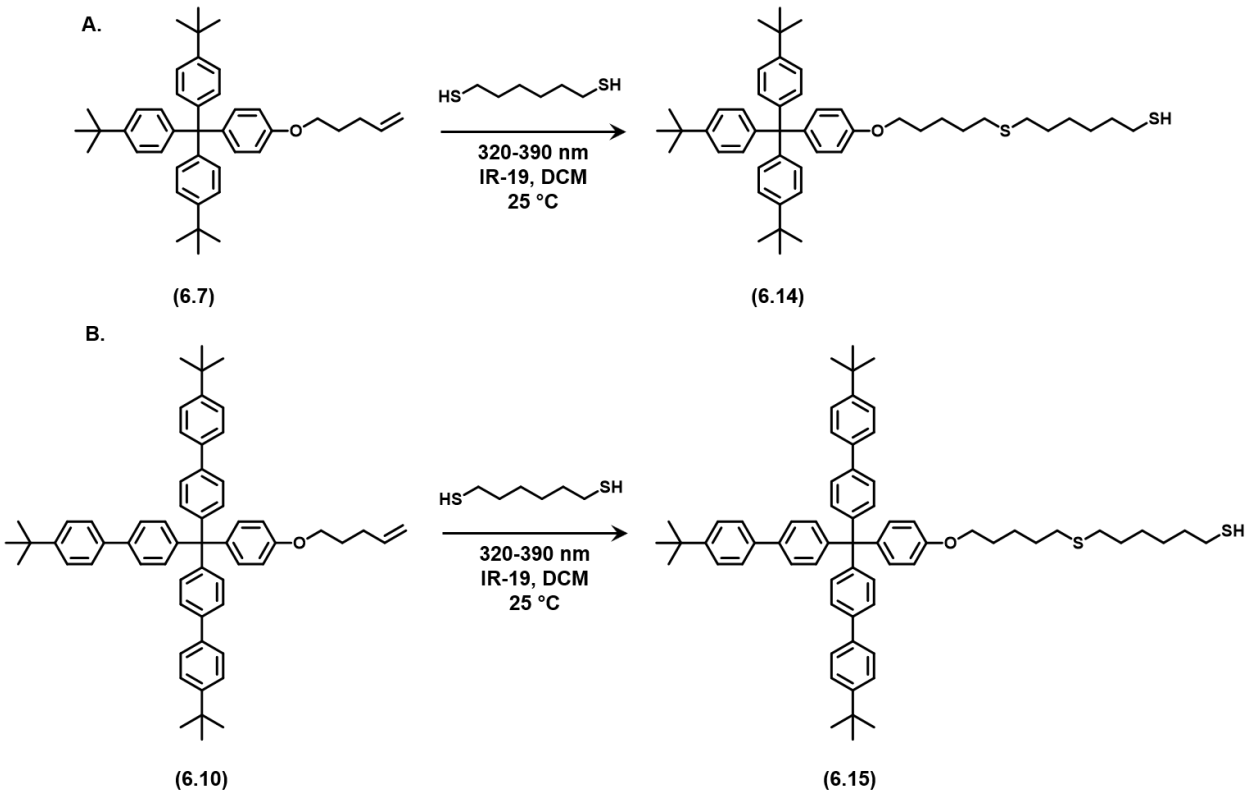

Figure 6.10. Addition of thiol end group to stopper compounds by reaction of 1,6-hexanedithiol with **6.7** (A) and **6.10** (B) under photoinitiated thiol-ene conditions.

This thiol functionality created an opportunity to utilize thiol-ene reactions to attach the stopper to the end of each thread. However, by using a metal-templated approach for the formation of the pseudo[3]rotaxane, there arose some complications in the application of the classic thiol-ene conditions. In particular, the Bip:Zn^{2+} complex is known to absorb light between the wavelengths of ca. 200-375 nm.[26] This absorption spans much of the ultraviolet (UV) light spectrum, thereby limiting the ability of any UV-activated thiol-ene initiators (such as the Irgacure-19® used for the thiol addition to the stopper group and thiol oligomer synthesis) to absorb enough energy to produce the radicals necessary for the reaction to take place. Therefore, alternative

methods for thiol-ene initiating were explored including thermal initiation (azobisisobutyronitrile, AIBN), redox initiation (benzoyl peroxide, BPO), and blue light initiation (camphorquinone, CQ). By using **6.13** in combination with stopper group (1:1 molar ratio of thiol:ene) and a catalytic quantity of initiator (see Experimental section 5.5.8 for detailed procedures), the subsequent thiol-ene reactions were monitored using ^{1}H-NMR. Table 6.1 summarizes the conversion capabilities of the different initiating methods.

Table 6.1. Efficacy of various thiol-ene initiators to initiate thiol-ene in the presence of Bip:Zn^{2+} complex.

Initiator	**% Conversion***	**Notes**
IR-19	0 %	UV-light is absorbed by the Bip:Zn^{+} complex
AIBN	0 %	After heating, no macrocycle Bip:Zn^{2+} interactions visible; only thread Bip:Zn^{2+}
BPO	0 %	Complex disrupted during reaction, macrocycle partially removed
CQ	30 – 95 %	Some complex disruption with long, high intensity exposure to light

*Calculated based on integration of 4-pyridine triplet and 2-alkene multiplet.

These studies served to shed light on the complexity associated with carrying out a thiol-ene reaction in the presence of **6.13**. The Zn^{2+} complex with Bip is reported to have a binding constant on the order of ca. 10^{6} M^{-1} which should be sufficient to firmly bind **6.13** in place.[27] However, the Bip:Zn^{2+} complex is also reported to be stimuli responsive, which creates a narrow window to define working conditions for the stoppering reaction. As shown in Table 6.1, while the thiol-ene conditions associated with CQ are capable of disrupting the metal-ligand complex

(as noted by the broadening of peaks associated with the complex and by the reappearance of free macrocycle in ^{1}H-NMR), it was the only initiator tested that showed any ability to initiate the thiol-ene reaction.

The first attempt at forming a [3]rotaxane was made using the smaller stopper group, **6.14**. 10 molar equivalents of **6.14** were added to 1 molar equivalent of **6.13** in 90 % deuterated dicholoromethane (d-DCM) with 10 % deuterated acetonitrile (d-MeCN) in a 1 dram vial. A catalytic amount of CQ was added to the solution as well as a magnetic stir bar. The vial was capped tightly and sealed with Teflon® tape. The solution was exposed to a UV light source (390 – 500 nm filter) situated 2 cm from the side of the vial while the solution stirred. After 1 hour of exposure, the solution was removed and evaluated. ^{1}H-NMR spectra of the crude reacted species (Figure 6.11, red spectra) revealed a completed reaction of the alkene peaks (6.0 – 4.8 ppm) and further showed that the reaction conditions were mild enough to keep the Bip:Zn^{2+} complex intact as evidenced by the remaining aromatic peaks associated with complexation (8.65 – 9.05 ppm).

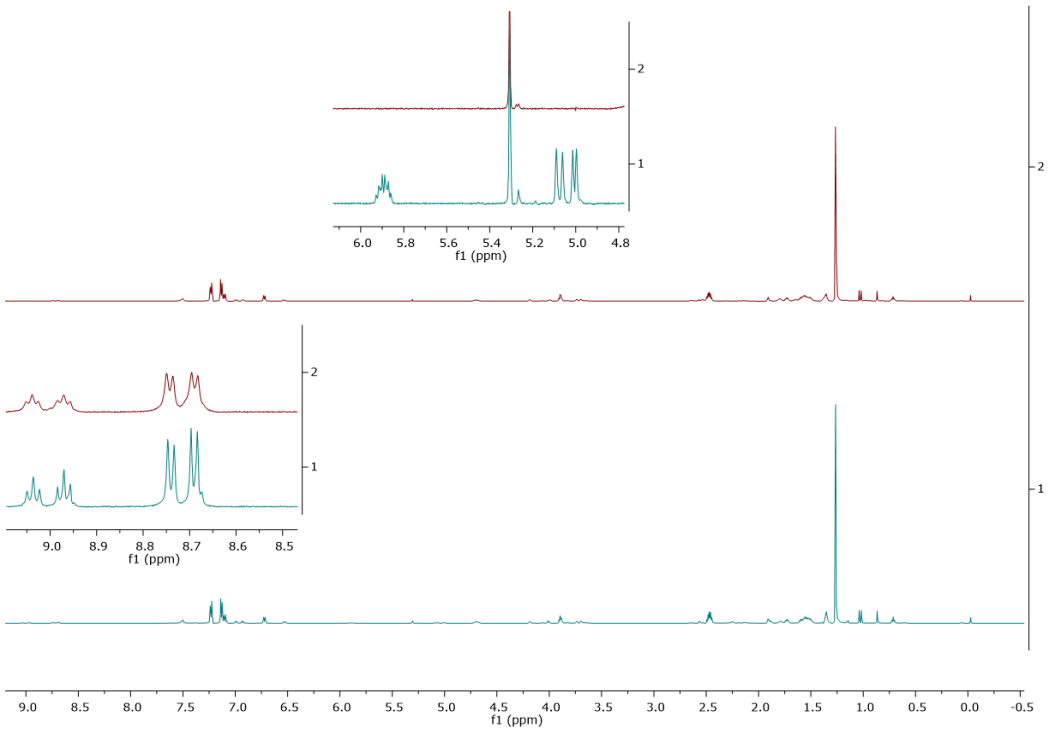

Figure 6.11. ^{1}H-NMR spectra tracking the thiol-ene reaction of **6.13** with **6.14**, specifically highlighting the presence of the alkene peaks between 6.0 – 4.8 ppm in the unreacted solution (bottom) which are absent after 1 hour of blue light treatment (top). The aromatic peaks corresponding to the metal-bound Bip remain intact after reaction.

Having verified the applicability of the CQ-initiated thiol-ene reaction, the metallated [3]rotaxane species was further purified via precipitation in ethyl ether. The ether mixture was refluxed for 3 hours to remove any residual contaminants and the product was isolated using vacuum filtration. The metal was then removed from the interlocked species using a bilayer extraction with the [3]rotaxane solubilized in DCM and stirred with a 1 M NaOH solution (1:1 vol/vol). Over the course of 1 hour, the organic solution went from yellow to colorless, indicating the loss of Bip-Zn^{2+} complex.

If the [3]rotaxane had been formed, it would be expected to maintain its interlocked structure after the removal of Zn^{2+}. Post-demetallation evaluation of this first [3]rotaxane revealed that this was not the case. ^{1}H-NMR spectrum of the demetallated species showed the Bip proton signals returning to their original shifts. TLC of the product revealed spots corresponding to macrocycle and dumbbell (thread with two stopper groups on either end) rather than to a single, interlocked molecule. MALDI-TOF mass spectroscopy further confirmed a lack of the targeted high molecular weight species, although the dumbbell and macrocycle (m/z 2161 and 1534, respectively) were noted (Figure 6.12). Based on this analysis, it was determined that **6.14** was not an effective stopper group for the 4PEG macrocycle.

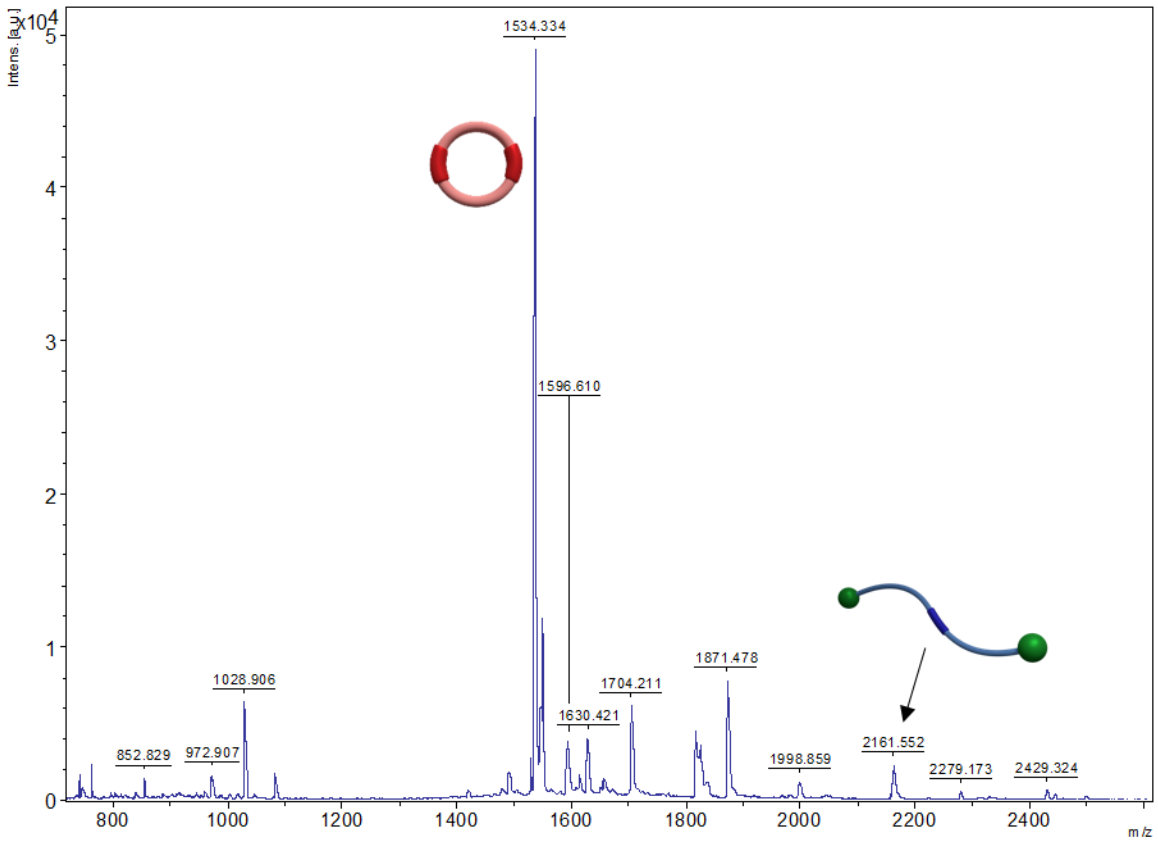

Figure 6.12. MALDI-TOF mass spectrum of demetallated [3]rotaxane using **6.14** as a stopper. Highlighted are the fragments associated with the macrocycle and dumbbell, indicating that the [3]rotaxane was not held together after Zn^{2+} was removed. (Linear positive mode, dithranol matrix, Na^{+} salt)

Moving forward, the stopper group size was increased by adopting **6.15**. Using similar methods as were used with **6.14**, the larger stopper was attached to the threads of **6.13** via thiol-ene click. Over the course of experimental optimization for the thiol-ene click reaction with **6.15**, the conditions were optimized to use CQ in equimolar quantities with **6.15**. Under these conditions, the reaction could proceed to >80% conversion, ensuring that a sufficient number of the alkene groups had been reacted to yield some [3]rotaxanes.

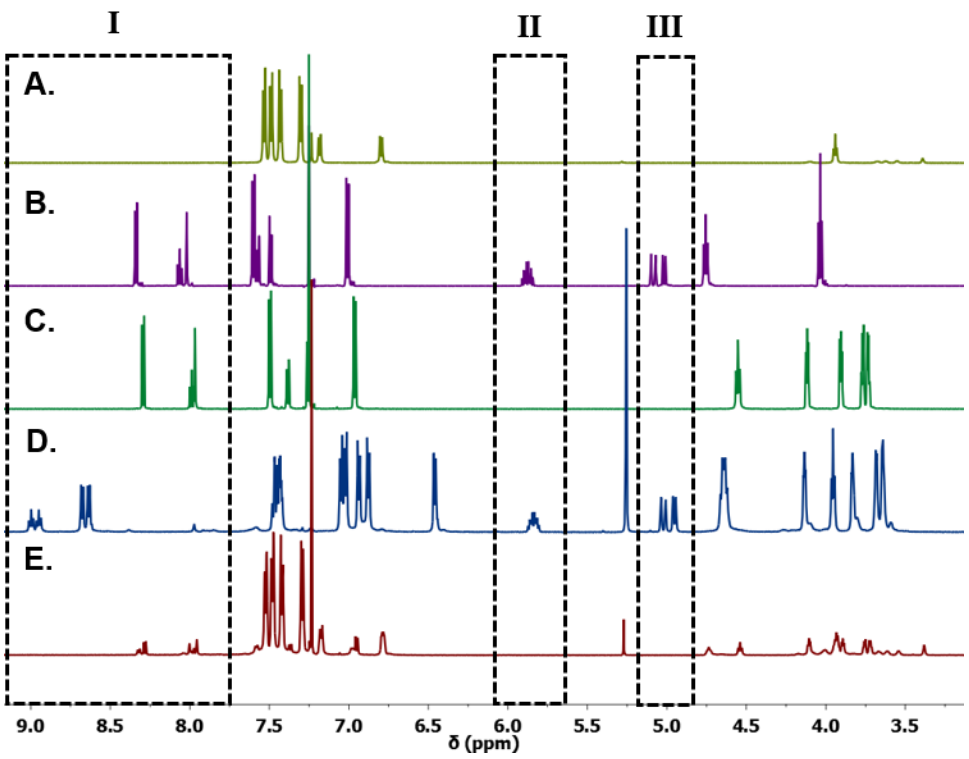

Figure 6.13. ^{1}H-NMR spectrum showing A) thiol-terminated stopper group **6.15**, B) thread **6.6**, C) 4PEG macrocycle **6.5**, D) metallated pseudo[3]rotaxane **6.13**, and E) demetallated [3]rotaxane. The spectra are highlighted to show the returned shift of the ligand peaks back to their original position (I) once the metal has been removed in E and the loss of the double bond peaks at 5.8 ppm (II) and 5.0 ppm (III) in E indicating a completed thiol-ene reaction. (Solvent = $CDCl_3$ A-C and E; d_2-DCM/MeCN for D); 600 MHz NMR; room temperature; Solvent peaks at 7.23 ppm for $CDCl_3$ and 5.31 ppm for DCM).

Once again, 1H-NMR was used to evaluate addition of the stopper group to the pseudo[3]rotaxane. Figure 6.14 presents a stack of relevant 1H-NMR spectra to highlight the changes associated with the formation of a [3]rotaxane molecule. Of particular note in comparing the final product (Figure 6.13E) to the preceding spectra is the return of the aromatic peaks from the Bip ligands to their original shifts after the metal was removed from the molecule (Figure 6.13,

I). Figure 6.13E also shows the absence of the peaks associated with the double bond at 5.8 ppm (*m*, 2H) (Figure 6.13, II) and 5.0 ppm (*dd*, 1H) (Figure 6.13, III) indicating the completion of the thiol-ene reaction. The initial evaluation of the [3]rotaxane by ^{1}H-NMR offers strong evidence that the stopper groups were indeed added to **6.13**, however, it does not provide concrete proof for the successful formation of an interlocked [3]rotaxane. The MALDI-TOF mass spectrum of the demetallated species shows the stopper group and macrocycle present in the product, as well as two higher molecular weight species in reflective mode. The likely architecture associated with the peak at m/z = 2445 is a [2]rotaxane with two zinc salts still associated with the compound. Table 6.2 lists possible m/z values for likely combinations of [3]rotaxane components and charged species. While not an exhaustive list (Table 6.2 excludes the many fragmented species that may be possible), it does provide some insight as to the many potential m/z variations that could be detected over the course of a [3]rotaxane evaluation. Unfortunately, there is no evidence of the formation of a [3]rotaxane, however, the current methodology developed throughout the course of this study provides a platform upon which future generations of [3]rotaxanes can be developed.

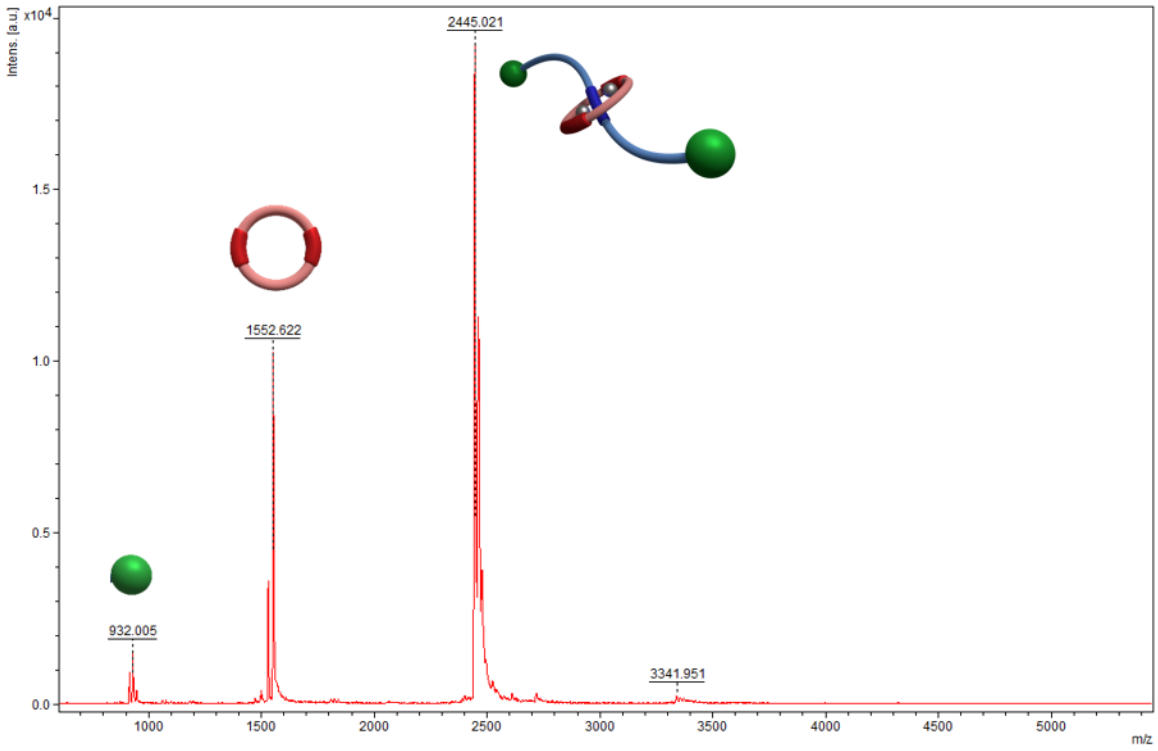

Figure 6.14. MALDI-TOF mass spectrum of products following [3]rotaxane formation attempt with **6.13** and **6.15**. (Positive reflective mode, matrix = dithranol, salt = Na^+)

Table 6.2. Potential m/z values for [3]Rotaxane system components with **6.13** and **6.15**.

	H^+	**$[Zn^{2+}(NTf_2)]^+$**	**Zn^{2+}**	**$[2Zn^{2+}2(NTf_2)]^{2+}$**	**$[2Zn^{2+}(NTf_2)]^+$**	**$2Zn^{2+}$**
[3]Rotaxane	6823.97	7168.48	3444.185	3756.5	2411.297	1738.445
[2]Rotaxane	4178.46	4522.97	2121.43	2433.745	1529.46	1077.068
2 Dumbells	5292.05	5636.56	2678.225	2990.54	1900.657	1355.465
Dumbell	2646.53	2991.04	1355.465	1667.78	1018.817	694.085
Macrocycle	1532.94	1877.45	798.67	1110.985	647.62	415.6875

6.2.4 Initial studies towards accessing slide-ring gels

In conjunction with the ongoing effort towards synthesizing a single [3]rotaxane molecule, steps were taken to initiate studies on gels crosslinked using the pseudo[3]rotaxane. The design of the slide-ring gels utilized a thiol-terminated oligomeric species to connect the pseudo[3]rotaxane crosslinks. Using previously reported methods, the thiol oligomer was synthesized using a UV-initiated thiol-ene reaction to combine 1,6-hexanedithiol and 1,5-hexadiene in a stepwise fashion. Briefly, the two components were combined in DCM with the UV initiator, Irgacure-19®. The solution was exposed to UV light for 1 hour and the resulting oligomer was precipitated in methanol, then isolated via vacuum filtration.

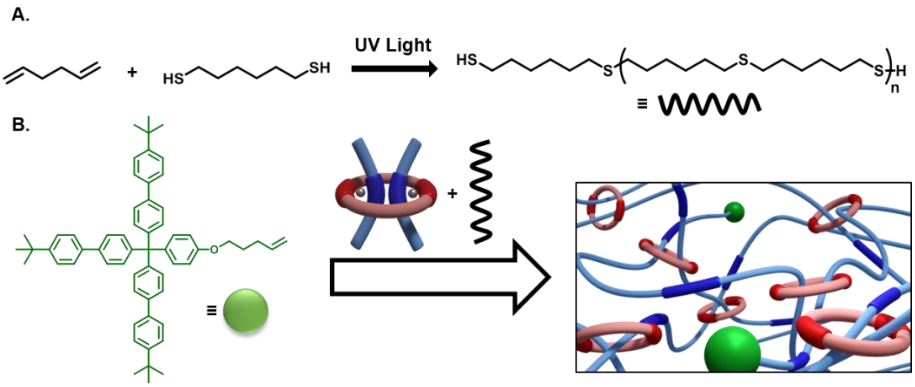

Figure 6.15. A) Reaction scheme for the synthesis of the thiol-terminated oligomer. B) General assembly of the slide-ring gel.

This thiol-terminated oligomer provided a means through which a crosslinked network could be formed through thiol-ene reaction with an alkene-terminated crosslinker. The pseudo[3]rotaxane assumed the role of a tetra-functional crosslinker and was combined with the

thiol-terminated oligomer under CQ-initiated conditions. 25 mg (5.85 μmol) of **6.13** and 21.89 mg (12.9 μmol, M_n = 1700 g/mol) of thiol oligomer were dissolved in 0.6 mL DCM/MeCN (9:1 v/v) with 4.28 mg CQ (25.8 μmol) in a 1 dram vial. The solution was exposed to blue light (390-500 nm, 50 mW/cm^2) for 1 hour, forming weak, yet cohesive gel. 1.88 mg (2.3 μmol) of **6.15** were dissolved in additional 0.6 mL of solvent along with 4.28 mg CQ and the solution was added to the existing gel. The system was exposed to blue light for another hour (Figure 6.17A), then the solvent was removed, resulting in a robust film (Figure 6.17B). However, the network dissolved upon addition of an ethylene diamine which is used to remove the metal ion from the network. Recalling the results of the [3]rotaxane small molecule trials whereby the current stoppering mechanism was found to be ineffective in sustaining a [3]rotaxane, it is hypothesized that the same issues are present within the gel. Although crosslinking between the metallated pseudo[3]rotaxane and the linear thiol component was sufficient to form a robust network (i.e. pseudo-slide-ring gel), the removal of the metal resulted in a disentanglement of the thread chains from the crosslinking macrocycles and subsequently, the gel dissolved. While this work holds much potential for exciting material studies, it is crucial to first confirm the formation of the [3]rotaxane before further progress can be made towards slide-ring gels.

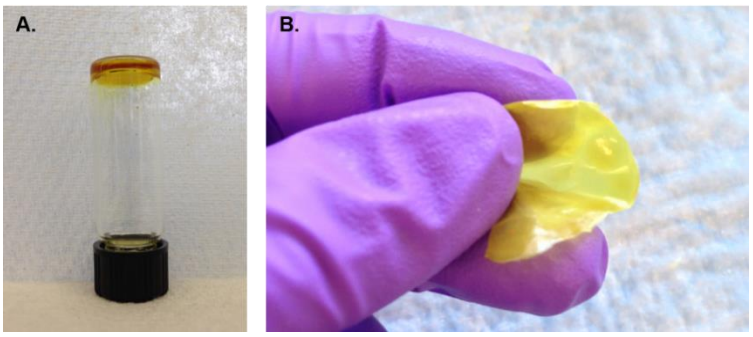

Figure 6.16. A) Metallated pseudo-slide-ring gel after blue light exposure. B) Metallated pseudo-slide-ring film after removal of solvent.

6.3 Conclusions

In this chapter, the synthetic groundwork for the construction of the [3]rotaxane molecule was established. Using a metal-templated approach, a pseudo[3]rotaxane was formed in quantitative yields, successfully combining a Bip-based thread with a ditopic macrocycle. The alkene functionality of the pseudo[3]rotaxane provides a convenient means by which to further utilized the metallated compound through thiol-ene reactions. Two bulky, tri-aryl compounds were synthesized and evaluated as stopper groups for the pseudo[3]rotaxane. By imparting both groups with thiol functionality, they were successfully attached to the termini of the pseudo[3]rotaxane using CQ-initiated thiol-ene reaction. Even with these bulky groups on either end of the thread moieties, the [3]rotaxane disassembled after the metal was removed, implying that the system requires further optimization of the macrocycle and stopper group combination in order to maintain an interlocked macromolecule.

Although the stoppering mechanism for the interlocked structure requires further investigation, the successful formation of a slide-ring gel precursor using the metallated pseudo[3]rotaxane creates a promising step forward in the evaluation of a topologically crosslinked network. In this effort, the CQ-initiated thiol-ene reaction was sufficient to establish a robust network between the pseudo[3]rotaxane and linear bis-functional thiol component. Upon the resolution of the stopper/macrocycle compatibility, future investigation into the slide-ring network will surely generate a host of intriguing results.

6.4 Future Work

The work detailed in this chapter has already spawned several new directions for future students. One of the primary thrusts in the new studies is the evaluation of different macrocycle sizes for the current system. Recent literature suggests that a macrocycle larger than 38 atoms (within the internal circumference) is not stoppered by the smaller stopper group (**13**).[28] As our currently selected macrocycle contains 68 atoms within the internal circumference, it is not entirely surprising that we have yet to isolate the proposed [3]rotaxane structure. With this in mind, it will be important to establish a minimum size of macrocycle in which two threads can still be incorporated, but the stopper still ensures that the assembly stays interlocked. That will provide a baseline from which new studies can grow that evaluate the effect of macrocycle size on properties in both the single interlock molecule and the slide-ring gels. These alternative sizes can be approached using a number of different methods including changing the linker (smaller PEG chains, ditopic phenyl units, etc.), eliminating the phenol extension on the Bip ligand, or altering the ligand itself.

Another optimization currently being investigated is the efficiency of the thiol-ene reaction. While the CQ conditions were shown to be adequate for reacting a majority of the alkene groups, the overall yield was certainly lacking, especially considering the thiol-ene reaction should be fast and quantitative. By utilizing different click reactions, such as Michael addition, Diels-Alder, or maleimide reactions, it may be possible to establish a means to attach the stopper groups in a more effective fashion.

6.5 Experimental Methods

6.5.1 Instrumentation

Matrix assisted laser desorption/ionization – time of flight (MALDI-TOF)

MALDI-TOF mass spectra was obtained using a Bruker AUTOFLEX III MALDI TOF/TOF mass spectrometer at Case Western Reserve University with 1,8-Dihydroxy-9(10H)-anthracenone (dithranol) as a matrix and sodium trifluoroacetate.

Nuclear magnetic resonance (NMR)

NMR spectra was obtained from a 600 MHz Varian Inova NMR spectrometer at Case Western Reserve University. NMR analysis was done using MNova Analysis software.

6.5.2 Synthesis of extended 2,6-bis(N-butyl-benzimidazolyl)pyridine (**6.4**)[23]

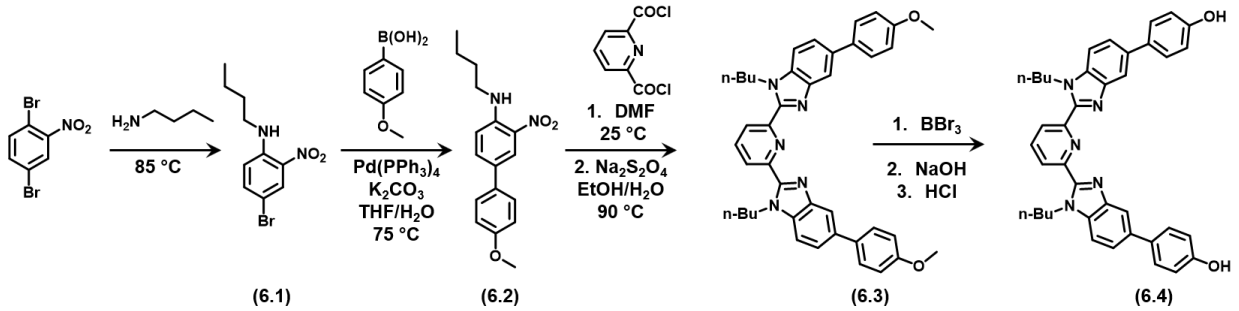

50 g (178 mmol) of 2,5-dibromonitrobenzene was combined with 150 mL of 1-butylamine in a 500 mL round bottom flask equipped with a magnetic stir bar and condenser. The solution was heated to 85 °C and stirred for 18 hours. The resulting orange solution was precipitated in 1L of ice water followed by an addition of 2 M HCl to neutralize the pH. The precipitate was collected via filtration and recrystallized in methanol to yield (ca. 90% by mass) product **6.1**. ^{1}H-NMR (500 MHz in $CDCl_3$; δ ppm: 1.01 (*t*, 3H), 1.50 (*m*, 2H), 1.74 (*m*, 2H), 3.37-3.27 (*m*, 2H), 6.79 (*d*, 1H), 7.51 (*dd*, 1H), 8.06 (*s*, 1H), 8.34 (*d*, 1H). ^{13}C-NMR (126 MHz in $CDCl_3$; δ ppm: 13.90, 20.34, 31.04, 43.02, 106.26, 115.68, 129.06, 132.14, 139.03, 144.66. MALDI-MS (295.2, $[M]+Na^+$).

30 g (109.8 mmol) of **6.1** was added to a 1L round bottom flask containing 16.9 g (110.9 mmol) of 4-methoxyphenylboronic acid, 138.2 g (440 mmol) of potassium carbonate, 360 mL of tetrahydrofuran and 180 mL of deionized water. The flask was equipped with a magnetic stir bar and condenser and the setup was purged (while stirring) with argon for 30 minutes. After 30 minutes, 0.64 g (0.55 mmol) of tetrakis(triphenylphosphine) palladium[0] catalyst was added, then

the reaction was heated to 75 °C and stirred for 24 hours under inert atmosphere. The resulting red solution was cooled to room temperature and the organic layer was collected using a separation funnel. The residual solvent was removed via rotary evaporation after which **6.2** was recrystallized from acetonitrile (yield = 85% by mass). ^{1}H-NMR (500 MHz in $CDCl_3$; δ ppm: 1.00 (*t*, 1H), 1.53-1.46 (*m*, 2H), 1.75 (*m*, 2H), 3.40-3.29 (*m*, 2H), 3.85 (*s*, 3H), 6.93 (*d*, 1H), 7.00-6.95 (*m*, 2H), 7.51-7.46 (*m*, 2H), 7.68 (*d*, 1H), 8.08 (*s*, 1H), 8.38 (*s*, 1H)). ^{13}C-NMR (126 MHz in $CDCl_3$; δ ppm: 13.91, 20.38, 31.21, 42.98, 55.49, 114.46, 114.48, 123.96, 127.38, 128.17, 131.62, 131.99, 134.88, 144.61, 159.14). MALDI-MS (323.3, $[M]+Na^+$).

20 g (78 mmol) of **6.2** was combined with 8 g (39 mmol) of 2,6-pyridinecarbonyl dicholoride in a 1 L round bottom flask with magnetic stir bar and flushed with argon. 200 mL of anhydrous dimethylformamide (DMF) was cannulated into the flask and the solution was stirred for 24 hours. Next, a solution of sodium hydrosulfite (33g, 188 mmol, saturated in 5:1 vol/vol solution of deionized H_2O/ethanol) and an additional 100 mL of DMF were added to the flask followed by the addition of a condenser to the top neck of the flask. The setup was flushed again with argon to re-establish inert atmosphere. The system was heated to 90 °C and stirred for 24 hours. After 24 hours, the solution was cooled to room temperature and refrigerated overnight (ca. 18 hours). The resulting precipitate was collected via vacuum filtration then boiled in choloroform and filtered once again to remove residual salts. The filtrate was dried using rotary evaporation and the product was recrystallized from chloroform/acetonitrile to yield (70% by mass) **6.3**. ^{1}H-NMR (500 MHz in $CDCl_3$; δ ppm: 0.73 (*d*, 2H), 1.11-1.19 (*m*, 4H), 1.71-1.79 (*m*, 4H), 3.88 (*s*, 6H), 7.01-7.04 (*m*, 4H), 7.50 (*d*, 2H), 7.58 (*dd*, 2H), 7.61-7.64 (*m*, 4H), 8.03 (*d*, 2H), 8.07 (*t*, 1H), 8.35 (*d*, 2H)). ^{13}C-NMR (126 MHz in $CDCl_3$; δ ppm: 13.66, 20.03, 32.32, 44.91, 55.51, 110.60,

114.43, 118.23, 123.25, 125.66, 128.53, 134.45, 135.63, 136.30, 138.30, 143.56, 150.14, 150.85, 159.05). MALDI-MS (636.4, $[M]+H^+$).

10 g of **6.3** was added to 150 mL of dicholoromethane (DCM) in a 500 mL round bottom flask with stir bar. The solution flushed with argon and cooled to 0 °C using an ice bath. While stirring the solution vigorously, 10 mL of boron tribromide were injected into the flask. (*CAUTION: boron tribromide is extremely reactive with water and will smoke even in the presence of humidity. Use appropriate precautions to avoid contact with water.*) The solution was allowed to naturally warm to room temperature with constant stirring over the course of 24 hours. The reaction was added to a 2 L beaker containing 1 L of 1 M NaOH solution and stirred until the mixture was yellow in color. Using 1 M HCl, the mixture was neutralized (pH = 7) and the product was collected via vacuum filtration. The crude product was recrystallized in chloroform/methanol to yield (89% by mass) **6.4**. ^{1}H-NMR (500 MHz in DMSO-d_6; δ ppm: 1.48 (*t*, 6H), 1.90 (*m*, 4H), 2.50 (*m*, 4H), 5.62 (*t*, 4H), 7.68-7.74 (*m*, 4H), 8.37-8.43 (*m*, 6H), 8.58 (*d*, 2H), 8.75 (*d*, 2H), 9.05-9.10 (*m*, 1H), 9.15-9.20 (*m*, 2H), 10.32 (*s*, 2H)). ^{13}C-NMR (126 MHz in DMSO-d_6; δ ppm: 13.20, 19.15, 31.69, 44.06, 54.88, 111.32, 115.70, 116.60, 122.36, 125.27, 127.95, 131.65, 135.15, 135.34, 138.74, 142.92, 149.55, 150.08, 156.71). MALDI-MS (608.4, $[M]+H^+$).

6.5.3 Synthesis of ditopic macrocycle (**6.5**)[10]

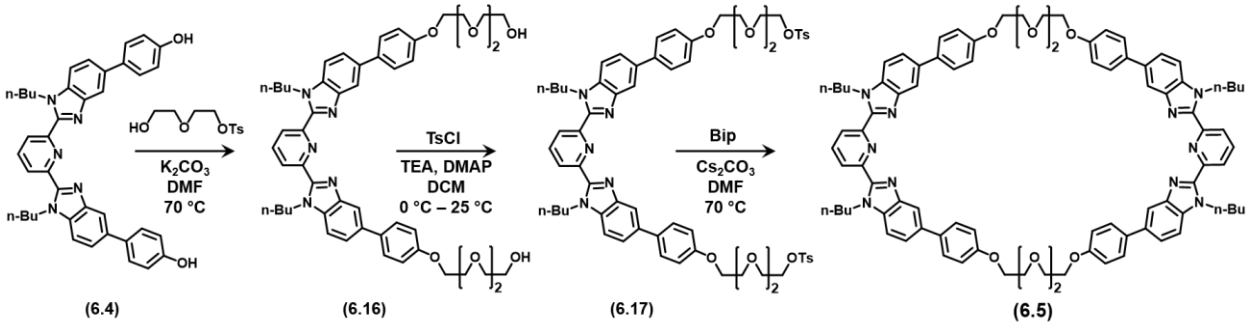

(procedure by Dr. Qiong Wu as described in reference 10 and 11)

In a 100 mL round-bottom flask equipped with stir bar, 5 g (8.23 mmol, 1 eq.) of **6.4**, 11.5 g (4 eq., 32.9 mmol) of tetraethylene glycol mono-p-toluenesulfonate and 6.8 g (6 eq., 49.4 mmol) of potassium carbonate were added. The flask was then flushed with argon and 40 mL dry DMF was then added by cannula. The mixture was heated in an oil bath to 70 °C and allowed to react for 24 hrs. DMF was then removed under reduced pressure and the resulting mixture extracted with $CHCl_3$ and then filtered. The filtrate was collected and the solvent removed under reduced pressure to yield a yellow-brown waxy solid. The product was purified by column chromatography (silica gel, chloroform/methanol gradient) to yield the pure product **6.16** in an 89% yield as light yellow waxy solid. ^{1}H NMR (600 MHz, $CDCl_3$; δ ppm: 8.39 (*d*, J = 7.9 Hz, 2H), 8.10 (*t*, J = 7.9 Hz, 1H), 8.05 (*s*, 2H), 7.62 – 7.58 (*overlapped*, 6H), 7.51 (*d*, J = 8.4 Hz, 2H), 7.04 (*d*, J = 8.4 Hz, 4H), 4.76 (*t*, J = 7.4 Hz, 4H), 4.21 (*t*, J = 4.8 Hz, 4H), 3.90 (*t*, J = 4.8 Hz, 4H), 3.79 – 3.59 (*m*,

20H), 2.66 (*br*, 2H), 1.75 (*p*, J = 7.4 Hz, 4H), 1.15 (*h*, J = 7.4 Hz, 4H), 0.73 (*t*, J = 7.4 Hz, 6H)). ^{13}C NMR (126 MHz, $CDCl_3$; δ ppm: 158.07, 150.66, 149.92, 143.33, 138.24, 136.11, 135.45, 134.43, 128.34, 125.56, 123.12, 118.00, 115.02, 110.52, 72.90, 72.61, 70.80, 70.65, 70.59, 70.51, 70.33, 69.98, 69.77, 67.53, 61.65, 61.51, 44.78, 32.17, 19.87, 13.53). MALDI-TOF MS (960.69, $[M]+H^+$).

5 g (5.21 mmol, 1 eq.) of **6.16** and a catalytic amount of 4- dimethylaminopyridine (DMAP) (0.41 mmol, 0.05 g, 0.08 mol. %) was added to a 100 mL round bottom flask (equipped with a stir bar) followed by 20 mL of dichloromethane (DCM) and 4.5 mL of triethylamine (TEA). The mixture was flushed with argon and then submerged in an ice bath. 2.48 g (13 mmol, 2.5 eq.) of TsCl (dissolved in 10 mL of DCM) was then added dropwise by syringe. The reaction was allowed to warm to room temperature and stirred overnight. The mixture was then filtered to remove the salt and the solvent was removed under vacuum yielding a yellow-brown oil. The resulting material was purified by column chromatography (silica gel, chloroform/methanol gradient) to yield colorless oil, **6.17**, in 76% yield by mass. ^{1}H-NMR (600 MHz in $CDCl_3$; δ ppm: 8.35 (*d*, J = 7.8 Hz, 2H), 8.07 (*t*, J = 7.9 Hz, 1H), 8.02 (*d*, J = 1.6 Hz, 2H), 7.80 (*d*, J = 8.3 Hz, 4H), 7.62 – 7.59 (*m*, 4H), 7.58 (*dd*, J = 8.4, 1.7 Hz, 2H), 7.50 (*d*, J = 8.4 Hz, 2H), 7.33 (*d*, J = 8.0 Hz, 4H), 7.03 (*d*, J = 8.7 Hz, 4H), 4.77 (*t*, J = 7.4 Hz, 4H), 4.22 – 4.18 (*m*, 4H), 4.18 – 4.14 (*m*, 4H), 3.91 – 3.88 (*m*, 4H), 3.76 – 3.73 (*m*, 4H), 3.71 – 3.68 (*m*, 4H), 3.68 – 3.65 (*m*, 4H), 3.63 – 3.59 (*overlapped*, 8H), 2.43 (*s*, 6H), 1.75 (*p*, J = 7.5 Hz, 4H), 1.15 (*h*, J = 7.4 Hz, 4H), 0.73 (*t*, J = 7.4 Hz, 6H)). ^{13}C-NMR (151 MHz in $CDCl_3$; δ ppm: 158.07, 150.67, 149.96, 144.72, 143.37, 138.13, 136.06, 135.46, 134.43, 132.99, 129.76, 128.31, 127.94, 125.49, 123.07, 118.03, 114.97, 110.44, 70.80, 70.74,

70.66, 70.61, 70.55, 69.75, 69.20, 68.66, 67.52, 53.38, 44.74, 32.15, 21.59, 19.85, 13.48). MALDI-TOF MS (1268.75, $[M]+H^+$).

A 125mL dropping funnel containing **6.4** (1.39 g, 2.29 mmol, 1eq.) and **6.17** (2.9 g, 2.29 mmol, 1eq.) in 100 mL of anhydrous DMF was fitted to a 1 L twonecked round bottom flask containing Cs_2CO_3 (2.98 g, 9.14 mmol, 4 eq.) and a stir bar. The reaction vessel was flushed with argon before anhydrous DMF (450 mL) was added by cannula. The reaction was submerged in an oil bath and heated to 70 °C while rapidly stirring. The dissolved mixture of components in the dropping funnel was then added dropwise to this suspension over the course of 2 days. The reaction was stirred at 70 °C for a total of 4 days, after which the solvent was removed and the crude product was triturated with $CHCl_3$ and filtered. The filtrate was collect and solvent was removed under vacuum. The resulting solid was purified by column chromatography (TEA pretreated silica gel, chloroform/methanol gradient) and recrystallization ($CHCl_3$/MeCN) to yield **6.5** as white solid crystals in 53% yield by mass. ^{1}H-NMR (600 MHz in $CDCl_3$; δ ppm: 8.30 (*d*, J = 7.8 Hz, 4H), 8.02 – 7 7.96 (*overlapped*, 6H), 7.52 – 7.48 (*m*, 8H), 7.39 (*dd*, J = 8.4, 1.7 Hz, 4H), 7.27 (*d*, J = 8.4 Hz, 4H), 7.00 – 6.94 (*m*, 8H), 4.56 (*t*, J = 7.3 Hz, 8H), 4.14 – 4.11 (*m*, 8H), 3.93 – 3.90 (*m*, 8H), 3.79 – 3.76 (*m*, 8H), 3.74 (*dt*, J = 6.0, 2.0 Hz, 8H), 1.60 – 1.52 (*m*, 8H), 1.01 – 0.91 (*m*, 8H), 0.59 (*t*, J = 7.4 Hz, 12H)). ^{13}C-NMR (126 MHz in $CDCl_3$; δ ppm: 158.16, 150.49, 150.01, 143.35, 138.05, 135.97, 135.40, 134.18, 128.26, 125.50, 123.11, 117.86, 115.02, 110.45, 70.91, 69.79, 67.65, 44.58, 32.07, 19.74, 13.54, 13.45). MALDI-TOF MS (1553.13, $[M]+Na^+$).

6.5.4 Synthesis of alkene-terminated thread (**6.6**)

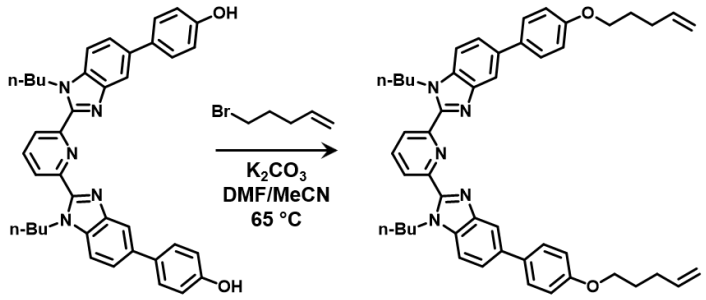

(6.4) (6.6)

0.5 g (0.82 mmol, 0.2 mM) of **6.4** was added to a 3:1 DMF/MeCN solution in a 25 mL round bottom flask (equipped with magnetic stir bar) along with excess potassium carbonate (ca. 8 eq., 0.9 g) and 3 eq. (0.12 g [0.98 mL], 2.46 mmol) of 5-bromo-1-pentene. The solution was stirred at 65 °C for 18 hours under argon atmosphere. After 18 hours, the reaction was cooled to room temperature and the product was extracted with DCM and washed with deionized water using a separatory funnel. The organic, DCM layer was dried with magnesium sulfate which was filtered off and the remaining solvent was removed via rotary evaporation. The product was isolated using silica gel column chromatography (chloroform/methanol gradient) to yield **6.6** in 68% yield. ^{1}H-NMR (600 MHz in $CDCl_3$; δ ppm: 0.73 (*t*, 6H), 1.15 (*m*, 4H), 1.75 (*m*, 4H), 1.93 (*m*, 4H), 2.28 (*m*, 4H), 4.04 (*t*, 4H), 4.76 (*t*, 4H), 5.00-5.11 (*dd*, 4H), 5.82-5.95 (*m*, 2H), 7.01 (*d*, 4H), 7.50 (*d*, 2H), 7.57-7.62 (*overlapped*, 6H), 8.03 (*s*, 2H), 8.08 (*t*, 1H), 8.35 (*d*, 2H)).

6.5.5 Synthesis of Generation #1 stopper group (**6.7**)

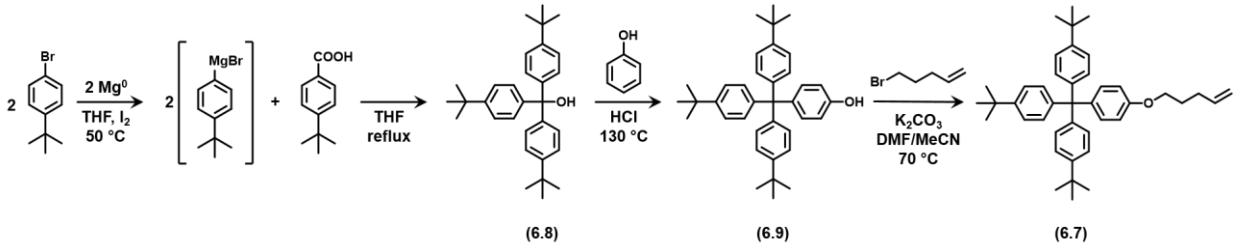

Note: Grignard reactions require completely anhydrous conditions. All glassware used here was dried for at least 24 hours in a drying oven, all solvents are anhydrous, and all liquid transfers were made using either a cannula or syringe.

1 g magnesium turnings (Mg, 41.1 mmol, 0.625 M in anhydrous THF) and a catalytic amount of iodine crystals were added to a 500 mL 3-neck round bottom flask equipped with a condenser, magnetic stirring bar, and under argon atmosphere. A solution of 7.0 mL of 1-bromo-4-tert-butylbenzene (40.3 mmol, 2.345 M) in anhydrous THF was added to an addition funnel which was then clamped into one arm of the round bottom flask containing Mg. The mixture in the flask was vigorously stirred while heating to 50 °C. Once at temperature, the addition funnel was opened and 1-bromo-4-tert-butylbenzene solution was added dropwise over the course of 2 hours. Following this addition, the Grignard reagent solution was cooled to room temperature and a second solution was prepared in the addition funnel consisting of 1 eq. (4 mL, 20.5 mmol) of methyl-4-tert-butyl benzoate and 10 mL of anhydrous THF. The second solution was added

dropwise to the round bottom flask with stirring. Once the funnel was empty, the solution was heated to reflux and allowed to proceed for 18 hours. Upon completion of the reaction, the reaction mixture was quenched in an acidic ice bath (25 ml of 1M HCl per 25 g of ice). The tri-aryl compound was removed from solution by washing the contents with hexanes and deionized water.

The organic layer was collected, dried with MgSO4, and the solvent was removed by rotary evaporation. The remaining powder was boiled in hexanes for 30 minutes in order to remove any remaining impurities. The hexane solution was recrystallized overnight. The solution was filtered to collect the remaining precipitate, which was then dried under high vacuum overnight to obtain **6.8** in 65% yield. ^{1}H-NMR (600 MHz in $CDCl_3$; δ ppm: 1.29 (*s*, 27H), 7.30 (*dd*, 12H)). MALDI-MS (411, $[M]+H^{+}$-O). Melting point (214 °C – 216 °C).

1.0 g of **6.8** (2.33 mmol) was dissolved in excess (ca. 10 eq.) phenol at 60 °C (above melting point of phenol) in 10 mL round bottom flask with stir bar and condenser. A catalytic amount of 36% HCl was added to the solution. The system was flushed with argon and reacted at 110 °C for 24 hours with stirring. Upon completion of the reaction, the solution was cooled to 60 °C and ca. 5 mL of toluene were added to the mixture. Any insoluble particulates were removed via vacuum filtration. The organic filtrate was washed with 1 M NaOH until the aqueous layer returned to a clear, colorless solution. The organic layer was collected and solvent was removed by rotary evaporation. The remaining powder was boiled in hexane for 15-20 minutes in order to remove any remaining impurities. The hexane solution was filtered to collect the remaining precipitate, which was then dried under high vacuum overnight to obtain **6.9** in 73% yield. ^{1}H-NMR (600 MHz in $CDCl_3$; δ ppm: 1.29 (*s*, 27H), 6.59 (*d*, 2H), 7.00 (*d*, 2H), 7.07 (*d*, 6H), 7.20 (*d*, 6H)). ^{13}C-NMR

(126 MHz in $CDCl_3$; δ ppm: 31.36, 34.24, 62.99, 114.36, 123.99, 130.66, 132.52, 138.91, 144.16, 148.16. MALDI-MS (524.2, $[M]+Na^+$).

1.0 g (1.98 mmol) of **6.9** was reacted with 1.18 g (4 eq., 7.92 mmol, 0.94 mL) of 5-bromo-1-pentene and 1.10 g (4 eq., 7.92 mmol) of potassium carbonate in a 3:1 solution of DMF/MeCN (0.10 M) at 65°C under argon atmosphere. All reactants were placed in a round bottom flask (equipped with stir bar and condenser) and dissolved in 3:1 DMF/MeCN. The system was then flushed with Ar(g) and reacted at 65°C for 18-24 hours while stirring. Upon completion of the reaction, the product was extracted with DCM and washed with deionized water. Solvent was removed through rotary evaporation and excess heptane was added to facilitate the removal of DMF. Product was further purified through silica gel column chromatography with a 5:2 solution of hexane/DCM to obtain **6.7** in 80% yield. ^{1}H-NMR (600 MHz in $CDCl_3$; δ ppm: 1.31 (*s*, 27H), 1.88 (*m*, 2H), 2.24 (*m*, 2H), 3.95 (*t*, 2H), 5.00 (*d*, 1H), 5.07 (*d*, 1H), 5.86 (*m*, 1H), 6.77 (*d*, 2H), 7.08-7.09 (*overlap*, 8H), 7.24 (*d*, 6H)).

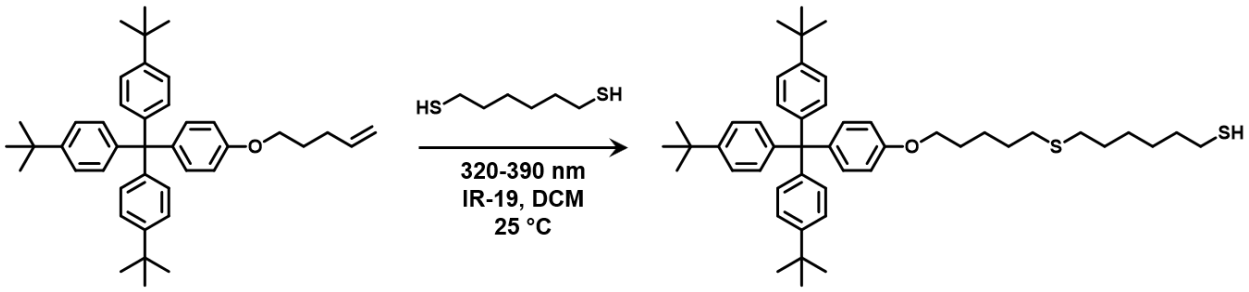

(6.7) **(6.14)**

100 mg (174.3 µmol) of **6.7** and 262 mg (0.27 mL, 17.4 mmol) of 1,6-hexanedithiol were dissolved in 7.2 mL (20 mL/g) DCM in a 25 mL round bottom flask equipped with a stir bar. A catalytic quantity of the photoinititor Irgacure-19® (IR-19, phenylbis(2,4,6-trimethylbenzoyl)phosphine oxide) was added to the mixture. The flask was capped with a balloon and exposed to high intensity UV light (320-390 nm, 50 mW/cm^2) for 1 hour. The product was precipitated in cold (-18°C) hexanes overnight and **6.14** was isolated via vacuum filtration in 70% yield. ^{1}H-NMR (600 MHz in $CDCl_3$; δ ppm: 1.29 (*s*, 27H), 1.39 (*m*, 3H), 1.55-1.67 (*overlapped*, 9H), 1.79 (*m*, 2H), 2.49-2.54 (*overlapped*, 6H), 3.93 (*t*, 2H), 6.75 (*d*, 2H), 7.06-7.08 (*overlapped*, 8H), 7.22 (*d*, 6H)). ^{13}C-NMR (126 MHz in $CDCl_3$; δ ppm: 24.51-34.25 (-CH_2 peaks), 63.00, 67.51, 112.87, 123.97, 130.68, 132.17, 139.39, 144.12, 148.23, 156.79). MALDI-MS (745.4, [M]+Na^+).

6.5.6 Synthesis of Generation #2 stopper group (**6.10**)

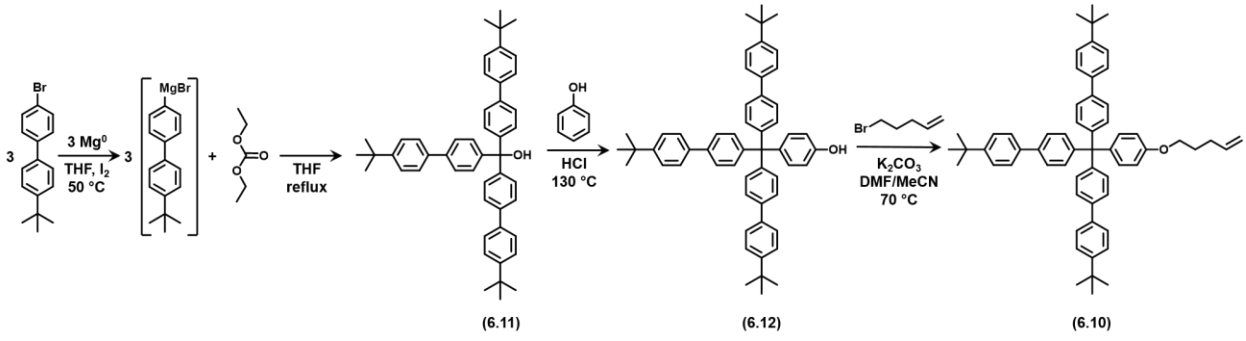

Note: Grignard reactions require completely anhydrous conditions. All glassware used here was dried for at least 24 hours in a drying oven, all solvents are anhydrous, and all liquid transfers were made using either a cannula or syringe.

1.0 g magnesium turnings (Mg, 41.1 mmol, 0.625 M in anhydrous THF) and a catalytic amount of iodine crystals were added to a 500 mL 3-neck round bottom flask equipped with a condenser, magnetic stirring bar, and under argon atmosphere. A solution of 11.9 g of 4-bromo-4'-*tert*-butylbiphenyl (41.1 mmol, 2.345 M) in anhydrous THF was added to an addition funnel which was then clamped into one arm of the round bottom flask containing Mg. The mixture in the flask was vigorously stirred while heating to 50 °C. Once at temperature, the addition funnel was opened and the 4-bromo-4'-*tert*-butylbiphenyl solution was added dropwise over the course of 2 hours. Following this addition, the Grignard reagent solution was cooled to room temperature and a second solution was prepared in the addition funnel consisting of 0.3 eq. (1.7 mL, 13.7 mmol) of methyl-4-*tert*-butyl benzoate and 33.5 mL of anhydrous THF. The second solution was added dropwise to the round bottom flask with stirring. Once the funnel was empty, the solution was heated to reflux and allowed to proceed for 18 hours. Upon completion of the reaction, the reaction mixture was quenched in an acidic ice bath (25 ml of 1M HCl per 25 g of ice). The tri-aryl compound was removed from solution by washing the contents with hexanes and deionized water. The organic layer was collected, dried with $MgSO_4$, and the solvent was removed by rotary evaporation. The remaining powder was boiled in hexanes for 30 minutes in order to remove any remaining impurities. The hexane solution was recrystallized overnight. The solution was filtered to collect the remaining precipitate, which was then dried under high vacuum overnight to obtain

6.11 in 65% yield. ^{1}H-NMR (600 MHz in $CDCl_3$; δ ppm: 1.35 (*s*, 27H), 7.40 (*d*, 6H), 7.45 (*d*, 6H), 7.53-7.56 (overlapped, 12H)).

1.0 g of **6.11** (1.52 mmol) was dissolved in excess (ca. 10 eq.) phenol at 60 °C (above melting point of phenol) in 10 mL round bottom flask with stir bar and condenser. A catalytic amount of 36% HCl was added to the solution. The system was flushed with argon and reacted at 110 °C for 24 hours with stirring. Upon completion of the reaction, the solution was cooled to 60 °C and ca. 5 mL of toluene were added to the mixture. Any insoluble particulates were removed via vacuum filtration. The organic filtrate was washed with 1 M NaOH until the aqueous layer returned to a clear, colorless solution. The organic layer was collected and solvent was removed by rotary evaporation. The remaining powder was boiled in hexane for 15-20 minutes in order to remove any remaining impurities. The hexane solution was filtered to collect the remaining precipitate, which was then dried under high vacuum overnight to obtain **6.12** in 73% yield. ^{1}H-NMR (600 MHz in $CDCl_3$; δ ppm: 1.35 (*s*, 27H), 6.74 (*d*, 2H), 7.17 (*d*, 2H), 7.31 (*d*, 6H), 7.44 (*d*, 6H), 7.50 (*d*, 6H), 7.54 (*d*, 6H)). ^{13}C-NMR (126 MHz in $CDCl_3$; δ ppm: 31.34, 34.50, 63.62, 114.31, 125.68, 125.90, 126.56, 131.41, 132.43, 137.66, 138.37, 139.23, 145.75, 150.13, 153.50). MALDI-MS (755.3, $[M]+Na^+$).

0.5 g (0.68 mmol) of **6.12** was reacted with 0.63 g (4 eq., 2.72 mmol, 0.60 mL) of 5-bromo-1-pentene and 0.38 g (4 eq., 2.72 mmol) of potassium carbonate in a 3:1 solution of DMF/MeCN (0.10 M) at 65°C under argon atmosphere. All reactants were placed in a round bottom flask (equipped with stir bar and condenser) and dissolved in 3:1 DMF/MeCN. The system was then flushed with argon and reacted at 65°C for 18-24 hours while stirring. Upon completion of the reaction, the product was extracted with DCM and washed with deionized water. Solvent was

removed through rotary evaporation and excess heptane was added to facilitate the removal of DMF. Product was further purified through silica gel column chromatography with a 5:2 solution of hexane/DCM to obtain **6.10** in 80% yield. ^{1}H-NMR (600 MHz in $CDCl_3$; δ ppm: 1.35 (*s*, 27H), 1.88 (*m*, 2H), 2.24 (*m*, 2H), 3.97 (*t*, 2H), 5.00 (*d*, 1H), 5.07 (*d*, 1H), 5.86 (*m*, 1H), 6.82 (*d*, 2H), 7.20 (*d*, 2H), 7.30 (*d*, 6H), 7.45 (*d*, 6H), 7.50 (*d*, 6H), 7.55 (*d*, 6H)).

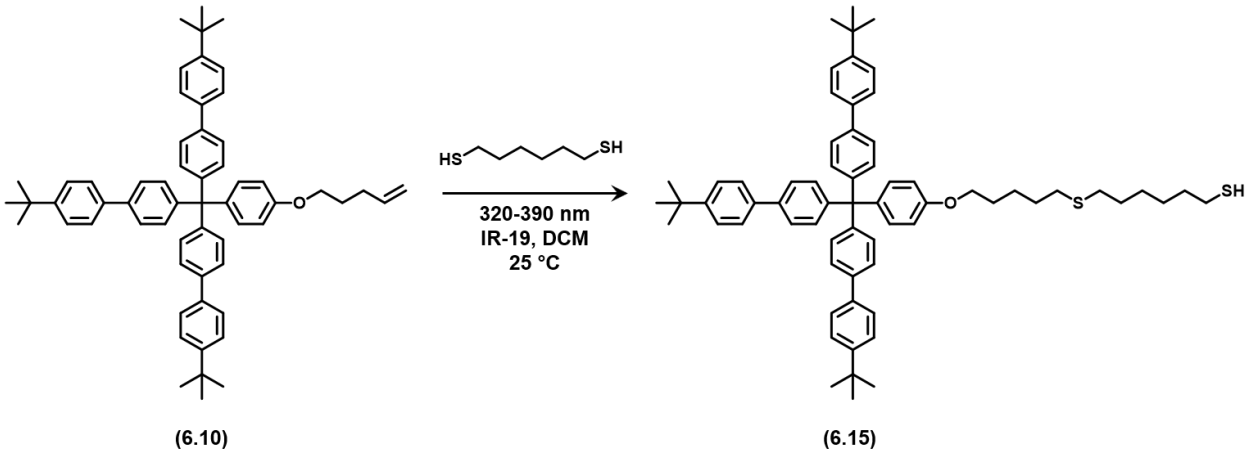

(6.10) (6.15)

100 mg (174.3 µmol) of **6.10** and 262 mg (0.27 mL, 17.4 mmol) of 1,6-hexanedithiol were dissolved in 7.2 mL (20 mL/g) DCM in a 25 mL round bottom flask equipped with a stir bar. A catalytic quantity of the photoinititor Irgacure-19® (IR-19, phenylbis(2,4,6-trimethylbenzoyl)phosphine oxide) was added to the mixture. The flask was capped with a balloon and exposed to high intensity UV light (320-390 nm, 50 mW/cm^2) for 1 hour. The product was precipitated in cold (-18°C) hexanes overnight and **6.15** was isolated via vacuum filtration in 70% yield. ^{1}H-NMR (600 MHz in $CDCl_3$; δ ppm: 1.35 (*s*, 27H), 1.39 (*m*, 3H), 1.50-1.67 (*overlapped*,

9H), 1.79 (*m*, 2H), 2.49-2.54 (*overlapped*, 6H), 3.95 (*t*, 2H), 6.80 (*d*, 2H), 7.19 (*d*, 2H), 7.31 (*d*, 6H), 7.44 (*d*, 6H), 7.49 (*d*, 6H), 7.54 (*d*, 6H)). ^{13}C-NMR (126 MHz in $CDCl_3$; δ ppm: 25.48-34.49 (-CH_2 peaks), 67.58, 113.25, 125.63, 125.87, 126.55, 131.41, 132.16, 137.68, 138.31, 138.80, 145.81, 150.10). MALDI-MS (973.5, [M]+Na^+).

6.5.7 Synthesis of thiol oligomer

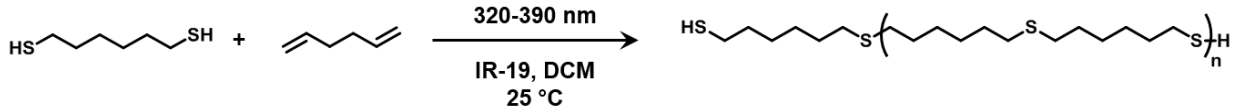

0.72 mL (0.70 g, 4.6 mmol) of 1,6-hexandithiol and 0.48 mL (0.33g, 4.0 mmol) were combined in 10 mL of DCM in a 25 mL round bottom flask with magnetic stir bar. 10 mg of IR-19 were added to the reaction. The flask was capped with a balloon and exposed to high intensity UV light (320-390 nm, 50 mW/cm^2) for 1 hour while stirring. After reacting, the solvent was reduced and the remaining solution was precipitated (dropwise) in methanol. Product was isolated via vacuum filtration. ^{1}H NMR (600 MHz in $CDCl_3$; δ ppm: 2.49 (*t*, CH_2), 1.58 (*m*, CH_2), 1.38 (*m*, CH_2)). ^{13}C NMR (150.8 MHz in $CDCl_3$; δ ppm: 33.8, 32.1, 29.5, 28.5, 28.3, 27.9, 24.5). M_n (by end group analysis) = 4210 g/mol.

6.5.8 Trial Thiol-ene Initiation Conditions

AIBN – 10 mg **6.13**, 9 mg **6.15**, 2.2 mg AIBN in 1 mL tetracholorethane. Reaction stirred in conical vial (with condenser and stir bar) at 70 °C for 4 hours.

IR-19 – 10 mg **6.13**, 13.1 mg **6.15**, 2 mg IR-19 in 0.2 mL DCM. Reaction stirred in 1 dram vial under argon atmosphere for 1 hour during exposure to UV-light (320-390 nm, 50 mW/cm^2).

BPO - 20 mg **6.13**, 10 mg **6.15**, 4.5 mg BPO, 2.5 mg trimethyl aniline (TMA, co-initiator) in 1.0 mL DCM/MeOH (9:1 v/v). **6.13** and **6.15** were added to 1 dram vial with 0.5 mL solvent. BPO in 0.25 mL solvent and TMA in 0.25 mL solvent (prepared in separate vials) were pipetted into vial containing **6.13** and **6.15**. Reaction was allowed to proceed for 1 hour.

6.6 References

(1) Bruns, C. J.; Stoddart, J. F. The Nature of the Mechanical Bond. John Wiley & Sons, Inc. 2016.

(2) Lin, S.-K. Molecular Catenanes, Rotaxanes and Knots. A Journey Through the World of Molecular Topology. Edited by J.-P. Sauvage. *Molecules* **1999**, *4* (12), 366–367.

(3) van Dongen, S. F. M.; Cantekin, S.; Elemans, J. A. A. W.; Rowan, A. E.; Nolte, R. J. M. Functional Interlocked Systems. *Chem. Soc. Rev.* **2014**, *43* (1), 99–122.

(4) Murakami, H.; Kawabuchi, A.; Kotoo, K.; Kunitake, M.; Nakashima, N. A Light-Driven Molecular Shuttle Based on a Rotaxane. *J. Am. Chem. Soc.* **1997**, *119* (32), 7605–7606.

(5) Kwan, C.-S.; Chan, A. S. C.; Leung, K. C.-F. A Fluorescent and Switchable Rotaxane Dual Organocatalyst. *Org. Lett.* **2016**, *18* (9), 2325.

(6) Jiménez, M. C.; Dietrich-Buchecker, C.; Sauvage, J.-P. Towards Synthetic Molecular Muscles: Contraction and Stretching of a Linear Rotaxane Dimer. *Angew. Chemie* **2000**, *39* (18), 3284–3287.

(7) Bruns, C. J.; Stoddart, J. F. Rotaxane-Based Molecular Muscles. *Acc. Chem. Res.* **2014**, *47* (7), 2186–2199.

(8) Ito, K. Slide-Ring Materials Using Topological Supramolecular Architecture. *Curr. Opin. Solid State Mater. Sci.* **2010**, *14* (2), 28–34.

(9) Ito, K. Novel Entropic Elasticity of Polymeric Materials: Why Is Slide-Ring Gel so Soft? *Polym. J.* **2011**, *44* (1), 38–41.

(10) de Gennes, P.-G. Sliding Gels. *Phys. A Stat. Mech. its Appl.* **1999**, *271* (3–4), 231–237.

(11) Wenz, G.; Han, B.-H.; Müller, A. Cyclodextrin Rotaxanes and Polyrotaxanes. *Chem. Rev.* **2006**, *106* (3), 782–817.

(12) Okumura, Y.; Ito, K. The Polyrotaxane Gel: A Topological Gel by Figure-of-Eight Cross-Links. *Adv. Mater.* **2001**, *13* (7), 485–487.

(13) Karino, T.; Shibayama, M.; Ito, K. Slide-Ring Gel: Topological Gel with Freely Movable Cross-Links. *Phys. B Condens. Matter* **2006**, *385–386*, 692–696.

(14) Ito, K. Novel Cross-Linking Concept of Polymer Network: Synthesis, Structure, and Properties of Slide-Ring Gels with Freely Movable Junctions. *Polym. J.* **2007**, *39* (6), 489–499.

(15) Zhao, C.; Domon, Y.; Okumura, Y.; Okabe, S.; Shibayama, M.; Ito, K. Sliding Mode of Cyclodextrin in Polyrotaxane and Slide-Ring Gel. *J. Phys. Condens. Matter* **2005**, *17* (31),

S2841–S2846.

(16) Beck, J. B.; Rowan, S. J. Multistimuli, Multiresponsive Metallo-Supramolecular Polymers. *J. Am. Chem. Soc.* **2003**, *125* (46), 13922–13923.

(17) Kumpfer, J. R.; Rowan, S. J. Thermo-, Photo-, and Chemo-Responsive Shape-Memory Properties from Photo-Cross-Linked Metallo-Supramolecular Polymers. *J. Am. Chem. Soc.* **2011**, *133* (32), 12866–12874.

(18) Burnworth, M.; Tang, L.; Kumpfer, J. R.; Duncan, A. J.; Beyer, F. L.; Fiore, G. L.; Rowan, S. J.; Weder, C. Optically Healable Supramolecular Polymers. *Nature* **2011**, *472* (7343), 334–337.

(19) Takata, T.; Kihara, N.; Furusho, Y. Polyrotaxanes and Polycatenanes: Recent Advances in Syntheses and Applications of Polymers Comprising of Interlocked Structures. *Polymer Synthesis*. Springer Berlin Heidelberg 2004, pp 1–75.

(20) Dietrich-Buchecker, C. O.; Sauvage, J. P.; Kintzinger, J. P. Une Nouvelle Famille de Molecules : Les Metallo-Catenanes. *Tetrahedron Lett.* **1983**, *24* (46), 5095–5098.

(21) Wojtecki, R. J.; Wu, Q.; Johnson, J. C.; Ray, D. G.; Korley, L. T. J.; Rowan, S. J. Optimizing the Formation of 2,6-Bis(N-Alkyl-Benzimidazolyl)Pyridine-Containing [3]Catenates through Component Design. *Chem. Sci.* **2013**, *4* (12), 4440.

(22) Wu, Q.; Rauscher, P. M.; Lang, X.; Wojtecki, R. J.; de Pablo, J. J.; Hore, M. J. A.; Rowan, S. J. Poly[n]Catenanes: Synthesis of Molecular Interlocked Chains. *Science (80-.).* **2017**, *358* (6369), 1434–1439.

(23) McKenzie, B. M.; Miller, A. K.; Wojtecki, R. J.; Johnson, J. C.; Burke, K. A.; Tzeng, K. A.; Mather, P. T.; Rowan, S. J. Improved Synthesis of Functionalized Mesogenic 2,6-Bisbenzimidazolylpyridine Ligands. *Tetrahedron* **2008**, *64* (36), 8488–8495.

(24) Wu, Q. Synthesis of Polycatenanes through Molecular Design, Case Western Reserve University, 2017.

(25) Wojtecki, R. J. Toward the Design and Synthesis of Mechanically Interlocked Polymers, Case Western Reserve University, 2013.

(26) Beck, J. B.; Ineman, J. M.; Rowan, S. J. Metal/Ligand-Induced Formation of Metallo-Supramolecular Polymers. *Macromolecules* **2005**, *38* (12), 5060–5068.

(27) Rowan, S. J.; Beck, J. B. Metal–Ligand Induced Supramolecular Polymerization: A Route to Responsive Materials. *Faraday Discuss.* **2005**, *128*, 43–53.

(28) Danon, J. J.; Leigh, D. A.; McGonigal, P. R.; Ward, J. W.; Wu, J. Triply Threaded [4]Rotaxanes. *J. Am. Chem. Soc.* **2016**, *138* (38), 12643–12647.

Appendix: Adhesives using alkyl-core thia-Michael acceptors

In an effort to explore the effect that changing the composition of the Michael acceptor has on the mechanical and adhesive behavior of the TM films, a second generation of ditopic acceptor was developed to contain an alkyl core. A series of ditopic benzalcyanoacetate compounds were synthesized using 6-carbon chain in combination with the same nitro-, methoxy-, and unsubstituted Michael-accepting groups utilized thus far. Using procedures adopted from literature,[1] 2 equivalents of methyl cyanoacetate (7.41 mL, 0.084 mol) were combined in bulk with 1 equivalent of 1,6-hexanediol (5.00 g, 0.042 mol) and catalytic amounts of titanium butoxide (0.35 mL, 0.001 mol) (Figure A1). The mixture was heated to 100 °C and stirred overnight (ca. 18 hours) with constant argon flow. Once the reaction was complete, the mixture was cooled and the titanium catalyst was removed using a deactivated alumina pad. 1,6-bis(cyanoacetate) hexane, **7**, crystallized from the residual oil and was isolated via vacuum filtration. **7** was then reacted with 2 equivalents of the selected benzaldehyde (R = -NO_2 (**8N**), -H (**8H**), or –OCH_3 (**8M**)) under Knovenagel conditions to yield a precipitate of the final, ditopic product (**8**, Figure 5.7B). Proton nuclear magnetic resonance (^{1}H-NMR) was used to verify the structures of **7** and **8** as shown in Figure A2 (see Experimental Methods for detailed synthesis and characterization).

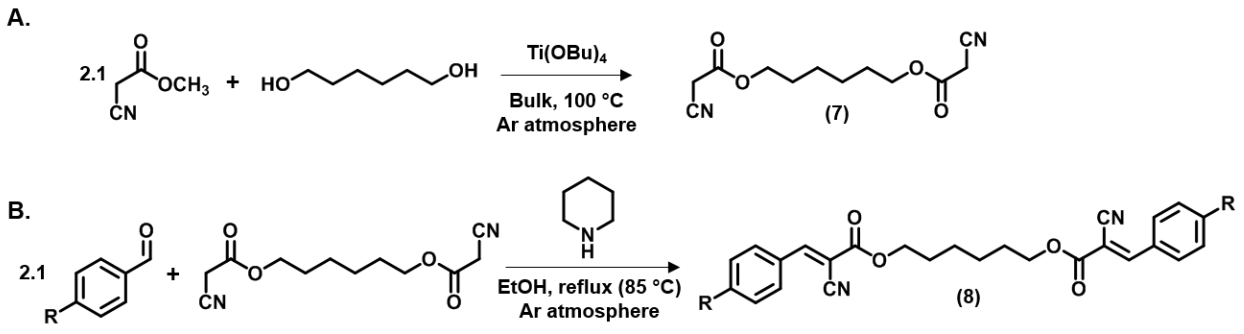

Figure A1. A) Transesterification of methyl cyanoacetate and 1,6-hexanediol using titanium butoxide catalyst to yield the bis-cyanoacetate precursor **7** B) Knovenagel condensation of **7** with *para*-substituted benzaldehyde to yield the final bis-benzalcyanoacetate with alkyl core, **8**.

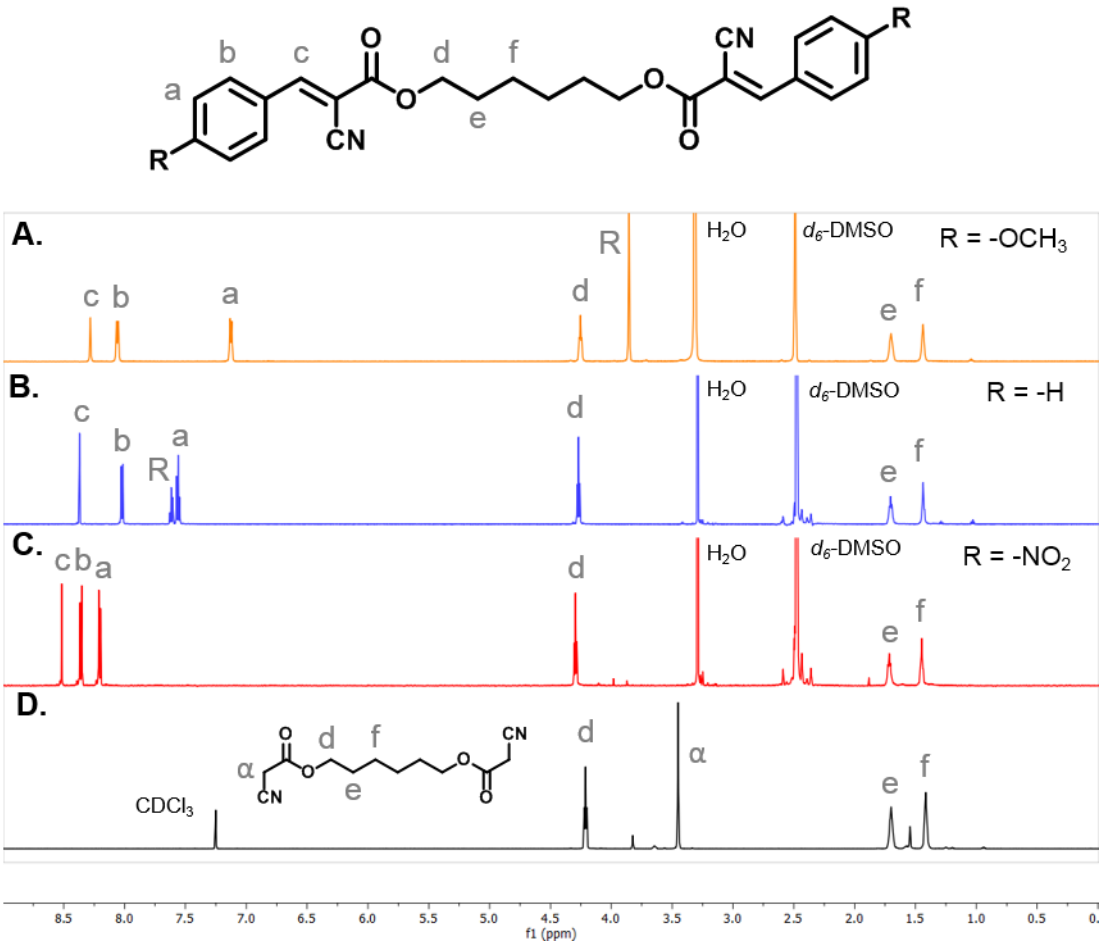

Figure A2. ^{1}H-NMR spectra of A) **8M**, B) **8H**, C) **8N**, and D) **7**. Peaks labeled R correspond to protons from respective *β*-phenyl group and the α peak in D corresponds to the protons of the α-carbon to the cyano group in **7**. (600 MHz NMR in d_6-DMSO (A-C) or $CDCl_3$ (D), 25 °C).

Thermal characterization was conducted on the derivatives of **8** using thermogravimetric analysis (TGA) and differential scanning calorimetry (DSC) (Figure A3, Table A1). As with the previous version of the ditopic linkers, the alkyl Michael acceptor compounds were found to be thermally stable up to approximately 300 °C, as determined by TGA (Figure A3A). It was with DSC that the differences within this class of compounds became apparent. In the TEG-core set, neither **3M** nor **3H** showed any crystalline behavior within the testing range (-80 °C – 200 °C),

but rather exhibited a phase transition, likely a glass transition temperature (T_g), below 0 °C. The calorimetric behavior of **3N** was dominated by a broad melting phenomenon (T_m) that peaked at 145 °C. In contrast, the hexyl-core electrophiles all exhibited highly crystalline characteristics, marked by the sharp endothermic peak at ca. 150 °C for **8M** and at ca. 200 °C for both **8N** and **8H** (Figure A3B). The strong crystalline characteristics of the **8** series, provides an opportunity to develop more mechanically robust materials while also exploring the utility of crystalline domains in these oftentimes phase separated systems. However, as the following discussion will show, the crystallinity can also contribute to challenges in developing a homogeneous polymeric film.

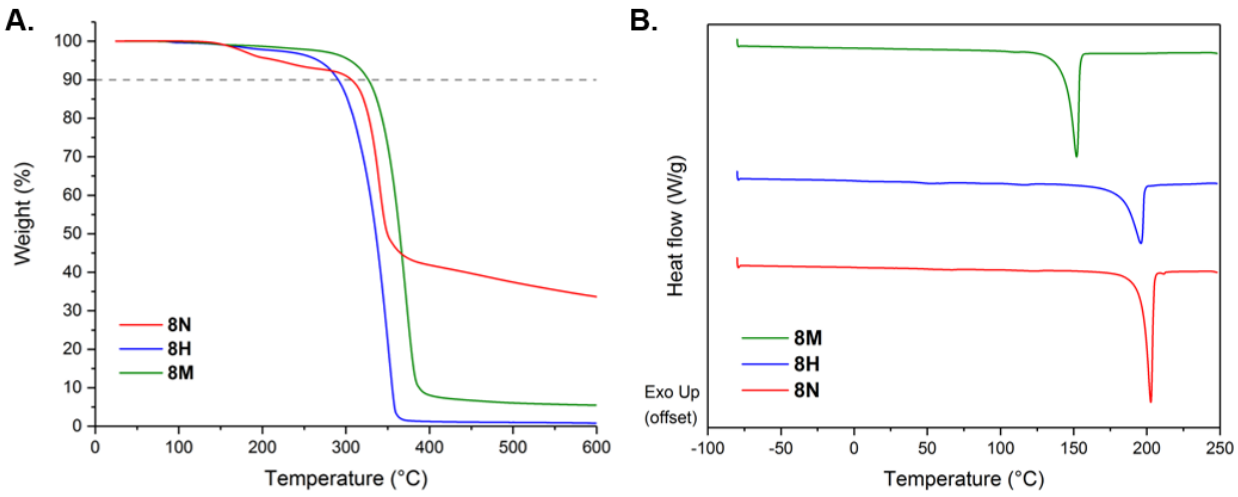

Figure A3. A) Thermogravimetric analysis (TGA) of alkyl bisbenzalcyanoacetate compounds and PMMS. B) Differential scanning calorimetry curves of the alkyl bisbenzalcyanoacetate compounds. **8N** (red), **8H** (blue), **8M** (orange), PMMS (black). Both analyses run at 10 °C/min, DSC pictured with exothermic heat flow up.

Table A1. Summary of thermal properties of neat alkyl electrophiles.

Sample	T_d (°C)[a]	T_m (°C)
8N	307	203
8H	290	196
8M	327	152

[a]T_d defined as the temperature required to reach 10% weight loss by TGA.

Having synthesized and characterized a series of alkyl-core bisbenzalcyanoacetate compounds, the investigation shifted to evaluating the viability of these compounds as cross-linkers in a thia-Michael network with PMMS. Films were prepared by first dissolving the PMMS and the electrophile in dimethylformamide (DMF, 150 mg/mL) in separate 20 mL vials. Given the high melting temperature of the neat acceptors, heat was applied as needed (via heat gun) to initiate dissolution, but once the components were fully solubilized, the solutions were stable at room temperature. The PMMS solution was added to the solution containing the electrophiles and the combined solution was stirred for 24 hours at room temperature. After 24 hours, the solution was cast onto a Teflon dish with a perforated aluminum foil cover and dried on a hot plate at 50°C for 18 hours. The films were further dried under vacuum in a vacuum oven at 40°C for 48 hours. The dried films were melt processed at 110°C (150°C for films containing **8N**) under 6,000 psi compression for 5 minutes. The resultant, robust films verified the applicability of the catalyst-free, benzalcyanoacetate-based thia-Michael reaction to form crosslinked networks under a completely different set of environmental conditions (reactants, solvent, etc.) as compared to those used in Chapter 3, while still maintaining the reversible, reprocessible behavior attributed to the dynamic bond.

The first series of studies focused on the material properties of networks composed of PMMS and either **8N**, **8H**, or **8M**. Two sets of networks were constructed using a single type of acceptor: one to target 100 mol% acceptor sites to thiol, denoted **9N$_{100}$**, **9H$_{100}$**, and **9M$_{100}$** and one to target 50 mol% acceptor sites to PMMS thiol, denoted **9N$_{50}$**, **9H$_{50}$**, and **9M$_{50}$**. Thermal characterization of the networks was carried out using TGA and DSC (Figure A4). TGA analysis demonstrated thermal stabilities of the films ranging from 270 °C – 290 °C (based on the temperature at 10% weight loss), which was reflective of the combined thermal stability of PMMS and **8**.

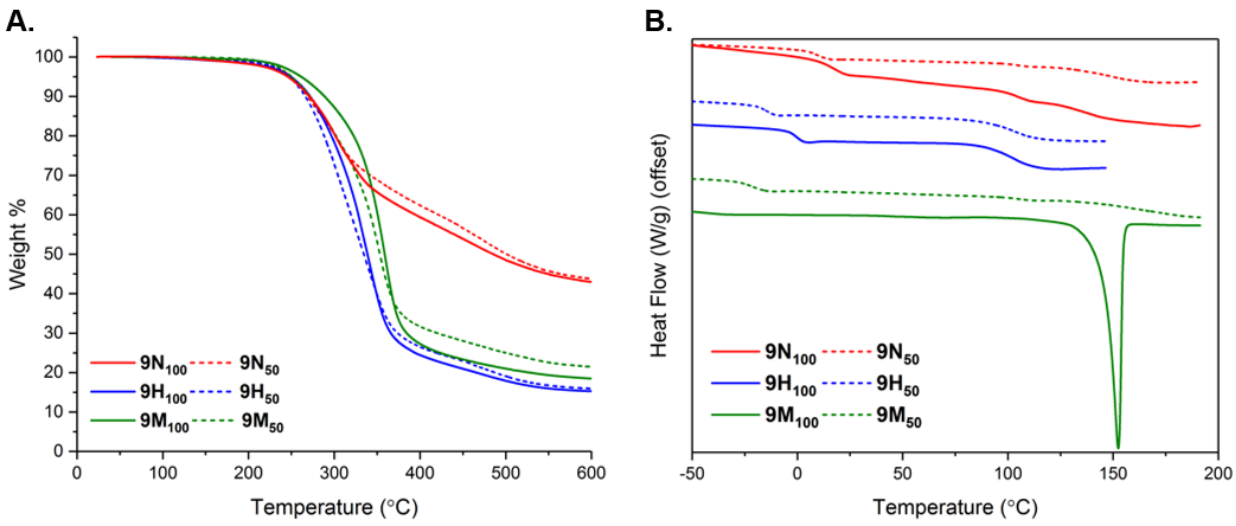

Figure A4. A) Thermogravimetric analysis (TGA) and B) differential scanning calorimetry (DSC) curves of networks containing **8**. **9N$_{100}$** (red solid), **9H$_{100}$** (blue solid), **9M$_{100}$** (green solid), **9N$_{50}$** (red dashed), **9H$_{50}$** (blue dashed), **9M$_{50}$** (green dashed). Both analyses run at 10 °C/min, DSC pictured second heating with exothermic heat flow up.

DSC showed variability in the thermal phase transitions dependent both on the composition of the acceptor group as well as the mol% acceptor group available for cross-linking (Figure A4B). **9N$_{100}$** exhibited multiple phase transitions with a first T_g below room temperature (onset at 23.5 °C) and two higher temperature transitions onset at 96 °C and 126 °C. Two phase transitions were present in **9H$_{100}$**, one below 0 °C (onset at -17 °C) and a second, higher temperature transition with an onset at 88 °C. While both **9N$_{100}$** and **9H$_{100}$** were amorphous in nature, the presence of multiple phase transitions points towards the formation of a phase separated system within the films. In contrast, the only phase transition apparent in **9M$_{100}$** was the melting peak at ca. 150 °C, coinciding with the melting point of the **8M** crosslinker. The combination of the highly crystalline nature of **8M** and the low K_{eq} of the methoxy-substituted benazalcyanoacetate reaction likely contributed to insufficient incorporation of **8M** into the polymer network, allowing it to become trapped in highly crystalline regions. The phase separation was visibly apparent in films at these ratios, resulting in an opaque, red-orange film for **9N$_{100}$** (the precursor, **8N**, is a beige powder that appears red-orange in solution), an optically clear, yellow tinted film for **9H$_{100}$** and a waxy, non-processable substance for **9M$_{100}$** (Figure A5).

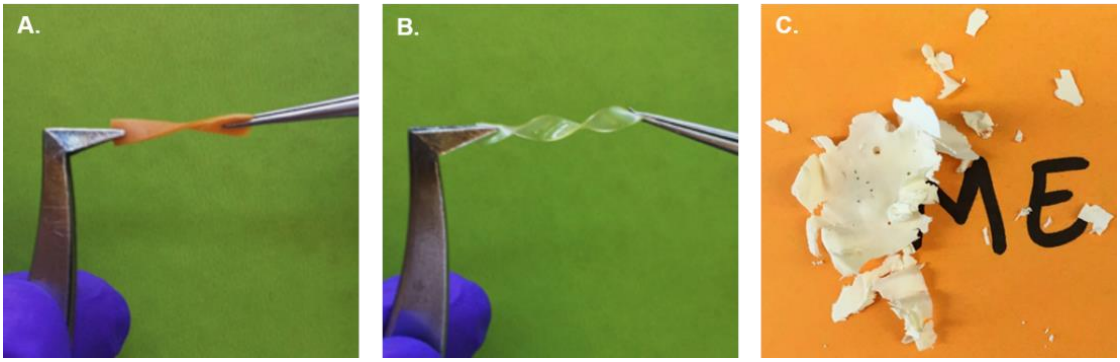

Figure A5. Photographs of films from A) **9N$_{100}$**, B) **9H$_{100}$**, and C) **9M$_{100}$**.

When the amount of acceptor group in the film was decreased to 50 mol% (versus thiol), DSC profiles of **9N$_{50}$** and **9H$_{50}$** maintained the same phase transitions as seen for **9N$_{100}$** and **9N$_{100}$**, but the temperature at which these transitions occurred decreased by approximately 10 °C. In contrast to the **9M$_{100}$** films, the **9M$_{50}$** networks were not dominated by the melting peak of the **8M** acceptor. Instead, the system exhibited the same phase behavior as its counterparts with a low T_g of -37 °C (lower than either **9N$_{50}$** or **9H$_{50}$**) as well as the step-like high temperature phase transitions at 95 °C and 125 °C.

Dynamic mechanical analysis (DMA) of the film-forming networks (**9M$_{100}$** was excluded as it did not form a robust film) shows a well-established rubbery plateau for both **9N$_{100}$** and **9H$_{100}$** (Figure A6A). As expected from previous thia-Michael films, **9N$_{100}$** has a higher plateau modulus and higher T_g as compared to **9H$_{100}$**. This follows the trend established with regards to K_{eq} as the electron-withdrawing β-phenyl substituent with the higher K_{eq} would be expected to form more thia-Michael adducts which is realized within the network as a greater number of crosslinks. **9N$_{100}$** also maintained its rubbery plateau well beyond the point at which **9H$_{100}$** demonstrated flow behavior. While the **9N$_{50}$** and **9H$_{50}$** films demonstrated the same trends (albeit at lower temperatures for the initial T_g and with lower plateau modulus), the 50 mol% films were more mechanically stable throughout the duration of the test than the 100 mol% samples. Presumably, the higher thermal stability of the 50 mol% films is less a reflection of the reversible nature of the dynamic bonds, but rather attributed to the overall stability of the films in the absence of catastrophic phase separation.

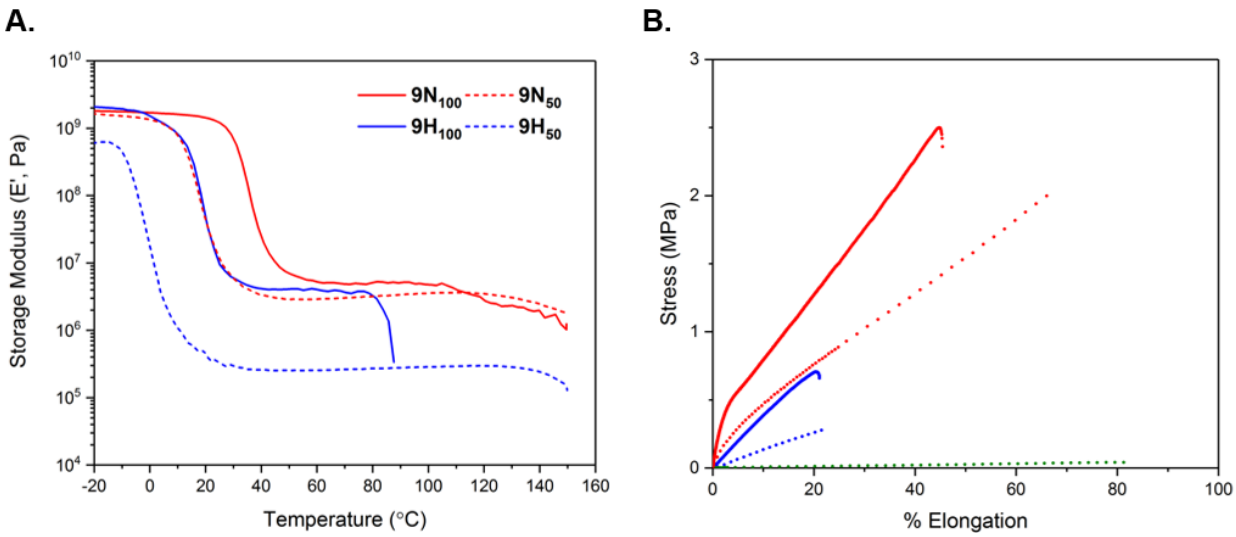

Figure A6. A) Dynamic mechanical analysis (DMA) temperature ramp curves for **9N$_{100}$** (red solid), **9H$_{100}$** (blue solid), **9N$_{50}$** (red dashed), and **9H$_{50}$** (blue dashed). Ramp rate = 3 °C/min, frequency = 1Hz, amplitude = 0.01%. B) Representative uniaxial tensile curves for **9N$_{100}$** (red solid), **9H$_{100}$** (blue solid), **9N$_{50}$** (red dashed), **9H$_{50}$** (blue dashed), and **9M$_{50}$** (green dashed). 25 mm dogbone geometry, thickness = 400 µm, Strain rate = 50 %/min.

The polymeric networks were further characterized using uniaxial tensile analysis (Figure A6B). Dogbone samples were cut (see Experimental Methods for dimensions) from the films and stretched uniaxially at a rate of 50 %/minute until failure. Figure 4.8B shows representative curves for **9N$_{100}$** and **9H$_{100}$** as well as **9N$_{50}$**, **9H$_{50}$**, and **9M$_{50}$**. From the tensile curves, it is apparent that tensile strength increases with increasing K_{eq} (**8M** < **8H** < **8N**). Furthermore, as a result of the lower acceptor content in the 50 mol% films, the tensile strength of the two networks containing **8N** and **8H** decreased while the ductility of the **9N$_{50}$** film increased to 1.5x the maximum elongation of **9N$_{100}$**. Notably in the **9M$_{50}$** system formed a robust enough film to test via tensile analysis. Although the material exhibited minimal mechanical strength, it was quite ductile, reaching out to ca. 80% elongation.

In an effort to probe the mechanical effect of combining two different equilibrium profiles into one film, two mixed-electrophile networks were prepared for preliminary testing: one containing **8N** with **8H** (**9N$_{50}$H$_{50}$**) and one containing **8N** with **8M** (**9N$_{50}$M$_{50}$**). Using identical methods as the previous films, both systems were prepared using an equimolar amount of electrophiles and a targeted 100 mol% acceptor group versus thiol. Tensile analysis on these films was particularly interesting as they exhibited emergent tensile properties of the parent networks (Figure A7). For example, **9N$_{50}$H$_{50}$** had a toughness of 140 MJ·m^{-3} as opposed to 63 MJ·m^{-3} for **9N$_{100}$** and 6 MJ·m^{-3} for **9H$_{100}$**. While the overall toughness of **9N$_{50}$M$_{50}$** did not exceed **6N**, the **9N$_{50}$M$_{50}$** sample stretched to 115% strain before breaking as opposed to **9N$_{100}$** breaking near 40% and **9N$_{50}$M$_{50}$** reached a maximum stress of approximately 1 MPa which was a marked improvement on the **9M$_{50}$** sample (Table A2).

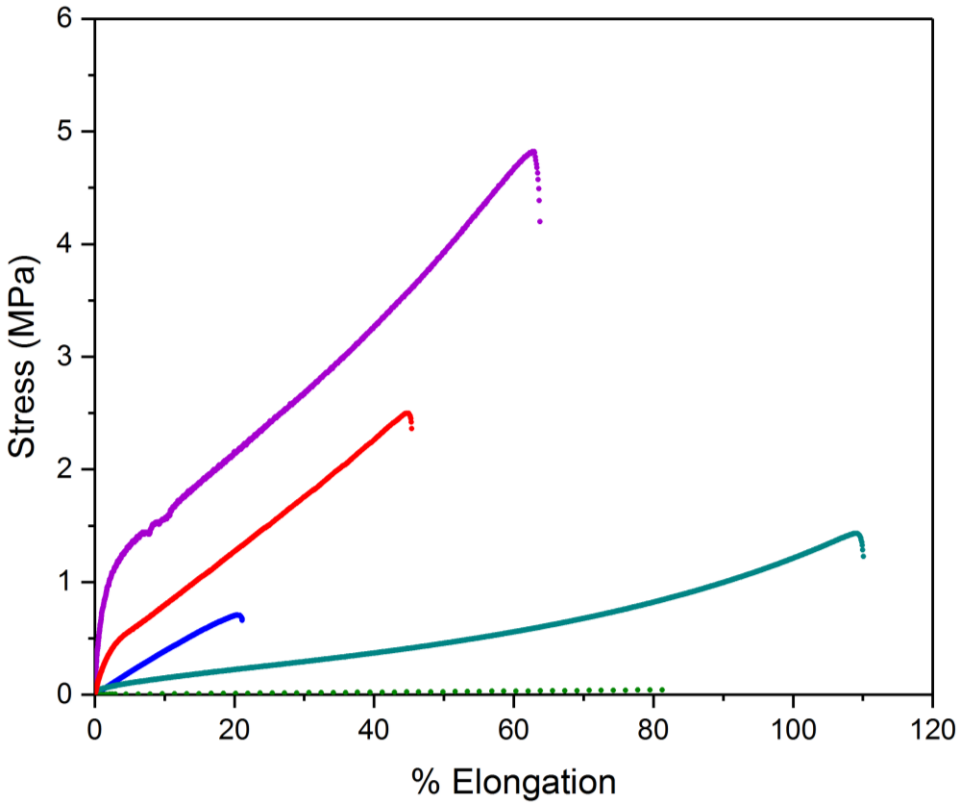

Figure A7. Representative uniaxial tensile curves for **9N$_{50}$H$_{50}$** (violet) and **9N$_{50}$M$_{50}$** (cyan) in comparison with **9N$_{100}$** (red), **9H$_{100}$** (blue), and **9M$_{50}$** (green dashed). 25 mm dogbone geometry, thickness = 400 µm, Strain rate = 50 %/min.

Table A2. Summary of mechanical properties of alkyl thia-Michael films.

Sample	Stress at break (MPa)	Strain at Break (%)	Toughness (MJ·m^{-3})
9N$_{100}$	2.6 ± 0.2	41 ± 4	63 ± 7
9H$_{100}$	0.9 ± 0.4	23 ± 7	6 ± 2
9M$_{100}$	n/a	n/a	n/a
9N$_{50}$	1.84 ± 0.18	72 ± 3	69 ± 6
9H$_{50}$	0.28 ± 0.03	23 ± 3	3.3 ± 0.7
9M$_{50}$	0.04 ± 0.00	85 ± 7	1.5 ± 0.6
9N$_{50}$H$_{50}$	4.2 ± 0.5	60 ± 4	140 ± 30
9N$_{50}$M$_{50}$	1.3 ± 0.3	115 ± 6	60 ± 10

Lap Shear Adhesion Studies

Lap shear adhesion studies were conducted as part of the preliminary studies probing the potential application of the alkyl-PMMS system as pressure sensitive adhesives. Focusing efforts on the hybrid films (**9N$_{50}$H$_{50}$** and **9N$_{50}$M$_{50}$**), samples were cut into 6 mm x 6 mm squares (exact dimensions were measured using calipers). The squares were loaded onto glass microscope slides (Figure A8) and clamped on either side of the overlap using large binder clips (approximately 4 N of force applied).

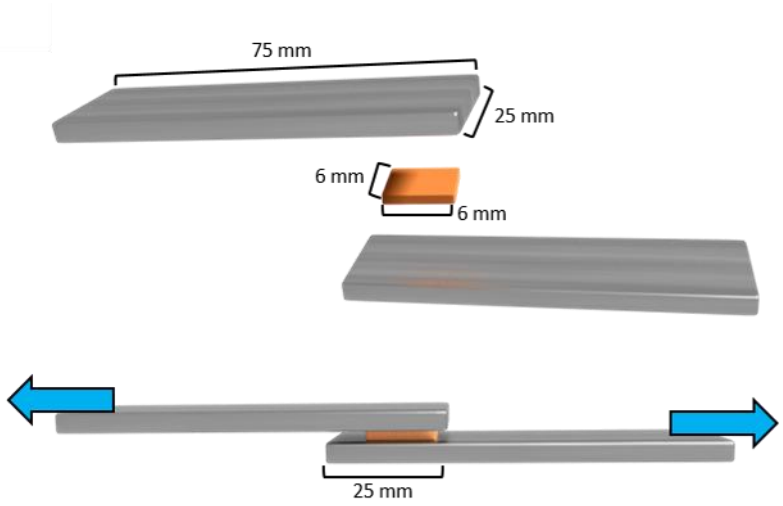

Figure A8. Schematic demonstrating lap shear adhesion setup.

In pressure sensitive adhesives, binding time often dictates the strength of the bond, therefore samples were left in a temperature-controlled oven at 25 °C for varying lengths of time before testing. After their time in the oven, the clamped samples were loaded onto a tensile analysis apparatus, secured in the tensile clamps, and the binder clips were removed once the lap shear

setup was secure. Tests were run in tensile mode at 1 mm/min and the shear stress (τ) was calculated post-failure of the adhesive using

$$\tau = F/(l * w)$$

$$F = \sigma_{max} * h * l$$

where *l*, *w*, and *h* refer to the length, width and height (or thickness) of the film, respectively, and σ_{max} is the maximum stress reached before the sample failed.

The studies showed that both **9N$_{50}$H$_{50}$** and **9N$_{50}$M$_{50}$** have potential as room temperature pressure sensitive adhesives, with **9N$_{50}$H$_{50}$** having a maximum shear strength of 0.60 MPa after 60 minutes of pressure and **9N$_{50}$M$_{50}$** demonstrating 0.30 MPa shear strength after 60 minutes (Figure A9). While these studies are only preliminary results, there is potential for future investigations to optimize both the mechanical properties of the thia-Michael films and the binding conditions in order to access a competitive pressure sensitive adhesive on a variety of substrates (over the course of this study, both the **9N$_{100}$** and **9M$_{50}$** materials were found to adhere to both Teflon® and Kapton® during the film preparation stage, although this line of inquiry was not pursued further).

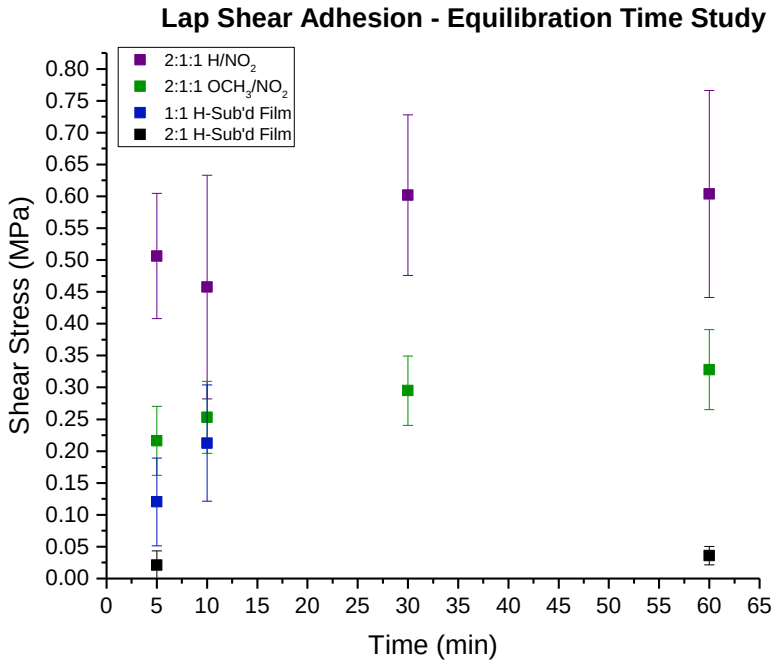

Figure A9. Lap shear adhesion results for alkyl/PMMS thia-Michael networks.

Conclusions

The use of the alkyl core in the synthesis of the ditopic benzalcyanoacetate electrophile in combination with the PMMS oligomer proved to be a viable means by which to produce thia-Michael networks. Once again using a catalyst-free method, we showed that robust films could be formed using a simple solution casting strategy. By incorporating a polymeric component into the thia-Michael system, the resultant films were notably more robust that their small molecule counterparts which allowed the mechanical properties of electron-donating and neutral Michael acceptors to be evaluated. When two different electrophiles were combined with the PMMS, the films demonstrated emergent mechanical properties that were reflective of both parent electrophiles. Early results from lap shear studies show that the alkyl-PMMS thia-Michael systems have the potential to act as room temperature pressure sensitive adhesives.

This preliminary work primarily functions to demonstrate the utility of the benzalcyanoacetate moiety as a part of a thia-Michael system. While this particular system has displayed a few flaws, mainly its challenges in processing and propensity to catastrophically phase separate, it was nonetheless capable of forming polymeric films without the use of a catalyst. Future work in this area to optimize the components of the thia-Michael networks could prove fruitful and reveal applications that are derivative of different core compounds.

Experimental Methods

Instrumentation

Nuclear Magnetic Resonance (NMR) spectroscopy

Nuclear Magnetic Resonance Spectroscopy was performed using the 500 MHz Bruker AVANCE II+ 500; 11.7 Tesla NMR at the NMR facilities at the University of Chicago. Analysis of NMR results was done using MNova NMR processing software.

Tensile analysis

Tensile analysis was performed using a Zwick-Roell zwickiLine Z0.5 Materials Testing Instrument with a 100N load cell in the Soft Matter Characterization Facility at the University of Chicago. Samples were cut into 25 mm dogbones (Gauge length x width x thickness = 25 mm x 6 mm x 0.5 mm). Specimens were clamped using silicon rubber clamps to prevent tearing of the soft material. Test were conducted at various rates as indicated and at room temperature under ambient conditions.

Attenuated Total Reflectance Infrared Spectroscopy (ATR-IR)

Attenuated total reflectance infrared spectroscopy (ATR-IR) was conducted using the Shimadzu IRTracer-100 Fourier Transform Infrared Spectrometer equipped with a GladiATR single bounce attenuated total reflectance attachment with a diamond prism.

Thermogravimetric Analysis (TGA)

Thermogravimetric analysis was performed using a TA Instruments Discovery Thermogravimetric Analyzer in the Soft Matter Characterization Facility at the University of Chicago. Samples were tested under nitrogen atmosphere using platinum pans. Tests were conducted using a ramp of 10 °C/min from starting operating temperature (ca. 35 °C) to 600 °C.

Differential Scanning Calorimetry (DSC)

DSC was performed using a TA Instruments Discovery 2500 Differential Scanning Calorimeter in the Soft Matter Characterization Facility at the University of Chicago. Samples were prepared in aluminum hermetic pans from TA Instruments and were hermetically sealed. Typical test conditions involved a cool-heat-cool-heat procedure from (-20 °C/200 °C/-80 °C/200 °C) run at 10 °C/min.

Dynamic Mechanical Analysis (DMA)

DMA was performed using the TA Instruments RSA-GA DMA with Forced Convection oven (20 °C – 500 °C) attached to an Air Chiller System (-120 °C – 20 °C) and running TA Trios Software in the Soft Matter Characterization Facility at the University of Chicago. Pressed films were cut on a warm plate (temperature slightly above T_g of the network) into strips ca. 4 mm wide

and ca. 10 mm long, then cooled back to room temperature on a flat surface. The strips were loaded into the tensile geometry and finger tightened to prevent film breakage and ensure good contact with the tensile geometry. A typical procedure included an amplitude sweep (0.01% – 5%) above T_g at a frequency of 1Hz to define the linear viscoelastic region (LVR) as well as maximize the oscillatory force signal being picked up by the instrument. After the amplitude sweep, the samples were cooled to -20 °C using an IsoForce Temperature Ramp (0.01 N tension, 3.0 °C/min). Samples were soaked for 1 minute at -20 °C and a second amplitude sweep (0.01% - 5%) was conducted at a frequency of 1 Hz to optimize conditions below T_g. The samples were quite brittle at low temperatures and as such, it was important to closely monitor both the cooling process and the amplitude sweep for critically high force values (> 15 N) that could break the films.

Once parameters had been identified for optimal amplitude and frequency, temperature ramps could be conducted. Samples were loaded as previously described. A typical procedure included cooling to -20 °C using the IsoForce temperature ramp (0.01 N tension, 3.0 °C/min) and holding at -20 °C for 1 minute. Following the cooling step, conditioning options were enabled to account for automatic axial force adjustment (0.01 N ± 0.5 N tension, Set Initial Value box unchecked) and automatic strain adjustment set to the minimum oscillatory force for LVR above T_g and maximum oscillatory force for LVR below T_g as determined by the amplitude sweeps.

Samples were then heated using the oscillatory temperature ramp procedure from -20 °C to 150 °C (or until failure) at a rate of 3.0 °C/min with an amplitude set in the LVR of the -20 °C amplitude sweep and a frequency of 1 Hz.

Synthetic Procedures

1,6-bis(cyanoacetate) hexane (7)

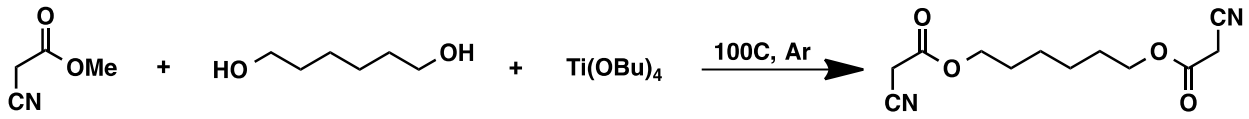

Scheme A1. Reaction scheme for the synthesis of the hexyl bis(cyanoacetate) core.

Methyl cyanoacetate (7.41 mL, 0.084 mol), 1,6-hexanediol (5.00 g, 0.042 mol), and catalytic titanium (IV) butoxide (0.35 mL, 0.001 mol) were added to a 25 mL round bottom flask with condenser. Mixture was heated, with stirring using a magnetic stir bar, to 100 °C and reacted overnight (~18 hours) with constant argon flow (nitrogen flow sufficient as well). After reaction, vial was cooled to room temperature under inert atmosphere.

Flask contents were solubilized in chloroform and filtered through deactivated neutral alumina pad (ca. 200 mL deionized water run through alumina pad to deactivate before exchanging solvent – water to methanol to chloroform – for filtering). Filtrate was dried using magnesium sulfate and excess chloroform was removed via rotary evaporation leaving a yellow-orange oil. Cyanoester was recrystallized from oil in freezer (-18 °C) for three days. Crystals were filtered and washed with ether then dried under high vacuum overnight. Final product was a white, crystalline powder. Product was characterized by ^{1}H NMR (600 MHz, $CDCl_3$; δ ppm: 1.41 (*m*, 2H), 1.72 (*m*, 2H), 3.43 (*s*, 1H), 4.22 (*t*, 2H)). Yield by mass = 45%. Melting point 69°C.

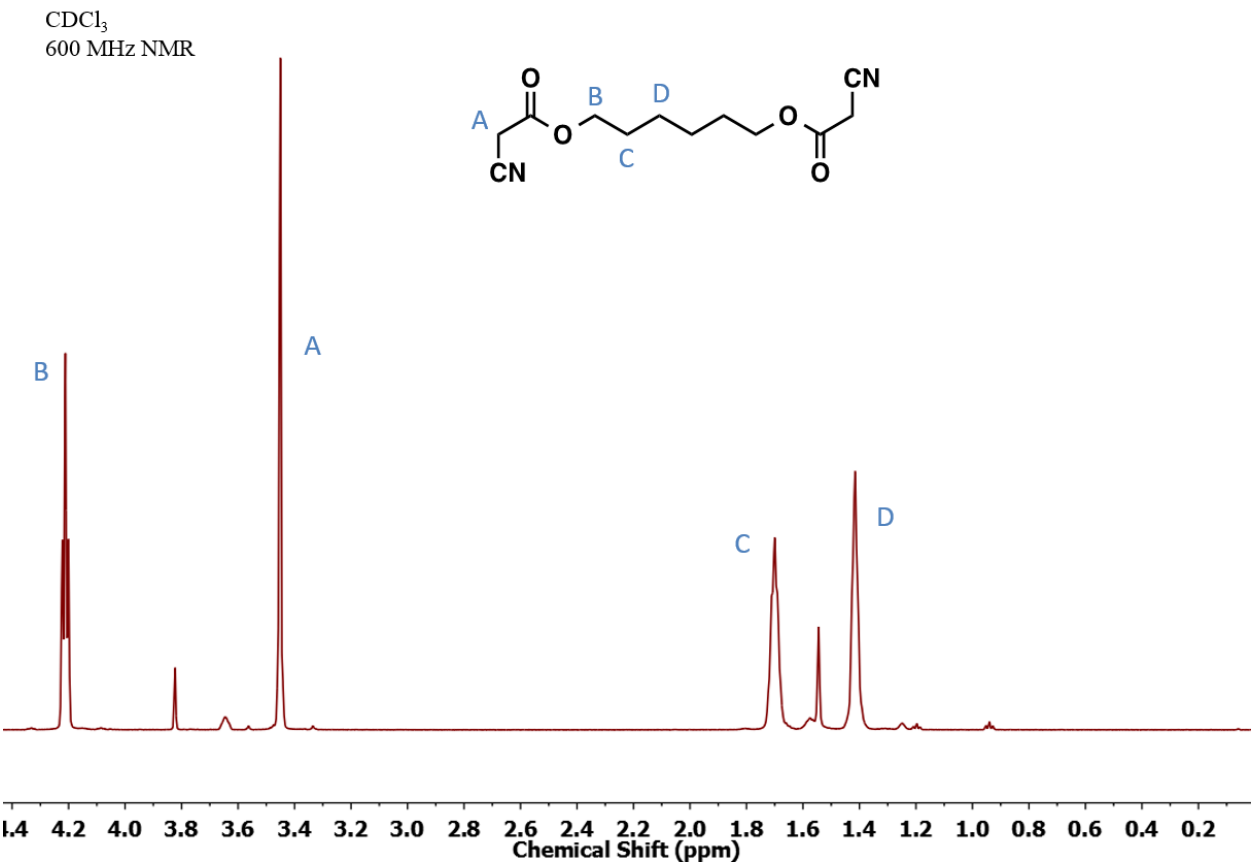

Figure A10. ^{1}H-NMR of 1,6-bis(cyanoacetate) hexane (**7**).

*1,6-(bis(4-nitrobenzalcyanoacetate)) hexane (**8N**)*

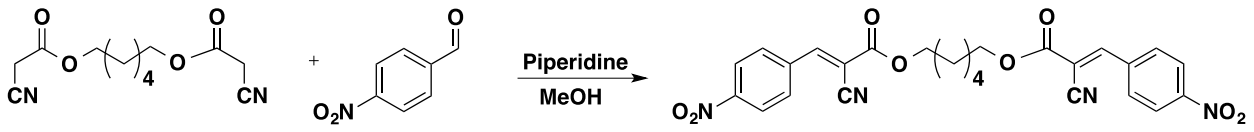

1,6-bis(cyanoacetate) hexane (1.00 g, 0.004 mol, .05 M) and 4-nitrobenzaldehyde (1.27 g, .0084 mol) were added to 80 mL methanol in a 250 mL round bottom flask. Piperidine (500 µL, .005 mol) was added to the solution and the reaction was stirred using a magnetic stir bar at room temperature for 3.5 hours. **8N** precipitated from solution and was filtered out upon completion of

reaction. Filtered solid was washed several times with methanol (until filtrate was clear) then collected and dried under high vacuum for 24 hours. Final product was a clumpy, beige powder. Product was characterized by ^{1}H NMR (600 MHz, d_6-DMSO; δ ppm: 1.48 (*m*, 2H), 1.70 (*m*, 2H), 4.27 (*t*, 2H), 8.18 (*d*, 2H), 8.32 (*d*, 2H), 8.51 (*s*, 1H). Yield by mass = 55%.

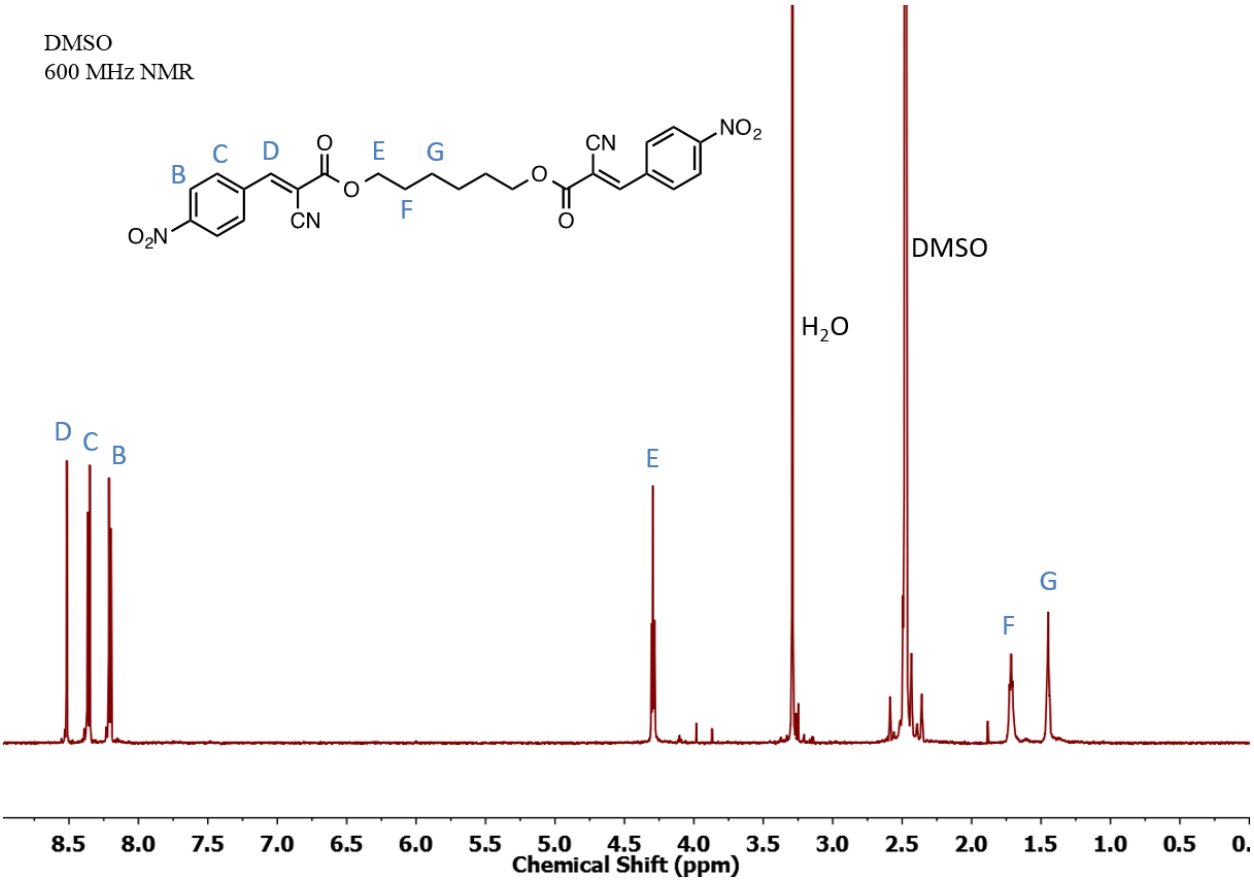

Figure A11. ^{1}H-NMR of 1,6-(bis(4-nitrobenzalcyanoacetate)) hexane (**8N**).

*1,6-(bis(benzalcyanoacetate)) hexane (**8H**)*

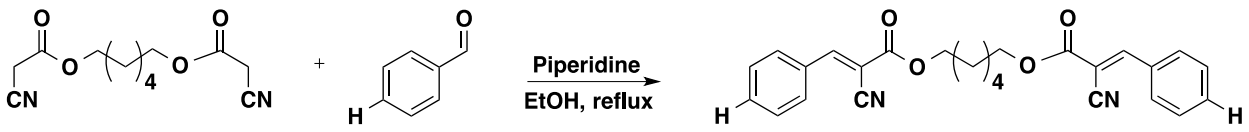

1,6-bis(cyanoacetate) hexane (1.00 g, 0.004 mol, .16 M) and benzaldehyde (0.90 g, .0084 mol) were added to 25 mL ethanol in a 100 mL round bottom flask. Piperidine (500 µL, .005 mol) was added to the solution and the solution was stirred using a magnetic stir bar. Reaction was heated to reflux (85 °C) and proceeded for 2 hours. After 2 hours, the reaction was cooled to room temperature and placed in a freezer (-18 °C) for 24 hours. **8H** precipitated from solution and was separated via vacuum filtration. Filtered solid was washed several times with ethanol (until filtrate was clear) then collected and dried under high vacuum for 24 hours. Final product was a fine white powder. Product was characterized by ^{1}H NMR (600 MHz, d_6-DMSO; δ ppm: 1.45 (*m*, 2H), 1.70 (*m*, 2H), 4.27 (*t*, 2H), 7.52 (*t*, 2H), 7.60 (*t*, 1H), 8.30 (*s*, 1H)). Yield = 67%.

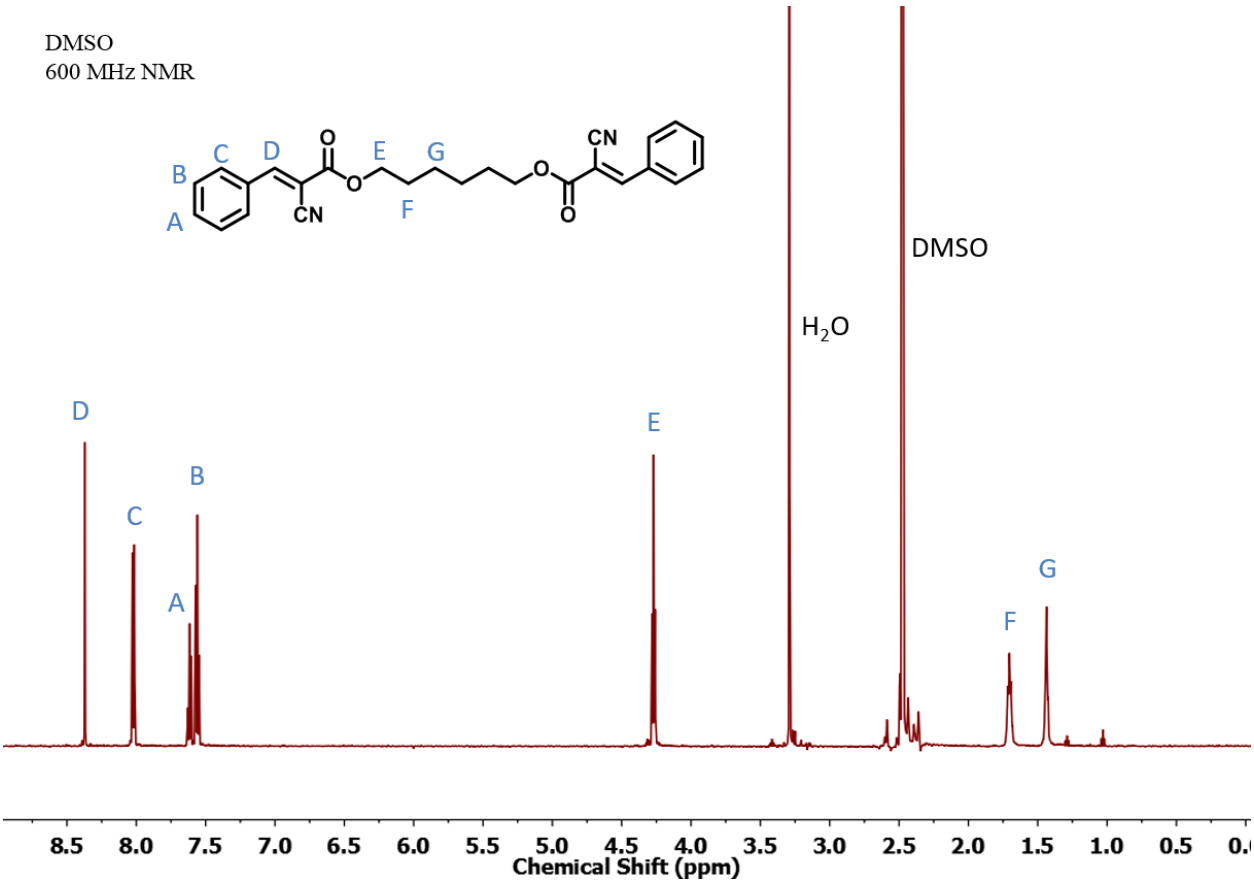

Figure A12. ^{1}H-NMR of 1,6-(bis(benzalcyanoacetate)) hexane (**8H**).

*1,6-(bis(benzalcyanoacetate)) hexane (**8M**)*

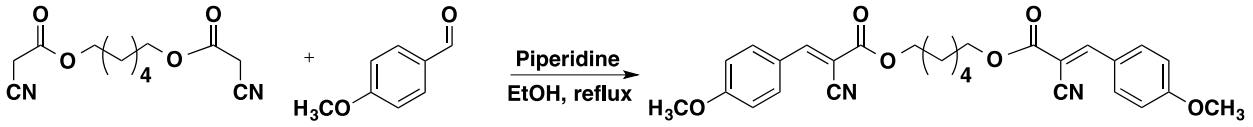

1,6-bis(cyanoacetate) hexane (1.00 g, 0.004 mol, .16 M) and 4-methoxybenzaldehyde (1.14 g, .0084 mol) were added to 25 mL ethanol in a 100 mL round bottom flask. . Piperidine (500 µL, .005 mol) was added to the solution and the solution was stirred using a magnetic stir bar. Reaction was heated to reflux (85 °C) and proceeded for 2 hours. After 2 hours, the reaction

was cooled to room temperature and placed in a freezer (-18 °C) for 24 hours. **8M** precipitated from solution and was separated via vacuum filtration. Filtered solid was washed several times with ethanol (until filtrate was clear) then collected and dried under high vacuum for 24 hours. Final product was a fine, light yellow-green powder. Product was characterized by ^{1}H NMR (600 MHz, d_6-DMSO; δ ppm: 1.45 (*m*, 2H), 1.70 (*m*, 2H), 3.80 (*s*, 3H), 4.27 (*t*, 2H), 7.14 (*d*, 2H), 8.05 (*d*, 2H), 8.30 (*s*, 1H)).

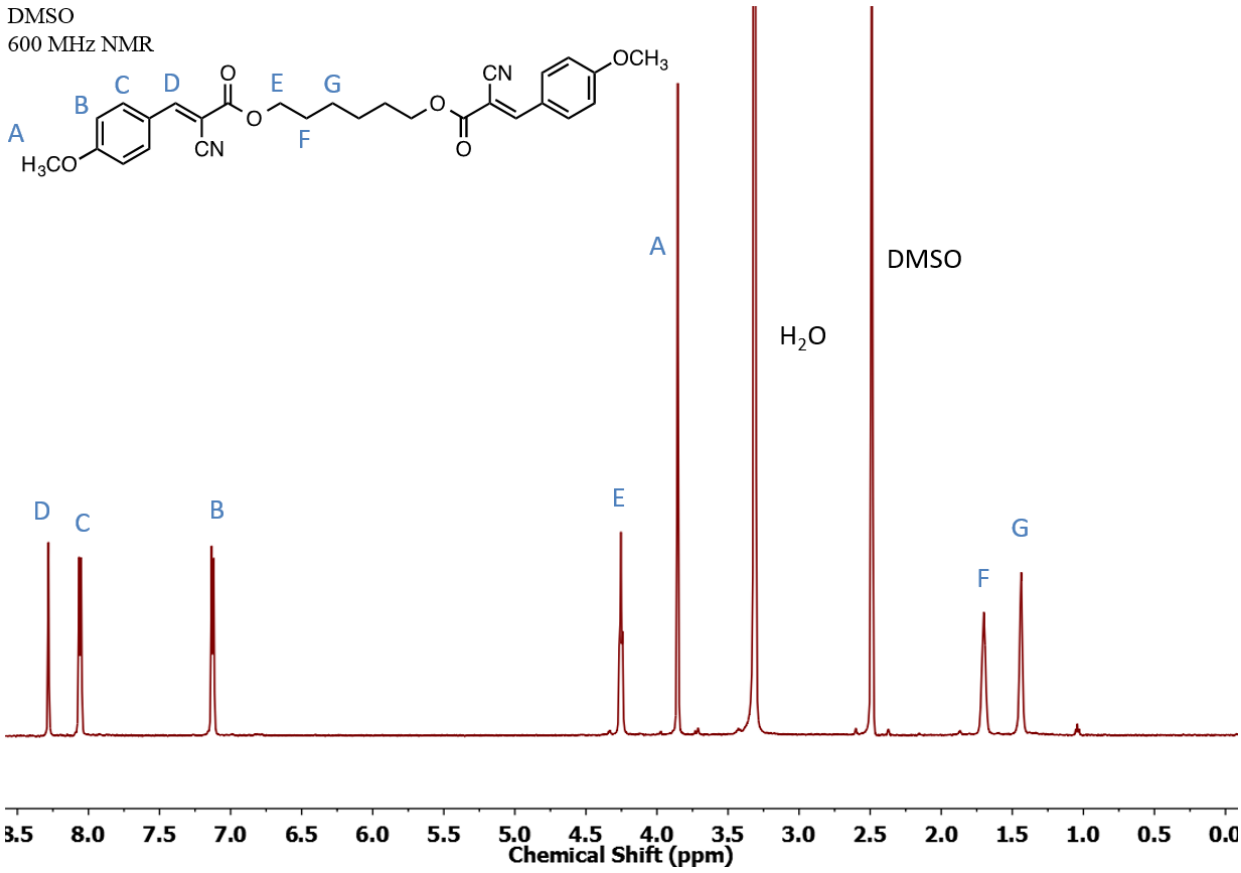

Figure A13. ^{1}H-NMR of 1,6-(bis(4-methoxybenzalcyanoacetate)) hexane (**8M**).

Film Preparation for films containing **8**

Electrophile(s) and PMMS were weighed into separate vial. To each vial, DMF was added (~0.5mL/100mg; extra solvent added if necessary to get solids into solution) and solutions were heated with heat gun until clear. PMMS in DMF was added to electrophile solutions (if mixed system, electrophiles were combined first, then PMMS was added to combined crosslinkers) and heated once more to ensure solution was clear. Solubilized networks were allowed to equilibrate for 24 hours (more than enough time for equilibration of all electrophiles based on NMR studies). Once equilibrated, the networks were cast onto Teflon dishes with aluminum cover, heated overnight on a hotplate (~50 °C), and dried in a vacuum oven for 24 hours.

Supplemental Results

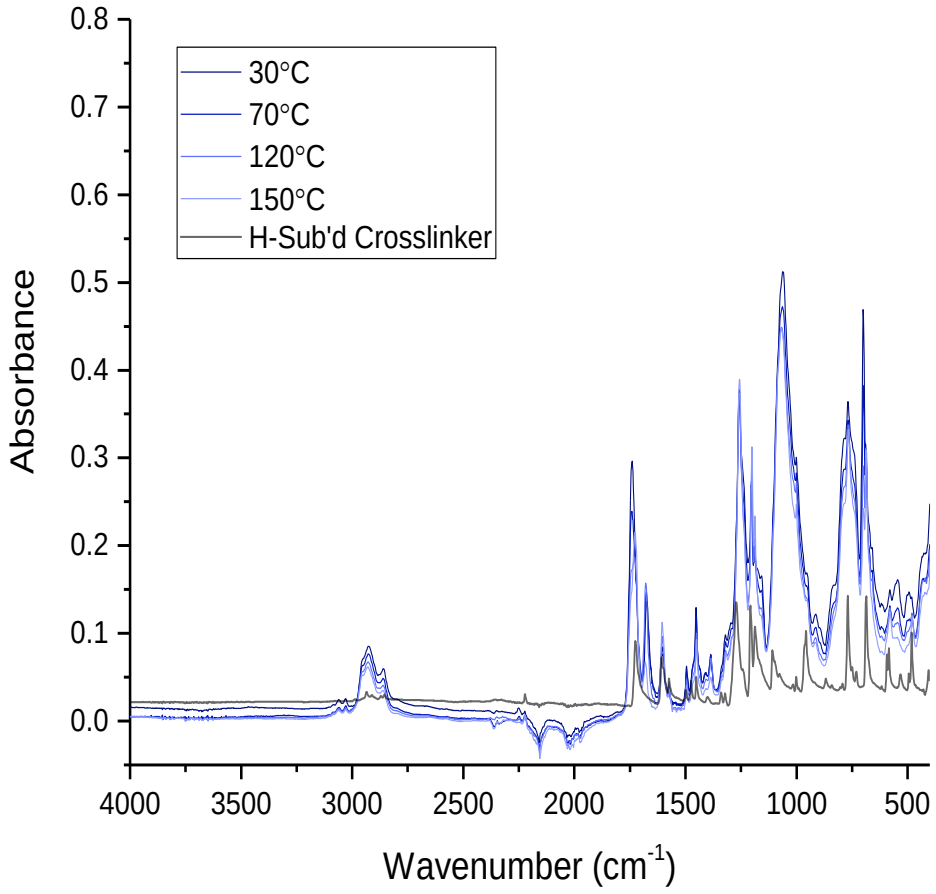

Figure A14. Full variable temperature ATR-IR of **9H$_{100}$**.

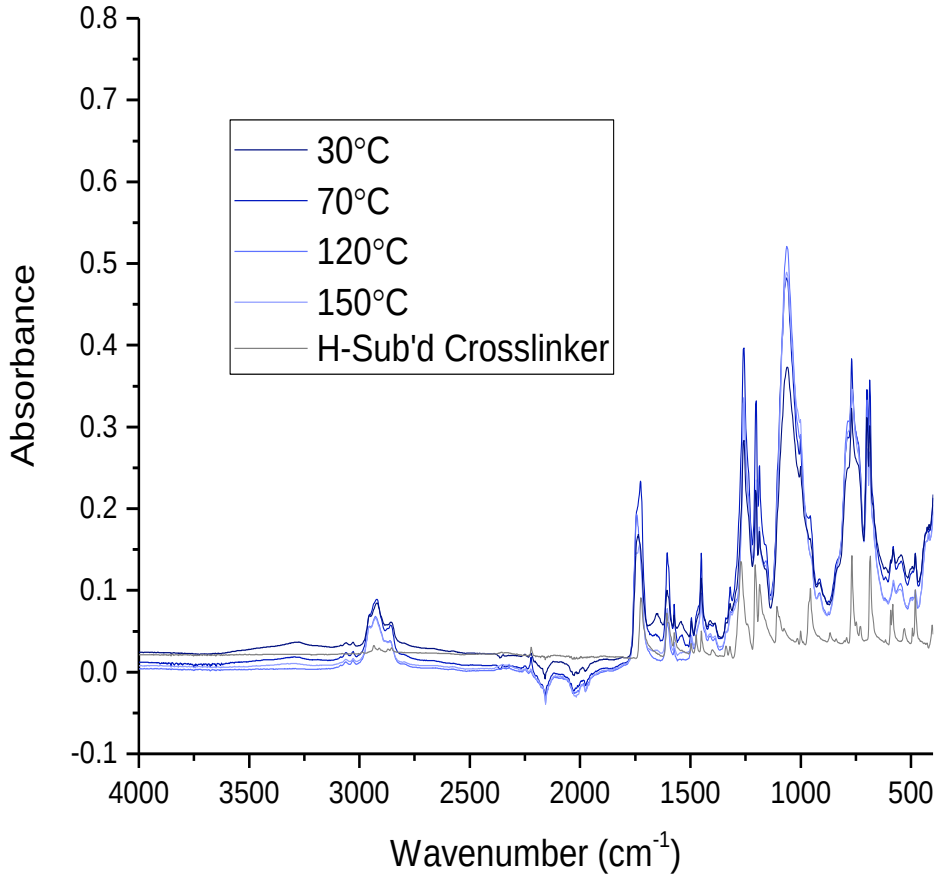

Figure A15. Full variable temperature ATR-IR of **9H$_{50}$**.

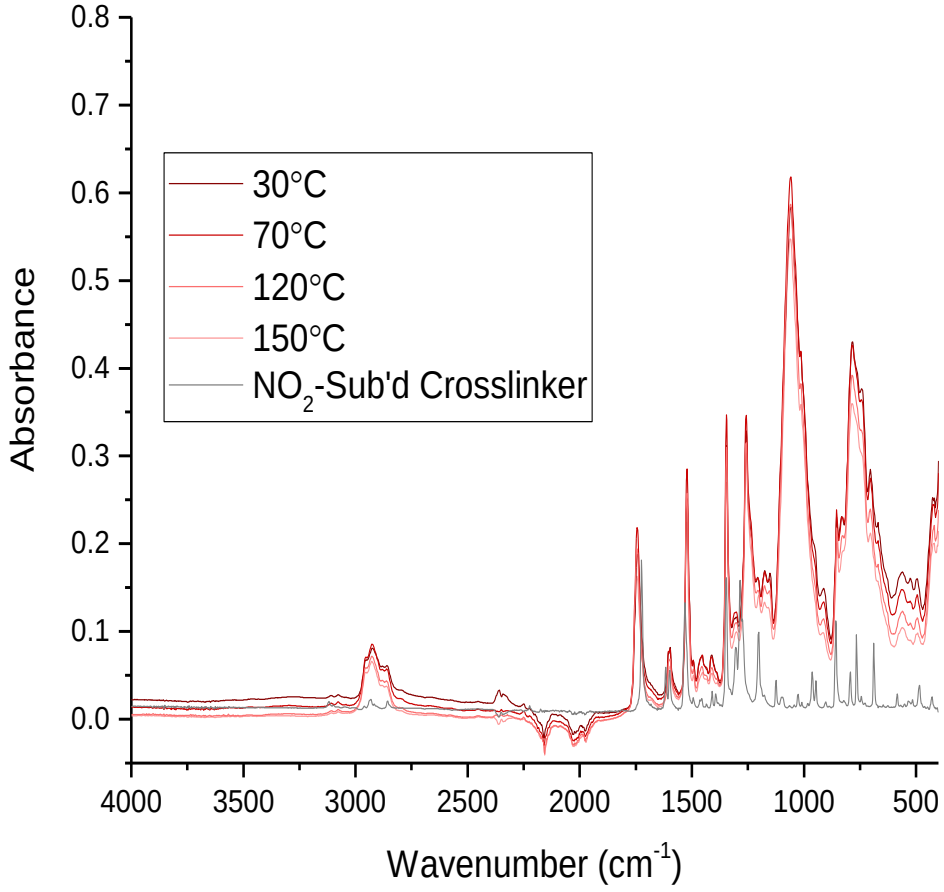

Figure A16. Full variable temperature ATR-IR of **$9N_{100}$**.

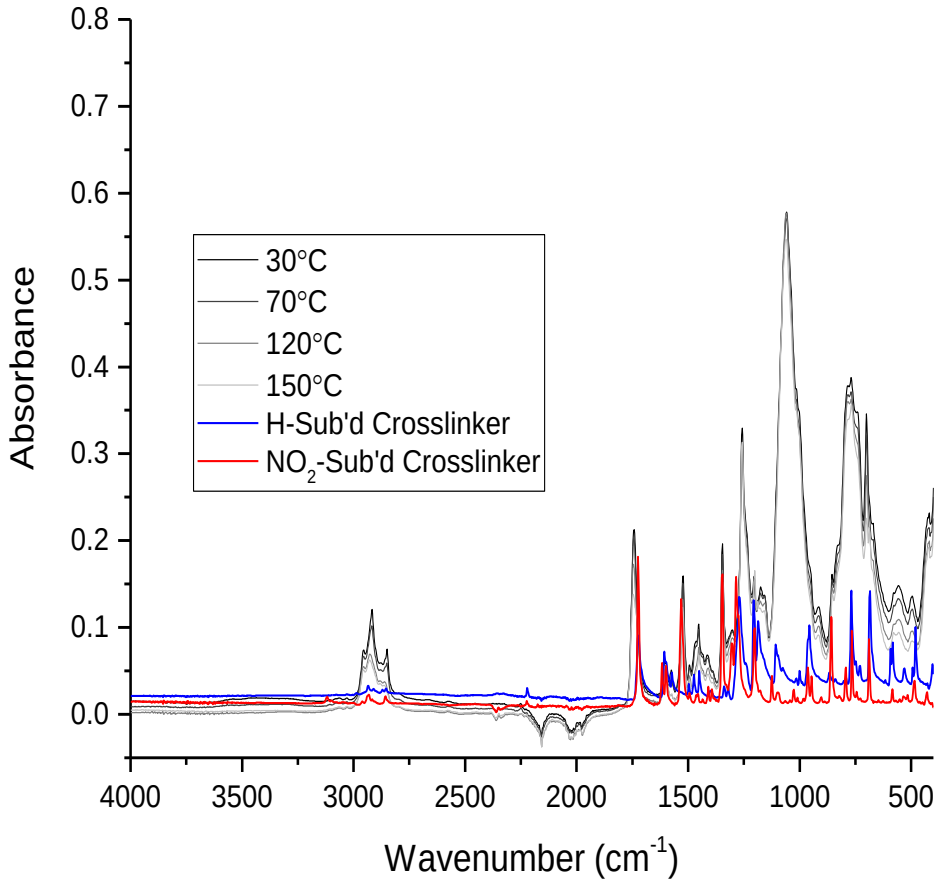

Figure A17. Full variable temperature ATR-IR of **$9N_{50}H_{50}$**.